INTERNATIONAL DOCTORAL
SCHOOL OF THE USC

Juan
Peñas Nadales

PhD Thesis

Production of radiotracers for medical imaging using laser-acceleration techniques

Santiago, 2023

Programa de doctorado en Física de Partículas

Universidad de Santiago de Compostela

Departamento de Física de Partículas

Production of radiotracers for medical imaging using laser-acceleration techniques

Author:
Juan PEÑAS NADALES

Supervisor:
Dr. José Fernando BENLLIURE
ANAYA

USC
UNIVERSIDADE
DE SANTIAGO
DE COMPOSTELA

May 21, 2023

UNIVERSIDADE DE SANTIAGO DE COMPOSTELA

Dr. José Fernando BENLLIURE ANAYA, PROFESOR DEL DEPARTAMENTO DE FISICA DE PARTICULAS DE LA UNIVERSIDAD DE SANTIAGO DE COMPOSTELA,

CERTIFICA:

que la memoria titulada:

Production of radiotracers for medical imaging using laser acceleration techniques

fue realizada por **Juan PEÑAS NADALES** en el Departamento de Física de Partículas de la Universidad de Santiago de Compostela bajo su dirección, y constituye el trabajo de **tesis** que presenta para optar al grado de **Doctor en Ciencias Físicas.**

Santiago de Compostela,
May 21, 2023

Dr. José Fernando BENLLIURE ANAYA
Departamento de Física de Partículas

"*Once he wore grey, he fell and slipped away,*

from everybody's sight.

The wizard of them all, came back from his fall,

this time wearing white."

Camel, *The White Rider*

UNIVERSIDADE DE SANTIAGO DE COMPOSTELA

Abstract

Facultad de Física

Dpto. de Física de Partículas

Doctor of Physics

Production of radiotracers for medical imaging using laser acceleration techniques

by Juan PEÑAS NADALES

The objective of the doctoral thesis is to study whether the acceleration of laser-induced particles can be a competitive option for the production of positron-emitting radiotracers. To do this, an experimental work is proposed using the laser of the Laboratorio Láser de Aceleración y Aplicaciones (L2A2) of the Universidad de Santiago de Compostela. This work will consist of putting into operation the necessary technology to accelerate a sufficient and continuous amount of protons or deuterons with energies of up to 10 MeV.

Acknowledgements

I would like to express my deepest gratitude and appreciation to all those who have supported and guided me throughout my journey in completing this doctoral thesis. First, I would like to thank my supervisor, José Benlliure, for their firm guidance, invaluable insights, and constant encouragement. His expertise, patience, and dedication played a pivotal role in shaping the direction of this research and enhancing its quality. Furthermore, I extend my heartfelt appreciation to my colleagues and fellow researchers who have shared their knowledge, ideas, and support during the extent of this thesis.

Special thanks to my family and friends, for their unwavering love, encouragement, and understanding throughout this challenging stage. Their constant support and belief in my abilities have been my greatest motivation.

Contents

List of Figures

List of Tables

List of Abbreviations

ASE	**A**mplified **S**pontaneous **E**mission
BR	**B**ranching **R**atio
CPA	**C**hirped-**P**ulse **A**mplification
EM,**EMP**	**E**lectro**m**agnetic **P**ulse
FWHM	**F**ull-**W**idth at **H**alf **M**aximum
IP	**I**mage **P**late
IR	**I**nfra**r**ed
MCP	**M**icro-**C**hannel **P**late
MEMS	**M**icro-**E**lectro**m**echanical **S**ystem
OAP	**O**ff-**A**xis **P**arabola
OD	**O**ptical **D**ensity (filter)
PET	**P**ositron **E**mission **T**omography
PIC	**P**article-**I**n-**C**ell
PMT	**P**hoto**m**ul**t**iplier
RCF	**R**adio-**C**hromic **F**ilm
RF	**R**adio-**F**reqcuency
RMS	**R**oot-**M**ean **S**quare
RPA	**R**adiation **P**ressure **A**cceleration
SPECT	**S**ingle-**P**hoton **E**mission **C**omputed **T**omography
TCC	**T**arget **C**hamber **C**entre
TNSA	**T**arget **N**ormal **S**heath **A**cceleration
ToF	**T**ime-**o**f-**F**light
TP	**T**homson **P**arabola
TTL	**T**ransistor-**T**ransistor **L**ogic
XPW	**C**ross-**P**olarised **W**ave

Physical Constants

Speed of Light	$c = 2.997\,924\,58 \times 10^{8}\,\mathrm{m/s}$ (exact)
Elemental charge	$e = q = 1.6 \times 10^{-19}\,\mathrm{C}$
Electron mass	$m_e = 0.511\,\mathrm{MeV}$
Proton mass	$m_p = 931\,\mathrm{MeV}$
Avogadro constant	$N_A = 6.02 \times 10^{23}\,1/\mathrm{mol}$
Vacuum permittivity	$\epsilon_0 = 8.85 \times 10^{-12}\,\mathrm{F/m}$
Boltzmann constant	$k_B = 8.62 \times 10^{-5}\,\mathrm{eV/K}$
Bohr radius	$a_B = 0.53 \times 10^{-10}\,\mathrm{m}$
Reduced Plank constant	$\hbar = h/2\pi = 6.58 \times 10^{-16}\,\mathrm{eV\ s}$

List of Symbols

A	atomic mass	
a_0	adimensional laser amplitude	
c_s	sound speed	m/s
E_L	laser energy	J
E_{max}	cut-off energy	MeV
L_g	plasma scale-length	m
n_c	critical density	m^{-3}
n_x	density of species x	m^{-3}
P	power	W (J/s)
T_e	electron hot temperature	K
Z_i	ion charge state	
γ	Lorentz factor	
ε	efficiency	
λ_L	laser wavelength	m
η	refractive index	
θ	angle	rad
ρ	density	g/m^3
σ	angular divergence	rad
σ_r	cross-section	m^{-2}
τ_L	laser pulse duration	s
Ω	solid angle	srad
ω_L	laser frequency	rad/s
ω_p	plasma frequency	rad/s

Dedicated to my parents, my family, and my beloved friends.

Chapter 1

Introduction

1.1 Motivation

1.1.1 Context on medical radiotracers

Positron Emission Tomography (PET) imaging has become an indispensable tool in medical diagnostics and research. As this technique allows for the real-time imaging of the distribution and metabolism of radiotracers inside the body, it provides *in vivo* information about physiological and pathological processes. Due to this, it is widely used for the early detection and treatment of cancer and neurodegenerative diseases. PET imaging is based on the correlated detection of the two backscattered photons produced at the annihilation of positrons emitted from β^+ radioactive isotopes. These radioisotopes, acting as the radiotracer, are administered to the patient coupled to a certain biochemical substance that targets an specific organ or tissue of interest inside the body. Upon reaching the destination, the escaping radiation —γ-photons at 511 keV— is detected by a PET scanner, typically composed of multiple ring detectors surrounding the patient. By measuring the time delay between the two photons, the scanner can determine the location of the radioactive decay process and generate a three-dimensional image (tomography) of the distribution and metabolism of the radiotracer.

The recent development of PET, as well as other medical imaging techniques like SPECT (Single-Photon Emission Computed Tomography) or gammagraphy, has led to an increase in the demand of nuclear radioisotopes for medical diagnostics. At present, radioisotope production for medical imaging and treatment is principally performed at conventional —or radiofrequency (RF)— accelerators and dedicated nuclear reactors. In the particular case of β^+ emitters used in PET imaging, the current approach is based on the mass-production at these large singular

facilities, which are in charge of maintaining the radioisotope supply at a regional or a national scale. Due to the expensive costs associated to the production centres, accelerators, radiopharmacy, and specially radiation shielding, the economic viability of these centres is based on the mass-scale production of single doses distributed to as many as possible hospitals, clinics, and research centres. As a result of this extensive scope, commercial production of PET radioisotopes is mainly limited to ^{18}F: having a half-life of $\sim$110 minutes, it can endure the overall time required for its production, post-processing, and distribution. In addition, higher doses than necessary must be produced to account for the decay time. On the other hand, the use of short-lived radioisotopes in PET imaging, such as ^{11}C ($\sim$20 min), ^{13}N ($\sim$10 min), or ^{15}O ($\sim$2 min), has become increasingly popular due to their accurate imaging resolution while providing a short exposition time for the patient. As they decay rapidly and require immediate use, the production of a limited number of doses is generally out of the scope of the producing facilities. On this subject, the use of ultra-short ultraintese lasers for radioisotope production has been proposed over the last decades(1,2) as a cost-efficient alternative to conventional production methods for the on-demand production of single doses of short-lived radioisotopes.

Laser-driven ion acceleration is based on the interaction between a high intensity laser pulse and a solid or fluid target, which results in the efficient acceleration of ions. Due to the unique properties of the laser-target interaction, such as the high peak intensity and ultra-short laser pulse duration, it allows for reaching electric fields around TV/m, in contrast to RF accelerators which saturate at $\sim$100 MV/m. This leads to a higher energy conversion and a more efficient ion acceleration. Furthermore, these laser systems are much more compact and affordable than RF accelerators. As both the interaction and the acceleration process occurs within a micrometric scale and over several picoseconds, the shielding requirements are mainly limited to the area close to the interaction point, resulting in a significant reduction in size and cost compared to conventional accelerators.

Regarding radioisotope production, laser-accelerated ions can be used to induce nuclear reactions on a secondary target, in order to produce the transmutation of the material to a certain isotope of interest. A key advantage of this technology in contrast to conventional production is the potential to produce a wide range of isotopes at the desired dose levels by modifying the laser and target properties, and the operation time. This could allow in principle to hospitals and research centres to produce the required doses on-demand. In this way, the regional or national scope of large producing facilities is translated to local production. Therefore, the use of laser-driven ion sources for radioisotope production offers significant advantages in terms of

cost-effectiveness, efficiency, and accessibility.

1.1.2 Objective of this thesis

Following the aforementioned arguments, ultraintense lasers may constitute a appropriate alternative for the on-demand production of single doses of short-lived radioisotopes used in PET imaging. The aim of this doctoral thesis is to explore the potential of laser-driven particle acceleration as an efficient means of the production of these radioisotopes. Typical required doses for PET are in the range of 10 – 30 MBq for preclinical, and between 200 MBq and 1 GBq for clinical imaging, being the scope of this work situated at a preclinical level. Concretely, the focus of this study relies on the production of ^{11}C through the proton-induced nuclear reaction ^{11}C(p,n)^{11}B using a proton beam from a laser-driven source. This includes the experimental characterisation of the production process as well as precise estimations and extrapolations for further investigations.

For this purpose, the first step consisted on the development of an ion source matching the requirements in stability and sustained operation over time for radioisotope production. This involved the design and construction of a multi-shot target system capable of overcoming the mechanical challenges commonly found in laser-plasma interaction. The performance of the design proposed in this thesis was firstly evaluated as part of the current commissioning campaign at the Laser Laboratory for Acceleration and Applications (L2A2) in the Universidade de Santiago de Compostela (USC), and finally employed as the main ion source at an experimental campaign at the Centro de Láseres Pulsados (CLPU), focussed on neutron generation.

The protons accelerated within the CLPU experiments were used to successfully produce and measure ^{11}C activities by irradiating a boron target. The thesis also involves the simulation and modelling of the production process, as well as the several mechanisms that govern laser-target interaction and particle acceleration, for their proper understanding and optimisation. Overall, the outcome of this research could contribute to the development of a more cost-effective, efficient, and accessible method for the production of radioisotopes used in PET medical imaging.

1.2 Structure of the thesis

The theoretical foundations and the current state-of-art that define the framework at which this thesis is enclosed are presented in Ch. 2. Within this chapter, the fundamentals on both

laser-driven particle acceleration and radioisotope production from a laser-accelerated ion source are presented. For the former, an overview of the principal mechanisms governing laser-plasma interactions that led to efficient electron and ion acceleration are detailed. Regarding the later, this chapter addresses the prevalent formalism for the induced production of radioisotopes and the characterisation of radioactive samples.

The next chapter, Ch. 3, presents the methods, devices, and tools employed in this work. This includes a detailed description of the two laser systems where the experiments that comprise this thesis were performed (STELA and VEGA), the properties of the main detectors that were used within these experiments, and the principles and functioning of the numerical simulation codes for the analysis of the results.

Ch. 4 delves into the complete development of the multi-shot target system used at the experimental campaigns. A description of the assembly is firstly presented, along with the designed positioning and correction procedure and its implementation through a self-developed control software. The evaluation of the system performance, regarding its shot-to-shot stability and sustained operation over time, is then discussed and validated. The operation process within the experiments is also depicted.

An entire chapter —Ch. 5— is dedicated to the experiments on laser-driven ion acceleration carried out within this work. This chapter is divided in four major parts: each of the two main experimental campaigns at which the author participated have a separate section, containing the description of the set-up and methodology, and an exposition of the obtained results; other section comprises the Particle-In-Cell numerical simulations performed in order to supplement the experimental data; the analysis and the comparison between results are finally presented in the last sections, focussing on the scaling of the main parameters characterising the accelerated ion beams with the laser and the target properties.

In Ch. 6, radioisotope production from laser-accelerated protons is addressed. The target and diagnosis system, developed for the transmutation and activity characterisation of ^{11}C from the proton-induced ^{11}C(p,n)^{11}B nuclear reaction, is described and depicted. Following the calibration of such system, the experimental arrangement and methodology are presented. The analysis of the activation results, as well as its comparison with recently published data and some future extrapolations, is given at the end of the chapter.

Final conclusions are then presented in Ch. 7.

1.3 Role of the author

The work presented in this thesis comprises the commissioning of an ion source at the L2A2, in a combined effort with the staff personnel and the researcher team. In particular, the author was mainly dedicated to the design of the multi-shot target system. A significant part of this work involved the complete development of the control software, which may not be reflected in this document but for a few mentions. Due to this facts, some of the contents of this document may appear rather technical, in comparison with other doctoral theses about the same topic.

The expertise obtained within the development of the on-site laser-plasma ion source was used in an experimental campaign at the Centro de Láseres Pulsados (CLPU) laser facility. The multi-shot target system was employed as a laser-induced ion source for the experiment, which was focussed on neutron production. Several modifications and tests were performed by the author in order to adapt the target assembly and its operation procedure to the distinctive features of the CLPU facility, either before and during the experiment. The author was in charge of the proper functioning of the target assembly within the CLPU campaign. Along with the researcher and technical staff participating in the experiment, measurements on laser-driven ion acceleration could be performed. In addition, a device for the activation of ^{11}C induced by laser-accelerated protons was designed at the L2A2 and mounted at the CLPU experiment. The operation of this system and the data acquisition relied on the author.

Several particle and radiation detectors were calibrated for their use at the laser driven ion acceleration and radioisotope production experiments. For the former, a Time-of-Flight detector, developed at the Instituto de Instrumentación para Imagen Molecular (I3M), was calibrated at the Centro Nacional de Aceleradores (CNA) by researchers from both institutions and the author. The radiation detectors used for the radioisotope decay activity measurements were calibrated and characterised by the author by means of experimental analysis and Montecarlo simulations (EnsarROOT code).

Regarding the data treatment, the author is responsible of the results presented in this work and their complete analysis, under the supervision of Dr. J. Benlliure and the assistance of Dr. A. Alejo. The author also performed several Particle-In-Cell (PIC) simulations in order to complement the experimental data. In particular, the Smilei code was used for the simulation of laser-plasma interaction and laser-induced ion acceleration.

Chapter 2

Background and state-of-art

This chapter details the theoretical framework, as well as a summary of recently published data, about the topics of this thesis, in order to provide a solid background for the work presented here. Thus, this chapter serves as a means of understanding the underlying physics that dominate the interaction of ultraintense laser pulses with matter for ion acceleration, and the production of radioisotopes, in the context of PET medical imaging, from them. Sect. 2.1 introduces the context on the interaction of electromagnetic radiation with matter, and in particular, the effects of a intense electromagnetic pulses on a ionised plasma. The principal absorption mechanisms that govern the laser-plasma interaction and that lead to efficient electron acceleration are discussed in Sect. 2.2. Then, Sect. 2.3 details the main mechanisms of ion acceleration from laser-driven interaction. Regarding the ratioisotope production scope of this thesis, Sect. 2.4 summarises the processes that arise in the interaction of ionising radiation with matter, and finally a description of the physics involved in the induction of nuclear reactions from laser-accelerated ions is given in Sect. 2.5.

2.1 Laser-plasma interaction

The properties of ultraintense ultra-short laser pulses will be described in detail in Ch. 3. For now, they will be simply defined as a finite huge electromagnetic oscillating field concentrated in an ultra-short pulse of several tens of femtoseconds to a few picoseconds and a micron-size area. The intensity of these laser pulses, defined as the energy density in time and space, can be estimated by equation

$$I_L \sim \frac{\epsilon_0 c}{2} E_0^2 \tag{2.1}$$

where ϵ_0 is the vacuum permittivity, c the speed of light, and E_0 the amplitude of the electric field, given by expression $E_0 = A_0\omega_L$ from the amplitude of the vector potential A_0 and the oscillation frequency of the laser ω_L.

When a pulse having these properties impinges on a fluid or solid target, it ionises the atoms of the material leading to the formation of an underdense or overdense expanding plasma, respectively. Eq. 2.1 can be compared with the atomic intensity given by the atomic electric fields of the Coulomb potential. Considering the ionisation mechanism with the most simple description, barrier suppression ionisation(1), this intensity can be calculated from Eq. 2.1 and the definition of electric field from the Coulomb's law

$$I_a = \frac{\epsilon_0 c}{2} E_a^2 = \frac{\epsilon_0 c}{2} \left(\frac{e}{4\pi\epsilon_0 a_B^2} \right)^2 \tag{2.2}$$

In this expression, $a_B = \frac{4\pi\epsilon_0\hbar^2}{m_e c^2}$ corresponds to the Bohr's radius of an atomic electron orbiting around the nucleus as described in the Bohr's atomic model. Here, e is the elemental charge, $\hbar$ is the reduced Planck constant, and m_e is the electron mass. Thus, the intensity associated to the atomic electric field can be estimated to be of the order of 10^{15} – 10^{16} W/cm^2. Laser pulses with intensities above this value will ionise the surface of the medium, hence generating a plasma of free —unbound— electrons and ions.

The ponderomotive force

The description of the effect of an intense and finite oscillating electromagnetic pulse on a plasma can be firstly understood by considering the simple case of a single electron. The temporal intensity profile of a laser pulse can be depicted as a Gaussian envelope with an internal oscillation given by its frequency. As will be seen in Ch. 3, the spatial intensity profile of a focussing laser pulse can be considered as a two-dimensional Gaussian as well, being more intense at the central point. A plasma electron, located at the centre of the laser focus and oscillating according to the field, is pushed away to regions of lower intensity during the first half-cycle of the laser pulse, i.e., the rise time of the Gaussian envelope. During the second half, the electron is accelerated in the opposite direction but, as the amplitude of laser pulse decreases

over time, it experiences a reduced restoring force. This results in a net-positive acting force that is commonly referred as ponderomotive force[1, 2]. It can be described in terms of the electric field gradient of the laser pulse as

$$\mathbf{F}_p = \frac{-e^2}{2m_e\omega_L^2}\boldsymbol{\nabla} E_0^2 \tag{2.3}$$

that, in regards to the pulse intensity from Eq. **??**, can be expressed as

$$\mathbf{F}_p = \frac{-e^2}{m_e\epsilon_0 c\omega_L^2}\boldsymbol{\nabla} I_L \tag{2.4}$$

It can be seen at these expressions that the force is directed along the field gradient, the propagation direction, and proportional to the laser intensity. Hence, an electron located at a certain distance from the focal spot will experience a reduced force and will be pushed at a certain angle with respect to the propagation direction. A key of this process is the finite duration of the laser pulses. An infinite plane wave would not produce a net force on the electrons as they would return to their initial position after the oscillations, thus not gaining net energy. For the relativistic regime, above 10^{18} W/cm^2, the ponderomotive force definition can be updated by including the Lorentz relativistic factor $\gamma^{-1} = \sqrt{1-\beta^2}$.

Propagation of a laser pulse in a plasma

In the real experimental case, the pedestal of the laser pulses preceding the main peak (see Fig. 3.2 in Ch. 3) produces an expanding plasma that, through the interaction with the main pulse, leads to the efficient acceleration of electrons. This preplasma spreads at a velocity given by the sound speed of the ions

$$c_s = \sqrt{\frac{Z_i k_B T_e}{m_i}} \tag{2.5}$$

being Z_i and m_i the ion charge state and mass, respectively, k_B the Boltzmann constant, and T_e the hot electron temperature. For the relativistic regime, this temperature can be roughly estimated to be equal to the ponderomotive potential[3, 4]. Assuming the poderomotive force is a conservative force, as it can be expressed in terms of a gradient, this potential U_p can be calculated from Eq. 2.3 as

$$k_B T_e \sim U_p = \frac{e^2 E_0^2}{2 m_e \omega_L^2 \gamma} = m_e c^2 \left(\sqrt{1 + a_0^2} - 1 \right) \tag{2.6}$$

$$a_0 = 0.85 \sqrt{\frac{I_L \lambda_L^2}{10^{18}\ \mathrm{W\ cm^{-2} \mu m^2}}} \tag{2.7}$$

In this expression, I_L is introduced in W/cm^2 units and λ_L is the laser wavelength in μm. The parameter a_0, formally called the dimensionless amplitude, determines the regime of the interaction. The relativistic limit is set at $a_0 = 1$, corresponding to $\sim 10^{18}$ W/cm^2 for a typical 800 nm laser system, above which the interaction can be considered as relativistic, whereas for $a_0 < 1$ it can be treated as classical.

The expanding plasma exhibits a density profile that grows close to the target surface. Assuming isothermal expansion, this density profile n_e can be described in good approximation by a exponential distribution along the propagation direction z as

$$n_e(z) \propto \exp(z/L_g) \tag{2.8}$$

where L_g is called *plasma scale-length* and is defined as the distance at which the plasma density is $1/e$ of its initial value. Other variations of this profile have been explored in literature, as for example linear and parabolic shapes[5] or an smoothed exponential $n_e \propto [\tanh(\frac{z}{L_g}) + 1]$. Following the isothermal assumption, the scale-length can be estimated from the ion sound speed (Eq. 2.5) and the duration of the pulse pedestal τ_{ASE}

$$L_g \approx c_s \tau_{ASE} \tag{2.9}$$

In some other cases, the duration of the laser pulse or the anticipation time with respect to the main pulse of the prepulses above the ionisation threshold, if any, can be used for calculating this parameter.

As the main pulse reaches the preplasma, it can only penetrate if its oscillation frequency satisfies the propagation condition $\omega_L > \omega_p$, obtained from the evaluation of Maxwell's equations. The parameter ω_p is the plasma frequency of the electrons, whose definition is

$$\omega_p = \sqrt{\frac{n_e e^2}{m_e \epsilon_0}} \tag{2.10}$$

where n_e is the density of the free electrons in the plasma. If the laser frequency is lower than the plasma frequency, the electrons are able to oscillate at such frequency and thus compensate the electric field. In this way, the energy from the laser pulse is dissipated in the plasma. If the laser frequency is higher, on the contrary, the electrons only "see" the Gaussian envelope instead of the oscillation, leading to their effective acceleration. This can be also explained in terms of the refractive index η of the plasma medium, given by expression

$$\eta = \sqrt{1 - \frac{\omega_p^2}{\omega_L^2}} = \sqrt{1 - \frac{n_e}{n_c}} \tag{2.11}$$

If the propagation condition is satisfied, the refractive index has a real value and the wave can propagate along the medium. On the contrary, if the condition is not satisfied, the refractive index becomes pure imaginary and the electromagnetic pulse is either absorbed or reflected at the plasma front. The parameter n_c in this equation is defined as the critical density at which $\omega_L = \omega_p$.

As the pulse propagates through the preplasma, the electrons are pushed due to the ponderomotive force towards the target. This leads to a density wave propagating along the plasma density profile with increasing amplitude over time, as more electrons are concentrated at the wavefront. For the case of solid targets, the main pulse follows the density wave until it reaches the critical density. Then, the pulse cannot propagate further and is mostly reflected. The accelerated electrons, on the contrary, are injected into the target.

2.2 Absorption mechanisms

As indicated in previous section, the incidence of a ultraintense ultra-short laser pulse at a solid target produces an expanding plasma where the electrons are accelerated. Several acceleration mechanisms that let the energy gain by the electrons can occur at the critical density limit, depending on both laser and target properties. These properties, as for example the pulse intensity, the angle of incidence, or the laser polarisation, will favour one or multiple acceleration mechanisms. Throughout this section, several mentions to the laser polarisation will be made.

In particular, p- or s-polarisation, which are two types of linear polarisation of the laser electric field. In the context of a laser pulse impinging on a solid target at a certain incidence angle, p-polarisation implies that a component of the electric field is perpendicular to the target surface, that is, parallel to the density gradient of the preplasma. In s-polarisation, on the contrary, the field oscillation is parallel to the target surface.

Some of the mechanisms described in this section are predominant at moderate intensities, i.e., below $a_0 = 1$. While the laser systems employed in the experimental part of this thesis are mostly relativistic (a_0 ranging between 1 and 10), these mechanisms are in principle not relevant. However, a brief description of them will be provided as they dominate the interaction of the laser pedestal with the targets, that produces the formation of the preplasma. For the following, only the interaction of a laser pulse with a solid target, hence an overdense plasma, will be considered. Other mechanisms for the efficient acceleration of electrons dominate the interaction of an underdense plasma and a laser pulse, as for example *wakefield* acceleration[6, 7]. Since no experiments were performed using gaseous or liquid targets, these mechanisms are not relevant in the scope of this thesis.

2.2.1 Moderate-intensity mechanisms

Resonant absorption

Resonant absorption[6, 8] is the principal collision-less mechanism for the electron acceleration at moderate intensities. It occurs for laser pulses incident at a certain non-zero angle with respect to the target normal, and p-polarisation. This conditions guarantee that a component of the electric field oscillates in the same direction as the density gradient at the target surface ($\mathbf{E} \cdot \boldsymbol{\nabla} n \neq 0$). The plasma electrons then follows the oscillation and a density wave —also called Langmuir wave— is generated at ω_L. At the critical surface, where $n_e = n_c$, this density wave is excited to a resonance at this frequency and a significant fraction of the laser energy is transferred to the electrons. This fraction can be estimated from expression[1]

$$f_{RA} \approx 1.15\tau^2 \exp\left(\frac{-4\tau^3}{3}\right) \tag{2.12}$$

where $\tau = (\omega_L L_g/c)^{1/3} \sin\theta$, and θ is the incidence angle. Ideally, the laser pulse is then reflected at the critical density and the excited plasma wave propagates towards the target transmitting its energy to the rest of the plasma electrons.

In reality, as the incidence of the laser pulse is oblique to the target surface, the electric field is reflected at a plasma density given by $n_e < n_c \cos^2\theta$ before reaching the critical surface. From this point, the electric field is only able to penetrate the plasma as an evanescent wave that tunnels into $n_e = n_c$. For certain values of the scale-length L_g and the incidence angle, the field that reaches the critical density may be too weak to induce the resonance. That means that there is a pair of optimal values for both parameters for which the resonant absorption mechanism is enhanced. From the evaluation of Eq. 2.12 it can be seen that this relation can be expressed as[1]

$$\theta_{RA} \sim \arcsin\left[\left(\frac{c}{\omega_L L_g}\right)^{1/3}\right] \tag{2.13}$$

where θ_A is the optimal incidence angle for each given plasma scale-length. It can be then inferred that for small incidence angles close to the target normal and steep density gradients resonant absorption becomes less efficient.

Inverse bremsstrahlung

In contrast to resonant absorption, inverse bremsstrahlung[9, 10] is a collisional acceleration mechanism. That means that the energy is converted to plasma heating by means of collisions between the electrons being accelerated by the laser and the ions. The electrons that were oscillating according to the laser frequency are abruptly out of phase with the electric field at the collision. The oscillation energy is then transferred to the medium as random thermal energy. For inverse bremsstrahlung, the fractional energy absorbed by the medium, assuming an exponential density profile as in Eq. 2.8, can be expressed as

$$f_{IB} \approx 1 - \exp\left(-\frac{8\nu^*_{ei} L_g}{3c}\cos^3\theta\right) \tag{2.14}$$

where $\nu^*_{ei} \propto n_c Z_i/(k_B T_e)^{3/2}$ is the collisional rate between electrons and ions at the critical surface, proportional to the electron temperature. Taking into consideration this expression

it can be seen that inverse bremsstrahlung benefits from long and gradual density profiles. In addition, electrons with low temperatures are favoured as they experience more collisions. Thus this mechanism is less efficient for high, relativistic intensities, typically corresponding to the main peak of the laser pulses.

2.2.2 Vacuum heating

Vaccum heating, also known as Brunel effect for its first postulation by F. Brunel[11], is a type of non-collisional "not-so-resonant" absorption mechanism at moderate to high laser intensities. The formulation of this process can be understood from the aforementioned resonant absorption, but considering a very steep density gradient. Thus, the laser pulse is again obliquely incidental and a certain component of the electric field oscillates parallel to the density gradient, i.e., p-polarisation.

The steep density gradient, which implies a short scale-length, can be regarded as an abrupt vacuum-plasma interface. If the laser intensity is high enough, the electrons are compressed up to the critical density in a very short distance. As the pulse impinges on the interface, the electric field is able to drag the electrons from the plasma to the vacuum during the first part of the oscillation. An intense electric field is also produced due to the charge imbalance between the electrons and the plasma ions. During the second part of the oscillation, the combination of the returning field and the charge-separation fields accelerate the electrons back to the target surface. Inside the plasma, as scale length is much shorter than the laser wavelength ($L_g << \lambda_L$), the electric field cannot propagate enough to reach its maximum oscillating amplitude. The electrons are then injected to the target without experiencing the restoring electric field, having a net energy gain that can be calculated from[12, 6]

$$f_{VH} \approx \frac{f}{a_0}(\sqrt{1 + f^2 a_0^2 \sin^2\theta} - 1)\frac{\sin\theta}{\cos\theta} \tag{2.15}$$

where $f = 1+\sqrt{1-\eta_{VH}}$, with $\eta_{VH} = (1-\frac{\omega_L^2}{\omega_p^2})^{-1}$ is a factor that accounts for the energy depletion of the incident electric field on the plasma. As the energy gain has a certain dependence on the incidence angle, t have been demonstrated, both analytically[13] and via simulations[14], that vacuum heating is enhanced at an optimum angle $\theta_{VH} = 45°$, and for scale-lengths below $0.1\lambda_L$.

2.2.3 J×B heating

At the relativist regime, that is, $a_0 > 1$, the most predominating acceleration mechanism is $J \times B$ heating[6, 15]. For laser intensities above this limit, $\sim 10^{18}$ W/cm^2, the magnetic factor of the well-known Lorentz force, $\mathbf{F}_L = e(\mathbf{E} + \mathbf{v} \times \mathbf{B})$, becomes relevant. In such case, the ponderomotive force in Eq. 2.3 can be expressed, assuming an oscillating electric field $\mathbf{E} = E_0(z)\sin(\omega_L t)\hat{x}$ propagating along $\hat{z}$, as

$$\mathbf{F}_p = \frac{-e^2}{2m_e\omega_L^2}\frac{\partial E_0^2}{\partial z}\sin^2(\omega_L t)\hat{z} \tag{2.16}$$

that, in terms of the oscillation speed of the electrons $v(z) = \frac{eE_0(z)}{m_e\omega_L}$,

$$\mathbf{F}_p = \frac{-m_e}{4}\frac{\partial v^2}{\partial z}(1 - \cos(2\omega_L t)\hat{z} \tag{2.17}$$

It can be seen from the expression that the poderomotive force is separated into two components. The first term, corresponding to the first-order or fundamental mode, coincides with the averaged description of the force in Eq. 2.3 regarding the laser envelope. This mode is responsible of pushing the electrons along the density profile. The second term, that corresponds to the second-order harmonic, represents the motion of the electrons oscillating at twice the laser frequency ω_L. This oscillation can be understood as a density wave at $2\omega_L$ travelling through the plasma that can be excited to a resonance at $n_e = 4n_c$, as for resonant absorption. If the preplasma extension is long enough, laser pulses of moderate intensity allow for reaching this critical surface and achieve resonance[16]. In the other case, if the density gradient is steep, the acceleration mechanism is similar to vacuum heating but at $2\omega_L$. The kinetic energy gained by the electrons within this mechanism can be characterised from the ponderomotive potential as in Eq. 2.6, which is commonly used as a scaling law between the electron temperature and the laser normalised intensity[17, 18].

It can also be observed in Eq. 2.17 that, as the ponderomotive force is exerted along the propagation direction, the electrons are consequently accelerated in the same direction. Thus, $J \times B$ heating allows for normal incidence angles and both types of linear polarisation, in contrast to resonant absorption and vacuum heating. The fraction of the laser energy that is transferred to the electrons can be estimated from[18]

$$f_{JB} \approx 1.2 \cdot 10^{-15} I_L^{0.74} \tag{2.18}$$

with I_L in W/cm^2, up to a factor of $f_{JB} = 0.5$[19]. Although it is not reflected in Eq. 2.18, it has been found[20] that this energy gain is optimal for incidence angles close to 0°.

In the context of the experimental campaigns performed within this thesis, $J \times B$ heating is the predominant laser-plasma acceleration mechanism. As will be described in Ch. 3, the laser systems that were used for the experiments belong to the relativistic regime of the interaction.

2.2.4 Electron beam properties and scaling

As seen, there are numerous absorption mechanisms that may occur under a certain set of laser and target conditions. These mechanisms may be dominant depending on parameters such as the pulse intensity or the angle of incidence, and thus they may compete between each other. In this way, it is complicated to provide a complete picture of electron acceleration. However, some properties can be inferred for most of the cases. Typically, laser-driven electrons exhibit a broad distribution in energy that can be approximated to a Maxwellian decay function[21] as

$$dn_e(E) = n_{e0} \exp(-E/k_B T_e) dE \tag{2.19}$$

described by a characteristic temperature T_e. The parameter n_{e0} stands for the distribution amplitude, in electron number. In some cases, a more accurate description leads to a bi-Maxwellian distribution[22, 23] with two different temperatures T_{hot} and T_{cold} originated at different processes. The cold temperature is commonly associated to returning currents from the propagation of the electron bunch trough the target[24]. The hot temperature comes from the aforementioned absorption mechanisms.

There is a significant interest in obtaining an scaling law between the hot electron temperature T_{hot} —or simply T_e for the following— and the intensity of the laser pulses. A general scaling can be expressed as

$$k_B T_e \propto (I_L \lambda_L^2)^{\alpha} \tag{2.20}$$

where the coefficient α ranges between 1/3 and 1.5[23] depending on the dominant absorption mechanism. For resonant absorption, experimental data suggest that the scaling law can be written as[25, 26]

$$k_B T_{RA}\ [\text{MeV}] = 0.215 \left(\frac{I_L \lambda_L^2}{10^{18}\ \text{W cm}^{-2} \mu\text{m}^2} \right)^{1/3} \tag{2.21}$$

In this expression, I_L and λ_L are introduced in W/cm^2 and μm, respectively. This mechanism can occur for non-relativistic laser intensities above 10^{15} W/cm^2, reaching an net energy gain of up to 50%[10]. Covering most of the same intensity range but for steep density gradients, vacuum heating exhibits an energy absorption of around 70%, that drops down to 10% at the relativistic regime. The scaling law of the electron temperature follows

$$k_B T_{VH}\ [\text{MeV}] = 3.7 \cdot 10^{-2} \left(\frac{I_L \lambda_L^2}{10^{18}\ \text{W cm}^{-2} \mu\text{m}^2} \right)^{1/3} \tag{2.22}$$

with the same units considerations as before. At relativistic intensities, vacuum heating is surpassed by $J \times B$ heating in terms of the absorption efficiency, which escalates with the laser intensity as given by the ponderomotive potential in Eq. 2.6,

$$k_B T_{JB}\ [\text{MeV}] = m_e c^2 \left(\sqrt{1 + \frac{I_L \lambda_L^2}{1.37 \cdot 10^{18}\ \text{W cm}^{-2} \mu\text{m}^2}} - 1 \right) \tag{2.23}$$

in this case, the electron mass is usually provided in energy units as $m_e c^2 = 0.511$ MeV. In addition, $J \times B$ is less restrictive regarding the polarisation and the incident angle, as is the only non-collisional mechanism that can occur at 0° and s-polarisation. For normal incidence, the energy gain by the electrons is of the order of 30 – 50% for the relativistic limit $a_0 \sim 1$[20, 18] that increase up to 60% for higher intensities around 10^{20} W/cm^2[27]. From this absorption efficiency, obtained analytically from Eq. 2.18, the total number of electrons accelerated into the target can be estimated as[18]

$$n_{e0} = \frac{f_{JB} E_L}{c \tau_L \pi r_0^2 k_B T_e} = \frac{f_{JB} I_L}{c k_B T_e} \tag{2.24}$$

where E_L is the energy of the laser pulses, that ranges from ∼J to several hundreds of J (see Sect. 3.1 in Ch. 3), τ_L the pulse duration, and r_0 the radius of the laser focus. In the relativistic regime, these electrons are accelerated up to MeV-order energies.

Depending on the composition of the target, these electrons may be utilised for different applications. The use of thick, high-atomic number materials such as copper or zinc favours the emission of bremsstrahlung stopping radiation and characteristic K- an L- atomic lines. In this way, beams of X-rays from laser-plasma interaction have been extensively studied(1,2) and some applications have been derived from them(3,4). On the contrary, light, low-atomic number materials as aluminium or some plastics allow for the propagation of the electrons while minimising the radiation losses. If the electron energy is high enough, they are able to go through the target and emerge at the rear side. As will be seen throughout the following sections, these electrons are responsible of the main ion acceleration mechanism in the range of application of the experiments presented in this thesis. Proper target engineering, as for example the use of nanostructures at the front target surface, can lead to the enhancement of some of the mechanisms presented in this section, as in (5,6,7), or of the resulting X-rays (8) or ion beams(9,10).

2.3 Ion acceleration mechanisms

Since its first formulation in 1965 by Tajima & Dawson[28], lasers as a means to efficient particle acceleration have developed continuously during the last two decades[29, 30], and it is considered today as an alternative to conventional RF accelerators in many fields related to basic science and applications [31, 32]. However, direct ion acceleration from laser pulses is not feasible, as it would require intensities of $\sim 10^{24}$ W/cm^2, beyond the current achieved limit. Instead, the mechanisms for efficient ion acceleration involve the charge-separation electric fields produced by the laser-driven electrons. These huge electrostatic fields are of the order of ∼TV/m, in contrast to those achieved at RF accelerators, which saturate at about 100 MV/m. For this reason, together with the arguments presented in the introductory chapter regarding size and scalability, laser accelerators have become a subject of study and research both experimentallyand through simulations.

In the previous sections, the mechanisms that lead to the efficient acceleration of relativistic electrons up to several MeV were described. Although there are various mechanisms as well

for the acceleration of ions from these hot electrons, only Target Normal Sheath Acceleration (TNSA) is relevant within this thesis. Other processes, such as Radiation Pressure Acceleration (RPA)(1,2), Hole Boring(3,4), Light Sail(5), or Collisionless Shock Acceleration (CSA)(6) take place at higher intensities (10^{20} – 10^{22} W/cm^2) and not applicable for the laser systems used in this work. An in-depth understanding of these mechanisms can be found in recent reviews on laser-driven ion acceleration[29, 6].

2.3.1 Target Normal Sheath Acceleration

Target Normal Sheath Acceleration (TNSA)[21, 33, 34] is the most studied and extended ion acceleration mechanism, as it provides a robust and efficient means to produce high-energy ion beams up to tens of MeV. In addition, its range of applicability covers a wide number of situations regarding laser and target parameters. It emerges from the interaction of an ultraintense laser pulse of $I_L > 10^{18}$ W/cm^2 with a thin solid foil of micron-size thickness.

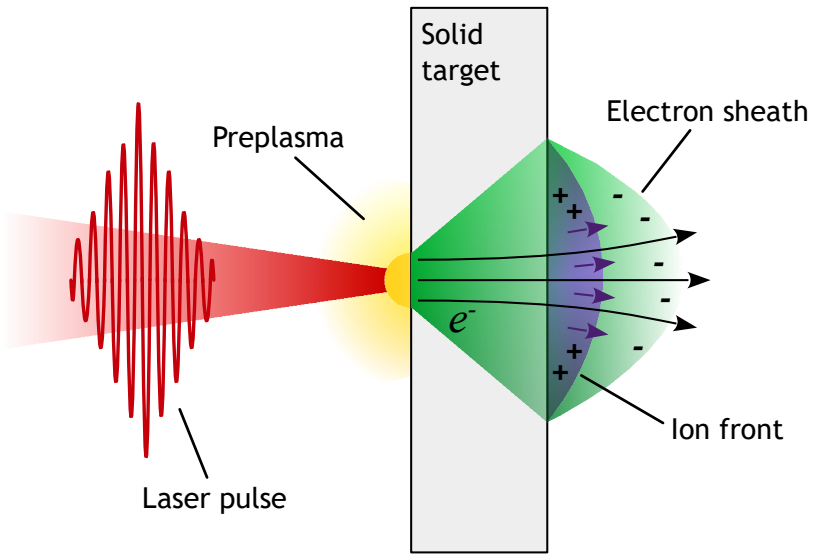

FIGURE 2.1: Schematic representation of the TNSA mechanism.

A basic scheme of TNSA is illustrated in Fig. 2.1. As the laser pulse impinges on the solid target, the pedestal preceding the main peak ionises the surface leading to an expanding plasma. From the interaction of the main pulse and the plasma, a relativistic electron beam is accelerated according to the mechanisms described, and injected into the target. If the electrons are enough energetic, they can traverse the target foil and emerge at the rear side as an expanding sheath.

The charge-separation electric field that is generated between the sheath and the positive ions from the target surface is strong enough (∼TV/m) to deflect the less energetic electrons back to the target, which then recirculate as returning currents. Unless specifically removed, the target foils used in laser-driven ion acceleration typically have a contaminant layer covering their surfaces, mainly composed of water vapour and hydrocarbons. The huge electrostatic electric field generated by the electron sheath is then able to ionise the material of these contaminants and pull the ions towards the direction normal to the target surface. A bunch of ions is in this way accelerated following the expansion of the electron sheath up to MeV-order energies. Due to their lighter mass and higher charge-to-mass ratio, protons are more efficiently accelerated and thus dominate the ionic composition of the resulting beam. Other heavier ions in different ionisation degrees, such as carbon, nitrogen, or oxygen, are also accelerated. This charge imbalance also occurs at the frontal surface of the target, due to the expansion of the preplasma. Thus, electron and ion acceleration is also produced, but is typically less efficient than at the rear side.

Fig. 2.2 depicts the evolution of the electron and proton densities (red and green curves), and the electric field (blue curve) during the last phase of TNSA, obtained from one-dimensional Particle-In-Cell simulations. The figure shows the rear side of a slab target at four different times after the formation of the electron sheath. The densities are normalised to the critical density, the spatial dimension to the laser wavelength, and the electric field to the laser amplitude. It can be seen that the electric field produced by the electron distribution peaks at the expanding ion front, producing a huge electrostatic pull on them at each time instant.

Analytically, the TNSA mechanism can be effectively described by a self-similar, isothermal expansion model formulated by P. Mora in [35]. It provides a one-dimensional description of the temporal evolution of the accelerated ions and the charge-separation field in terms of parameters both from the laser and the target. This model assumes that the hot temperature of the electron sheath remains constant during the acceleration process due to the short, picosecond temporal scale at which it occurs. It also imposes the quasi-neutrality of the expanding plasma at the rear side of the target: $n_e = Z_i n_i$, where n_e and n_i are the electron and ion densities, respectively, and Z_i the ion state of charge. A step-by-step derivation of the model can be found in [35, 21].

From the evaluation of the Poisson's equation at the sheath-vacuum interface an electron energy distribution as depicted in Eq. 2.16 can be obtained. From a classical point of view, the

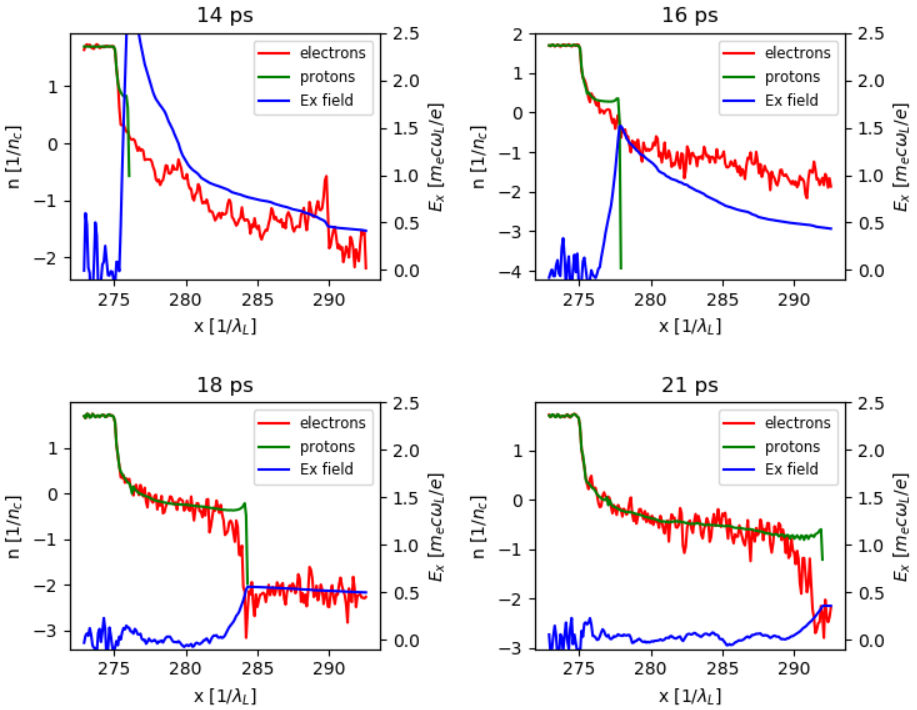

FIGURE 2.2: Evolution of the electron and proton densities, and the electrif field, from 1D PIC simulations.

broadening of the electron distribution to a Maxwellian dependence is explained by binary collisions with the plasma particles as they are injected into the target. In this case, the distribution amplitude n_{e0} can be updated from Eq. 2.24 to consider the angular spread of the electron beam while traversing the target foil, as

$$n_{e0} = \frac{f_{JB} E_L}{c \tau_L S_s k_B T_e} \tag{2.25}$$

where $S_s = \pi(r_0 + D\tan(\theta_e/2))^2$ is the area of the electron sheath, defined by the target thickness D and the angular divergence θ_e of the electrons inside the target. For foils thinner than 10 μm this angle can be taken as $\theta_e \sim 16 - 25°$[18].

From the electron spectral distribution and the quasi-neutrality condition, the density distribution in terms of the energy of the ion front expanding at a velocity given by the ion sound

speed (Eq. 2.5) can be obtained as

$$dN_i = \frac{N_0}{\sqrt{2Z_i k_B T_e E_i}} e^{-\sqrt{\frac{2E_i}{Z_i k_B T_e}}} dE_i \tag{2.26}$$

which corresponds to a Maxwell-Boltzmann distribution. The parameter $N_0 = n_{0e} c_s t S_s$ is the distribution amplitude in number of particles per unit of energy at a given time t, T_e is again the hot electron temperature, and E_i the ion energy. The isothermal model is valid for a $t > 0$ that in first approximation it can be estimated to be comparable to the pulse duration τ_L (fs – ps). This restriction is introduced *ad hoc* in the model formulation in order to avoid an infinite energy gain by the ions with time. A more detailed description leads to an empirical expression for the acceleration time in terms of the laser intensity, as introduced by [18]

$$t_{acc} \approx [-6.07 \cdot 10^{-20}(I_L - 2 \cdot 10^{18}) + 3] \cdot (\tau_L + t_{min}) \tag{2.27}$$

for $2 \cdot 10^{18} \leq I_L \leq 3 \cdot 10^{19}$ W/cm^2, and

$$t_{acc} \approx 1.3(\tau_L + t_{min}) \tag{2.28}$$

for $I_L > 3 \cdot 10^{19}$ W/cm^2. In these expressions, t_{min} is defined as the minimum time that the ions need to absorb energy from the electrons. This time was found to be around 60 fs for laser pulse durations below 100 fs[18]. The separation of the acceleration time in two regimes given by Eqs. 2.27 and 2.28 take into consideration that for lower intensities the expansion time is in principle slower, so the acceleration time must be longer.

From the definition of the normalised acceleration time $\tau = \omega_{pi} t_{acc} / \sqrt{2\exp(1)}$, being $\omega_{pi} = \sqrt{n_{e0} Z_i e^2 / m_i \epsilon_0}$ the ion plasma frequency, the model also predicts a maximum, or cut-off energy gained by the ions, given by

$$E_{max} = 2k_B T_e [\ln(\tau + \sqrt{\tau^2 + 1})]^2 \tag{2.29}$$

As shown, for intensities above 10^{18} W/cm^2, $J \times B$ heating is the predominant acceleration for electron acceleration. The ponderomotive potential provides a scaling for the hot temperature proportional to a_0, as in Eq. 2.23, in the order of several MeV. Considering the relation between

the temperature and the cut-off energy in Eq. 2.29, a similar scaling $E_{max} \sim k_B T_e$ can be expected. The isothermal model has been extensively compared to results from Particle-In-Cell simulations, in good agreement for intensities up to 10^{20} W/cm^2[18, 17]. This scaling has been also experimentally evaluated in terms of the pulse duration in [36], showing good agreement below 200 fs.

2.3.2 Proton beam properties

Typically, the obtained ion energy spectra at laser-driven acceleration experiments show a Maxwellian-like decay distribution with a sharp cut-off in energy[29]. As explained in the previous section, this is a result of the broad distribution of the sheath electrons. The ions are emitted with a certain cone-shaped angular distribution, with a narrower dispersion for the particles of highest energy than for the less energetic ones. This angular divergence can be considered as a Gaussian angular profile[37, 38]

$$g(\theta) = \frac{1}{\sqrt{2\pi}\sigma} e^{-\frac{1}{2}\left(\frac{\theta}{\sigma}\right)^2} \tag{2.30}$$

with a dispersion σ that depends on the proton energy with a linear or parabolic profile, as

$$\sigma(E) = m \cdot E + n \tag{2.31}$$

$$\sigma(E) = \sqrt{|a \cdot E + b|} \tag{2.32}$$

Due to the origin of laser-driven ions being at the contaminant layer at the surface of the acceleration targets, multiple ionic species typically compose the resulting beams. Ions with higher charge-to-mass ratio are in principle accelerated more efficiently. So is the case of protons which, as they are the lightest species, usually tend to dominate the acceleration process. However, the use of certain specifically processed targets may allow for the enhancement of a different ionic species. For example, the use of deuterated targets has been explored in [39] to produce deuteron beams. In other cases, special treatment of the target surface in order to remove the hydrocarbon impurities has lead to the direct acceleration of heavier ions [40]. This could also be achieved by modifying the laser properties [41].

Other properties of laser-accelerated ions, regarding the typical magnitudes in the context of particle acceleration, are a high particle flux (10^9 – 10^{13} particles per pulse), a short pulse duration (∼ps), and a micron source size. A very low emittance, defined as the the dispersion of the particles in the phase space, is also a fundamental property of laser-driven ions. For tabletop or high-repetition rate laser systems, these ion bunches are produced at the operation rate of the laser, in the order of a few Hz.

2.4 Radiation-matter interaction

2.4.1 Interaction of charged particles with matter

When a charged particle propagates through matter, it can experience several mechanisms such as elastic collisions with atomic electrons, inelastic scattering, or radiation emission within the electric field of the nucleus, also called bremsstrahlung. The transmutation of the atoms of the medium through nuclear reactions can also occur, although they are not considered in this section. On average, these processes will lead to the gradual loss of energy of the particle within its propagation. The rate at which the particle losses its energy can be characterised by the linear stopping power, defined as

$$S_p = -\frac{1}{\rho}\frac{dE}{dx} = -\frac{1}{\rho}\left[(\frac{dE}{dx})_{col} + (\frac{dE}{dx})_{rad}\right] \tag{2.33}$$

where dE is the amount of energy lost along a distance dx inside a material of density ρ. It can be divided in the energy loss due to mechanical processes, i.e., collisions, and radiation processes.

Charged particles traversing a medium can be separated into two categories depending on their mass. In the range of application of this thesis: light leptons such as electrons and positrons, and heavier hadrons like protons or ions. The description of the energy loss is slightly different for each group of particles, as some processes dominate the interaction depending on the type of particle, its energy, and its mass. In the case of heavy charged particles, collisional processes are dominant in the ∼MeV range. Therefore, the sopping power in Eq. 2.33 can be approximated to the collisional component, whose description is given by the Bethe-Bloch formulation[42]. The expected maximum range of an hadron inside matter can be calculated from its stopping power as

$$R_{max}(E) \approx \int_{E_{min}}^{E} (dE/dx)^{-1} dE \tag{2.34}$$

where E_{min} is the minimum energy at witch the Bethe-Bloch formulation is valid ($v < 0.25c$). From the evaluation of Bethe-Bloch formula, a particular phenomenon for hadrons travelling through matter is derived: they deposit most of its energy at the end of its range and within a very short distance. This energy deposition distribution is commonly referred as the Bragg peak of the hadron beam. Some detection configurations, as will be mentioned in Ch. 3, take advantage of this circumstance. The emergence of other applications such hadron therapywere also motivated by this phenomenon.

In the case of leptons, in contrast, as their mass is about a factor of 1000 lighter than the mass of protons, the relativistic regime is reached for lower energies. Thus, for the ∼MeV energy range, radiation losses (bremsstrahlung) are much more predominant than for hadrons. In addition, positrons can be disintegrated by means of electron-positron annihilation when their energy is low enough, in the order of ∼100 keV. This is the fundamental base of PET imaging. Due to their lighter mass, collisional processes on electrons or positrons produce larger scattering angles than for heavier hadrons. It can be then defined the mean free path as $\lambda_e = 1/\sigma_{col} N$, in terms of the collisional cross-section σ_{col} and the particle density of the medium $N = \rho N_A/A$, being ρ its density, N_A the Avogadro constant, and A the atomic mass. This parameter represents mean distance that a lepton can travel through a material without experiencing a collision.

2.4.2 Interaction of photons with matter

There are three main mechanisms that govern the interaction of a single photon with matter: photoelectric effect, Compton scattering, and pair production. In this section, a brief description of the three processes will be provided.

Through the photoelectric effect, the photon is totally absorbed by an atomic electron of the medium, which will be striped from the nucleus with energy equal to the difference between the photon energy and the binding energy of the atomic level. After the absorption of the photon, the vacancy left by the electron at the atomic level will be occupied by another electron at a later time, producing a characteristic X-ray or an Auger electron in the process.

Compton scattering consists on the inelastic scattering between the photon and an atomic electron. In this mechanism, the photon transfers only a part of its energy to the electron and it is scattered at a certain angle. A correlation between the scattering angle θ and the absorbed energy can be expressed as

$$\Delta\lambda = \lambda_f - \lambda_0 = \lambda_C(1 - \cos\theta) \tag{2.35}$$

where λ_f and λ_0 are the final and initial wavelengths of the photon, related to its energy through $E = hc/\lambda$, and $\lambda_C = h/m_e c$ is the Compton wavelength.

In pair production, a photon under the atomic electrostatic field can suddenly be totally absorbed to produce an electron-positron pair. In contrast to the other two mechanisms, pair production exhibit a energy threshold below which it cannot occur. This threshold correspond to the sum of the electron and positron rest masses, which is 1.022 MeV.

The probability of these mechanisms mainly depends on the photon energy and the atomic number of the propagation medium. For low-energy photons the predominant mechanism is the photoelectric effect. It is also favoured for materials with high atomic number. In the keV range of energies, this mechanism effectively compete with the Compton scattering, which predominates up to the MeV energy scale. For relativistic energies above 1 MeV, the probability of pair production increases dramatically and becomes dominant.

The overall effect of the three mechanisms described here can be averaged by means of the linear attenuation coefficient μ_γ. In this way, a photon beam traversing a material will experience a certain attenuation depending on its energy, following expression

$$I(z, E_\gamma) = I_0 \exp(-\mu_\gamma(E_\gamma) \cdot z) \tag{2.36}$$

where I_0 is the initial intensity of the ion beam before entering the material, $I(z)$ is the intensity at depth z, and μ_γ is the attenuation coefficient at the energy E_γ. In contrast to the case for charged particles, the propagation of a photon beam within matter leads to its gradual attenuation but maintaining a constant energy, on average.

TABLE 2.1: Nuclear reactions of interest for the production of radioisotopes used in PET. Dash lines indicate a energy threshold below 1 MeV.

Nuclear reaction (-)	Energy threshold (MeV)	Product half-life (min)
^{11}B(p,n)^{11}C	1.13	20.23
^{10}B(d,n)^{11}C	-	20.23
^{14}N(p,α)^{11}C	4.5	20.23
^{16}O(p,α)^{13}N	6.6	9.97
^{15}N(p,n)^{15}O	3.8	1.87
^{14}N(d,n)^{15}O	-	1.87
^{18}O(p,n)^{18}F	2.5	109.77

2.5 Radioisotope production

Through previous sections, the diverse mechanisms that result in the efficient acceleration of ions were described. As introduced in Ch. 1, one of the potential applications for laser-accelerated ions is the production of radioisotopes. As the spectrum of laser-driven ions spans over several MeV and is characterised by a high flux, it is suitable for the induction of nuclear reactions on a secondary target. The fact that protons are the predominant species in laser-driven sources is another advantage, as most of the production reactions are induced by light particles such as protons or deuterons[43, 44]. In some experiments, these nuclear reactions are used as a diagnostic of the proton acceleration process[45, 46].

Experimentally, laser-accelerated protons can induce nuclear reactions by locating a secondary target within the path of the proton beam[47, 48, 49]. Through the proper election of the target material and an adequate study regarding the available reaction channels, the radioisotope of interest can be produced. In the context of PET medical imaging, there are several nuclear reactions induced by MeV-order protons or deuterons that produce the desired isotopes. Table 2.1 lists some of these reactions[43, 44, 50], along with the threshold energy of the reaction, if any. Regarding the work presented here, the reaction ^{11}B(p,n)^{11}C is the main channel for the production of ^{11}C from the proton beams generated within the experiments performed on laser-driven acceleration. This will be addressed in the corresponding chapter, Ch. 6.

The probability that a nuclear reaction occurs at a certain energy of the incidental particle

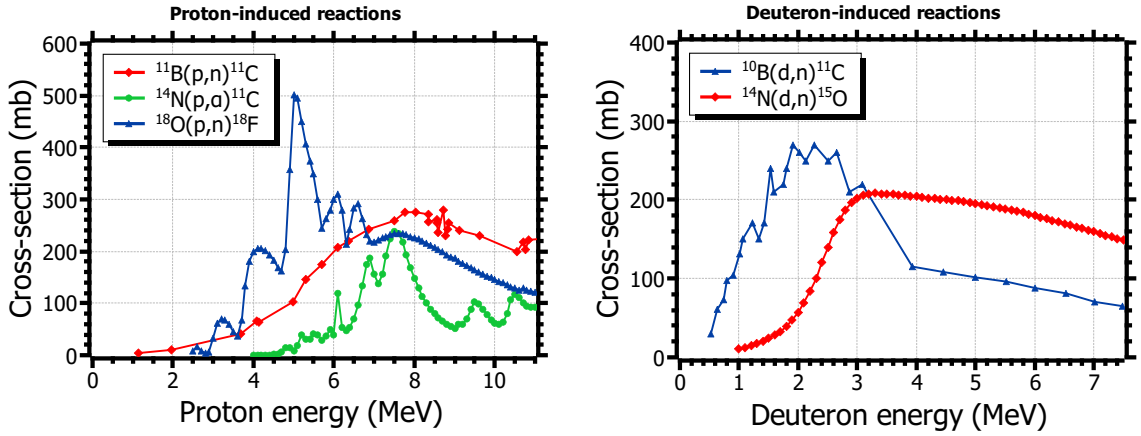

FIGURE 2.3: Cross-sections of some production reactions of radioisotopes of interest in PET.

is determined by the cross-section, also known as excitation function. Fig. 2.3 depicts the cross-section of some of the nuclear reactions included in Table 2.1, induced by protons (left) or deuterons (right). As can be seen, the main peak of the curves is below 10 MeV, which is the typical range of energies achieved in most of the ultraintense laser facilities.

The activity of a radioactive source is defined as the amount of disintegrations per time unit. This decay rate is often characterised by the disintegration constant λ_c or the half-life $T_{1/2}$ of the radioactive nucleus, which are related via $\lambda_c = \ln(2)/T_{1/2}$. The later is defined as the the period of time in which half of the radioactive activity has decayed. Thus, the activity at a given time t can be expressed as

$$A(t) = A_0 \exp(-\lambda_c t) \tag{2.37}$$

where A_0 is the initial activity. From this expression, the number of nuclei of the radioactive source N can be simply derived as

$$N(t) = A(t)/\lambda_c = N_0 \exp(-\lambda_c t) \tag{2.38}$$

being N_0 again the initial number of nuclei. Eq. 2.38 is commonly known as the law of radioactive decay.

There are some radioactive nucleus that can decay through two or more different modes, or channels. In these cases, the overall disintegration constant can be expressed as the sum of the partial constants of each mode, as $\lambda_c = \lambda_c^1 + \lambda_c^2 + ...$ The *branching ratio* of each mode is then defined as the ratio between the corresponding partial decay constant to the overall constant. This magnitude indicates the fraction of disintegrations that would be produced through a certain channel with respect to the total.

The expressions above can be updated for a case on which the amount of nuclei is increasing over time. This can occur at radioactive decay series, where a parent nucleus decays on a daughter nucleus that is radioactive as well, or for artificial production. The later is the case for radioisotope production from laser-based sources, which emit laser —and ultimately proton— pulses at a nominal repetition rate over a certain time. The evolution of the amount of nuclei, considering its decay during the production, can be then expressed as

$$N(t) = A(t)/\lambda_c = R(1 - \exp(-\lambda_c t))/\lambda_c \tag{2.39}$$

where for pulsed sources $R = P \cdot f_N$ is the production rate in terms of the shot frequency f_N, and the number of nuclei produced for each shot P.

The production of a radioisotope through a certain nuclear reaction induced by a incidental beam of particles can be calculated from the convolution between the cross-section and the distribution of the beam, as

$$P = N_t \int_{E_{th}}^{E_{max}} \sigma_r(E) n_p(E) dE \tag{2.40}$$

The parameter $N_t = \rho N_A t_z / A$ depends on the properties of the target material, being ρ its density, N_A the Avogrado constant, t_z its thickness, and A its atomic mass. Inside the integral, σ_r is the reaction cross-section in terms of the energy E, and n_p is the spectral distribution of the incidental particles. In the case of laser-accelerated protons, this distribution can be obtained from Eq. 2.26. The integration limits refer to the reaction threshold energy E_{th} and the maximum energy of the particle beam E_{max}, which corresponds to the abrupt cut-off for laser-driven ions. In the case that n_p is given in flux units —particles per unit area—, an extra term accounting for the extension of the beam must be introduced in Eq. 2.40. For ions beams

produced via ultraintense lasers, this area can be estimated from the solid angle integral of the angular divergence in Eq. 2.30, which as indicated, depends on the particle energy.

If the production rate of the radioactive nuclei is initially much greater than its decay rate, the production curve tends to a maximum value in the called *secular equilibrium* regime. As the activity of a radioactive sample increases with the number of radioactive nuclei, this regime is achieved when the amount of produced nuclei equals the number of disintegrations per unit time. This leads to a maximum achievable production rate after a certain operation time, which remains constant over time. In the experiments, the typical picture is that the amount of nuclei grows according to Eq. 2.39 during the production phase. After the production stops, ideally close to the equilibrium phase, the achieved activity level continues its decay following Eq. 2.37. The characterisation of the produced amount of radioisotopes, in terms of its activity, is measured at this phase. The identification of the produced radioisotopes can be then performed through the determination of their emission spectrum and their half-life.

2.5.1 Review of radioisotope production for PET imaging

As indicated in the introductory chapter, the activity levels typically handled in PET preclinical imaging are in the range of 10 – 30 MBq. For clinical imaging, these requirements are escalated up to several hundreds of MBq up to 1 GBq. The recent interest in laser-induced acceleration for medical radioisotope production has led to numerous studies, both experimental and theoretical, of the achievable activities in terms of laser and target parameters for wide variety of laser systems[51]. The action plan of current laser facilities can be separated in two different approaches for achieving the required doses. On one hand, high power laser systems (see Ch. 3) focus on reaching huge, petawatt laser pulses that are able to produce a huge number of activations on a single shot. Its repetition rate, however, is limited to a several minutes between shots. On the other hand, tabletop high-repetition rate laser systems produce moderate doses per shot but maintaining an acceptable production rate over long operation times. As will be discussed in Ch. 4, the later leads to a series of mechanical difficulties regarding the design and operation of high repetition rate target systems.

Kimura and Bonasera[52] calculated $1.5{\cdot}10^{9}$ ^{11}C nuclei per shot through the ^{11}B(p,n)^{11}C reaction at the Titan laser, capable of delivering pulses of 150 J and 600 fs at a rate of 2 shots per hour, which corresponds to $\sim$1 MBq/shot. By considering the ^{10}B(d,n)^{11}C deuteron-induced reaction instead, they estimate $7.4{\cdot}10^{9}$ ^{11}C nuclei per shot, i.e., 4.2 MBq/shot. At the VULCAN

laser (120 J, 1 ps), experiments performed in [53] resulted in ^{11}C activities of 200 kBq/shot from proton beams with energies up to 37 MeV via the same nuclear reaction. Despite the high radioisotope activities per shot obtained, the production of at these large-scale lasers is mainly limited by their pulse repetition rate and technologically restricted to single-shot operation.

On the contrary, tabletop high-repetition rate lasers allow for multi-shot operation sustained over time. At typical repetition rate of most table-top lasers, in the range of 0.1 - 10 Hz, particle fluxes of 10^{14} ions per second during the irradiation time can be achieved. Fritzler *et al.*[48] estimated an activity of 13.4 MBq of ^{11}C after 30 min of irradiation of thin 6 μm-thickness Al foils with a 10 Hz high-repetition rate laser ($\sim$1 J, 40 fs) via the ^{11}B(p,n)^{11}C reaction. Tayyab *et al.*[47] have measured 5.2 kBq/shot of ^{11}C with a similar laser system and 1 μm Cu targets, which corresponds to 58.5 MBq at 10 Hz after 30 min. Despite some discrepancies, these measurements and calculations give number in the order of preclinical PET requirements. The STELA laser, where part of the experimental work of this thesis was performed, has similar parameters as these two systems. Therefore, dose levels of the same order can be expected. The next generation of table-top lasers may be able to increase the repetition rate up to 100 Hz and extend its scope to clinical doses. Lefevre et al.[54] have extrapolated calculations for a 1 J, 36 fs laser and obtained 94.8 GBq of ^{11}C and 9.7 GBq of ^{18}F at 1 kHz for one hour of irradiation time (698 MBq at 10 Hz after 30 min). Activities of 1.3 GBq of ^{11}C after 30 min at 1 kHz are also estimated in [48]. Based on proton spectra from this publication, possible scenarios for the generation of various PET isotopes from a table-top laser system have been explored, concluding that ^{15}O and ^{11}C activities exceeding 100 MBq may be accumulated within 10 - 30 min at 100 Hz-repetition rate[55].

The aim of this work is to provide realistic estimates of ^{11}C activities for PET imaging using laser-solid accelerators. In most of the previous works addressing this issue, the scope of analysis is focussed on the maximum energy of the resulting particle spectra[18, 17, 56, 57]. Other key parameters for radioisotope production like the shape of the spectrum —characterised by its temperature— and the particle flux are rarely examined. The relevancy of the spectral temperature regarding radioisotope production is illustrated in Fig. 2.4. The ^{11}C production per shot and the activity after 1 hour of irradiation at 10 Hz are shown as a function of the proton temperature. The calculations were performed by means of a simple MATLAB code , considering the ^{11}B(p,n)^{11}C reaction and a proton distribution characterised by an arbitrary N_0 =10^{12} MeV^{-1} and for two different cut-off energies of 6 and 10 MeV. As can be seen in the figure, the increase in the temperature can lead to an enhancement in the per shot and total

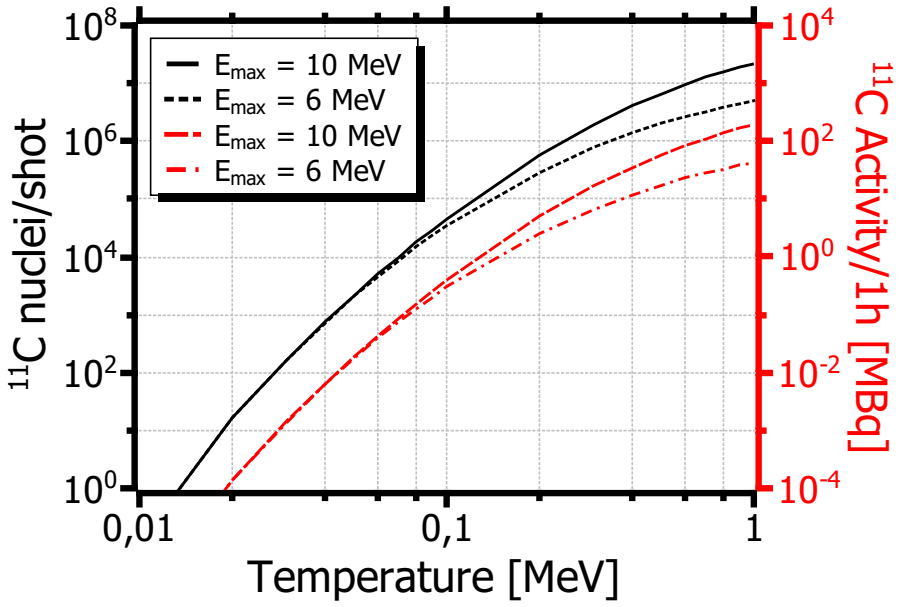

FIGURE 2.4: Estimated activity after one hour of irradiation at 10 Hz as a function of the temperature of the proton distribution for two different cut-off energies.

production by several orders of magnitude. In particular, within the typical range in temperature given by the ponderomotive potential (Eq. 2.23) of 0.1 – 1 MeV, the production per shot varies about a factor of $\sim$400. Besides, both the production per shot and the final activity scale lineally with the number of accelerated protons per pulse, given by N_0.

Chapter 3

Methods

This chapter describes the experimental and simulation tools that were utilised within this work. The fundamental and unique properties of ultraintense lasers are explained in Sect. 3.1. In this same section, the parameters of the laser systems at which the experimental part of this thesis was performed, STELA at the L2A2 and VEGA at the CLPU, are also detailed. Sect. 3.2 and 3.3 move on to a description of the main diagnostics and detection devices used at these experiments, and Sect. 3.4 depicts the basic functioning of the Particle-In-Cell simulation code employed for complementing the experimental data.

3.1 Ultraintense lasers

The first operable laser system dates back to 1960, developed by T. H. Haiman[58] based on previous and contemporary works by C. Townes[59] and N. Básov[60]. Since then, its range of applications have reached numerous fields in science and technology, such as biology, chemistry, and physics. In order to increase the achievable power by these laser systems, the paradigm soon change to pulsed sources, which concentrated a certain energy within a short time scale. Following this direction, techniques as *Q-switching*[61] and *Mode-locking*[62] allowed for reducing laser pulse duration down to the femtosecond scale, thus extending their range of applications to more specific fields. Concerning this thesis, some of these applications are particle acceleration[63, 64], and plasma and nuclear physics. The development of the Chirped Pulse Amplification (CPA) technique in 1985 by D. Strickland and G. Mourou[65] facilitated a significant growth of this field — laser-driven particle acceleration— as it enabled reaching pulse intensities above 10^{15} W/cm^2, sufficient for the ionisation of matter.

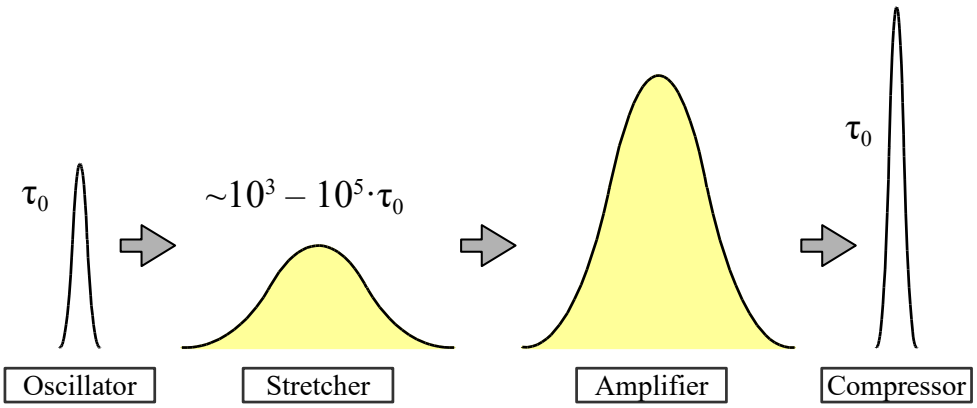

FIGURE 3.1: Schematic representation of the CPA technique.

Until the development of CPA, the main constraint limiting the escalation of the attainable pulse power was the damage threshold of the gain medium of the laser, typically Ti:Sa (Ti:Sapphire), Nd:YAG (Nd:Yttrium-Aluminium-Garnet), or Nd:glass, at about 10^{12} W/cm^2. Due to self-focussing mechanisms as the Kerr effect(1), the energy density could even reach higher values at the central area of the laser pulses, simply not supported by the laser medium or other optical elements of the laser transport line. The approach of the CPA technique, schematically depicted in Fig. 3.1, consists of the temporal lengthening of the laser pulses to reduce the effective intensity under the damage threshold of the optical components after the amplification phase. In this way, the initial fs – ps pulse generated at the laser oscillator, formally called *seed*, is time-stretched about several orders of magnitude. Given that a finite electromagnetic pulse has a wide spread in the frequency domain, certain optical systems can be used to produce a difference in the optical path of the pulse components in terms of their frequency, thus elongating the pulse duration. The most common devices for this procedure are diffraction gratings. The resulting pulse is so-called *chirped pulse*, which is then amplified in subsequent phases. Although there are several amplification techniques, through all of them the laser pulse is maintained oscillating inside a pre-pumped medium that amplifies the pulse on each cycle. The last step in the treatment of the pulses is the temporal compression down to pulse durations of the same order as the initial seed, performed with a similar diffraction grating as for the pulse stretching.

In this manner, most of currently operating lasers are composed of a ultra-short laser Ti:Sa or Nd:YAG oscillator, producing the seed pulses, and a CPA system for their amplification up

to 10^{18} – 10^{22} W/cm^2. Ultraintense lasers can be separated into two main types. High power petawatt lasers based on Nd:YAG or Nd:glass crystals exhibit pulse durations of the order of several hundreds of femtoseconds, up to a picosecond, and pulse energies reaching more than 50 J. On the other hand, table-top high repetition rate laser systems, composed of Ti:Sa crystals as the gain medium, produce shorter pulses, of few tens of femptoseconds, and pulse energies below 10 J. Regarding multi-shot operation, the later can achieve pulse rates typically in a Hz-order or above, even reaching frequencies up to the kHz scale for certain configurations, while high power lasers are mostly limited to a single shot each few minutes.

Relevant parameters of ultraintense lasers

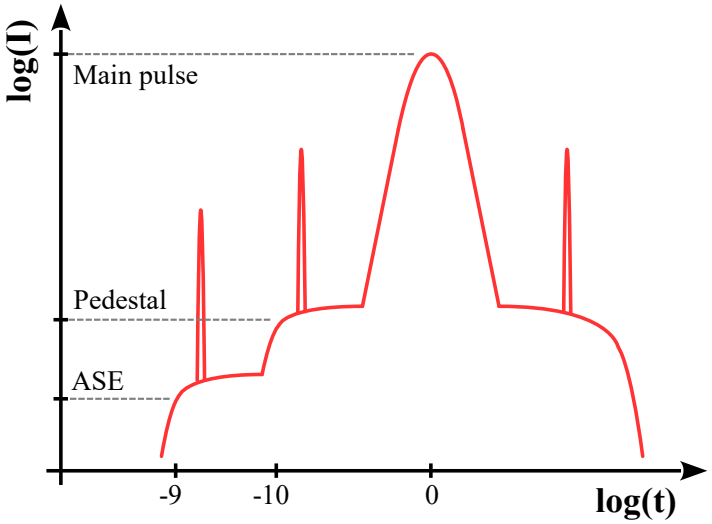

FIGURE 3.2: Schematic representation a ultraintense ultra-short laser pulse.

Despite their output and operation differences, most laser systems exhibit pulses characterised with the same parameters and a similar temporal distribution. Fig. 3.2 depicts a schematic representation of an ultrintense ultra-short laser pulse. Several components at various relative intensities from different origins can be observed. The main pulse, which carries the peak intensity of the laser pulse, has a typical duration in the order of femtoseconds for table-top lasers, or up to a picosecond for high power low repetition rate laser systems. In a nanosecond scale preceding the main pulse, the distribution show a contribution with a relative intensity of 10^{-6} – 10^{-10} orders of magnitude below the peak value. This long pedestal is produced due to the Amplified Spontaneous Emission (ASE), coming from the pumping and amplification phases.

Other component within 1 – 10 picoseconds is produced by uncompensated dispersion as a result of imperfections and misalignment of the components in the compressor gratings or some other optical elements during the pulse processing. Its relative intensity is of the order of 10^{-3} with respect to the main pulse. Due to some unavoidable leakages of the laser pulses during the pumping phase, additional prepulses are expected to appear before the main pulse. Although the relative intensity of the prepulses varies from laser to laser, they are typically above the ionisation threshold, at about 10^{15} W/cm^2. Both the pedestal and these prepulses are responsible of preplasma formation when an ultraintense pulse impinges on a solid target, which allow for the efficient acceleration of electrons and ultimately ions upon the arrival of the main pulse, according to the mechanisms described in Ch. 2.

An important parameter of ultraintense laser pulses in the context of particle acceleration is the formally called contrast ratio, which is defined as the relative intensity between the main pulse and the nanosecond and picosecond pedestals. Two contrast ratios are thus usually given concerning the nominal temporal characterisation of a laser system. One of them at the nanosecond scale, accounting for the ASE contribution, and the other one at $\sim$10 ps, related to the uncompensated dispersion. There are several techniques for the suppression of these components and the enhancement of the contrast ratio, for example XPW (cross-polarised wave) modules[66] or Pockels cells[67], being one of the most extended the use of a plasma mirror[68] within the laser transport. Some applications require proper prepulse cleaning and ultra-high contrast conditions. In particular, for the irradiation of thin targets below 1 μm-thick, it has been demonstrated that a non-optimised laser contrast can lead to the destruction of the target before the arrival of the main pulse, hence reducing the efficiency of the subsequent particle acceleration[69, 70].

The spatial distribution of ultraintense laser pulses can be considered as Gaussian in good approximation. Depending on the laser system and its optical elements, the laser pulse diameter ranges between 2 and 10 cm. Ti:Sa lasers tend to be shorter than Nd:YAG systems as generally the size of the crystals are smaller, due to the technical difficulty to grow large pieces. In most of the experimental cases, pulses are focussed via reflecting systems, typically a Off-Axis Parabola (OAP), down to micron spot-sizes thus reaching peak intensities of up to 10^{20} – 10^{22} W/cm^2. Refractive focussing systems are avoided due to their propensity to being damaged at the achieved pulse intensities. Due to the spatial profile of the laser beam and the focalisation process, a 84% of the pulse intensity is concentrated in a central Airy disc of diameter d_A and FWHM (Full Width at Half Maximum) d_{FWHM} given by

$$d_A = 2.44\lambda_L f \tag{3.1}$$

$$d_{FHWM} = 2.05\lambda_L f \tag{3.2}$$

being λ_L the laser wavelength and f the f-number of the OAP, defined as the quotient of the focal length divided by the entering beam diameter. A focussing Gaussian beam along a z-direction follows a size profile as determined by expression

$$w(z) = w_0\sqrt{1 + (\frac{z}{z_R})^2} \tag{3.3}$$

In this equation, $w(z)$ denotes the beam radius within its focussing profile and w_0, called the beam waist, corresponds to its radius at the narrowest point. In the experimental situation, this parameter is often referred as the focal spot. The parameter z_R is known as the Rayleigh length of the optical system, and is defined as the distance from the focal spot at which the radius of the focussing beam is reduced by a factor of $\sqrt{2}$. From Eq. 3.3, it can be calculated as

$$z_R = \frac{\pi w_0^2}{\lambda_L} \tag{3.4}$$

in terms of the minimal spot size of the focussing system, measured either experimentally or estimated via Eq. 3.1. The Rayleigh length is of special interest from an experimental perspective as it defines the required accuracy in the positioning of the surface of the acceleration target with respect to the laser focus. Beyond this value, the peak intensity rapidly decay and therefore, the energy transferred to the electrons or ions is dramatically reduced. This issue will be further explored in Ch. 4, regarding the development of the target assembly and the procedure for its precise positioning at the laser focus at high repetition rates.

Lastly, the peak intensity of the focalised laser pulses is typically depicted by using the dimensionless amplitude a_0, from its definition in Eq. 2.7. This magnitude is typically used as a comparison parameter between laser systems with different experimental conditions and specifications in most published reviews[6, 29], as for example the pulse duration, the focal spot size, or the pulse energy.

3.1.1 The STELA system

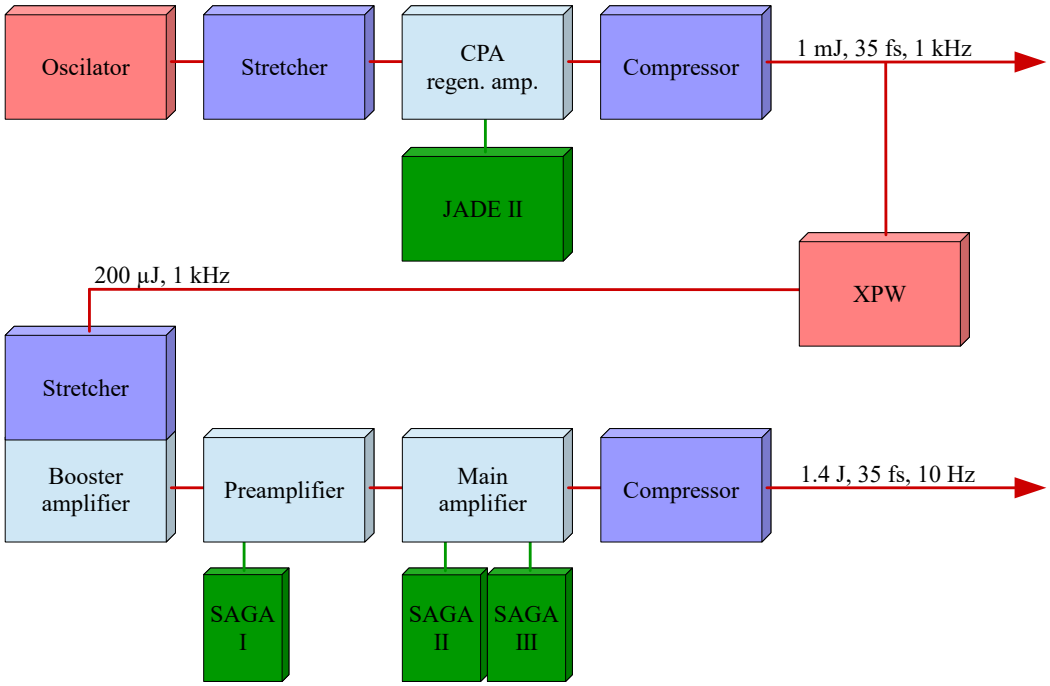

FIGURE 3.3: STELA scheme.

The Laser Laboratory for Acceleration and Applications (L2A2), at the Universidade de Santiago de Compostela[71], is equipped with a compact high repetition rate femtosecond ALPHA 10/XS Ti:Sa laser system (THALES) of 45 TW called STELA (**S**antiago **Te**rawatt **La**ser). This laser system has two laser outputs (Fig. 3.3): the low energy beam line can deliver s-polarised laser pulses of 1 mJ and 30 – 50 fs at a repetition rate of 1 kHz with a ns-contrast ratio of 10^{-6}. This line is used in X-ray generation and dedicated to novel imaging techniques[72]. The high energy beam line is mainly intended for ion acceleration. It can deliver p-polarised laser pulses of 1.4 J and 25 – 50 fs at a repetition rate of 10 Hz and an improved contrast ratio down to 10^{-10}, achieved with the XPW technology.

Fig. 3.3 depicts a scheme of the front-end structure of STELA. The s-polarised seed from the oscillator is stretched, amplified, and compressed in an initial phase via the CPA technique.

A JADE unit containing a Nd:YAG laser is utilised for the population pump of the crystal at the regenerative amplifier, as these lasers have a wavelength of 1060 nm, twice the distance between the atomic levels for the population inversion of a Ti:Sa crystal. The resulting outcome of this phase correspond to the low energy line of the laser. For the line at high energy, the beam is attenuated by removing a component of its polarisation, and then directed to the XPW module, in order to clean the laser pulses from their pedestals and prepulses. After this phase, the nominal pulse energy has reduced to a few μJ. In order to increase this energy up to the $\sim$J level, another amplification cycle is performed. As the Ti:Sa crystals would not tolerate such energy density at 1 kHz, the repetition rate is decreased down to the pumping operation rate, 10 Hz, through a pockels cell. Several SAGA units are employed for the pumping at the amplifiers by means of Nd:YAG lasers.

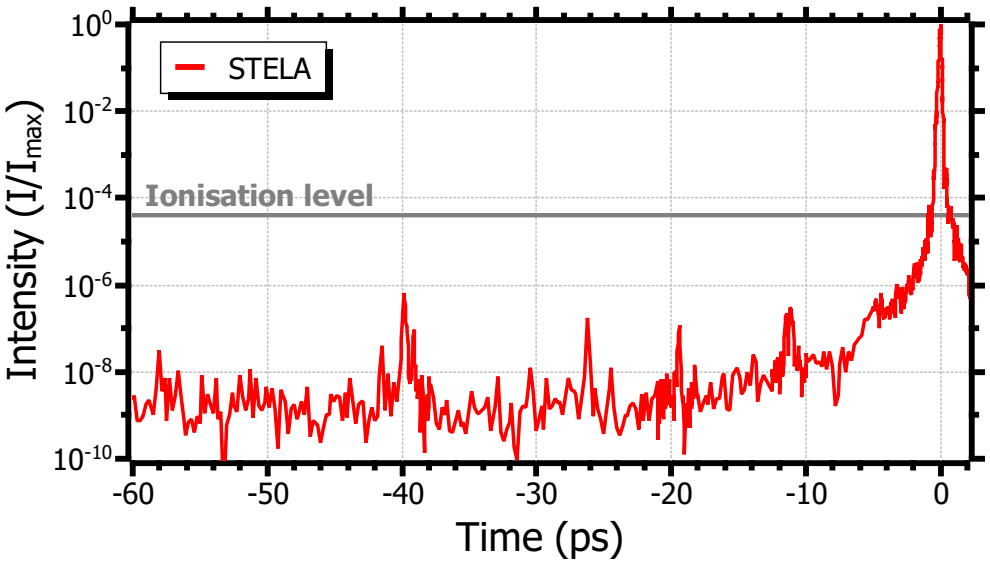

FIGURE 3.4: Contrast of the laser pulses at L2A2.

The temporal distribution of the laser pulses of the high energy beam line, measured with a SPIDER diagnosis system after the compressor, is shown in Fig. 3.4. As can be seen in the figure, the main pulse present an ultra-high contrast ratio (about 10^{-9} and it is clean of prepulses at the nanosecond scale. A short prepulse close to the main pulse of the at around 0.5 – 1 ps of the order of 10^{16} W/cm^2 can be observed.

3.1.2 The VEGA 3 system

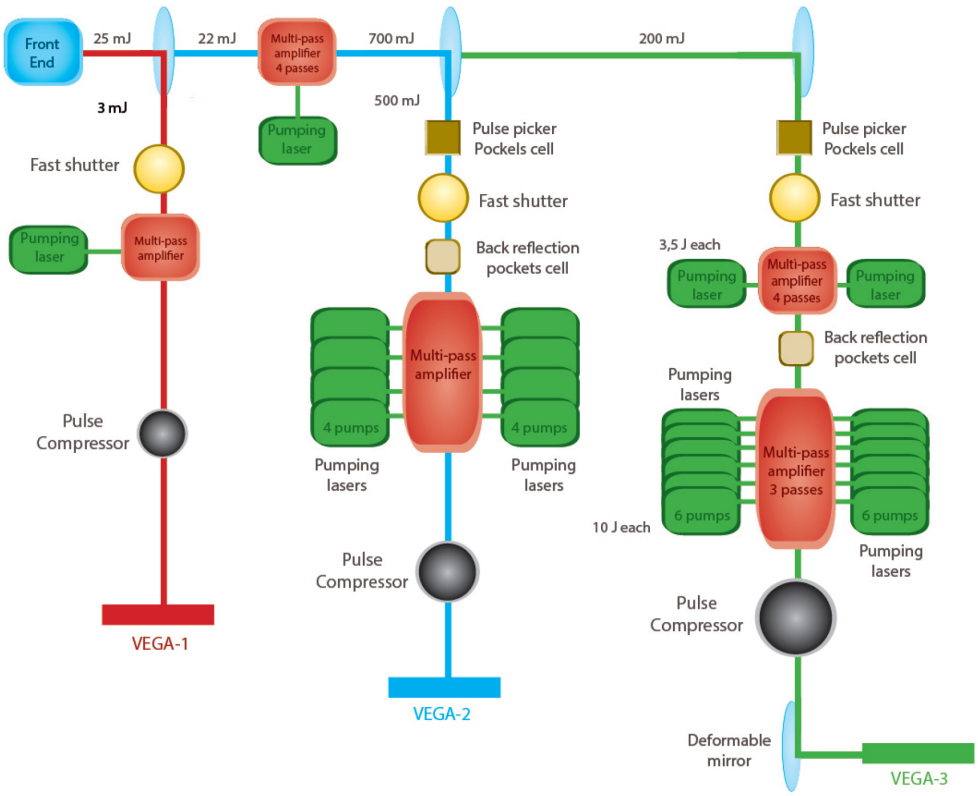

FIGURE 3.5: Schematic representation a ultraintense ultra-short laser pulse (image from https://www.clpu.es/).

The VEGA laser system, held at the Centro de Láseres Pulsados (CLPU) in Salamanca, Spain, counts with three main laser lines at increasing maximum powers: VEGA 1 (20 TW), VEGA 2 (200 TW)[73], and VEGA 3 (1 PW). Fig. 3.5 shows a layout of the overall laser structure. From the front-end, that contains a Ti:Sa oscillator, a double CPA system for the pulse amplification, and a XPW unit for contrast reduction, the laser beam is split to the first output line (VEGA 1). Throughout this line, laser pulses are again amplified by means of multi-pass amplifier and compressed down to 30 fs at 600 mJ-pulse energy and a repetition rate of 10 Hz. For the second laser arm (VEGA 2) several phases of amplification by multi-pass amplifiers before compression lead to laser pulses of up to 6 J. For the third and last laser output, at which the experiments of this thesis were carried out, a component of VEGA 2 laser line is amplified to higher energies and compressed. After that, the beam wavefront is properly corrected by

means of a deformable mirror. Laser pulses up to 25 J and 30 fs at a repetition rate of 1 Hz thus arrive at the interaction chamber, for ion acceleration experiments.

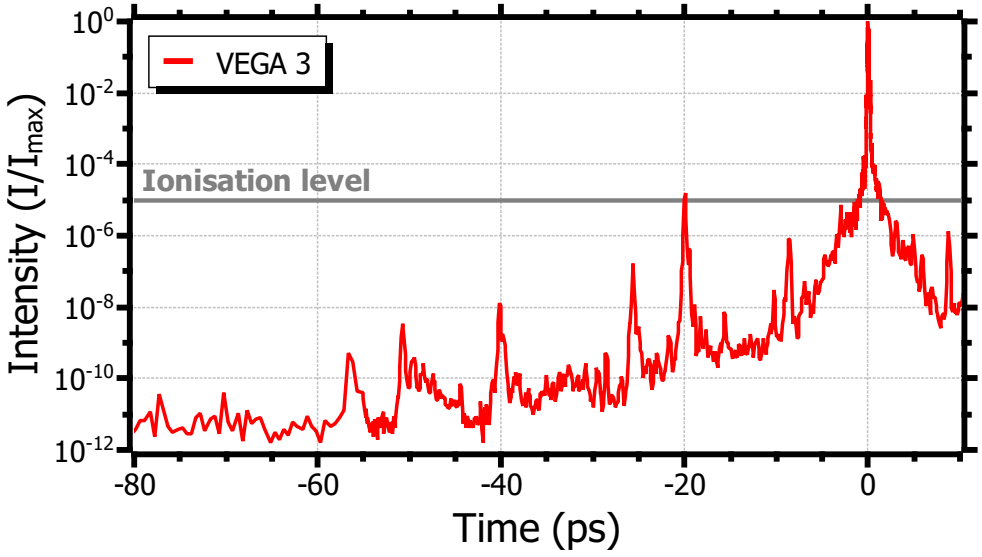

FIGURE 3.6: Contrast of the laser pulses at CLPU.

Due to the use of a XPW module at the laser front-end, the achieved contrast ratio after compressor of VEGA is about 10^{-12} at the nanosecond scale, and of the order of 10^{-8} – 10^{-5} for the picosecond pedesta. This is illustrated in Fig. 3.6, that depicts a temporal trace measured at the CLPU for the VEGA system. Some intense prepulses up to 10^{-5} can be observed as well in the $\sim$10 ps-range. As the intensity of these prepulses is above the ionisation level, they are responsible for the formation of preplasma at the front side of the acceleration targets, and in principle discard the possibility of using thin targets.

3.2 Diagnoses for laser-driven ion acceleration

Due to the ultra-short regimes for the laser-plasma interaction and the particle acceleration mechanism depicted in Ch. 2, in the sub-picosecond range, particle-to-particle measurements are not experimentally feasible. Instead, detection systems that integrate the whole pulse are required[74, 75]. In addition, these diagnostic technologies must be capable of functioning at high-rate multi-shot conditions for at last several minutes of operation. Until the development

and standardisation of high-repetition rate laser systems, the properties of laser-accelerated ions were diagnosed by means of single-use, passive detectors, that required a certain post-processing after the irradiation to extract relevant data. Some of these detectors are CR-39[76], Radio-Chromic Films (RCF)[77], or image plates (IP)[78]. Although they are very popular and are still widely used for some ion beam diagnostics such as beam divergence or particle flux, the interest and the development of detection systems for pure multi-shot operation that offer real-time information on a shot-to-shot basis have been recently increased.

Aside from the high-repetition rate and the short ion bunch duration, special concerns arise from the high particle fluxes that are generated through laser-driven acceleration. Saturation of the detectors is an actual issue in most of the experiments on this topic, which is solved by using optical or particle filters. Together with bursts of charged particles and energetic photons, huge electromagnetic pulses (EMP) emerge from the laser-plasma interaction at high power laser facilities. These EMPs, that have been also studied in literature[75], can affect the electronics of nearby devices to the interaction point. Electron beams and X-rays are also produced according to the mechanisms described in Ch. 2. The former are typically removed via magnet systems, or used as secondary diagnosis of the laser-plasma interaction. For the later, detection devices that are not sensible to electromagnetic radiation are favoured. Traslucent or opaque filters to visible light are also commonly located enclosing the detectors to reduce undesired noise at the retrieved signals.

This section compiles an overview of some of the most extended diagnostic systems used in laser-driven ion acceleration, with special emphasise on those that were used in the experiments performed within this thesis.

3.2.1 Micro-channel plates

Micro-channel plates (MCP)[75, 79] are detectors for high-vacuum environments that consist of a matrix of thin micron-size tubes, or channels, arranged under an electric field and acting as electron multipliers. Incidental particles on the MCP will generate secondary electrons at the active medium that, impelled by the electric field, pass throughout these channels. The electrons are then multiplied in subsequent collisions with the channel walls, hence amplifying the initial charge by several orders of magnitude. Typically, MCPs are attached to a phosphor screen that converts these electronic cascades to visible light via phosphorescence, whcih can be retrieved by a CCD camera. Fig. 3.7 pictures a schematic section of a MCP. The spatial resolution of

a MCP is roughly given by the diameter of the channels, around 4 – 25 μm. Multiple MCPs can be stacked in order to enhance the amplification of the signals, yet at the expense of reducing the measuring resolution. The working principle of MCPs is based on secondary electrons from primary interactions, therefore they are sensitive to all types of ionising radiation, i.e., ions, electrons, X-rays, and neutrons. This may suppose a complication for the detection of laser-accelerated ions due to the significant electron and photon fluxes that are produced in the laser-plasma interaction.

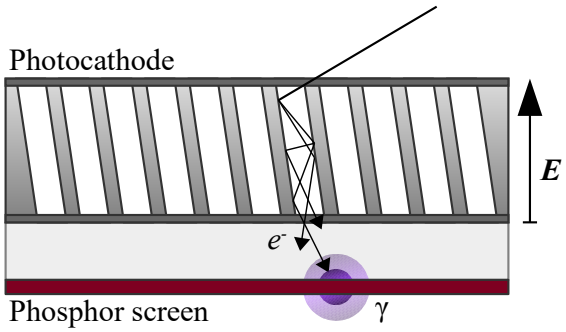

FIGURE 3.7: Schematic representation of the section of a micro-channel plate (MCP).

As multiple parameters characterise both the signal amplification, such as the plate thickness, the relative angle of the channel axis, the electric field strength, or the particle incidence angle; and the visible light detection, like the CCD gain, the exposure time, or the distance to the camera, the calibration of MCP detectors must be performed for a fixed configuration MCP-CCD. For Thomson Parabola spectrometers, that involve multiple incidence angles, as described in Sect. 3.2.4, this issue is of special relevance. A common calibration procedure involves the use of a Thomson Parabola and a stripped CR-39 placed in front of the MCP to cross-correlate the light ratio at the CCD with the single particle counting of the CR-39[79].

3.2.2 Scintillators

Inorganic scintillators[80] are a type of plastic material that converts energy deposition from external ionising radiation to visible light. This light can be then collected via a photomultiplier (PMT) that amplifies the signal to a detectable level. When a particle traverses a scintillator material, it creates a trail a excitations on the medium molecules along its path. These excited

states rapidly decay through fluorescence de-excitations and a certain, proportional fraction of the energy deposited by the particle is emitted as visible photons at a central, characteristic wavelength given by the transition energy. A key feature of scintillator materials is that they are transparent to their own light. The typical configuration consists of a plastic scintillator attached to a fast PMT readout. Light entering the PMT photocatode produces electron excitations that are accelerated by the electric field on a series of dynodes. Secondary electrons are induced as well, leading to an electron avalanche whose charge is proportional to the input energy. The signal from the PMT is retrieved by an acquisition system, usually a fast oscilloscope.

As the light is produced and collected in a picosecond to nanosecond temporal scale, plastic scintillators exhibit a fast response and constitute a suitable choice for online measurements at high repetition rates. In addition to their output stability, they are available in most sizes and shapes as they are usually cut from larger pieces to the desired dimensions. Stacks of scintillator sheets at different central wavelengths have been used as a beam profiler to characterise the spatial transversal distribution of ion beams at various energy ranges[74, 81]. However, a noticeable drawback of PMT readouts is that they tend to saturate for high input particle fluxes. This is a common circumstance for laser-driven particle acceleration, at which an intense bunch of photons, electrons, and ions arrive at the detector within several nanoseconds. This issue is typically addressed by using sets of optical density (OD) filters between the scintillator and the PMT.

3.2.3 Time-of-flight

Time-of-flight (ToF) detection systems provide time-resolved measurements of particle beams according to their kinetic energy. They are based on the principle that particles travelling at different velocities reach the detector at different times given by their energy. Through this approach, a detection device, typically composed of a scintillator and a PMT readout attached to a fast oscilloscope, is placed at a fixed distance from the acceleration source. The bunch of accelerated particles, upon reaching the detector, generates a bump signal extended over a short time. By knowing the travel distance and the expected mass of the detected particles, each temporal bin of the retrieved signal can be related to a energy. Hence, the signal can be analysed to obtain an spectral distribution for the particle beam. In the case of laser-accelerated ions, this corresponds to a broad maxwellian-like spectrum, as explained in Ch. 2.

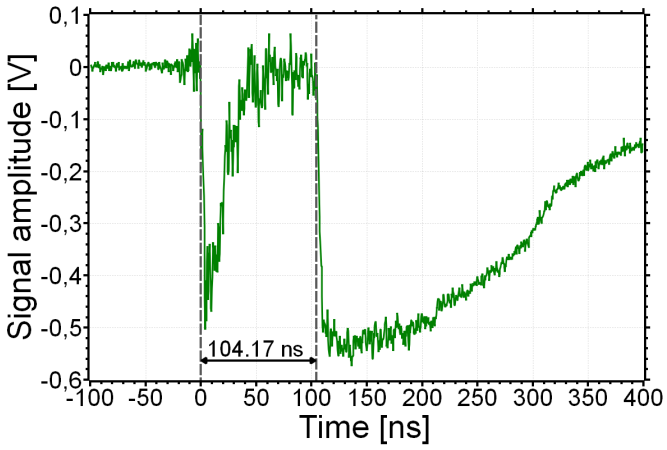

FIGURE 3.8: Typical ToF signal from laser-driven ion acceleration experiments.

Fig. 3.8 depicts an example of a typical signal produced by laser-accelerated ions at a ToF detector. The signal shows a first peak —formally called the *gamma-peak*— produced by the photons generated in the laser-plasma interaction, which is taken as the reference time for the arrival of the laser pulse. The second bump in the signal corresponds to the incoming protons and ions that arrive at the scintillator time depending on their energy E_i, determined by

$$E_i = \frac{1}{2} m_{ion} \left(\frac{D}{\Delta t_i + \frac{D}{c}} \right)^2 \tag{3.5}$$

where m_{ion} is the ion mass, D is the length of the flight path, c is the speed of light and Δt_i is the time interval. The term D/c in the denominator takes into consideration the time the photons spend in reaching the detector. From the raw signal obtained at the detector, a certain calibration can be performed to obtain the particle flux. In this way, for each energy bin in the ray signal, the number of particles N_i equivalent to the signal amplitude U_i can be estimated from expression[55, 82]

$$N_i = \frac{U_i}{m - \alpha U_i} \cdot \frac{1}{E_i} \tag{3.6}$$

where m and α are two constants that account for the calibration. This equation corresponds to a linear dependence in the number of particles with the signal amplitude with an extra term αU_i that represents the saturation of the PMT. The second term in Eq. 3.6 comes from the fact

that, under the assumption that each incoming particle loses all its energy inside the scintillator material, more energetic particles produce higher output signals. Thus, the number of particles in each energy bin must be corrected by a factor inversely proportional to its energy value.

The detector used in the experimental campaigns within this work consisted of a plastic scintillator (NE102A) with an area of 25×25 mm^2 and 5 mm-thickness —sufficient to stop incoming protons with energies up to 22.5 MeV—, wired with optical fibres to a PMT. Additional details on this device are presented in references[55, 82]. For this detector, constants m and α were determined for various optical filters OD1-3 through a calibration[55] performed at the Centro Nacional de Aceleradores (CNA) in Sevilla, Spain. Through this calibration, the response of the detector to proton pulses with energies ranging from 1 to 3 MeV was studied. The tests were performed for constant intensity and variable duration, and for variable intensity and fixed duration, in order to consider possible non-linear behaviours. Calibration measurements were carried out with a time resolution of 100 ns, therefore a correction factor due to the different resolution for other acquisition systems must be considered in Eq. 3.6. Thus, the expression can be updated to

$$N_i = \frac{U_i}{m - \alpha U_i} \cdot \frac{1}{E_i} \cdot \frac{\delta t}{100\ \text{ns}} \tag{3.7}$$

where δt is the temporal resolution of the acquisition. While this resolution is fixed to the bandwidth of the oscilloscope, the energy resolution of the detector can be improved by increasing the flight distance between the source and the detector. This leads to a broader signal in time, according to Eq. 3.5.

3.2.4 Thomson parabola

Thomson parabola (TP) spectrometers[83] constitute the most extended diagnostic device in laser-driven particle acceleration. In addition to energy and flux information, TP detectors provide ion discrimination, of especial interest in this field as the ion beams are typically composed of multiple species of carbon, oxygen, and hydrogen from the contaminant layer at the rear side of the acceleration targets. The spectrometer works by using a combination of parallel electric and magnetic fields to deflect charged particles onto a detection screen in terms of their charge-to-mass ratio q_i/m_i —or simply Z/A— and their kinetic energy.

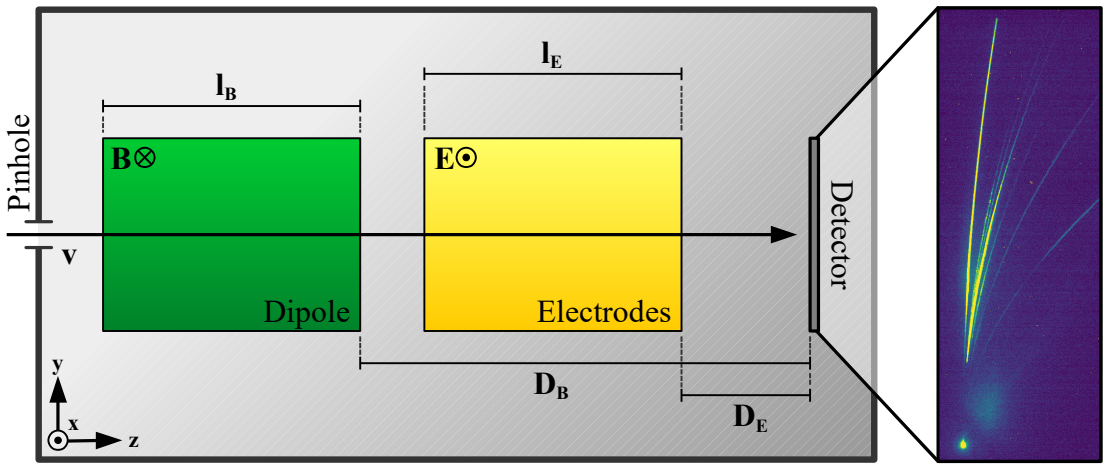

FIGURE 3.9: Schematic representation of a TP spectrometer. An example of a trace is also shown.

An scheme of a TP spectrometer can be seen in Fig. 3.9, where the relevant dimensions are indicated: the longitudinal extension of the magnetic and electric fields (l_B, l_E) and the distance from the end of these fields to the detection plane (D_B, D_E). The trajectory of a charged particle travelling along a direction $\hat{z}$ under a transverse electromagnetic field in $\hat{x}$, as depicted in the figure, can be described by the well-known Lorentz force

$$\mathbf{F}_L = q_i(\mathbf{E} + \mathbf{v} \times \mathbf{B}) \tag{3.8}$$

Here, $\mathbf{E} = E_x\hat{x}$ and $\mathbf{B} = -B_x\hat{x}$ denote the electric and magnetic fields and $\mathbf{v} = v_z\hat{z}$ is the velocity of the particle. In the context of this thesis, protons up to 20 MeV are studied, far from the relativistic regime ($v_z << c$). The same approximation can be considered for heavier ions. Therefore, their kinetic energy can be estimated via the classical expression $E_i = \frac{1}{2}m_i v_z^2$. From these considerations, the evaluation of the equations of motion results in a (x,y)-position at the detection plane given by

$$x = \frac{ZeE_x}{2E_i}[\frac{l_E^2}{2} + l_E D_E] \tag{3.9}$$

$$y = \frac{ZeB_x}{\sqrt{2m_i E_i}}[\frac{l_B^2}{2} + l_B D_B] \tag{3.10}$$

From these expressions, a parabolic relation can be obtained

$$y^2 = \frac{Ze}{m_i} \frac{B_x^2 \left[l_B^2/2 + l_B D_B\right]^2}{E_x \left[l_E^2/2 + l_E D_E\right]} x \tag{3.11}$$

Fig. 3.9 illustrates an example of a trace measured at a TP detector. As neutral particles such as X-rays or neutrons are unaffected by the electromagnetic fields of the spectrometer, they travel through the detector in a straight trajectory until they hit the detection screen. This produces a circular spot at the screen called zero-point, which serves as the origin of the parabolic traces of the protons and ions for the calculation of their energy. From Eqs. 3.9 – 3.11 some implications can be obtained. Ions will be separated forming parabolas depending on their charge-to-mass ratio. Hence, ions with the same ratio will produce the same trace in the detection plane. Within the same curve, the higher the particle energy, the closer to the zero-point it will reach the screen. The spatial resolution in the detection plane mostly depends on the size of the pinhole at the entrance of the detector, which is used to have a pencil-like beam entering the field region.

These unique properties of TP spectrometers allow for their use to measure the species composition of ion beam and, for each of them, the spectral distribution. Through proper calibration of the detection screen and the image system[79], TP detectors can also provide particle flux information. Different detectors can be utilised for the active screen. While CR-39, RCFs, or IPs can be used for this purpose[84], in the context of this thesis only MCPs are relevant. The design of the TP detector used in the experimental campaign at the CLPU within this work can be found in [85].

Some limitations may arise from the working principle of these detectors. First, for highly-energetic particles reaching the detector, if the strength of electric field is not high enough, the limit of the TP traces of different species closer to the zero-point may be overlapped. Thus, it may complicate the determination of the cut-off energies of these species. In laser-plasma interaction experiments, where huge EMPs are produced, sensitive devices as the electrode plates producing the electric field may be affected, easily reaching breakdown voltage. Second, as ions with the same charge-to-mass ratio produce the same traces at the screen plane, it is difficult to characterise their spectral distribution. These issues will be experimentally addressed in Ch. 5.

3.3 Radiation dectectors

One of the most extended uses of scintillators, in combination with a PMT and an acquisition system, is the characterisation of radioactive sources by detecting the products of their decay. In most cases, this corresponds to γ-photons from the direct decay transitions or secondary processes. In the particular case of β^+ radioisotopes, the annihilation of the positrons from the decay produces two photons at 511 keV in opposite directions. As explained in Ch. 2, photons traversing a material can deposit energy through several mechanisms: total energy absorption via photoelectric effect and pair production, or partial deposition by Compton scattering. For the typical range of energies of photons originated at radioactive decay processes, pair production can be considered as negligible in comparison with the other two mechanisms.

The characterisation of a radioactive source consists of measuring its activity curve during its decay, i.e., its emission spectrum within several time intervals. From the number of photopeak counts per time unit $R_{ph} = N_{ph}/\Delta t$ from the measured decay spectrum, the activity can be obtained from

$$R_{ph} = A \cdot I_\gamma \cdot BR \cdot \varepsilon_t^{ph} \tag{3.12}$$

where I_γ and BR are the emission intensity and branching ratio, respectively, and ε_t^{ph} is the total photopeak efficiency (see paragraph below). Together with the half-life, which can be obtained from the activity in Eqs. 2.37 and 2.39, the photopeak energy serve as an identification of the radioisotope from the radioactive source, and the amount of nuclei can be determined from Eq. 2.38.

A fundamental characteristic of radiation detectors is their efficiency curve, which accounts for their response to incoming photons in terms of their energy. Typically, the efficiency of a detection system is separated into the geometric factor ε_g, which depends on the shape of the detector and its spatial configuration with respect to the radioactive source, and the intrinsic factor ε_i, relative to the detector composition and dependant on the energy of the photons. From these two magnitudes, the total detection efficiency at a certain energy E can be defined as

$$\varepsilon_t(E) = \varepsilon_g \cdot \varepsilon_i(E) \tag{3.13}$$

The empirical calibration of a radiation detector is commonly performed by using radioactive sources of well-known activity that emit primary or secondary photons at very specific energies —the photopeak energy—. Thus, through various radioisotopes with one or more photopeaks over a wide range of energies the complete efficiency curve can be obtained. From the activity A of the radioactive source, the experimental detection efficiency at the emission energy can be calculated from Eq. 3.12. In some cases, the radioactive source can be approximated to a point source, for which the geometric efficiency can be estimated from the solid angle covered by the detector, Ω, via expressions

$$\varepsilon_g = \Omega/4\pi \tag{3.14}$$

$$\Omega = 2\pi(1 - \frac{d}{\sqrt{d^2 + R^2}}) \tag{3.15}$$

being d the distance between the source and the detector, and R the radius of the detector, assuming a cylindrical shape.

Montecarlo simulations[86] constitute a very suitable tool for the calculation of the efficiency of a detector, on the other hand. This type of simulation methods are based on random number generation, that, in the context of nuclear physics, are utilised for modelling the interaction of electromagnetic radiation and charged particles with matter. By simulating the pass of particles through a detector, Montecarlo methods can estimate its response to different types and energy of radiation. This approach is particularly useful for situations with complex geometries, both regarding the detection system or the source distribution, where analytical solutions are difficult to obtain.

There are other commonly used types of radiation detectors, such as semiconductoror gaseous, which offer different specifications in terms of their response, resolution, or efficiency. However, they are not relevant in the context of this thesis as were not utilised. The efficiency of scintillator detectors to γ-photons is generally higher than of semiconductor or gaseous detectors.

Coincidence configuration

Coincidence measurements are a special type of event detection that involves two or more detectors. It is used for radioactive sources that emit several correlated photons in a short temporal window, as for example the cascade emission from the decay of certain nuclei, or the backscattered photons from the annihilation of positrons, associated to β^+ radioisotopes. A typical experimental configuration for activity characterisation consists of two detectors located along the same axis facing each other, being the radioactive source placed in between them. To select events corresponding to the emission of two γ-photons in temporal coincidence, counts are only registered and histogrammed if an interaction occurs at both detectors within a time window specified by the acquisition. As an initial approximation, the total efficiency of the detection assembly can be set as the multiplication of the individual efficiencies of both detectors. In this case, Eq. 3.12 can de adjusted to

$$R^c_{ph} = A \cdot I_\gamma \cdot BR \cdot (\varepsilon^{ph}_{t,1} \cdot \varepsilon^{ph}_{t,2}) \tag{3.16}$$

where R^c_{ph} is defined as the number of photopeak counts per unit time in coincidence configuration, and the $\varepsilon^{ph}_{t,j}$ factors correspond to the total photopeak efficiency of detector j. Some advantages of coincidence measurement are the significant background suppression and the reduction of secondary interactions. In this way, all the registered photopeak counts can be assumed to be single and distinct disintegration events from the radioactive source.

3.4 Particle-In-Cell simulations

Numerical simulations have become a powerful and effective computational tool for the comprehension of the underlying physics of complex experimental situations. In the context of plasma physics, and in particular laser-plasma interactions, Particle-In-Cell (PIC) simulation codes are widely extended[87, 88]. The large number of parameters and acceleration mechanisms involved in the interaction, as explained in Ch. 2, make PIC simulations an effective means of understanding the experimental case and complement the empirical data[89, 90].

While some modern PIC algorithms contemplate collisions and other processes as dynamic ionisation[91, 92], the core Particle-In-Cell method in plasma physics assumes a collisionless plasma which can be described by the Vlasov-Maxwell equation

$$\frac{\partial f_s}{\partial t} + \mathbf{v} \cdot \boldsymbol{\nabla} f_s + \mathbf{F}_L \cdot \frac{\partial f_s}{\partial \mathbf{p}} = 0 \tag{3.17}$$

where $f_s(t,\mathbf{x},\mathbf{p})$ denotes the distribution function of a particle species s with position $\mathbf{x}$, velocity $\mathbf{v}$, and momentum $\mathbf{p}$. As in Eq. 3.8, $\mathbf{F}_L$ corresponds to the Lorentz force. The approach of PIC algorithms for solving this equation consist of the discretisation of the particle distribution into "*macro-particles*", which are arranged into the elements —or cells— of a static spatial grid. Each of these macro-particles represent a group of weighted particles characterised by their mass and their charge. Then, the evolution of these particles is separated into two solvers: the movement of the particles under the presence of electromagnetic fields, and the calculation of the updated electromagnetic fields produced by these charged particles, along with external ones.

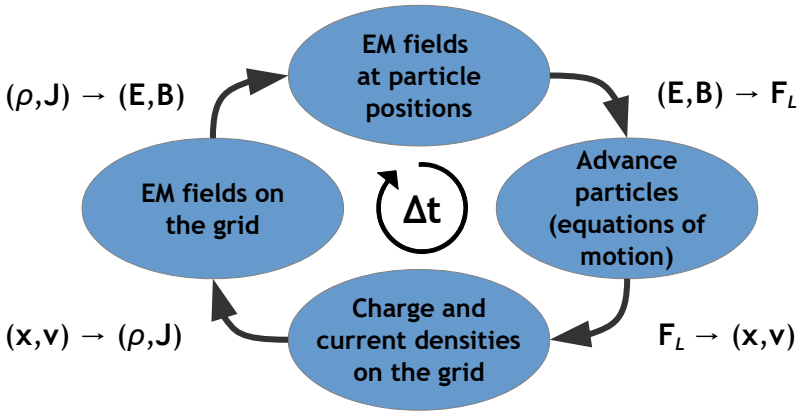

FIGURE 3.10: Typical temporal scheme for Particle-In-Cell simulations.

For each temporal cycle of the simulation, four computational steps are performed, as schemed in Fig. 3.10: given that the electromagnetic fields are initially defined at the grid points, they are firstly interpolated at the particle positions. Secondly, the particles are advanced according to the Lorentz force (Eq. 3.8) an their equations of motion. In this way, for each macro-particle, the new position and momentum are calculated via the Boris pusher[93]. For the third step, the charge and the current densities are calculated on the elements of the simulation grid from, respectively,

$$\rho(\mathbf{x}) = \sum_{j=1}^{N} q_j S(\mathbf{x}_j - \mathbf{x}) \tag{3.18}$$

$$\mathbf{J}(\mathbf{x}) = \sum_{j=1}^{N} q_j \mathbf{v}_j S(\mathbf{x}_j - \mathbf{x}) \tag{3.19}$$

In these expressions, N is the number of macro-particles, whose shape is described by a function $S(\mathbf{x}_j - \mathbf{x})$. The evolution of the electromagnetic fields is finally computed from the charge and current densities, along with the presence of external contributions —for example, a laser pulse—, by solving the Maxwell's equations

$$\frac{\partial \mathbf{B}}{\partial t} = -\boldsymbol{\nabla} \times \mathbf{E} \tag{3.20}$$

$$\frac{\partial \mathbf{E}}{\partial t} = c^2 \boldsymbol{\nabla} \times \mathbf{B} - \frac{\mathbf{J}}{\epsilon_0} \tag{3.21}$$

A relevant constraint for PIC simulations is the CFL (Courant-Friedrichs-Lewy) condition[94], that imposes a relation between the spatial and temporal resolutions to guarantee the stability of the numerical algorithm. In this way, the chosen time-step must satisfy

$$\frac{c\Delta t}{\Delta x} \leq 1 \tag{3.22}$$

$$\Delta t(\sum_{i}^{n} \frac{c_i}{\Delta x_i}) \leq 1 \tag{3.23}$$

for the one-dimensional and n-dimensional cases. The parameter c_i is defined as the velocity magnitude at each dimension.

3.4.1 The Smilei code

Regarding the PIC simulations performed within this thesis, the Smilei code[92] was utilised. Smilei is an open source collaborative code for plasma simulation with a multi-purpose perspective for its application in many related fields. Thus, it include a list of several modules that

account for other interaction processes as field-ionisation, binary collisions, or QED (Quantum Electro-Dynamic) processes. As intended for high-performance execution in super-computer clusters, it is based on a hybrid MPI-OpenMP (Message Passing Interface) parallelisation protocol. The simulation space is split into groups of cells called *patches*, which are associated to MPI regions that share the same memory and are executed as the same task. As a novel approach with respect to other PIC codes, Smilei redistributes the patch-MPI region assignation during simulation to reduce the load weight of those regions with higher computation requirements, by giving patches to adjacent regions with less load. This procedure, so-called *dynamic load-balancing*, leads to a better computing optimisation. Smilei has an additional module, called *happi*, for the processing, analysis, and representation of the simulated data.

Within this thesis, this code was used for simulations on laser-driven ion acceleration by ultraintense laser pulses. The experimental situation at each of the campaigns of this work was replicated in order to complement the measured data, and to obtain relevant scalings with some the interaction parameters to obtain precise estimations on radioisotope production. In the context of this thesis is worth noting the Smilei module that accounts for dynamic field-ionisation, which is not contemplated in the standard PIC formulation. A detailed description of the ionisation model can be found in [92]. The use of this module allows for the ionisation of a ion species by the influence of external electromagnetic fields or those produced by other particles. The implementation of this module in the simulations described in this work, as well as the impact of dynamic field-ionisation on the results, will be further explored in Sect. 5.3 in Ch. 5.

Chapter 4

The multi-shot target system

4.1 Motivation and state-of-art

While laser-plasma acceleration is characterised by a huge peak power, as explained in Ch. 2, many of the foreseen applications of this technology require a minimum average power. This average power is related to the continuous operation of the laser accelerators, that is based on the energy and pointing stability of the laser system, and the shot-to-shot replacement and positioning of the target material. Moreover, the repetition rate of the laser pulses[95] together with the design and operation mode of the target assembly[96] are both crucial to achieve a high average-power regime.

Concerning target engineering, several multi-shot technologies have been proposed. Tape-drive-based targets allow for tens of thousands of shots, that at 10 Hz would correspond to almost one hour of continuous operation[97]. The main drawback of these systems is the limited variety of tape materials and thicknesses suitable to withstand the mechanical stress caused by the continuous movement. An alternative is a multi-target holder system that is capable of moving along three or more degrees of freedom, allowing for rectangular[82] or cylindrical geometries[98]. The total number of possible shots for this option is in general smaller, around a few thousand, corresponding to few minutes of continuous operation. However, the variety of suitable target material and thicknesses is higher as the foils are externally supported by a rigid structure. In particular, the idea of using MEMS technology to fabricate micro-nano targets on silicon wafers represents a very attractive option[99, 100, 101]. This technology allows for manufacturing large volumes of micro-targets made of different materials and thicknesses,

including composites of various distinct layers. Moreover, more recent and promising developments related to the use of liquid targets[102], or cryogenic solid hydrogen targets[103] will open the possibility for long operation periods. However, one of the challenges to be solved is the micrometric positioning of the liquid jet or the solid-hydrogen ribbon.

The accurate positioning of the target material at the laser focus is indeed a common challenge for all multi-shot target technologies. The typical thicknesses of the target material, and the values of the Rayleigh length for short focal lengths, require shot-to-shot position accuracy of the order of a few microns. Therefore, the target assembly should guarantee not only the replenishing of the target material, but also its accurate position at the laser focal point at a speed compatible with the laser pulse rate. These requirements are not only valid for laser-plasma acceleration, but also for other applications of laser-matter interaction as the generation of coherent XUV in forthcoming facilities[104].

In this chapter, the multi-shot target assembly, designed and commissioned at the Laser Laboratory for Acceleration and Applications (L2A2), will be presented (Sect. 4.2). In Sect. 4.3, the implemented procedure to guarantee the shot-to-shot replenishing of the target material and its accurate positioning at the laser focus at high repetition rates will be described. The operation of the target system, concerning its automation and synchronisation with the laser pulses during the irradiation experiments will be explained in Sect. 4.4. As the development of the target system presented in this work is comprised within the L2A2 commissioning campaign, it was originally designed according to the characteristics and constraints of this facility. However, as it will be seen through the following sections and in the experimental chapters (Chs. 5 and 6), this system can be easily adapted to other laser systems. Final conclusions will be given in 4.5.

4.2 Target assembly design

The target assembly designed at the L2A2 is based on a multi-target wheel mounted on a set of three moving stages, to guarantee the shot-to-shot replacement and positioning of the target material. Several models of wheel-like holders were considered and tested during this work (Fig. 4.1). Since the beginning of this thesis within the commissioning of the L2A2 ion source, the target wheel has evolved from a purely single-shot design, used at the initial proof-of-concept experiments, to more advanced versions, aiming to exploit the performance

FIGURE 4.1: Evolution of the target wheel design within this work.

of the laser system and optimise the operation time. Although a sustained operation over time is a relevant factor to achieve, so it is the stability and repeatability of the target system, which ultimately determine the stability of the ion source. Thus, the manufacturing material and quality has been improved in the same direction, from 3D-printer plastic to aluminium and steel versions, offering the required grade of robustness and flatness.

The first version of the multi-target wheel that allow for multi-shot operation, shown in the left **(a)** panel in Fig. 4.2, consists of a drilled aluminium disk with eight apertures for the allocation of the target foils. These apertures are divided into two different arrangements, four of them consisting of five discrete circular holes for single-shot measurements, and another four long slots intended for multi-shot operation. On top of each orifice, a bored plate is screwed to the wheel to fit the target sheets. Both the holes and the slots are bevelled with an aperture of 70° in order to allow for incidence angles up to 45° from the normal direction. Taking 1000 μm as a conservative reference value for the distance between impact positions, the maximum number of possible shots in multi-shot operation is 4 series of 25. This amount can be doubled if two parallel rows of impact positions are used for each slot.

The second version of the multi-shot target wheel, designed for multi-shot operation, is shown in the right **(b)** panel in Fig. 4.2. It is composed of a larger iron disk (200 mm-diameter)

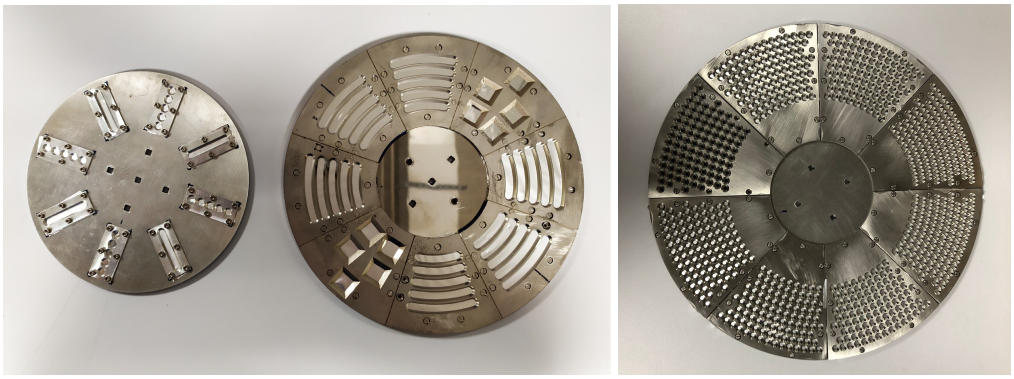

FIGURE 4.2: Target wheels.

and eight frontal circular sector plates, mechanically pressing and tightening the target foils. Six of the sectors have five curved target slots of 4 mm-wide and a 70°-bevelling, separated 8 mm, whose length depends on the slot radius. This configuration represents a clear increase in the number of possible shots in comparison to the first version. Given the same reference distance between impact positions (1000 μm) the typical number of possible impacts per slot can vary between 26 for the inner slots and 42 for the outer ones. According to these values, the total number of shots using the six target sectors would be 1020 (2040 for two-row series of shots per slot). The two other sectors have squared slots to host micro-target arrays produced using the MEMS technology[100]. An update of this wheel version replaces these two sectors by standard ones, for which the number of possible shots increases up to 1360 (2720 for two-row series of shots per slot).

A slightly different approach was considered for the development of the third version of the multi-shot target wheel (Fig. 4.2, right panel). This target holder was designed for a experimental campaign at the Centro de Láseres Pulsados (CLPU), Salamanca, Spain (see Sect. 5.2), for a laser system with 20 - 30 times higher energy per pulse. Thus, in order to prevent the possible effects of each laser pulse on adjacent impact positions, a pattern of circular individual holes was chosen over long curved slots. As for the previous version, the wheel-like holder consists of a base stainless steel disk of 244 mm-diameter, and eight sector plates that fit the target foils. Each sector, both for the disk and the plate, is drilled with a matrix of 101 holes of 2.3 mm-diameter and a 70°-bevelling, arranged along nine arcs at different radii. The center-to-center distance between holes, as well as the distance between radial arcs, was set to 5.5 mm, enough for the maximum operation rate of 1 Hz at CLPU. The total number of targets of this holder

version is 808.

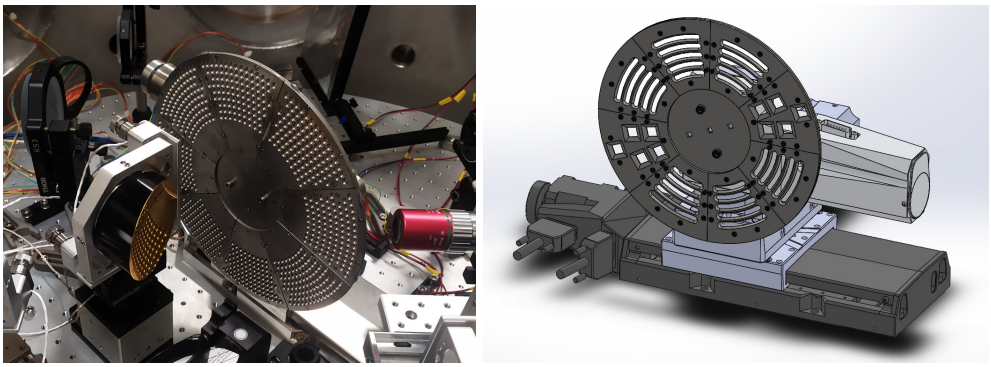

FIGURE 4.3: Target assembly.

Following the same conception, an upgraded version of this target wheel, capable of operating at 10 Hz, was designed and manufactured. In this case, each sector of the base disk was completely bored and two sector plates, drilled with the hole pattern and hosting the target foils in between, were screwed on top of each sector aperture. With respect to the previous version, the size of the base disk was increased to 304 mm-diameter and the center-to-center distance between holes was reduced to 2.5 mm, both in the radial and angular axes. In order to achieve the later, the bevelling of the holes was removed by reducing the width of the sector plates from 2 mm to 0.5 mm. The hole pattern consists of eighteen arcs at different radii containing between 29 and 43 holes each, for a total number of 650 per sector, and of 5200 for the whole wheel.

The target wheel, whichever version, was mounted on one rotating and two linear moving stages (Fig. 4.3). The rotating stage and one of the linear stages, that move perpendicularly to the target normal, were used to refresh the target material between shots, whereas the second linear stage, that moves longitudinally to the target normal, was used to place each target position at the laser focus. The stages are vacuum compatible from PI miCos: LS-110 and PLS-85 for the linear ones and DT-65N for the rotating stage, with spatial resolutions of 20 nm, 10 nm, and 20 μdeg and maximum speeds of 22 mm/s, 12 mm/s, and 22 °/s, respectively. These values are more than enough to match the small tolerance for the positioning of each target at the laser focus, $\sim$10 μm (explained below).

4.3 Target characterisation

The estimated Rayleigh length of the focussing beam in the experimental set-up at the L2A2, of $\sim$10 μm, defines the tolerance for the positioning of the targets. Due to the mechanical deformations in the multi-target wheel and the target foils surface, as well as the wobbling angle of the rotating stage, it is not possible to guarantee such accuracy in the target positioning and therefore, an automated correction system is required. The implemented solution consists of a correction procedure based on the complete characterisation of the target surface, via a detailed 3D-mapping of the impact positions of the laser pulses on target. To obtain this 3D map, the transversal coordinates of the desired impact positions on the target surface are defined prior to the irradiation. The longitudinal coordinate along the target normal, which is affected by the surface deformation, is measured with an OptoNCDT ILD1320 distance sensor by Micro-Epsilon. The 3D position map (see Fig. 4.4 for two examples) is then converted into a matrix of encoder positions for the moving stages, which is used by the LabVIEW-based control software of the target assembly to correct the surface deviation on a shot-to-shot basis during the laser operation.

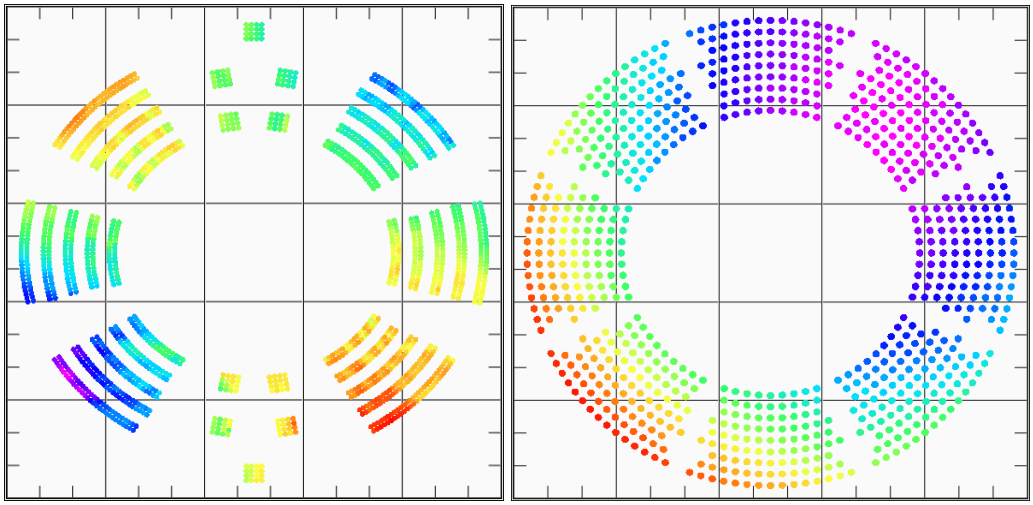

FIGURE 4.4: Deformation map for two of the target wheels. Color ramp in arbitrary units.

As the target characterisation is performed before the laser irradiation, it allows for achieving high operation repetition rates during the ion acceleration experiments. The commonly extended procedure for the positioning of the surface of the targets at the laser focus involves

the individual alignment of the impact positions in vacuum conditions. After determining the three-dimensional location of the laser focus inside the vacuum chamber (formally the Target Chamber Center, or TCC), the target surface for each impact position is brought to it by means of an optical and mechanical system. This is performed before each laser shot in the case of high power single-shot lasers, or a certain amount of them for tabletop laser systems.

The procedure presented in this chapter must be executed in a vacuum-free environment, as the distance sensor cannot operate in vacuum. In exchange, the complete set of impact positions is characterised in a single series of measurements at about 2 - 3 points per second (i.e., around 12 minutes for each 1000 impact positions). This 3D map is still valid in vacuum, but for a certain offset in the focal position along the incidental direction of the beam due to drift of the TCC (detailed in Sects. 5.1.1 and 5.2.1). In contrast to the standard procedure, the target surface for only one of the map impact points (typically the first one) is brought to the TCC and serve as reference for the rest. All the characterised shot positions become then available at the laser focus, with micron accuracy, for the irradiation experiments. The control software allows for both single-shot or multi-shot operation. For the later, the number and range of map points for the series and the positioning rate can be also selected.

Hence, this procedure results in a very flexible and agile method for the characterisation of the target impact positions and its positioning at the laser focus, that also provides a great and reasonable number of available points. In fact, it maximises the efficiency of target systems such as the one described in this chapter for applications that require continuous operation at high repetition rates. In the following sections, the correction and positioning procedure will be explained in detail, including its development from the initial proof-of-concept tests to the validation measurements and the practical results used during the experiments.

4.3.1 The correction and positioning procedure

The principle of the correction procedure consists of the complete spatial characterisation of the target surface profile. This includes the intrinsic deformation of the target wheel from its manufacturing, as well as the surface roughness of the target foils, specially relevant for thicknesses below 7 μm and for plastic materials. An auxiliary visible diode laser at 640 nm, coupled to the optical path of the high power laser (the complete set-up picture is shown in each experimental section), is used within this whole procedure, in order to serve as reference and for alignment purposes.

Base map conversion

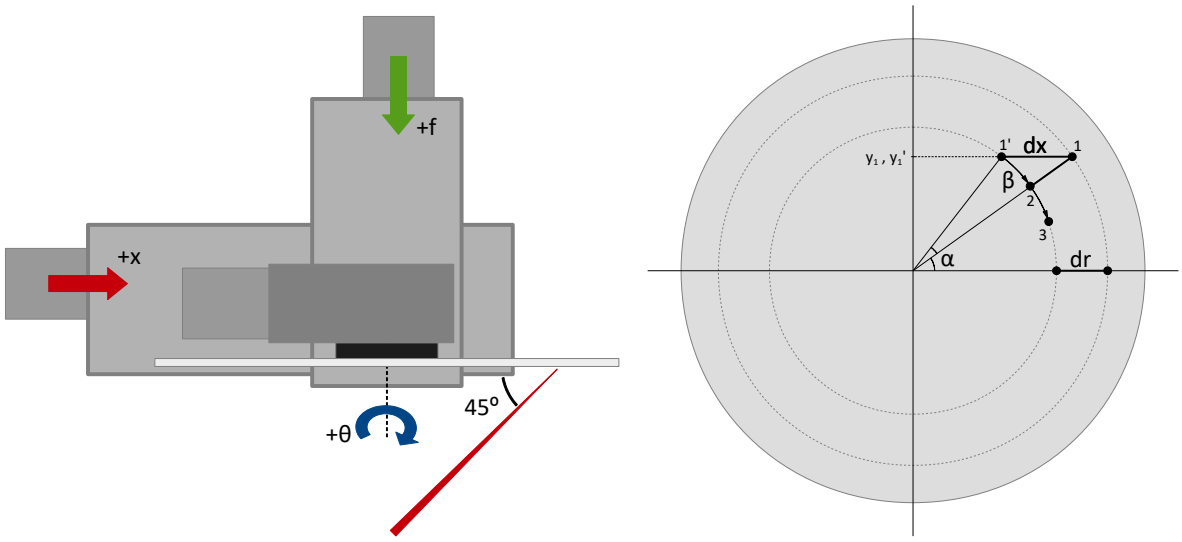

FIGURE 4.5: Coordinates conversion.

For the first step, a base map that contains the transversal coordinates of each impact position over the target wheel is generated by the control software. Depending of the version of the wheel, some additional parameters can be set, as the distance between points and the number of rows. This base map is defined in polar coordinates in the wheel reference system $(r_i; \alpha_i)$, being the (0,0) located at the center of the wheel. In order to translate this set of coordinates to encoder positions for the moving stages, a coordinate transformation must be performed. Fig. 4.5 (left panel) depicts a schematic representation of the axes definition of the moving stages. The two-dimensional coordinates of a map point in the stages reference system $(x_i; \theta_i)$ are determined by the encoder positions of the transversal moving stages for which the auxiliary laser beam impinges on it at the plane $f = 0$ (being f the encoder position of the linear-longitudinal stage). The incidental point of the laser over the target wheel, for $x = 0$ and a θ for which the wheel $\alpha = 0$-axis is parallel to the chamber board, defines a reference point that will be used for the coordinate transformation. The coordinates of this point can be measured both in the wheel reference system $(r_r; \alpha_r)$ and in the stages reference system $(x_r; \theta_r)$. The angular coordinate of each reference system differs by a certain offset, δ, given by the home position of the rotating stage, which follows the relation

$$\delta = \alpha_r - \theta_r \tag{4.1}$$

For the linear-transversal coordinate x, the conversion from one reference system to the other one is not as direct, as the direction of each of them are the opposite (displacing the linear stage towards its positive limit places inner target positions at the laser incidental point) and there is a dependency on the laser beam height over the rotation axis. From the reference point, the coordinates in the stages reference system of any other map point can be calculated as $(x_i = x_r + dx_i; \theta_i = \theta_r + d\theta_i)$ according to

$$d\theta_i = \alpha_i - \alpha_r - \beta_i = d\alpha_i - \beta_i \tag{4.2}$$

$$dx_i = r_r \cos\alpha_r - r_i \cos\alpha_r - \beta_i \tag{4.3}$$

where $(r_i; \alpha_i)$ are the coordinates of that point in the wheel reference system and β_i is defined as

$$\beta_i = \arcsin(\frac{r_r}{r_i}\sin\alpha_r) - \alpha_r \tag{4.4}$$

Fig. 4.5 (right panel) shows a graphical representation of this coordinate conversion. A change of radius movement dr from a arbitrary point **(1)** to another **(2)**, both at the same angle α, is composed of a shift in the x-axis, according to Eq. 4.3, and an angular displacement β given by Eq. 4.4. If the destination angle is at a different angular position **(3)**, an extra term $\alpha_3 - \alpha$ that accounts for this difference is added. This calculation is integrated in the control software. By providing the coordinates of the reference point for both the wheel and the stages coordinate systems, the conversion from the base map in the wheel reference system to the stages reference system is automatically performed.

Surface mapping

After generating the base map and setting the correspondence between map points and encoder positions, the relative longitudinal deviation of the target surface at each predefined impact position is measured with a distance sensor (ILD1320-10, by Micro-Epsilon), which has

a reproducibility of 1 μm and a detection range of 10 mm. The functioning principle of this sensor is the following: it emits a continuous visible (670 nm) laser beam with a spot size of 45 μm-diameter amidst its measuring range, that increases up to 150 μm at its upper and lower range limits. Upon impinging over the target surface, it determines the sensor-object distance from the diffuse part of the reflection by means of the optical triangulation technique.

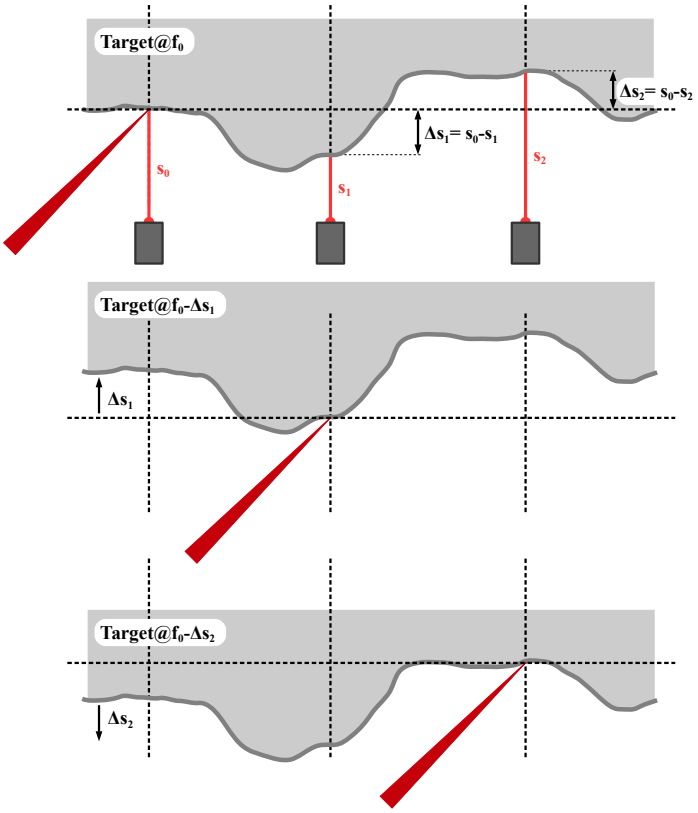

FIGURE 4.6: Scheme of the measuring and correction principle.

For the map measurement, the sensor is placed perpendicular to the target wheel and heading to the reference point (i.e., matching the optical path of the auxiliary laser). From the converted set of coordinates, the control software is able to position each predefined impact position under the sensor laser. Fig. 4.6 depicts the basic principle of the correction procedure. In this figure, the distance measurements of the sensor for each map position are denoted as s_i, while the encoder position of the linear stage moving normal to the target surface is defined as f_i (the index i = 0, 1, 2,... identifies the map point). Taking as reference the distance to a impact point at a certain longitudinal position, s_0, the relative deviation of each other map point s_i can be

calculated as $\Delta s_i = s_0 - s_i$. In order to correct these deviations and place each map point at the transversal plane of that arbitrary point, f_0, the linear stage must move the target surface the very same distance, i.e, following the relation

$$f_i = f_0 - \Delta s_i = f_0 - (s_0 - s_i) \tag{4.5}$$

This ensures that, for each impact position, the auxiliary laser beam —and hence, the high power laser during the irradiation experiments— impinges on the same spot over the target surface that has been measured by the distance sensor, and whose coordinates were defined in the base map. This calculation defines a transversal plane, located at f_0, containing the corrected positions for all the map points.

Positioning at the laser focus

The last step in the alignment of the target system consist of placing the whole set of corrected map points, i.e., this transversal plane of corrected positions, at the real focus of the high power laser. The corresponding procedure and set-up will be explained on detail in each experimental chapter of this thesis, as each experiment has its own method for retrieving the three-dimensional location of the TCC and placing the target surface at it.

The underlying basis, however, consists of the following steps: the target surface for one point of the map (typically the first one, i = 0) is placed under the path of the alignment laser beam. Note that the distance sensor laser was aligned to the reference point over the target wheel (x_r; θ_r), so positioning the stages at the location at which the surface deviation was measured for this first point serves at the starting point. Then the target is drifted along the laser incidental direction z with micron precision until the target surface is at the laser focus. This displacement is only performed for the linear stages (transversal x and longitudinal f, being $z = \sqrt{x^2 + f^2}$), as the heigh of the laser beam does not change. Once this position is determined, the control software sets it as the focal reference position (X_0; Θ_0; F_0) and refers the rest of map points to this offset according to

$$X_i = X_0 + \Delta x_i = X_0 + (x_i - x_0) \tag{4.6}$$

$$\Theta_i = \theta_i \tag{4.7}$$

$$F_i = F_0 - \Delta s_i = F_0 - (s_0 - s_i) \tag{4.8}$$

i.e., the transversal plane of corrected positions is shifted to the focal reference. In Eqs. 4.6 – 4.8 variables with capital letters X_i, Θ_i, and F_i refer to the three-dimensional position of the impact point i at the laser focus, while x_i and θ_i are the base map coordinates of the same point. Variables s_i denote the distance sensor measurements, as in Eq. 4.5. As stated in the previous section, this set of coordinates will be used by the control software to place the target surface corresponding to each map position at the focus of the laser in a shot-to-shot basis.

4.3.2 Initial tests

The performance of the distance sensor was tested for target materials with different reflectivities and opacities. In particular, transparent targets as kapton or Mylar, matte targets as paper or cardboard, and shiny targets as polished copper were used. The targets were mounted on a micrometric linear stage in front of the distance sensor and moved at fixed steps of 250 μm along the whole sensor measuring range (10 mm). For each step, a sensor reading was stored.

While the manufacturer indicates that the sensor repeatability decreases for shiny or transparent targets, the results shown in Fig. 4.7 indicate that the performance is rather similar than for matte targets. The upper panel depicts the relative deviation from the previous measured position, i.e., the step width measured by the sensor. Three cases are shown in the graph: a transparent Mylar target (dashed-blue line), a matte paper target (solid-green line), and a shiny copper target (dotted-red line). The mean value of each curve differs by around 1 - 2 μm with respect to the real physical displacement, 250 μm. The fluctuations are slightly larger for transparent and shiny targets, but the standard deviation is always below 4 μm. This value is of the same order of the precision of the linear stage, of $\pm$2.5 μm.

The lower panel in Fig. 4.7 depicts the absolute deviation from the initial position within the sensor range. This accounts for the total displacement from the initial position measured by the sensor. It can be seen that there is a certain drift along the range between 15 and 40 μm, more pronounced for the transparent target. However, as it will be shown in the following sections,

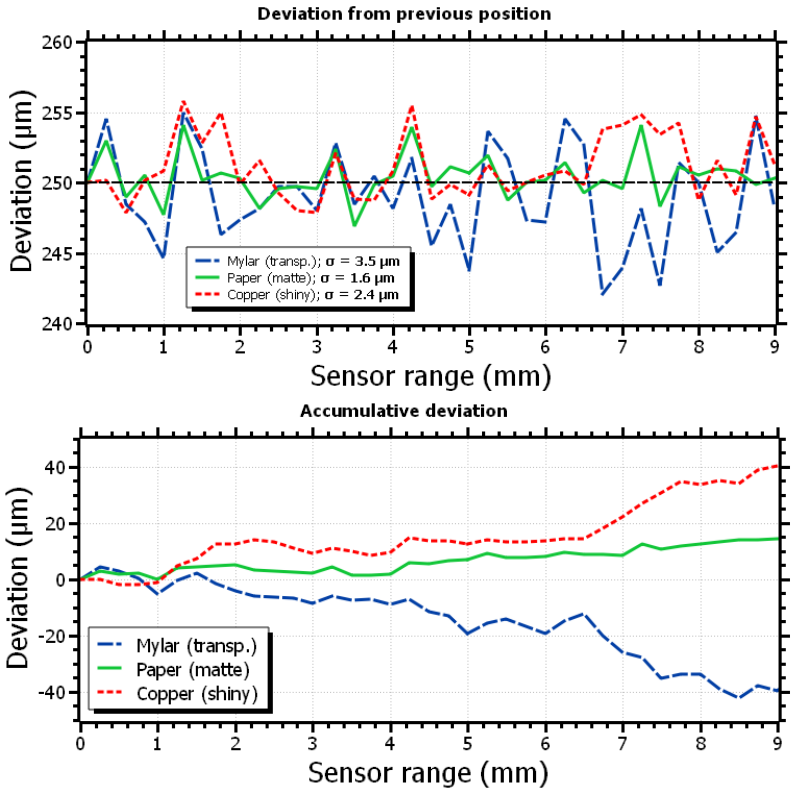

FIGURE 4.7: Distance sensor performance tests for materials with various reflectivities.

the typical total deformation of the target wheels is of the order of 500 to 1000 μm, which corresponds to a few 250 μm steps. The precision of the distance sensor within this distance is below 10 μm.

In order to study the validity of the 3D-mapping technique, the surface profile of a 100 mm-radius 1 mm-thickness uniform copper disk, mounted on the target assembly, was measured. In the image displayed in Fig. 4.8, the distance sensor and the dummy copper target, mounted on the three moving stages, are shown. The measurements were performed by moving the disk with the same speed as during target irradiations in order to include the effect of the wobbling angle of the rotating stage. The black solid and the red dashed lines in the left panel in Fig. 4.9 represent the deviation of the disk surface with respect to the normal plane measured for two radii of 74.2 mm and 64.2 mm, respectively. As can be observed, the surface deviates up to 500 μm at some positions. The gradual deviation of the surface profile for certain angles

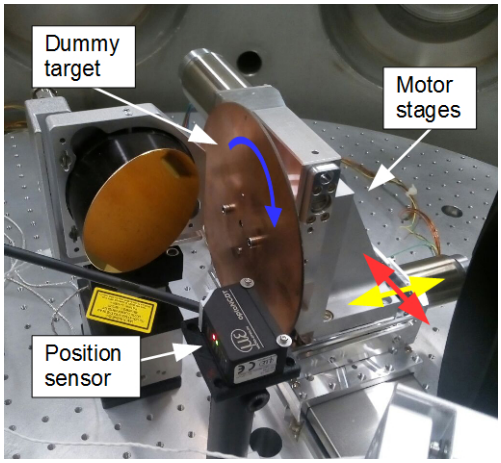

FIGURE 4.8: Image of the set-up used for the validation of the mapping procedure.

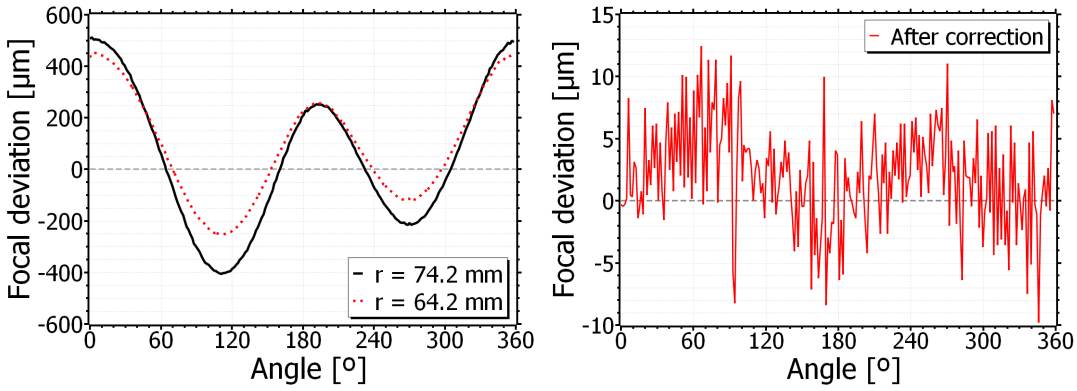

FIGURE 4.9: Deviation of the copper disk surface before and after the correction.

clearly indicates a deformation of the target, probably due to the way the disk is screwed to the rotating stage. In fact, the amplitude of the deformation decreases with the radius, as shown in the figure.

The 3D map obtained with this method was then used as an input for the control software of the target assembly, in order to apply the corresponding longitudinal correction for each measured point at the target surface. To evaluate the performance of the position correction, a second measurement of the surface of the dummy target along the normal direction during the correction was performed. The results are reported in the right panel in Fig. 4.9 for the 74.2 mm radius. It can be seen that the correction procedure reduces the initial deviations in the dummy

target surface along the longitudinal axis from around 500 μm to final deviations in the order of a few micrometers. However, the results still show a slight oscillation of about 3 μm, which can be attributed to the vibration of the copper dummy target due to the rotating movement. Nevertheless, this vibration is within the Rayleigh length of the L2A2 system and is expected to be smaller for the target wheels.

4.3.3 Validation

The reliability of the correction and positioning system was also verified by means of a secondary diagnostic, independent from the distance sensor (ILD1320-10). A schematic representation of the experimental set-up can be seen in Fig. 4.10 (left panel). The beam from a visible diode laser was expanded with a two lens arrangement ($f = -30$ and $f = 200$) and then focussed on the surface of the targets by using a microscope objective (M Plan Apo NIR **x50** by Mitutoyo). The backscattering light was then recollimated by the microscope and focussed on a CMOS camera (CMOS 5MP by Mightex) with a $f = 75$ lens. The position of the target surface with respect to the beam focus could be measured by comparing the relative size of the resulting spot shown in the image retrieved by the camera. A schematic representation of this principle is depicted in the right panel in Fig. 4.10. In this way, a correlation between the spot size of the beam at the target surface and the deviation from focus could be obtained for each point of the surface map, in order to validate the correction procedure. For the following, the positive direction considered for the deviation is given by the pointing direction of the incidental beam on target.

As a first step, a 3D map of the target surface, using the long-slots version of the wheel-like holder, was measured with the distance sensor. As targets, 12 μm-thickness aluminium foils with two different surface qualities, shiny and matte, were used, in order to study the sensor performance at measuring materials with different reflectivity. The laser beam from the sensor was aligned, normal to the target surface, to a reference position on the target wheel given by the incidence point of the laser coming from the microscope objective (Fig. 4.10). After the surface characterisation, the correction from the map was applied to the whole set of target points, and the corrected positions were measured again with the distance sensor. This positioning verification was performed at a repetition rate of 10 Hz with the same movement profile as in the irradiation experiments at the L2A2, i.e., each 100 ms a new target point was placed at the path of the sensor laser and measured. The results, which can be seen in Fig. 4.11, present

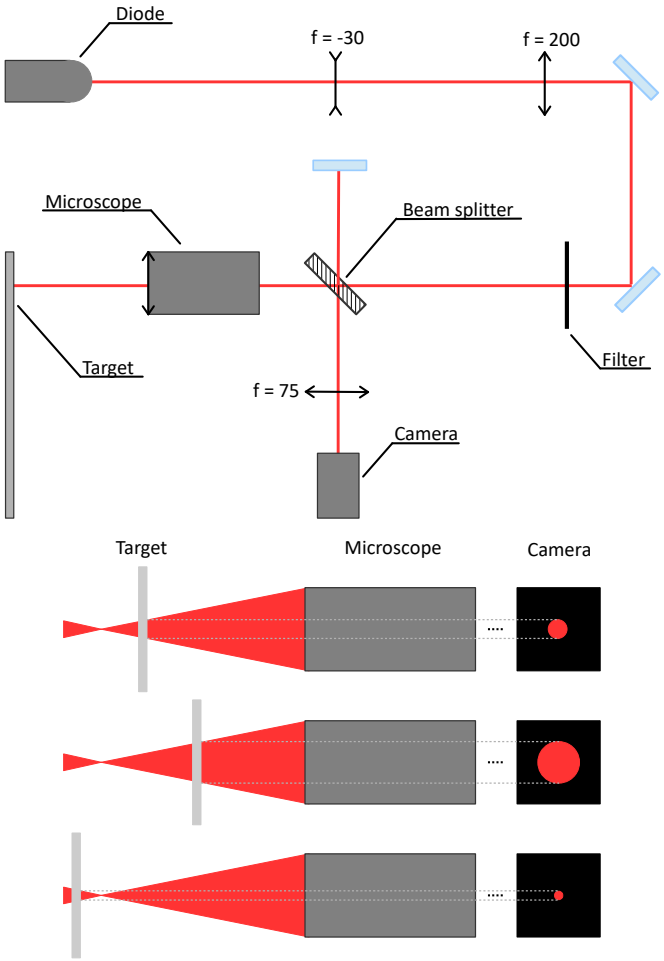

FIGURE 4.10: Positioning validation set-up and principle.

a systematic dispersion of ∼3.5 μm. The map curves had been normalised to the first map value, while the verification curves had been subtracted by its mean value. This procedure was repeated for several days under the same conditions, showing a great stability and coherence between measurements, as expected.

After the mapping and the correction verification procedures, the distance sensor was removed from its location and the laser coming from the microscope objective was focussed to the same reference position over the target wheel. Then, the target surface corresponding to one of the measured map points was positioned at the focus of the laser beam (zero position). A focal scan was performed by moving the target along its normal direction from -150 to 150 μm

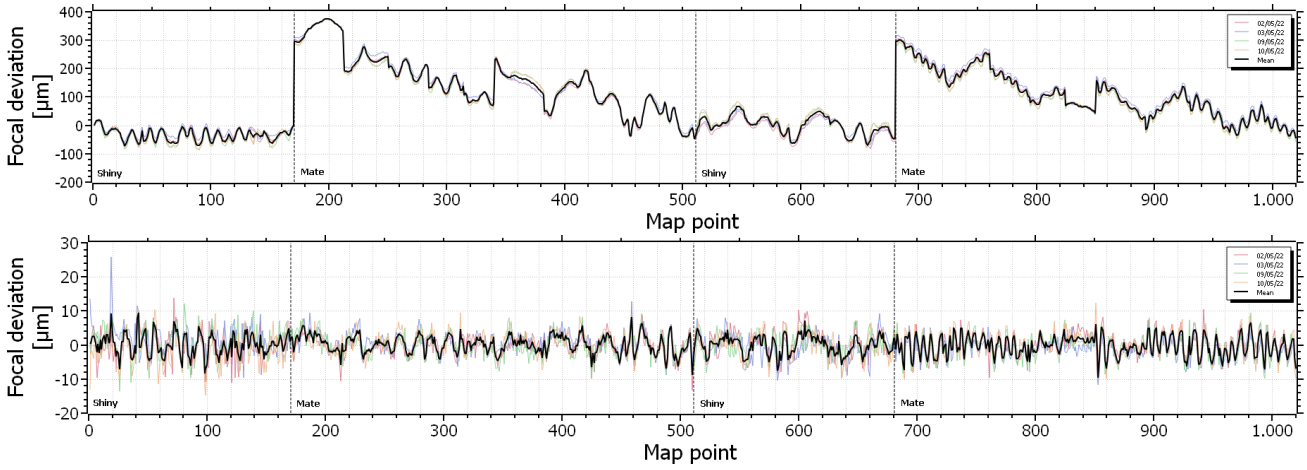

FIGURE 4.11: Maps and verifications.

with respect to the zero position at a step size of 5 μm. For each scan position, an image of the backscattered beam was stored. Thus, a calibration that correlates the relative position displacement with the spot size of the backscattered beam, i.e., the focussing beam profile, could be obtained. This procedure was performed for four map points, two of them for shiny targets and the other two for matte ones. In particular, the first map point of every two sector plates.

Two methods were used for the calculation of the spot size of the backscattered beam from the retrieved images. For Method I, the X and Y sizes were directly determined from the intensity profiles (Fig. 4.12, green line), in number of pixels, from which the Root Mean Square (RMS) can be obtained as

$$RMS[px] = \sqrt{\frac{X^2[px] + Y^2[px]}{2}} \tag{4.9}$$

which was used as a comparison parameter.

For Method II, the beam spot size was characterised by the RMS (Eq. 4.9) of the FWHM (Full Width at Half Maximum) obtained by applying a Gaussian fit to the X and Y intensity profiles (Fig. 4.12, red line).

The calibration curves for both methods are reported in Fig. 4.13. Panels **(a)** and **(c)** show the results for each one of the four measured points (two shiny and two matte) for Methods I and II, respectively, while in panels **(b)** and **(d)** the mean values of these four measurements

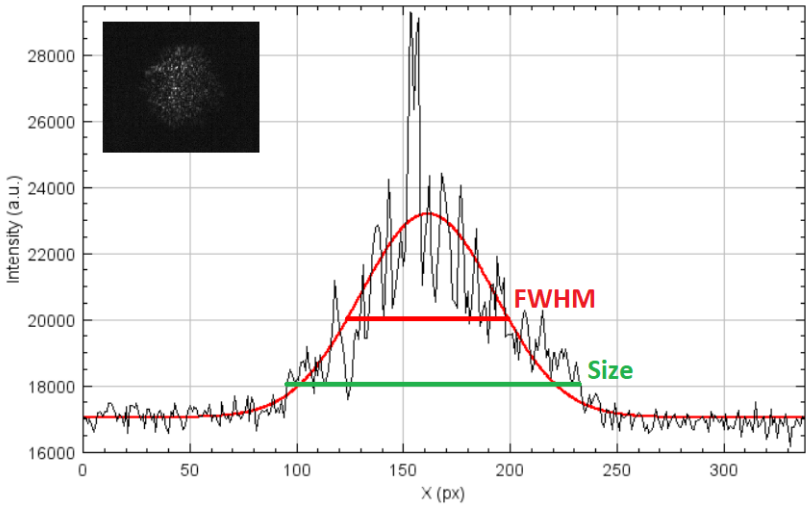

FIGURE 4.12: Example of the intensity profile of the backscattered beam and its analysis. Inset: image of the backscattered beam.

are depicted. The resulting curves from Method I, in panel **(a)**, exhibit a very good consistency between them, regardless of the target reflectivity. However, for distances greater than 100 μm with respect to the zero position in the negative direction a certain saturation can be observed (see Fig. 4.14). This may be attributed to an aberration introduced by the optical arrangement. The calibration curves shown in panel **(c)**, corresponding to Method II, present a greater dispersion in the spot size determination, specially noticeable for the farthest regions of the focal scan ($\pm$100 μm). For these regions, the backscattering beam intensity profile was weak and slightly inhomogeneous, so the Gaussian fit was not as reliable.

As shown in panels **(b)** and **(d)** in Fig. 4.13, the calibration curve, namely the focussing beam profile, can be adjusted to a parabolic fit over a range of about 1 - 1.5 Rayleigh lengths around the zero position. From that point on each direction, the divergence can be fitted to an increasing or decreasing linear profile. The fit parameters for both Methods can be found in Table 4.1.

The correction procedure was then evaluated by positioning the target corrected plane at a fixed distance from the zero position and measuring the backscattering beam size for the corrected target positions. Any deviation in this positioning would result in a modification of the retrieved beam size at the camera. The fixed distance was not set to zero (focal incidence), as it would be difficult to determine the direction of the deviation and changes in the spot size,

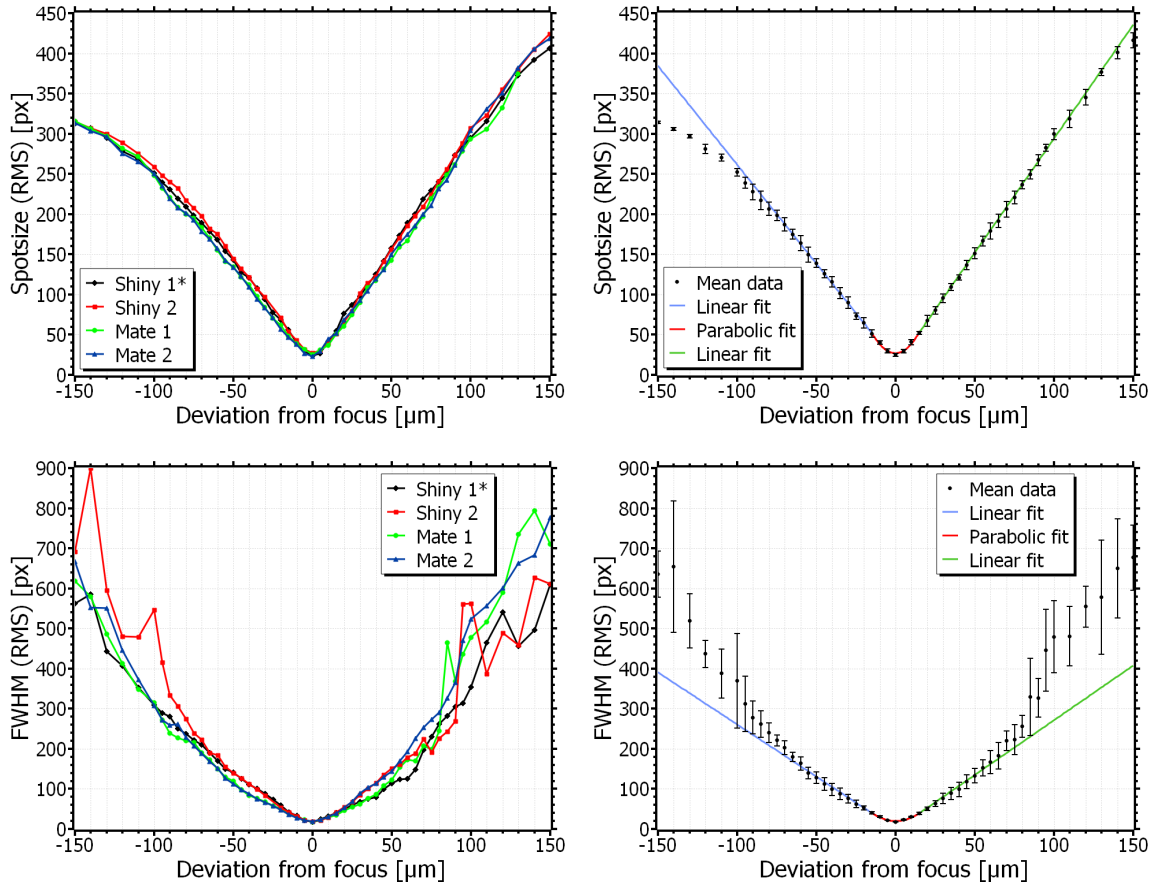

FIGURE 4.13: Calibration - Methods I & II.

but to a certain offset within the linear regions of the focussing profile (>15 μm or <-15 μm). For each corrected target position, an image of the backscattering beam size was stored and analysed according to Methods I and II. From the beam size values and the focussing profile calibration, the relative distance with respect to the zero position could be calculated for the whole map, and compared to the fixed distance. To reduce the amount of time taken on each measurement, only one of each five map points were measured.

The results, for the two analysis methods and for various offsets, along with the correction verification measured by the distance sensor, are shown in Fig. 4.15 **(a - d)** and Fig. 4.16 **(a - c)**. All the plotted curves have been subtracted by its mean value. The calculated standard deviation, between 4.5 and 7 μm for Method I and between 5 and 9.5 μm for Method II, is slightly greater than for the sensor measurement ($\sim$3.5 μm), but still within the Rayleigh length

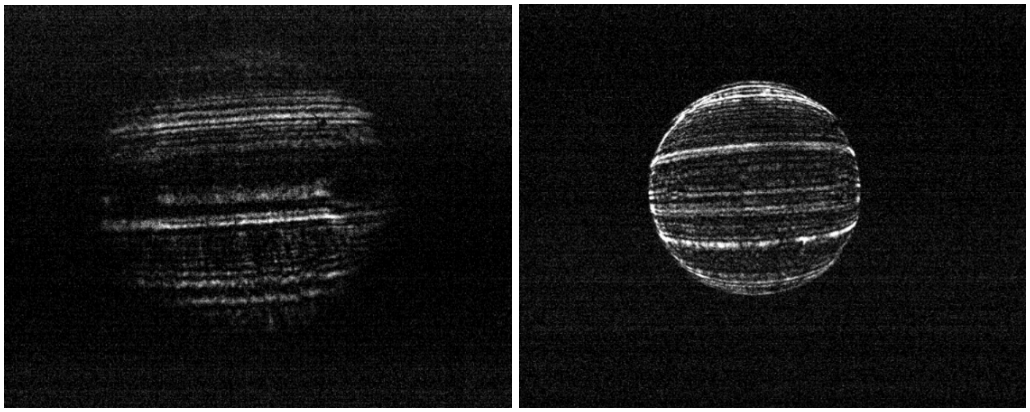

FIGURE 4.14: Example of a non-saturated (left) and a saturated (right) images of the reflected beam at +150 μm and -150 μm, respectively.

TABLE 4.1: Calibration curves fit parameters. Linear fit: $RMS = mf + n$; parabolic fit: $RMS = af^2 + bf + c$

	Linear fit		**Parabolic fit**			**Linear fit**	
	m	*n*	*a*	*b*	*c*	*m*	*n*
Method I	-2.5	15.4	0.1	0.03	26.9	2.8	10.3
Method II	-2.6	0.8	0.09	-0.03	19.7	2.7	-1.6

of the L2A2 system. The dispersion also seems to increase for the shiny targets. Fig. 4.16 **(d)** directly compares the results from Methods I and II for the same measurement, showing great consistency between them. The mean difference between curves from Method I and II is smaller than 5 μm. However, some of the points from Method II present a dispersion of about 2 - 3 times the standard value. For these measurements, the Gaussian fit applied in the calculation only fitted a part of the intensity profile corresponding to one or more peaks coming from the micrometric structure pattern of the target surface.

Overall, the correction verifications measured both with the position sensor and with the set-up presented in this section are in good agreement. Thus, the correction and positioning procedure, used in the experiments described in the following chapters, can be validated.

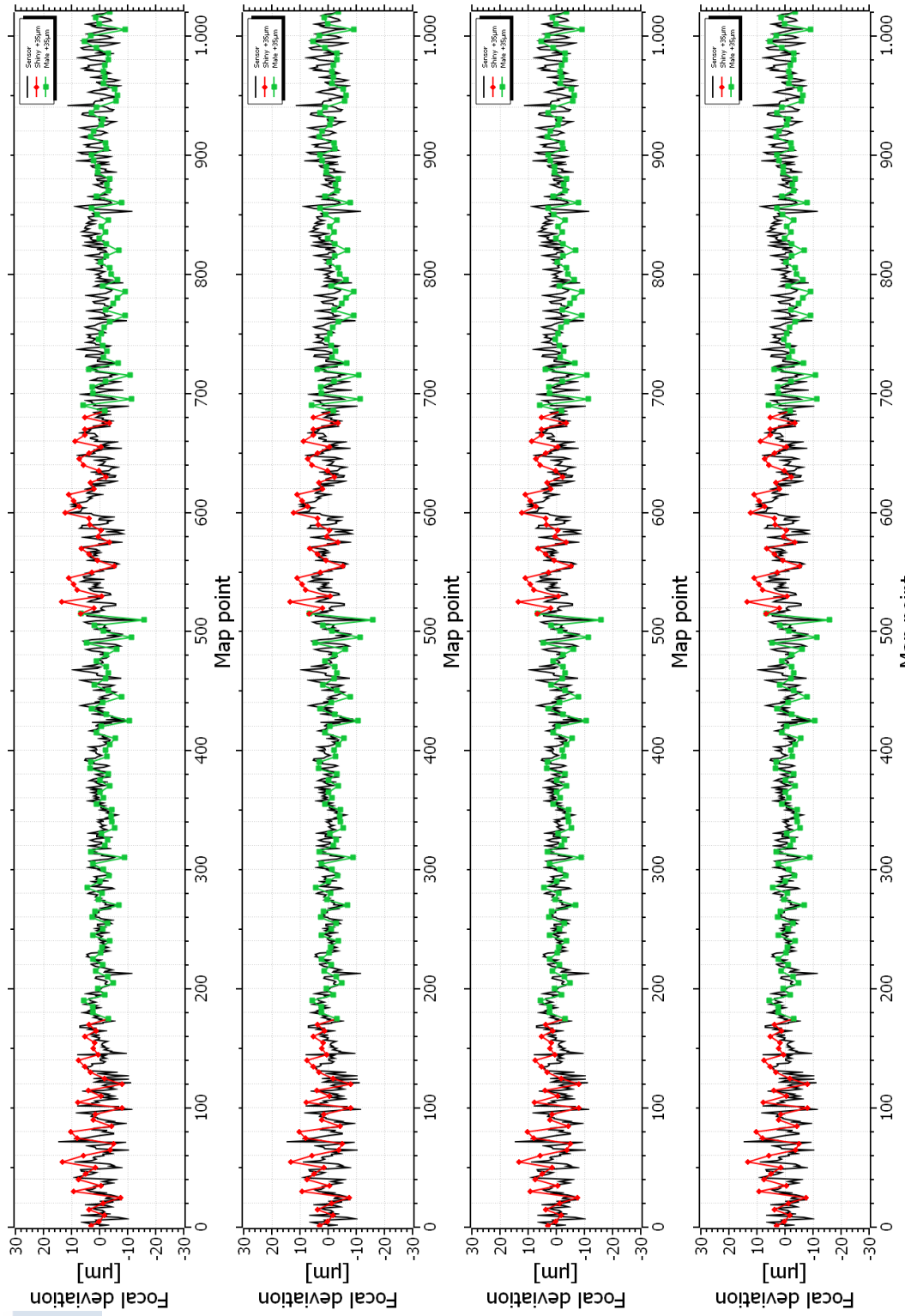

FIGURE 4.15: Comparison between map and methods

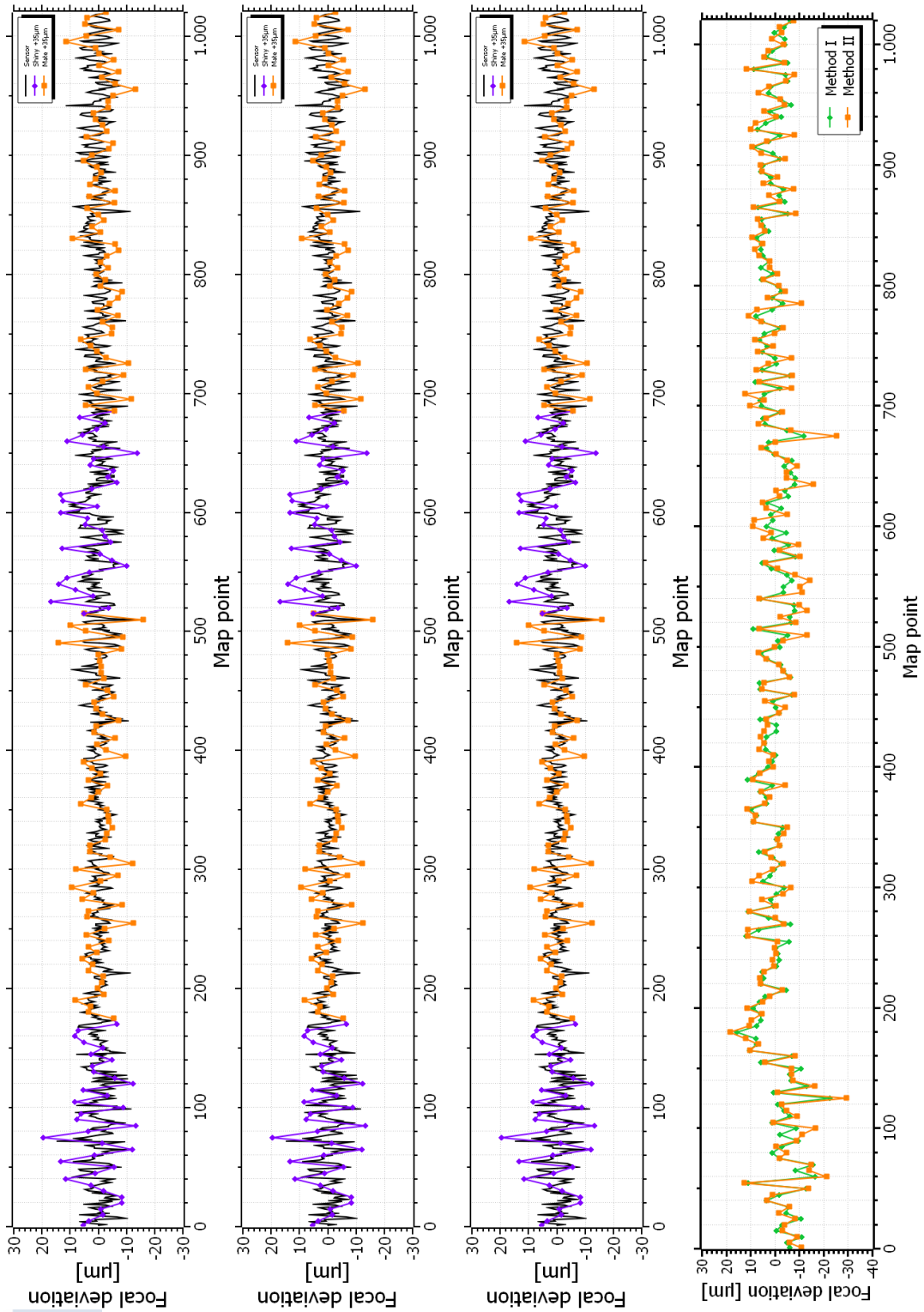

FIGURE 4.16: Comparison between map and methods (cont.)

4.3.4 Target wheel measurements

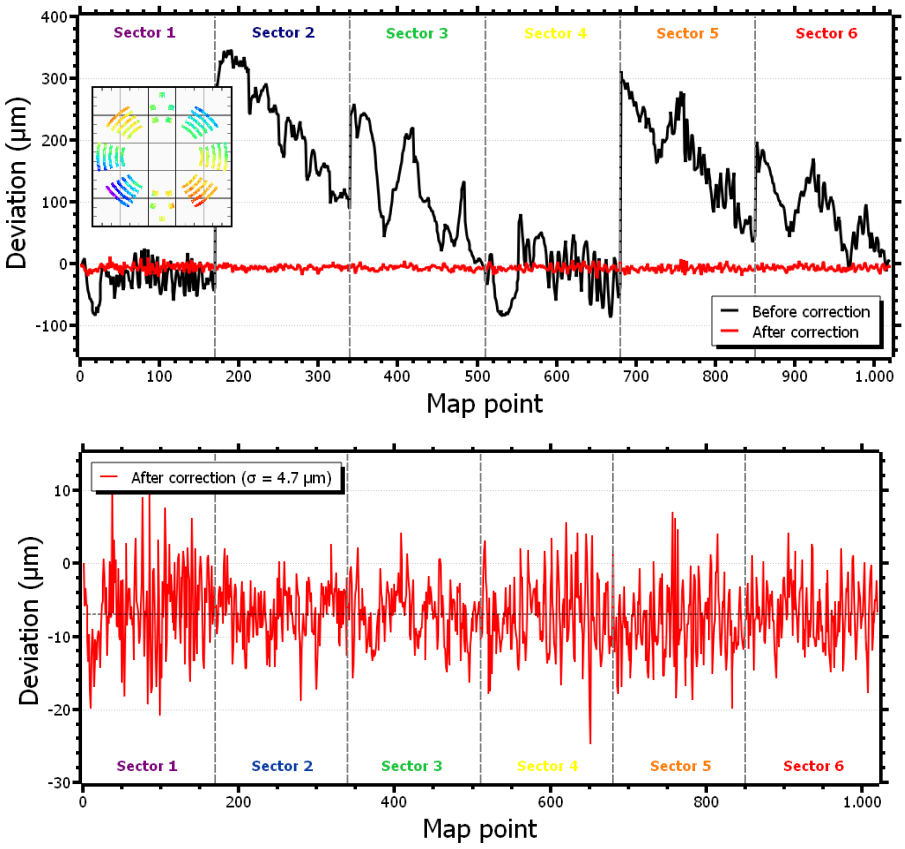

FIGURE 4.17: Deviation of the wheel-like holder target surface before and after the correction.

For the multi-target wheels used in the ion acceleration experiments, the 3D-mapping and verification method was applied for a set of predefined impact positions. As for the primary tests, a second measurement of the target surface deviation was performed during the correction procedure, to compare with the initial surface profile. The obtained results for the long-slots wheel, before and after the correction, are shown in Fig. 4.17. All the curves in this figure are normalised to their first value, thus denoting the relative deviation of the target surface instead of the raw values measured by the sensor. The sectors with squared holes for MEMS targets are not included in the graph, but only the six sectors with long slots. In this case, only one row of impact points was defined for each slot. It can be seen that the initial deformation (black solid line in upper panel) is of the order of several hundreds of microns. This deviation is even

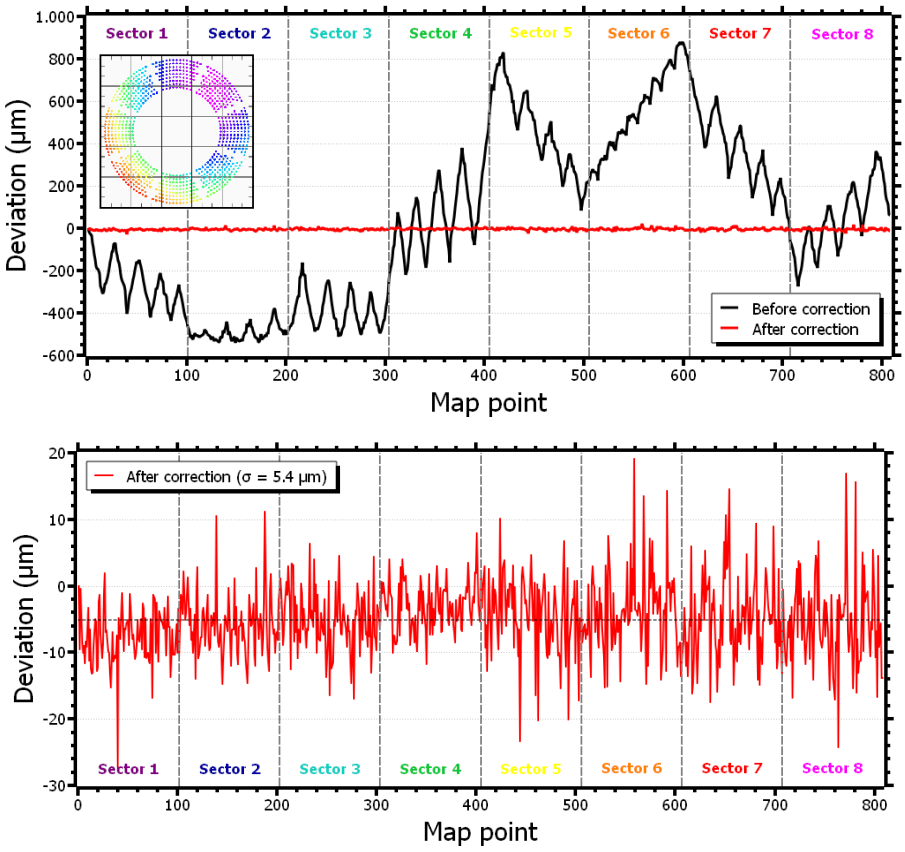

FIGURE 4.18: Deviation of the wheel-like holder target surface before the correction.

noticeable between adjacent sectors and within the same sector. It increases for outer radii for most of the sectors, suggesting that the central screws that fix the wheel to the rotating stage produce a certain bending effect, as for the copper dummy disk. The red solid curve in the upper and lower panels of Fig. 4.17 refers to the measured target deviation after the correction procedure. The intrinsic target deformation is reduced to micron-size fluctuations, being their standard deviation $\sigma = 4.7$ μm.

Fig. 4.18 depicts the same results for the version of the target wheel with individual holes. As in Fig. 4.17, the curves are normalised to their first value. The black-solid curve in the upper panel, corresponding to the surface profile before the correction, indicates a more pronounced total deviation than in the long-slot wheel, of about 1300 μm, due to the larger size of this version. As in the previous cases, this deviation increases for the outer radii, presumably for

the same reason. After the correction procedure (red-solid lines in both panels in Fig. 4.18), the surface profile deviation is reduced to a few microns with an standard deviation of σ = 5.4 μm.

The target positioning procedure described in this chapter ensures shot-to-shot laser incidence at focus with an accuracy of few microns, which is a key issue for the stability of the ion source in terms of maximum energy, spectral shape and particle number, as will be discussed in the following chapters. In the case of the long-slots version of the target wheel, the distance between adjacent points of the base map can be selected by the user. This distance must be sufficient that the damage produced by each laser shot does not generate a deformation of the target surface at the next incidental position. In that case, the implemented corrections with respect to the laser focus are no longer valid. This would lead to a significant reduction of the maximum energy of the ion spectra. Further analysis is required in order to determine the minimum distance between adjacent impact positions, which will be commented in the next chapter (Sect. 5.1.2).

4.4 Target operation and functioning

As described in previous sections, the surface 3D map is loaded to the control software and referenced to the laser focal position for the irradiation experiments. From this set of corrected coordinates, the moving stages are able to place the target surface for any of the map points at the TCC for single-shot operation. For multi-shot mode, the operation and the functioning of the control software are slightly different for each version of the target wheel.

The target wheel with long slots, used in the first part of the L2A2 experiments, allows for burst operation at high repetition rates. As the maximum speed of the linear-transversal stage is not sufficient to move from one target slot to the next one within the time interval between shots (for the 10 Hz-nominal repetition rate at the L2A2), the operation consists of a succession of series of shots, one series per slot. Through the control software the user can select which slots are about to be shot. The control software generates a PLC (Programmable Logic Controller) program in the internal programming language of the motion controller (Turbo PMAC) that contains a list of motion commands corresponding to each corrected impact position for each target slot. Then, the shot sequence is as follows. The control software uploads the PLC program of the first selected slot to he motion controller and starts its execution. On trigger (see Sect. 5.1.1 for a detailed explanation), the controller starts positioning each impact point at the

TCC in synchronisation with the arrival of the laser pulses, at the laser repetition rate. Once the slot is finished, the control software uploads the PLC program of the next selected slot and starts the execution. This procedure is repeated until all the selected slots are completed.

The operation repetition rate within the irradiation bursts is determined by the maximum speed of the rotating stage (22 °/s), the distance between adjacent impact positions, and the laser rate. Although the maximum laser rate at the L2A2 is 10 Hz, if a distance between shot points of 1000 μm is selected, the target assembly using this target wheel version could in principle operate at repetition rates between 18 and 30 Hz, for the minimum and maximum radii of the target holder, respectively. The number of shots per slot, for the same distance between adjacent points, varies from 26 to 42 depending on the radius, for a total of 1360 considering eight slots. This would correspond to 40 bursts of about 25 - 40 shots at high repetition rates within the whole target wheel.

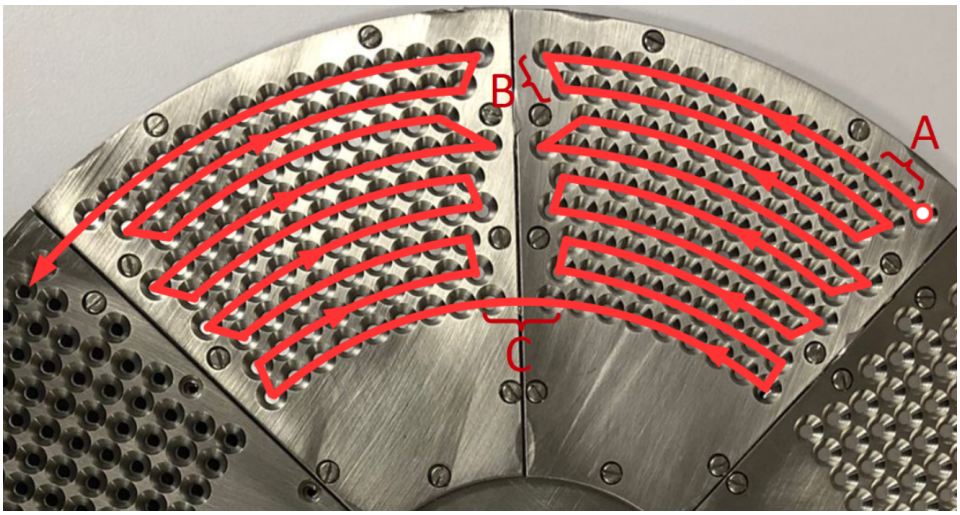

FIGURE 4.19: Shot order for the CLPU target wheels.

The target wheel designed for the CLPU experiment, on the other hand, allows for a total of 808 shots in a single series in continuous operation, intended for a repetition rate of 1 Hz. In this case the separation between adjacent points and consecutive radii is short enough so the rotating and linear-transversal stages are capable of moving from one position to the next one within the same sector. In addition, the programmed positioning sequence, which is shown in Fig. 4.19, optimises the change between one sector to another by reducing its amount and performing it at the innermost and outermost radii, for which the distance is shorter. These changes of sector

are feasible at repetition rates up to 2 Hz, limited by the maximum speed of the rotating stage. Within the same sector, operation at 3.3 Hz can be achieved.

The user can select, via the control software, the number of shots and starting point for each irradiation series. In principle, this target wheel can operate following the same procedure described above for the long-slots version, —the control software generates a PLC program containing the list of motion commands for the set of selected impact positions, that is executed and triggered—, but at a lower repetition rate. However, some experimental constraints present at the CLPU experiment, that will be explained in the corresponding section (Sect. **??**, prevented from operating with this procedure. Instead, the positioning and synchronization was performed by the control software itself.

4.5 Conclusions

The procedure introduced in this chapter for the shot-to-shot correction of the target positioning at the laser focus solves most of the limitations present in similar multi-target assemblies that have been recently developed. In particular, one of the main improvements concerns the target replenishment rate, which directly affects the operation rate and stability of the ion source.

Gershuni *et al.*[99] propose a target delivery system based on 100 mm-diameter Si wafers where hundreds of micro-targets can be created using MEMS technology. The maximum 0.2 Hz repetition rate reached with this system results from the time required for a fully on-line measurement and correction sequence. In this sequence, the position of each irradiation point at the laser focus is measured and corrected shot-to-shot via a closed feedback loop between the linear-longitudinal stage and a distance sensor. In the approach of this work, the surface correction and focal position of all of the impact positions is determined prior to irradiation, therefore no on-line measurements are required, hence reducing the movement time in the target positioning.

Gao *et al.*[98] use a similar system to the one proposed in this chapter, based on a metallic target wheel hosting target plates accommodating up to almost 1700 impact positions. However, the maximum operation rate of this target assembly is 0.5 Hz. The main limitation is caused by the time between laser shots required to reduce the amplitude of the target holder vibrations after reaching each shot position. In our case, this factor is not relevant during the irradiation,

as the movement between impact positions is continuous and no vibrations in the target wheel are produced.

More recently, Chagovets *et al.*[105] have developed a target replenishment system based on a raster configuration, holding up to about 1000 individual targets. Such a system presents a great flexibility in terms of target thicknesses, target materials, and structure. The alignment of the individual targets is also performed prior to irradiation by adjusting and recording their three-dimensional positions. The time reported for this operation is, however, rather long, about 100 minutes for the 1000 targets. On the other hand, the final operation rate of the system is 1 Hz.

Chapter 5

Laser-driven ion acceleration

The structure of this chapter is separated into two experimental campaigns performed under the extent of this work: at the Laser Laboratory for Acceleration and Applications (Sect 5.1) and at the Centro de Láseres Pulsados (Sect. 5.2). Within each section, the experimental set-up and the diagnostics used in each experiment are described in Sects. 5.1.1 and 5.2.1, respectively. Results are reported in Sects. 5.1.2 – 5.1.3 for the experiment at the L2A2, and in Sects. 5.2.2 – 5.2.3 for the experiment at the CLPU. After the experimental sections, Sect. 5.3 addresses the Particle-In-Cell simulations on particle acceleration carried out during this thesis, while Sect. 5.4 establishes a comparison between results from the experiments and the simulations. Final conclusions are given in Sect. 5.5.

5.1 Experiments at the Laser Laboratory for Acceleration and Applications

The current experimental campaign at the Laser Laboratory for Acceleration and Applications (L2A2), covering the whole extent of this thesis, is focussed on the development and commissioning of a long-term operation ion source. This comprises the development of the multi-shot target system, described in Ch. 4, the optimisation of the STELA laser performance, and the complete characterization of the accelerated ion beam. The following sections describe the outcome of the initial phase of the commissioning of the facility since its construction. Hence, the results and methodology presented here correspond to the first experimental measurements

and are not completely optimised. As an ion source intended for multi-shot operation —in particular for radioisotope production—, special interest relies on the shot-to-shot and long-term stability.

5.1.1 Experimental set-up

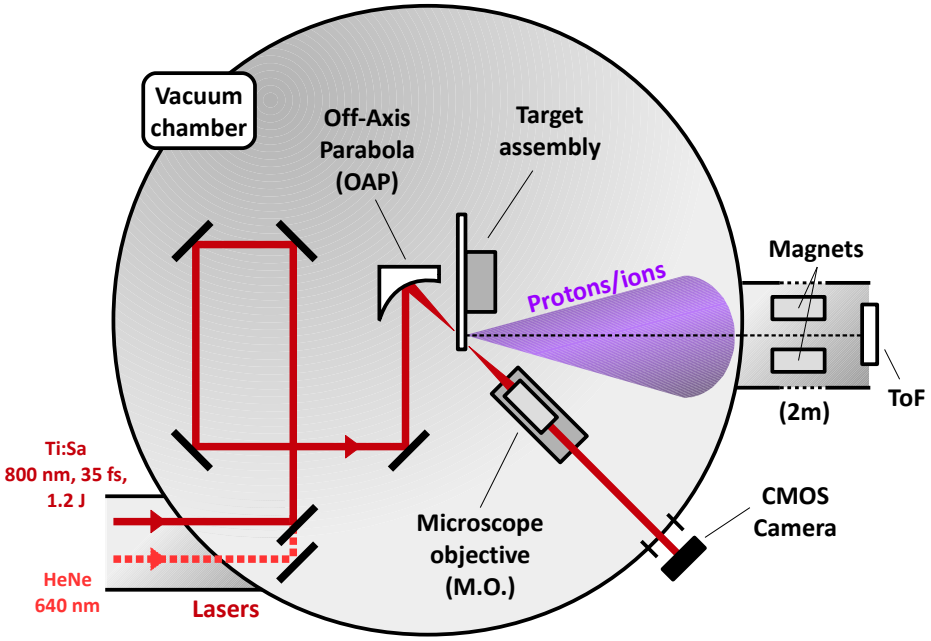

FIGURE 5.1: Chamber scheme.

A scheme of the experimental set-up at the L2A2 experimental campaign is shown in Fig. 5.1. Inside the interaction chamber, laser pulses of up to 1.2 J-pulse energy (0.9 - 1 J on target), around 30 fs-pulse duration (FWHM), p-polarization, and 800 nm-wavelength were focussed with a 45°, $f/2.8$ off-axis parabolic mirror (OAP) down to a $\sim$4 μm-diameter spot size, reaching intensities of above $1{\cdot}10^{20}$ W/cm^2. The targets were μm-thickness Al and Mylar foils placed on the multi-shot target system described in the previous chapter. The target correction and positioning procedure was applied, ensuring the shot-to-shot positioning of the target surface at laser focus with a few micron accuracy at the laser repetition rate. An auxiliary HeNe laser at 640 nm was coupled to the optical path of the Ti:Sa laser for the alignment of the distance sensor and the targets. The beam transport optical arrangement, consisting of four mirrors with

a reflective coating for near-IR and equipped with micron-accuracy actuators, allowed for the precise alignment of the laser beam arriving at the OAP.

The initial tests, both for single-shot and multi-shot operation, were performed with the first version of the target wheel (Fig. 4.2 **(a)**). For the major part of the commissioning campaign the long-slot version (Fig. 4.2 **(b)**) was used, and a few measurements were carried out using the individual-holes version (Fig. 4.2 **(c)**) at pulse rates up to 3.3 Hz. The upgraded version for 10 Hz-operation (Fig. 4.2 **(d)**) was being tested within the last month of this work.

A time-of-flight (ToF) system was used as the main diagnostic tool during the ion acceleration experiments. Being placed at 2 meters-distance behind the acceleration target inside a vacuum tube (see Fig. 5.1), it was used to measure the flight times of the accelerated ions. The ToF device consisted of the scintillator detector described in Sect. 3.2.3. The PMT was connected to a fast oscilloscope (Yokogawa DL9140 or Tektronix MSO64) to control the data acquisition and to visualize the PMT output signals. In order to reduce the external light noise in the detection system, the scintillator piece was covered by an aluminised Mylar sheet of 2 μm thickness. Saturation of the PMT was avoided by placing a neutral density filter OD1 between the photomultiplier and the optical fibres. A dipole magnet system was located inside the vacuum tube, close to the scintillator detector, to deviate electrons coming from the acceleration target. The whole experimental set-up (laser, beam line, chamber and ToF) was maintained under high vacuum conditions (10^{-5} – 10^{-6} mbar) during the measurements.

Target alignment at the laser focus

A secondary laser line impinging at the centre of the ToF detector and propagating along the normal direction with respect to the targets surface was firstly defined using a leak of the HeNe auxiliary laser at one of the alignment mirrors (see Fig. 5.1). The focus of the main laser beam line, coming from the OAP, was then pre-aligned to this secondary line, thus establishing the TCC location at the point where the two laser lines approximately crossed each other.

For the first part of the experimental campaign at the L2A2, the positioning of the target surface at the TCC was performed via the speckle technique[106]. This technique is based on the analysis of the speckle pattern produced by the reflection of the laser beam on the target surface. By moving the target along the propagation direction of the laser beam coming from the OAP, focal incidence conditions were achieved when the size of the speckles reached its maximum. An example of this principle is shown in Fig. 5.2. In this way, the first impact

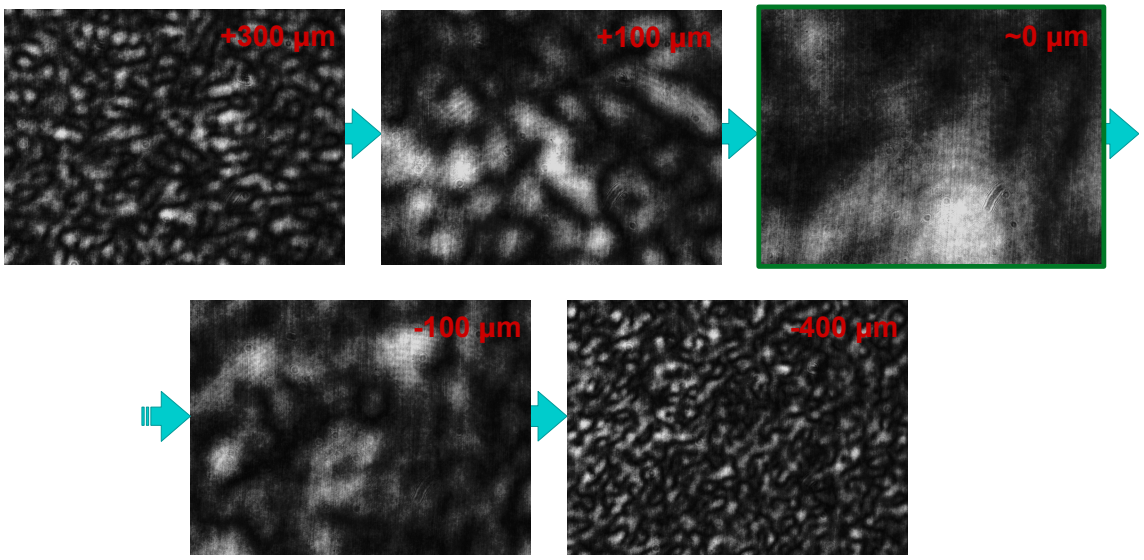

FIGURE 5.2: Speckle pattern for a focal scan.

position of the three-dimensional surface map was positioned under the auxiliary laser from the OAP, and then the target was displaced at minimal steps of 1 μm along this direction until the laser focal position was found. This procedure was performed in air, and then a certain offset of $\sim$20 μm in the laser incidental direction was applied in order to compensate both the drift of the laser focus in vacuum conditions and the difference in the focalisation between the visible and the IR laser. This drift was estimated by comparing the position of the laser focus for three cases: the HeNe laser in air, the Ti:Sa laser in alignment mode in air, and the HeNe laser in vacuum.

At a certain point in time of the experimental campaign this positioning method was upgraded to a rear-imaging system, assembled inside the vacuum chamber as depicted in Fig. 5.1. This optical arrangement consisted of a microscope objective (MO), placed behind the target wheel orientated to the laser beam coming from the OAP, mounted on a motorised linear stage moving along the same direction. In order to determine the location and the spot size of the laser focus, the focussing laser beam after the OAP was collimated by the microscope objective and retrieved by a CMOS camera located at a fixed distance outside the interaction chamber. By displacing the MO within the range of the stage, the TCC position could be found and the size of the laser focus could be retrieved through the comparison with a USAF calibration target (Fig. 5.3, panels **(a)** - **(c)**). By means of a MATLAB code, its effective area above the FWHM

threshold could be measured, as depicted in panel **(b)** in Fig. 5.3. In this example, the obtained spot size is about 2.5 μm in diameter, and the averaged intensity results in $\sim 5 \cdot 10^{20}$ W/cm^2.

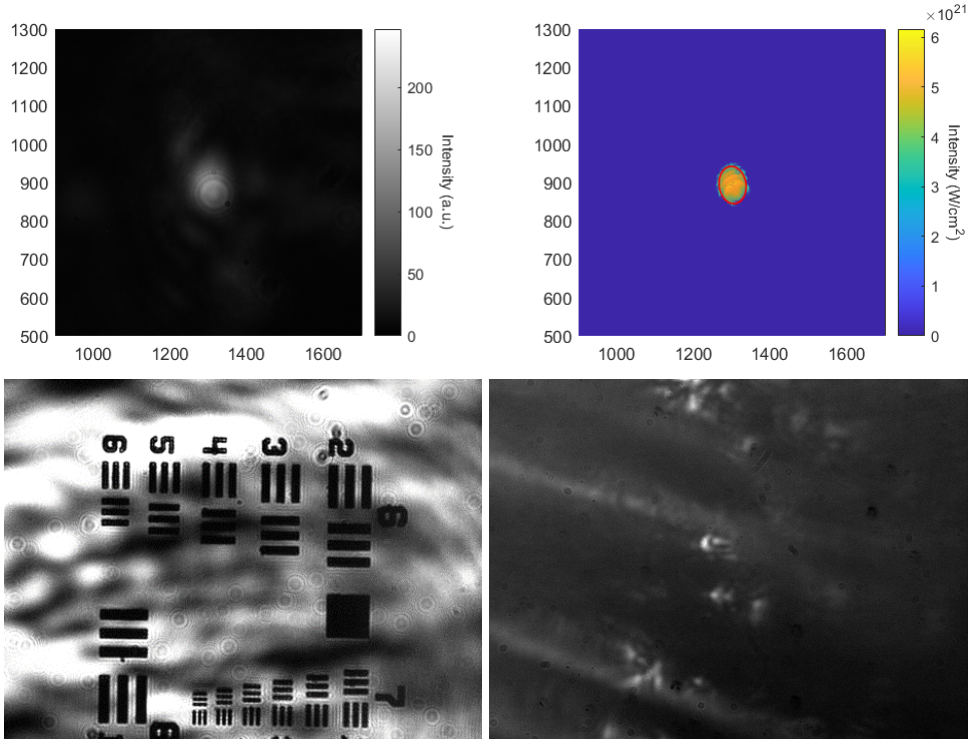

FIGURE 5.3: (a) laser focus. (b) Area of the laser focus above the FWHM in intensity. (c) USAF calibration target. (d) target rear-side surface

Once the TCC position was determined, the same optical system was used for the positioning of the target at the laser focus. The surface of the first point of the target 3D-map was placed under the focussing beam path, thus the microscope objective was aiming at its rear face. The target was then displaced along the laser incidental direction with micron accuracy until the image of the rear side of the target was resolved in the CMOS camera (Fig. 5.3 **(d)**). An additional offset accounting for the foil thickness was applied. This standard procedure is valid both in air and vacuum conditions. In fact, it allows for the measurement of the drift of the laser focus during the vacuum process and its correction.

Triggering and synchronisation

As introduced in Ch. 4, a triggering and synchronisation procedure was developed in order to automatically perform the positioning of the target surface at the laser focus at the operation

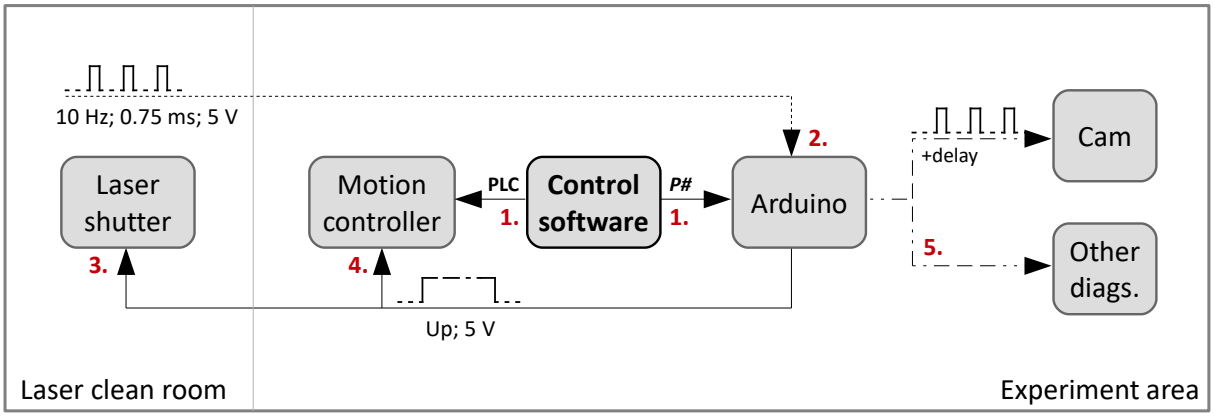

FIGURE 5.4: Trigger scheme at L2A2 experiments.

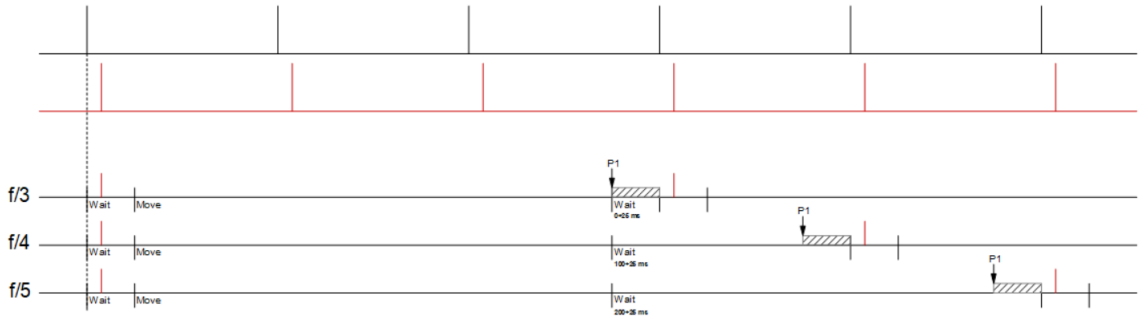

FIGURE 5.5: Synchronisation scheme at L2A2 experiments.

rate. This procedure was performed by the control software, and consists of a master-slave configuration at which an Arduino unit and the stages motion controller function as the master and the slave elements, respectively. A TTL (transistor-transistor logic) trigger signal of duration $\sim$1 ms was emitted by the laser system in advance of each laser pulse by 5 ms. This signal was continuously monitored by the Arduino unit, which in turn emitted a delayed trigger to the other devices.

In the case of the long-slots target wheel, after selecting via software which slots were about to be shot and generating the corresponding PLC motion programs, the implemented trigger system performed the following operation loop (depicted in Fig. 5.4):

1. The motion program of the first slot is uploaded and executed. The motion controller moves

the target to the initial position of the current slot. When the movement is completed, the control software sends a command with the number of shots ($P\#$) to the Arduino unit.

2. The Arduino takes the next pulse of the laser trigger signal and sends a rise-edge signal to the laser shutter and the motion controller. The duration of this signal depends on the number of shots of the current slot.

3. & **4.** The laser shutter is opened for the span of the signal. The motion controller receives the Arduino signal and then moves the target to a new impact position every 100 ms.

5. The Arduino sends a delayed signal to some diagnosis devices.

6. When the whole slot is completed, the Arduino signal goes down and the shutter is consequently closed. The next PLC motion program is uploaded and executed, and the controller moves the target to the initial impact position of the next selected slot.

The functioning of this target wheel is entirely designed for an operation rate of 10 Hz within each slot.

For the target wheels with individual holes, the trigger signal of each shot is monitored and used to start each individual movement, instead of only the first one of the sequence. A schematic representation of the temporal synchronisation of this operation is shown in Fig. 5.5. For repetition rates below the maximum value (f_r/2, f_r/3, f_r/4, etc), a command containing the fraction with respect to the laser rate is sent to the Arduino ($F2$, $F3$, $F4$, etc, respectively) before each series. This operation rate can be selected by the user via the control software, along with the number of shots of the current irradiation series which is equally provided by means of the pertinent ($P\#$) command. Within irradiation, the Arduino then sends a separated trigger signal to the shutter and the motion controller for each individual laser pulse at the selected operation rate. The duration of this signal is sufficient to allow for a single pulse each. Functioning at 5 Hz (f_r/2) is in principle not achievable as the shutter cannot perform the close-open operation within 200 ms.

On the other hand, for the case at 10 Hz using the upgraded version of the long-slots wheel, the schemed triggering procedure for the initial tests is similar as for the target wheel with long slots. In this way, a single rise-edge signal is sent to the shutter for the entire extent of the irradiation series, and the positioning is automatically performed by the stages controller by executing a PLC motion program. By the time of writing, no change of sector within the same series at this repetition rate is neither possible. Further programming, both for the control

software and the Arduino unit, will be required in order to achieve a single irradiation series of the whole target wheel at 10 Hz.

5.1.2 Ion beam characterisation

The commissioning experiments at the L2A2 facility aimed to the complete characterization of the accelerated ion beam, in terms of its angular divergence, species composition, and spectral distribution (cut-off energy, temperature, and flux). This study, still ongoing, was performed for targets of different materials and for a range of thicknesses between 1 and 12 μm, in order to evaluate the scaling of the ion energy with these parameters. Targets thinner than 1 μm were expected to be significantly affected by the ASE component of the laser pulses or the prepulses, hence decreasing the ion acceleration efficiency.

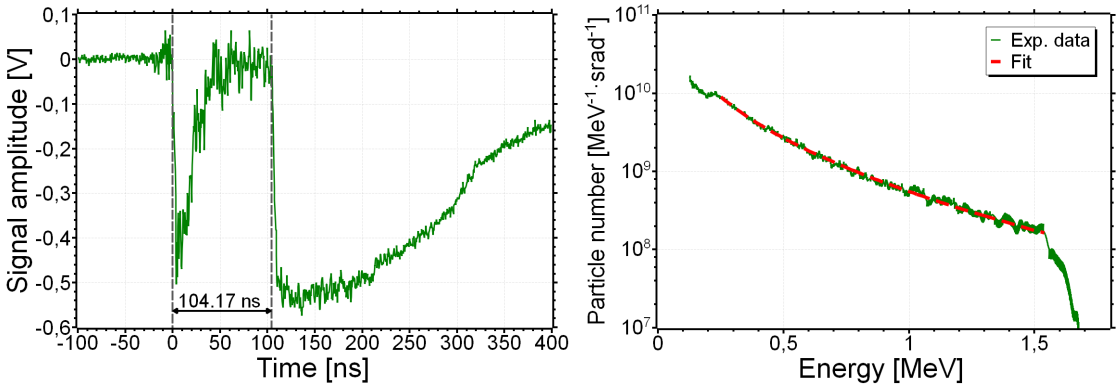

FIGURE 5.6: ToF signal and corresponding proton spectrum.

Fig. 5.6 depicts a typical signal registered by the ToF detector (left) and the reconstructed energy distribution (right) according to Eqs. 3.5 and 3.7. This measurement was obtained by irradiating a 12 μm-thickness aluminium foil with a laser pulse of 0.9 J and 35 fs, focussed onto a non-optimised 24 μm-diameter spot. The spectral distribution of the detected beam shows the expected maxwellian-like distribution with a sharp cut-off in the high energy limit. In this case, and for the analysis throughout this and the following sections, protons were assumed as the dominant and sole ion species. A Thomson parabola detector is currently being under construction and calibration at the L2A2 for ion species discrimination. Once this diagnostic is operating, a cross-correlation with the data from the ToF detector will be possible.

As introduced in Ch. 2, the angular divergence of laser-accelerated ions depends on the particle energy, being broader for the lower region of the energy spectrum. Due to this, the slope —i.e., the temperature— of the energy distribution obtained from the detector measurement varies with respect to the spectrum considering the entire ion beam, depending on the solid angle covered by the detector. The ion angular divergence can be described by a Gaussian-like distribution (Eq. 2.30) whose FWHM, or standard deviation, depends on the energy following a linear (Eq. 2.31) or a parabolic (Eq. 2.32) behaviour. According to this, the number of counts of each energy bin i of the spectrum must be corrected with a solid angle factor given by

$$f_{\Omega}^{i} = \frac{\Omega_{tot}^{i}}{\Omega_{det}^{i}} = \frac{\int_{tot} g_i(\theta) \sin\theta d\theta}{\int_{det} g_i(\theta) \sin\theta d\theta} \tag{5.1}$$

From that,

$$N_{tot}^{i} = N_{det}^{i} \cdot f_{\Omega}^{i} \tag{5.2}$$

where N_{det} is the particle number per bin of the spectrum measured at the detector, that subtend a solid angle Ω_{det}, and N_{tot} corresponds to the particle number per bin of the spectrum evaluated in the entire solid angle of emission Ω_{tot}. Other commonly extended units for displaying the particle number of the spectral distributions, or flux, are MeV^{-1}·srad^{-1}. This conversion can be obtained by simply applying the solid angle of the detector, Ω_{det}^{i}, to each bin of the spectrum, as N_{tot}^{i} [MeV^{-1}·srad^{-1}] $= N_{det}^{i}/\Omega_{det}^{i}$. Due to the absence of experimental measurements on beam divergence, a typical profile having a half-opening angle of $\sim$10° at $E = E_{max}$ and $\sim$30° at $E = 0.2E_{max}$ was considered[107]. For the 25×25 mm^2 scintillator located at 2 meters from the ion source, this assumption leads to a solid angle correction as depicted in Fig. 5.6. The blue curve represent the spectrum retrieved by the ToF detector, while the green and the red curves correspond to the respective linear and parabolic corrections. It can be noticed the change in the slope of the corrected energy distributions.

To perform a quantitative comparison of this correction, those spectra were fitted to Eq. 2.26 to obtain their characteristic temperature. As an example, the fit to the energy spectra shown in Fig. 5.6 (right) is depicted by the dashed lines in the same figure. The parameters of these fits are displayed in Table 5.1. A variation of a factor of 4.5 can be observed in the calculated temperatures of the base and corrected spectra. As will be seen through following sections and

TABLE 5.1: Spectral parameters for the base and corrected energy distributions.

	N_0	T_e (MeV)	E_{max} (MeV)
Base	$1.74{\cdot}10^{10}$	0.114	1.65
Linear	$2{\cdot}10^{11}$	0.05	1.65
Parabolic	$2{\cdot}10^{11}$	0.04	1.65

chapters, a precise identification of this spectral parameter is fundamental for some applications requiring absolute calibration, as for example radioisotope production. The same analysis as detailed in these paragraphs was applied to the experimental data obtained at different laser shots and series, for the comparison in regard to the multi-shot stability of the ion source.

5.1.3 Proton source stability

To validate the shot-to-shot stability and the repeatability of our ion source, and thus reinforce the reliability of the target correction procedure, several series of multi-shot irradiations were performed. For the initial tests, up to 24 consecutive shots at 10 Hz were achieved using the first version of the target wheel (Fig. 4.2 **(c)**), holding 12 μm thickness aluminium foils. The laser parameters for these series of irradiations were the same as for the spectrum shown in Fig. 5.6. In this case, the impact positions were defined along two parallel rows at each slot, for a distance of 1000 μm between positions within the same row and of 750 μm between rows. During the irradiation, the motorized stages were synchronized with the arrival time of the laser pulses on target at the laser repetition rate, 10 Hz, according to the triggering procedure described in Sect. 5.1.1.

The left panel in Fig. 5.7 depicts the energy spectra of the proton bunches for the first twelve consecutive shots along a single row. All the spectra exhibit a coherent maxwellian-like trend, similar both in temperature and cut-off energy. Only for a few shots the cut-off energy and in some cases the temperature seems to be smaller. The inset in the left panel in Fig. 5.7 shows a picture of one of the aluminium foils after the irradiation. In this image one can clearly observe the holes produced by the laser impacts along the two rows. The holes have a average radius of around 500 μm.

In order to quantify the reproducibility of the proton source, the temperature and the cut-off energy of the proton energy spectra were retrieved by fitting those spectra to Eq. 2.26, as in the

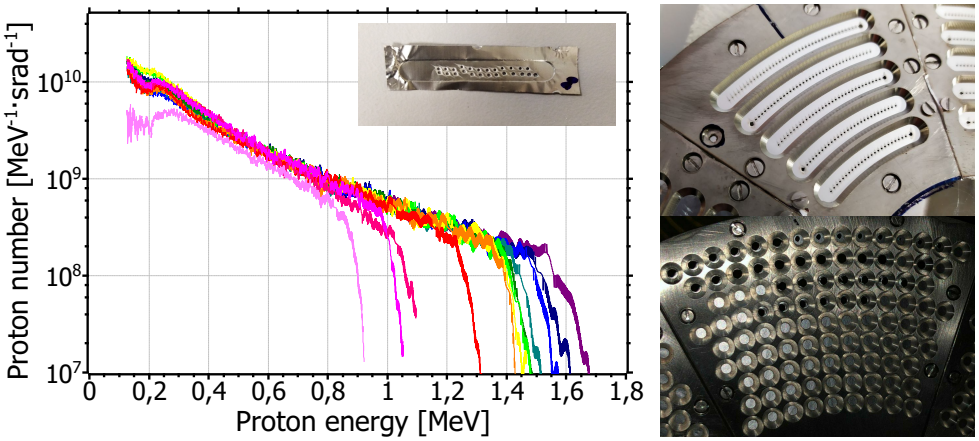

FIGURE 5.7: Proton spectra obtained in a multi-shot series. Inset: image of the target foil after the irradiation.

previous section. Panel **(a)** in Fig. 5.8 depicts the maximum energy (green lines, left axis) and the temperature (red lines, right axis) of the proton spectra measured in three different series of 12 consecutive shots. The resulting cut-off energies for these 36 shots have a mean value of 1.38 MeV and a standard deviation of 0.18 MeV, corresponding to a relative dispersion of 13%. The temperature of the distribution, on the other hand, exhibit a mean value of 0.21 MeV with a dispersion of 0.03 MeV, representing a 16% of standard deviation.

The analysis of the energy spectra considering the two rows of impact positions is depicted in panel **(b)** in Fig. 5.8 for the same three multi-shot series. The first 12 points, corresponding to the first row, represent the same data discussed in the previous paragraph. Points corresponding to the second row of impact positions, on the other hand, clearly show a reduction in the maximum energy about a factor of 2.5. This behaviour can be explained by the proximity of the two rows of impact positions (see the inset in the left panel in Fig. 5.7). The laser shots on the first row may bend the aluminium target foil, hence alter the surface profile in the adjacent area around. If this area of effect is large enough, the implemented positioning corrections from the mapping procedure for the near points are no longer valid. This leads to a reduction of the laser pulse peak intensity deposited on target and therefore, of the energies of the accelerated protons for the shots in the second row. The focal spot size of the laser was rather large and non-optimised within these measurements, so a certain effect in the size of the produced holes and in the minimum distance eligible between shot positions can be expected.

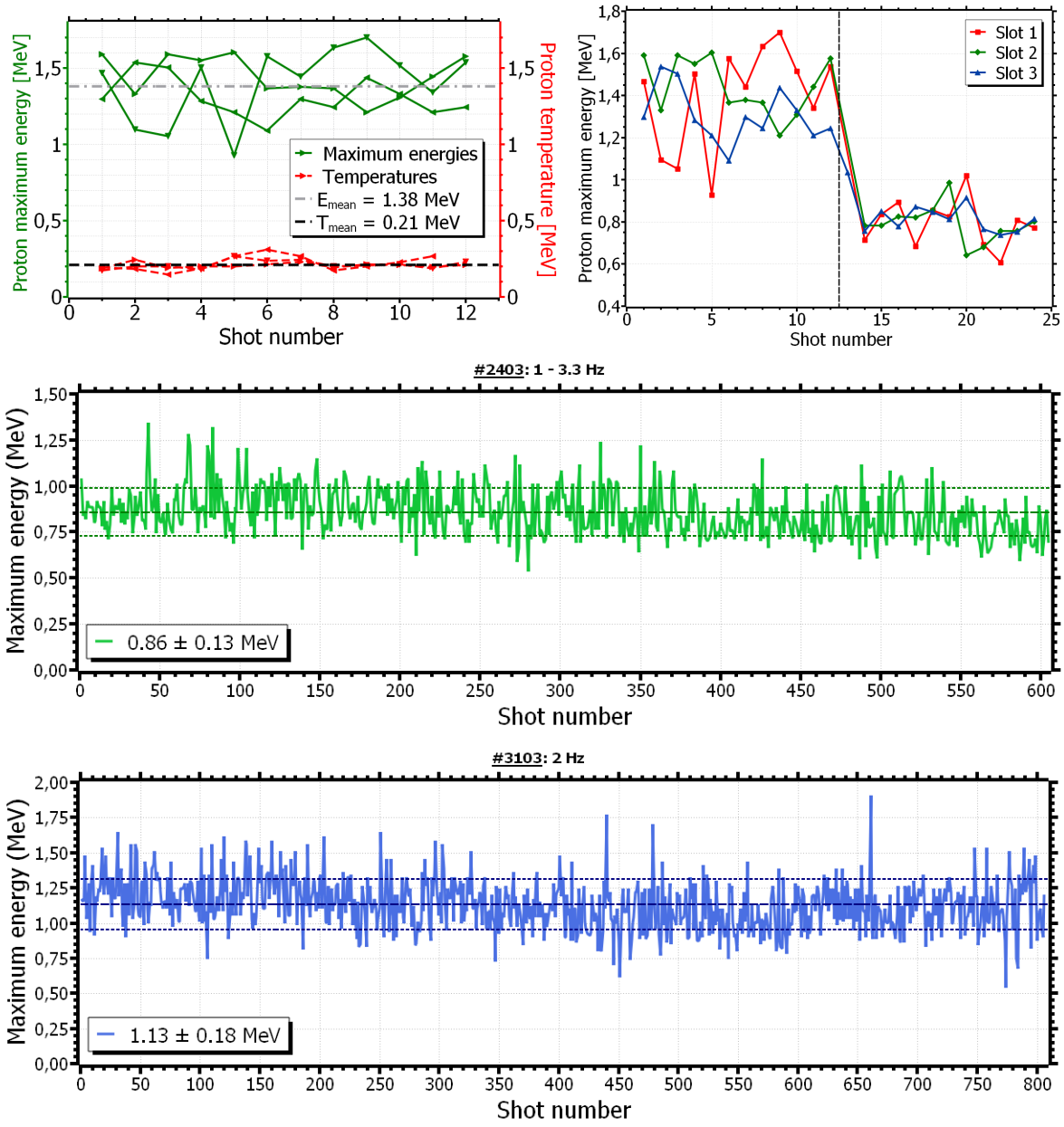

FIGURE 5.8: Multi-shot stability at the L2A2.

The performance of the target assembly regarding prolonged multi-shot operation was tested by using the advanced versions of the target wheels. The panels in the right in Fig. 5.7 show the aluminium target foils after the irradiation for the long-slots (top) and the individual-holes (bottom) versions. The hole pattern produced by the laser pulses can be clearly observed in

both images. In these cases, as the focal spot size and the aligning procedure were improved with respect to the previous conditions (see paragraph below), the size of the holes (about 100 - 200 μm) and the surrounding affected area could be reduced. Thus, for the long-slots wheel, the separation between adjacent shot positions was maintained to 1000 μm, enough to avoid the deformation caused by nearby laser impacts, and defined along a single row.

The results obtained at the irradiation aluminium foils of 12 μm, mounted on the individual-holes target wheel, with laser pulses of 1 J and 30 fs focalised down to a 2 μm-diameter spot are presented in panels **(c)**-**(d)** in Fig 5.8. Panel **(c)** depicts the stability in the cut-off energy of the accelerated protons for several series of between 20 and 300 shots at 1 - 3.3 Hz-repetition rate. Panel **(d)** shows a similar measurement for a single series of 707 shots at 2 Hz-repetition rate, along with some single-shot and short multi-shot irradiations up to the entire target wheel capacity of 808 shots. In both cases, the calculated dispersion is in the order of 15%, and show a slight decreasing of the cut-off energy over time. This energy loss can be attributed to the expected deterioration of the laser pulses within its sustained operation, as the measurements were performed over a span of a few hours. The shot-to-shot dispersion in the stability curves may be partly explained by fluctuations in the laser pulse energy during the irradiation series. According to the experimental measurement of this parameter over long series, fluctuations of $\sim$5% can be expected, that can lead to a average variation on the proton cut-off energy of around 4%. According to Eq. 2.23, this maximum fluctuation observed in the laser pulse energy will also affect the temperature of the spectra about a 7%-dispersion. While the proton cut-off energies measured at these long series are lower than expected, the results presented in this section confirm the high reproducibility of the proton source, which validates the shot-to-shot stability of the target assembly system.

The stability of the spectral temperatures, for the long multi-shot series depicted in panel **(d)** in Fig. 5.8, is shown in Fig. 5.9. Again, these results were obtained by fitting the spectra to a Maxwell-Boltzmann distribution (Eq. 2.26). The results are shown for the base spectra (blue curve) and for the corrected proton spectra assuming a linear angular profile (orange curve). In this case, the solid angle correction was evaluated in MeV^{-1}·srad^{-1} units. In comparison with the cut-off energy, the temperature exhibit lower stability, about a 35% for the base spectra and a 25% for the corrected data. As the results of these multi-shot series seem to be non-optimised in maximum energy —having $a_0 \sim 9.5$, proton energies up to 4 - 5 MeV would be expected for a 12 μm-thick target—, the observed dispersion in the spectral temperature could be produced by the shot-to-shot inhomogeneity of the ToF raw signals and the presence of other heavier

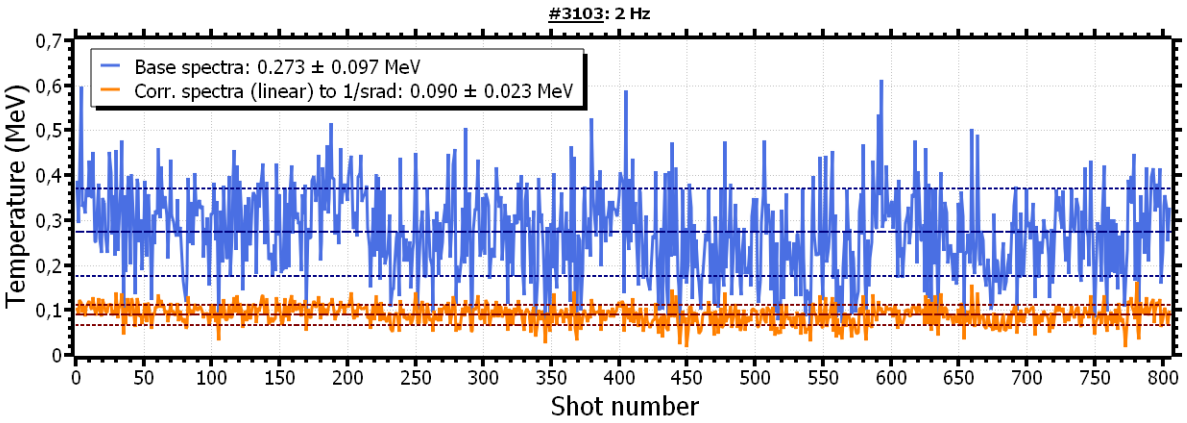

FIGURE 5.9: Multi-shot temperature stability at the L2A2.

ionic species. Regarding the later, future work with a TP detector, under construction at the L2A2, will clarify the species composition of the accelerated ion beam. A certain periodical oscillation is also observed in the shot-to-shot temperature profile. It can be explained by taking into consideration the shot sequence of the target wheel operation: the target foils for the shot positions at the outer radii are slightly bended in comparison with the points at the inner radii, due to the screws holding the wheel to the stage assembly. Hence, the emission angle of the ion beam, normal to the target surface according to the TNSA mechanism, and therefore the subtended component of the beam that reaches the detector, may differ between these cases. As depicted in Fig. 4.19, the shot sequence periodically moves the shot position between the outermost and innermost radii, leading to a gradual variation of the aforementioned emission angle.

5.2 Experiments at the Centro de Láseres Pulsados

An experimental campaign on laser-driven neutron generation was carried out at the CLPU. Neutrons can be generated by irradiating LiF or Cu targets (formally called *catchers*) with proton or ion beams of enough particle energy. The target assembly developed in this work was utilised as the ion source —the *pitcher*— during the campaign. The detection of neutrons is far from being efficient, as it involves the generation of secondary particles through nuclear reactions which are the ones detected, so as much as possible data is necessary in order to infer some statistics and results. As a system designed for multi-shot operation, the target assembly

from the L2A2 resulted in a very suitable choice for the ion source, as in principle it could offer great stability in terms of energy and flux for long runs, both in time and number of shots, at high repetition rates. The system was adapted to the experimental constraints at the CLPU and a new target wheel (Fig. 4.2 **(c)**) was designed, according to the VEGA 3 nominal repetition rate of 1 Hz.

While the main objective of this campaign was neutron generation, and ultimately neutron-induced activation for uranium fission, the first part of the experiment involved the optimisation and characterisation of the ion source. This took place during the first week, so-called the preparation week. Within the following experimental weeks, some multi-shots series of different duration, as well as single-shot measurements, were daily performed without catcher, in order to test the proper functioning of the target assembly and the detectors, and evaluate the properties of the ion beam. The results presented in this section correspond to these measurements, which were performed using the VEGA 3 laser line at the CLPU facility.

5.2.1 Experimental set-up

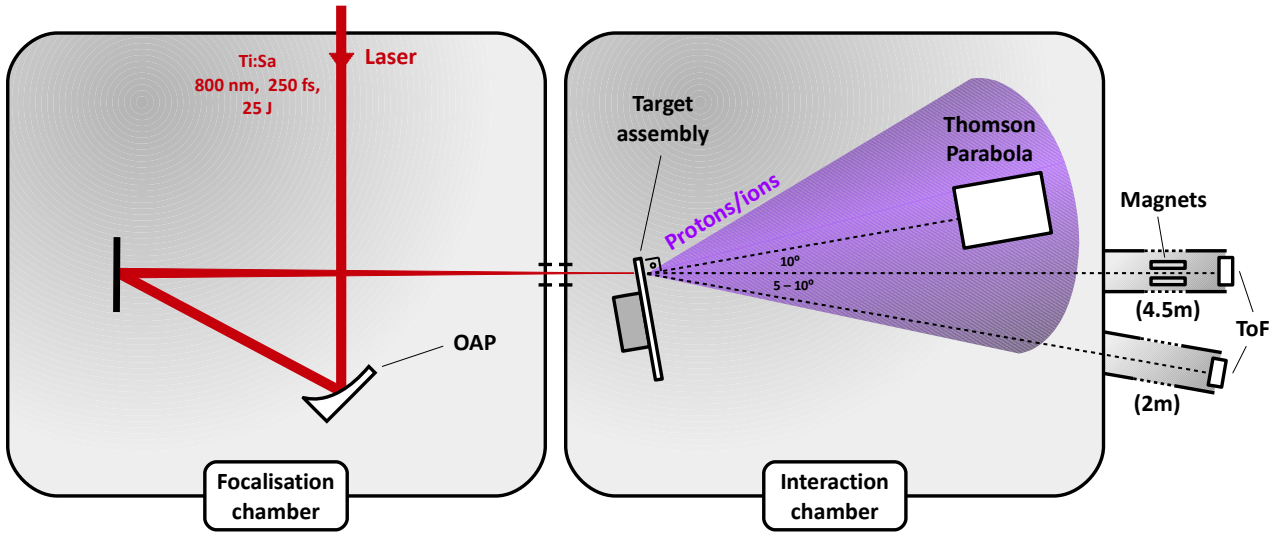

FIGURE 5.10: Chamber scheme at CLPU.

Fig. 5.10 depicts a schematic representation of the experimental set-up. P-polarised laser pulses of up to 25 J from VEGA 3 were focussed at an incidence angle of 10° onto 7 μm-thickness Al target foils with an spot size of $\sim$20 μm-diameter (FWHM). The pulses were

artificially elongated to ∼250 fs from the nominal pulse duration of the laser, 30 fs, for this campaign. A long focal length OAP (250 cm), located inside a separated vacuum chamber, was used for the beam focalisation, having a Rayleigh length of about 260 μm. Hence, the accurate positioning of the irradiation targets surface at focus was not as critical as for the experimental case at the L2A2. The target wheel with a pattern of individual holes (Fig. 4.2 **(c)**), designed for operation rates up to 1 Hz and to minimise the damage produced by the laser pulses on adjacent shot positions, was used during this experimental campaign.

A Thomson parabola (TP) detector was located inside the vacuum chamber at 0.72 m from the interaction point and at 0° with respect to the target normal direction (i.e., at 10° from the laser propagation direction). A pinhole of diameter 200 μm was placed at the entrance of the TP, covering a solid angle of 60.60 nsr. The images of the MCP were retrieved by means of a CCD camera, located behind the TP. This device was the main diagnostic for the characterisation of the accelerated ion beams, providing both the species composition and their energy spectra. As it was not calibrated in number of particles, the ion flux could not be determined in principle. The description of this device can be found in Sect. 3.2.4.

As a secondary ion diagnostic, two ToF systems were mounted at 10 - 12° and at 20 - 25° with respect to the target normal. The former, located at 2.39 m from the TCC during the first two weeks and at 4.53 m after that for improved energy resolution, is the same device as the one used at the L2A2 campaign and described in Sect. 3.2.3. Optical filters OD3 and OD4 were employed within the last week of campaign to avoid the saturation of the retrieved signals. A raster holder of CR-39 chips was mounted on a motorised linear stage and placed at the front of the ToF scintillator. Each column of the raster consisted of a central squared hole that let the ions imping on the scintillator behind, and two other holes hosting the CR-39 chips, one on top of and the other below the central hole. Moving the raster with the linear stage allowed for positioning each column at the ion flight path while placing the rest behind a shielding lead sheet. This device was intended for the cross-calibration of the ToF signals in terms of the particle flux. A set of two magnets was placed inside the vacuum tube in front of the ToF detector to deflect any accelerated electrons that may produce an undesirable bump at the retrieved signal.

The other ToF detector was placed at 1.99 m from the interaction point at the aforementioned

angle. It consisted of a MCP from Jordan TOF Products, having an active area of 25 mm-diameter, attached to a cathode to collect the excitation electrons. The diameter of the micro-channels was 10 μm, and the centre-to-centre separation was 12 μm. An aluminised-mylar filter of 2 μm-thickness was placed at the MCP to avoid saturation and for external noise reduction. This detector was not calibrated in particle number so it could solely provide ion energy data.

For the series of measurements using the catcher targets for neutron generation, only the TP was in principle available for ion diagnostics. The catcher samples (LiF or Cu) had a pinhole in their centre, therefore only the ions emitted at $\sim 0^{\circ}$ could be detected, by the TP in this case. However, due to the accumulation of debris from the pitcher target during long multi-shot series, the pinhole could be partly obstructed within the series and thus a part of the ion beam blocked. After a certain amount of debris material was accumulated, it could fall off by its own weight. This could lead to a significant and progressive attenuation, or even vanishing, of the traces at the TP during the multi-shot series.

Target alignment at the laser focus

The location of the TCC inside the interaction chamber was predefined by the tip of a thin needle, mounted on a linear stage. At the beginning of the experiment and before the assembly of the target system inside the interaction chamber, the high power or the auxiliary laser were focussed to this tip by slightly adjusting the OAP alignment. This procedure was monitored with a microscope objective (MO), mounted on top of two linear stages, one horizontal and one vertical to the board of the chamber. Once the laser focus was located at the predefined TCC, the encoder positions of the microscope stages were stored. On each day during the experimental campaign, any possible drift of the laser focus was accounted for by updating these encoder positions. The left panel in Fig. 5.11 shows an image of the focal spot of the high power laser in alignment mode, retrieved by means of this procedure on one of the experiment days. A visible diode laser was coupled to the optical path of the high power laser as a reference for the target alignment.

Placing the microscope objective at this position and moving the target wheel along its normal direction, the point over the sector plate of the target wheel for which the surface was resolved by the objective defined the reference point for the alignment of the position sensor (Fig. 5.11, right panel). A second visible HeNe laser was pointed at this reference —the focus

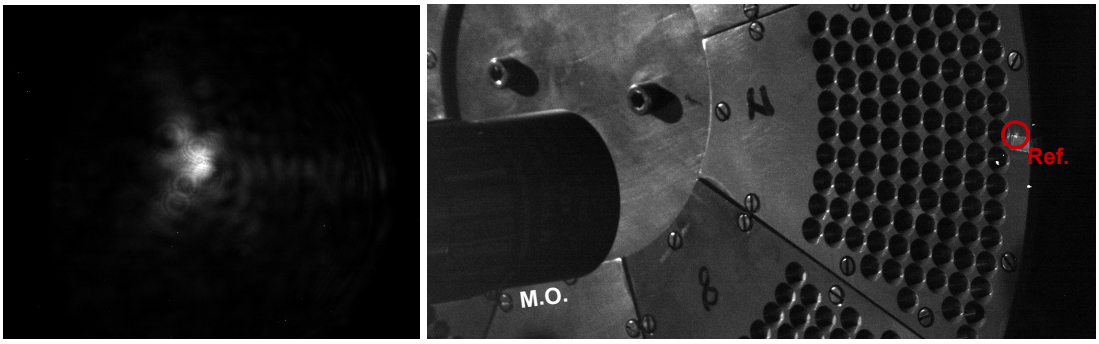

FIGURE 5.11: Image of the reference point defined by the microscope objective (MO).

of the MO— as a visual guide for the following steps. After determining the coordinates of the reference point, the 3D mapping procedure of the entire wheel was performed.

The alignment of the targets at the laser focus was carried out by means of the same optical system. The target surface for the first impact position of the 3D map was positioned under the optical path of the auxiliary beam, i.e., centred in the microscope field of view. The target was then moved along the incidence direction with micron accuracy until the surface was resolved by the MO. As described in Ch. 4, this position was then set as the focal reference position to which the rest of the corrected map points were referred. The reference position was re-evaluated once in vacuum conditions on each experimental day that used the same surface map, and readjusted if necessary.

EM pulse and relay system

Due to the high amount of energy coming from the laser pulses deposited on target, a huge electromagnetic pulse was produced at the laser-plasma interaction. This EM pulse propagated through the wired connections affecting all the electronic devices within a few meters around the interaction point. This phenomenon is a common output in high power laser facilities. For most of the devices, the arrival of the EM pulse translated to a certain recovery time for which the device could not be operated. Other devices, on the other hand, were restarted or completely shut down. This circumstance was produced for each laser pulse at the operation repetition rate.

To overcome this issue and prevent the motion controller from not working properly (or being damaged), a relay system was designed and implemented. For each of the three moving

stages and the encoder connections, a relay unit was inserted between the stage or encoder and the motion controller, properly shielded with aluminium and lead outside the interaction chamber. Each relay unit consisted of an Arduino board (Uno or MEGA) equipped with four relays by Arduino. In the case of the moving stages, two of these relays were bypassing the cables corresponding to the internal induction spools responsible of the movement, in order to prevent any undesired retro-induced current produced by the EM pulses. For the encoder cable, on the other hand, two relay units were used to interrupt its entire connection to the motion controller.

On activation, the relays were programmed to disable the wired connections and the communication between the controller and the devices for a certain number of milliseconds. During the irradiation, the operation of the relay system was automatically performed by the control software of the target assembly, concerning the synchronization with respect to the arrival of laser pulses and the positioning movements (see section below).

As this issue was not addressed before at the L2A2 and could not be tested there, a significant part of the development of this system took place during the experiment itself. Specifically, the response of the stages and the motion controller to these huge EM pulses. It was early found that most of the times the encoder position of the moving stages was reset to zero —i.e., lost— after the arrival of each laser pulse, so the positions corresponding to the 3D map of the target, either corrected or not, were no longer valid. This might happen even with the relay system connected and working. In some other cases, the motion controller was permanently frozen until reboot, which lead to the interruption of the current irradiation series. The former issue was solved by storing the stages encoder position in the control software memory at the action of the relay system. After the arrival of the laser pulse, that position was recovered by means of the pertinent commands sent to the motion controller. No attempt of shooting the laser without shutting down the connections with the relay system was performed.

Triggering and synchronisation

The synchronisation scheme for the positioning of the targets with respect to the laser pulses in the experimental campaign at the CLPU differed from the one described in Sect. 5.1.1 for the experiments at the L2A2: the operation of the relay system was included, the start of the irradiation series or single shots was performed by the laser team —not by the user via the control software— and the main trigger signal came from the laser system and not from an

Arduino unit as in the master-slave configuration detailed in Sect. 5.1.1. In this case, the TTL trigger signal corresponding to each laser pulse was monitored and used to start each movement. These signals had a duration of about 10 ms, and preceded the laser pulses by 100 ms.

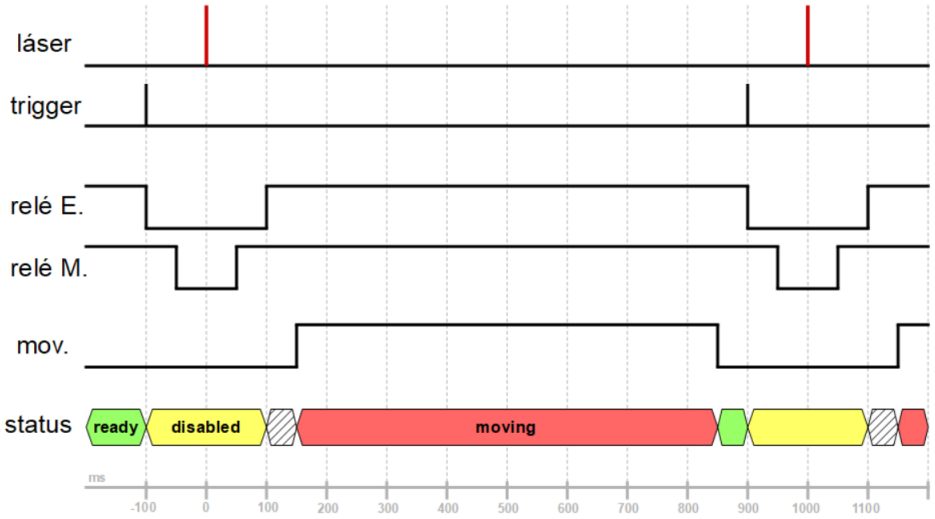

FIGURE 5.12: Trigger temporal scheme at CLPU experiments.

Using the individual-holes target wheel, the number and the index of shot points about to be shot were selected via software. During the irradiation, the implemented trigger system performed the following operation loop:

- The motion controller moves the target to the first impact position of the series.
- The control software starts monitoring the trigger signal coming from the laser system.
- On trigger, the relay system disables the connection between the stages and the motion controller. The current position of the stages is stored in memory by the control software.
- The laser pulse impinges on the target and the EM pulse is produced.
- The relay system enables the connection between the stages and the motion controller after a fixed time interval.
- The control software waits for a certain dead time and then recovers the stages position, which may be lost due to the EM pulse.
- The motion controller moves the target to the next impact position of the series.

The timing scheme of this loop is represented in Fig. 5.12. The dead time between the reconnection of the relays and the beginning of the following movement was introduced to account for the recovery time of the motion controller after each laser pulse. Any instruction sent to the motion controller before the end of that dead time, as the position recovery commands, was ignored. Its duration was found to be dependent on the laser pulse energy, i.e, on the intensity of the EM pulse. The minimum values were 250 ms for 6 and 12 J laser energies, 3000 ms for 20 J and between 4000-5000 ms for >25 J. As the movement time was fixed to 250 ms, the only difference between each case was the duration of this waiting time. Thus, the operation rate for each energy was limited to 1, 0.2, and 0.1 Hz, respectively.

Some stochastic errors were still produced, for which the positioning during an irradiation series failed after an arbitrary laser shot. Even being aluminium- and lead-shielded, the final conclusion was that the EM pulse was slowing down the Arduino units of the relay system as well. The reconnection of the relays was then produced later than expected and the following instructions given to the motion controller were not properly applied. The control software was updated daily during the experiment to minimise these failures.

5.2.2 Ion beam characterisation

Aluminium foils of 7 μm-thickness were irradiated with laser pulses of energies ranging from 6 to 25 J. The nominal energies for operation were 6, 12, 17, 20, and 25 J, and a dispersion of about 13% was observed for each central value. At the beginning of each day of the experimental campaign, several single-shot measurements on ion acceleration —i.e., without catcher— were performed at some of the nominal laser energies to characterise the beam properties and its scaling with the pulse energy. Several multi-shot series of different duration, repetition rate, and laser energy were performed as well to evaluate the stability of the ion source and the performance of the target assembly. Within the entire experimental campaign, protons with peak energies up to 15 MeV were achieved both in single-shot and multi-shot series. Considering the experimental parameters both of the laser system and the target, TNSA was the predominant ion acceleration mechanism.

Single detector measurements

The species composition of the ion beam, as retrieved by the measurements at the TP, is illustrated in Fig. 5.13 (left panel), showing the expected traces due to protons ($^{+}$H) and a collection

of carbon (C), nitrogen (N), and oxygen (O) ions in different degrees of ionisation. The proportion between each species varied shot-to-shot as the relative composition of the contaminant layer at the rear side of the acceleration foils may differ from target to target. Nevertheless, the trace produced by protons was typically the most intense one.

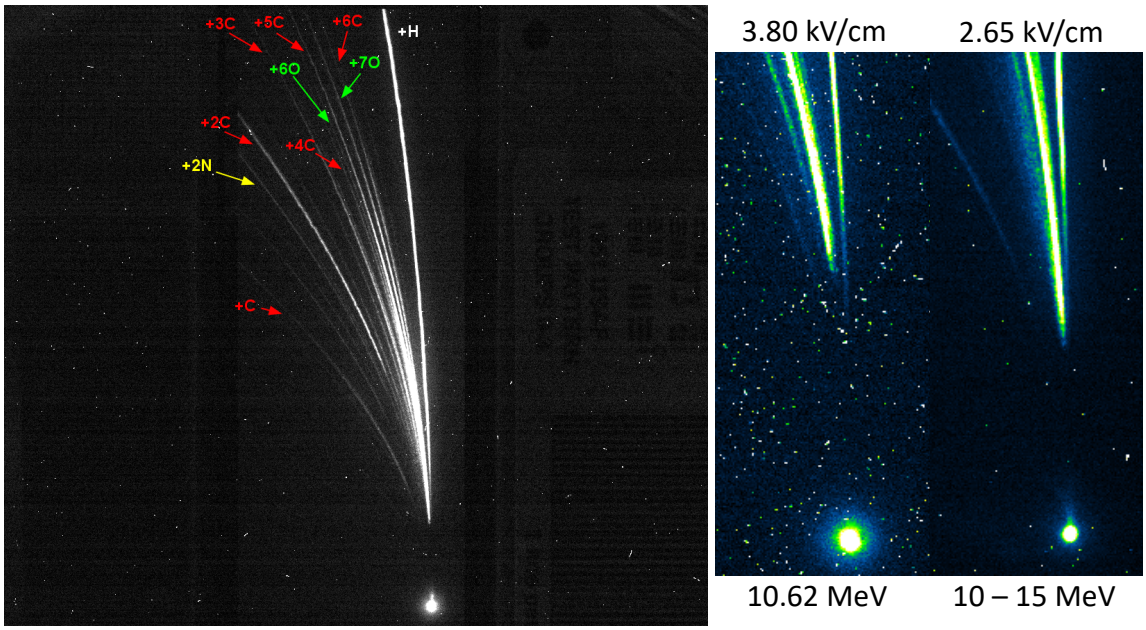

FIGURE 5.13: Species composition of the ion beam accelerated by a 25J laser pulse (left). Observed superposition of the traces of different ions (right).

The superposition between the traces due to protons and other heavier ions supposed a complication in the data analysis of several measurements, specially for the highest nominal energies of the laser pulses. The degree of superposition was dependant on the electric field intensity at the TP plates. The right panel in Fig. 5.13 depicts two signals measured at different days for different plate voltages at the same laser energy. It can be clearly seen that, for the case at 3.80 kV/cm, the proton trace is well separated from the trace produced by heavier ions. In this case, the cut-off energy of the protons can be precisely resolved at 10.62 MeV. On the contrary, in the signal measured at 2.65 kV/cm, the two traces overlap within the high energy region, hence the proton cut-off energy cannot be determined but over a range of several MeV. This led to a certain uncertainty in the ion maximum energies for some series of measurements. The electric field at the TP was set as higher as possible during the irradiations. However, during long multi-shot series, plate voltages above a certain level caused the TP plates to go down, presumably

affected by the EM pulses from the laser-plasma interaction.

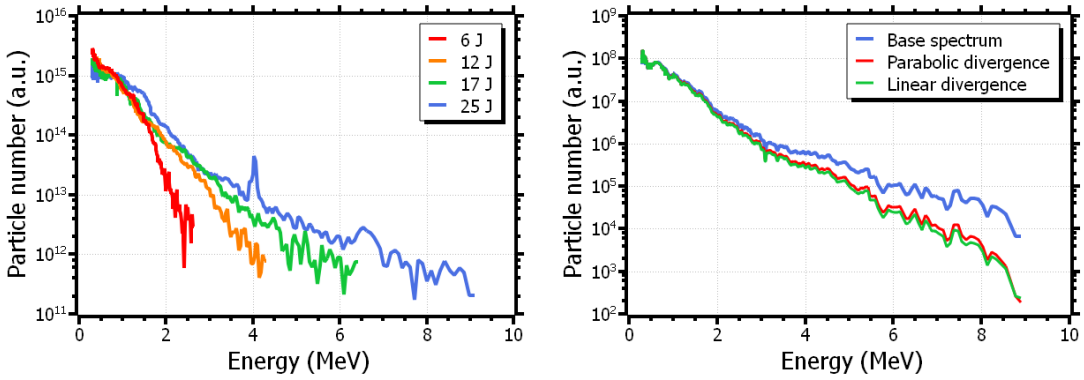

FIGURE 5.14: Proton spectra retrieved from the TP traces for various laser energies.

The energy spectrum of the accelerated ions was retrieved from the TP traces by using a MATLAB code (*TPA*) developed by A. Alejo. Fig. 5.14 (left panel) depicts the energy spectra corresponding to protons for various laser energies measured at single-shot irradiations. Results show the typical maxwellian distribution at multi-MeV order energies. As expected, increasing the pulse energy leads to an increase in the cut-off energy of the accelerated proton beam. For this particular set of measurements, a linear dependence of the proton maximum energy with respect to the laser energy is observed. The TP, located at 0° and 0.72 m from the TCC, had a pinhole of 200 μm-diameter, thus only a part of the entire proton beam was detected. The solid angle factor at the TP was evaluated using Eqs. 5.1 and 5.2, considering a Gaussian-shaped angular distribution with a linear or a parabolic dependence on the particle energy given by Eqs. 2.30 – **??**. The corrected spectra, i.e., the assumed distribution of the entire proton beam, were then fitted to Eqs. 2.26 in order to obtain the characteristic temperature. An example is shown in the right panel in Fig. 5.14, where a raw spectrum (blue curve) —as retrieved from the TP— is depicted along with the corrections considering both angular profiles (green and red curves for linear and parabolic divergences, respectively). The three spectra are normalised to the same total number of counts to facilitate the comparison. A significant variation in the slope of the corrected distributions with respect to the base spectrum can be clearly observed. As the disagreement between both corrections is below 10% for the high energy range, only the linear divergence profile will be considered through the following analysis. Concerning the acceleration of heavier ions, due to the fact that most of their traces at the TP were superposed

within an extensive energy range and that the relative intensity of each line varied on a shot-to-shot basis, the retrieval of their spectral distributions was not trivial and was not attempted. Instead, the cut-off energy of a few species was calculated for some multi-shot series, in regard to the target stability.

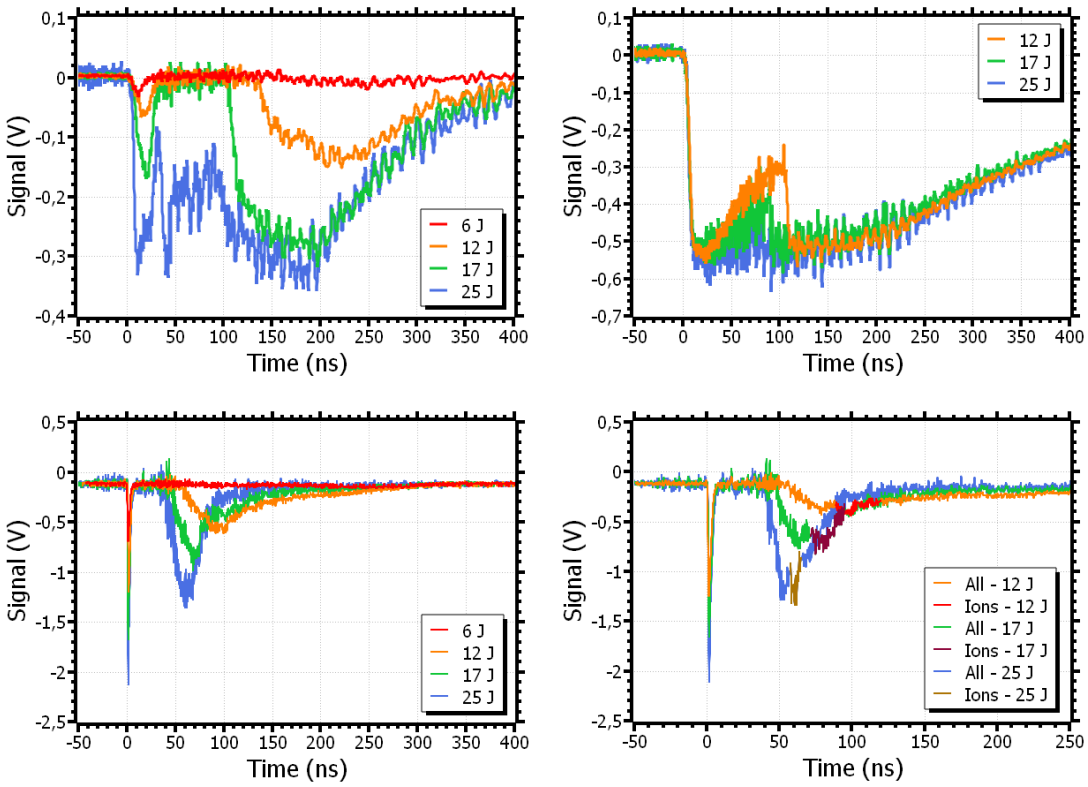

FIGURE 5.15: Proton spectra retrieved from the ToFs (i3M and CLPU) traces for various laser energies.

The raw signals measured by the ToF detectors are depicted in Fig. 5.15. Panels **(a)** and **(b)** show the results from the detector developed at the I3M for the indicated nominal laser energies. As during the first experimental weeks the detector was a placed at a shorter distance from the TCC (2.39 m) and low or none optical filters were used, the measurements from these weeks (panel **(b)**) are visibly saturated. In addition, the signal produced by the ion bunch is overlapped with the decay of the gamma-flash. This was partly solved by increasing the ToF distance to 4.545 m and the optical density of the filters in the last week of campaign. This improvement is reflected in the signals shown in panel **(a)**, measured during this week, for which the ion bump is separated and no saturation is observed. Despite this, some of the raw signals, principally for

laser energies above 20 J, exhibited an artefact between the gamma-flash and the ion bump, as can be seen in the blue signal in **(a)** (25 J). In some cases, these artefacts were superposed to the signal due to ions, hence complicating the analysis. The origin of such spurious signals could not be identified by the time of writing this work. The calibration of this detector, mentioned in Sect. 3.2.3, was in principle not applicable to the measured data as it was performed for a range of ion energies between 1 and 3 MeV, far below the typical experimental energies within this campaign. As for the experiments at the L2A2, protons were assumed to be dominant and the fastest species reaching the detector, therefore the initial rise of the ion bump in the raw signals —thus the cut-off energy— was attributed to them. Both this maximum energy and the signal amplitude, i.e., the particle number although the detector was not calibrated, seem to escalate with the laser energy.

Panels **(c)** and **(d)** in Fig. 5.15 present the results for similar measurements retrieved at the ToF detector developed at the CLPU. In comparison with the signals obtained with the ToF from the I3M, this detector shows better time resolution and significantly experiences less saturation. In this way, the gamma-flash is well resolved and completely separated from the ion bump for the case at 25 J, in contrast the equivalent signal displayed in panel **(a)**. As for the previous cases, a scaling of the main beam parameters with respect to the laser pulse energy can be observed. Some of the measured raw signals exhibit a second bulge due to heavier ionic species. This is illustrated in panel **(d)**, showing the presumed ion contributions in a different color in each signal at the indicated laser energies. Besides, no in-depth study on heavy ion laser-driven acceleration was performed within this work. Given that only reactions induced by protons were contemplated for neutron generation and radioisotope production, no attempt on optimising the ion acceleration efficiency was regarded.

On the other hand, the analysis of the data from both ToF systems, regarding the temperature calculation, was limited to the raw spectra. The detectors were not aligned to the ion 0°-emission direction but placed at $\sim$10 and $\sim$20°, thus complicating the estimation of the solid angle factor from the angular divergence profiles, as the detected cut-off energies were not the maximum energy of the accelerated proton beam. This maximum energy could be in principle obtained from the corresponding TP spectra, yet no clear angular cross-correlation between detectors was found, as discussed below. Moreover, a variable and not negligible component of the ToF signals was due to the heavier ion contribution. For these reasons, the solid angle corrections were not as conclusive and the temperature of the raw, base spectra were only examined for comparison, concerning shot-to-shot stability.

Comparison between detectors

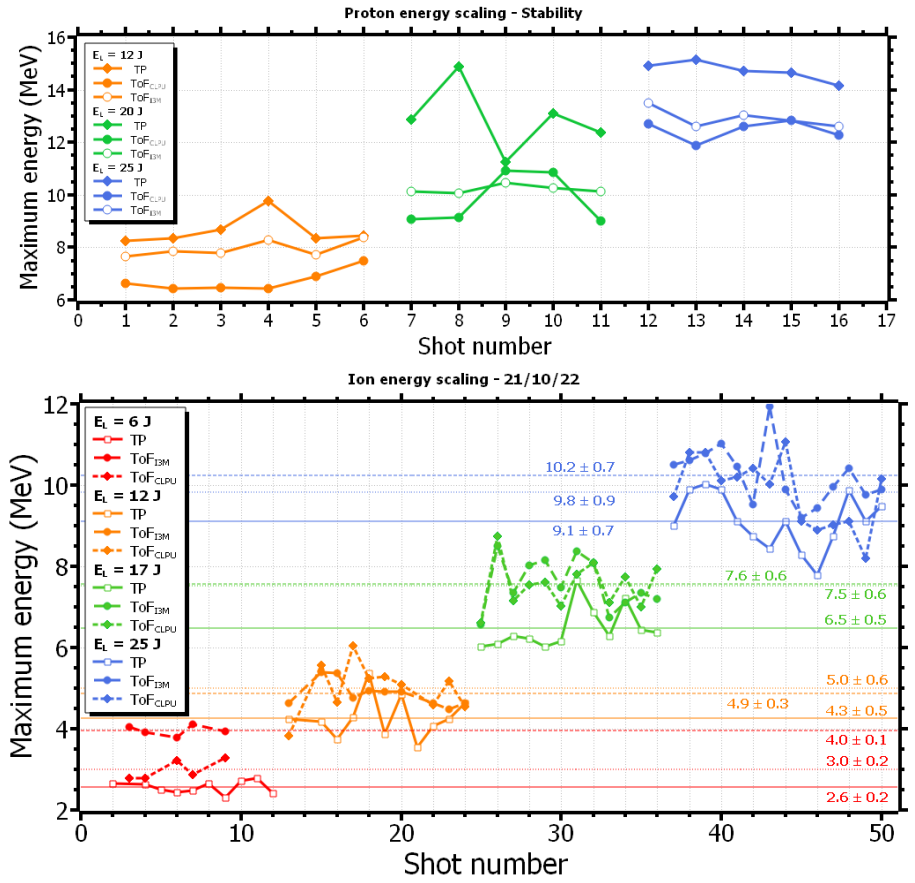

FIGURE 5.16: Scaling of the proton cut-off energies given from the signals retrieved at the three main detectors (top), and proton cut-off energies measured at the TP and the two detectors for the same series at 12 J and 1 Hz (bottom).

A direct comparison of the three aforementioned diagnostics is shown in Fig. 5.16. The cut-off energy of the laser-accelerated protons from the same single-shot series at various pulse energies is depicted in the upper and lower panels, corresponding to two different measuring days (18/10/22 and 21/10/22, respectively). Solid diamonds represent the values retrieved from the TP traces, open circles the measurements obtained at the ToF from I3M, and solid squares the same values as given by the ToF from CLPU. Each color depicts each laser pulse energy: red for 6 J, orange for 12 J, green for 17, and blue for 25 J. The scaling between both parameters can be directly observed for the three sets of data in both panels. In regard to the upper panel, the comparison between the average cut-off energy measured at the three devices seems to be

TABLE 5.2: Maximum energies in MeV measured by the TP and the two ToF detectors at 18/10/22.

$E_L =$	12 J	20 J	25 J
TP	9.9 ± 0.7	12.9 ± 1.3	14.6 ± 0.8
ToF_{I3M}	8.2 ± 0.5	10.1 ± 0.1	13.3 ± 1.0
ToF_{CLPU}	6.7 ± 0.7	9.8 ± 1.0	12.5 ± 0.4

TABLE 5.3: Maximum energies in MeV measured by the TP and the two ToF detectors at 21/10/22.

$E_L =$	6 J	12 J	17 J	25 J
TP	2.6 ± 0.2	4.3 ± 0.5	6.5 ± 0.5	9.1 ± 0.7
ToF_{I3M}	4.0 ± 0.1	4.9 ± 0.2	7.6 ± 0.6	10.2 ± 0.7
ToF_{CLPU}	3.0 ± 0.2	5.0 ± 0.6	7.5 ± 0.6	9.8 ± 0.9

consistent for each laser energy. As each detector was located at a different measuring angle with respect to the normal direction of the targets, a certain dependence of the detected cut-off energy on this parameter is expected. Thus, the TP at 0° is able to detect the most energetic ions, emitted normal to the target surface, while the two ToF detectors, located at 10 and 20°, gradually observe lower maximum energies. Table 5.2 shows the numerical values of the proton cut-off energies measured at each detector for this reference day. These results correspond to the average values of data from the initial single-shot measurements (depicted in the upper panel in Fig. 5.16) and from some long multi-shot series.

On the contrary, results compiled in Table 5.3 and shown in the lower panel in Fig. 5.16, for a different measuring day, systematically exhibit lower cut-off energies for the TP measurements than for the two ToF detectors. A similar inconsistency can be observed between both ToF detectors. This issue only happened on this day of campaign, and no explanation has been found by the time of writing. Besides, the expected scaling of the cut-off energies with the laser pulse energy was obtained. Having a slight dispersion of about less than 10% for each series at each laser energy, results shown in both panels in Fig. 5.16 exhibit great shot-to-shot stability (see the next section for the detailed study about the multi-shot stability of the ion source).

The dependence of the measured cut-off energies with the detection angle can be compared

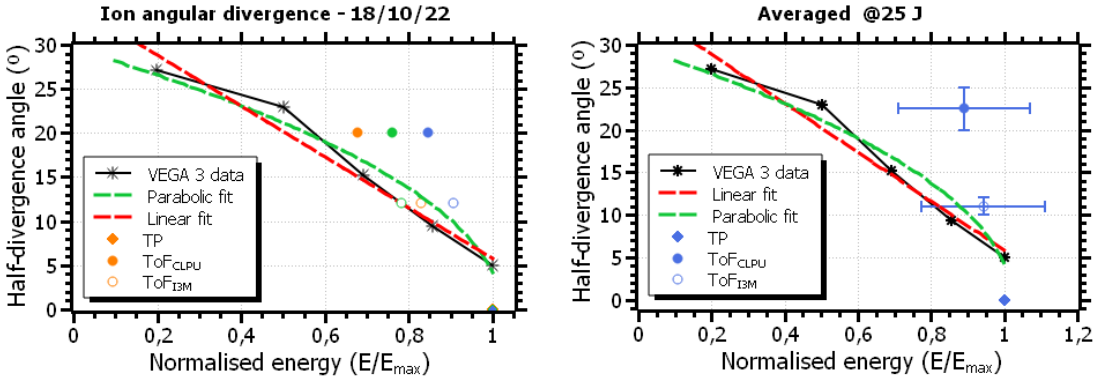

FIGURE 5.17: Ion angular divergence at VEGA 3 and measured maximum energies at each detector.

to the experimental angular divergence profile of the ion beam at the CLPU. The average cut-off energies in Table 5.2 for each detector and at various laser energies, normalised to the maximum energy of the beam (E_{max}) given by the spectra at the TP, are depicted, along with the divergence profile, in the left panel in Fig. 5.17. It can be seen that the relative cut-off energies at the ToF detectors, assuming that the emitted ion beam is completely centred to the TP, are not totally compatible with their angular location inside the interaction chamber. This circumstance is reinforced by looking at the left panel of the same figure, were the average cut-off energy at each detector within the entire experimental campaign, for the case at the maximum nominal laser energy, is depicted. Error bars indicate the systematic dispersion of the data. Although some of the values at 10° may be coherent with the angular divergence profile, the energies measured at the ToF of CLPU, at ∼20°, are a factor of 1.5 higher than expected.

Day-to-day variability

While results presented so far within this section correspond to the same two measuring days, some additional concerns emerge by taking into consideration the entire experimental campaign. The aforementioned analysis was applied to the data obtained on each day. A certain day-to-day variability the of proton cut-off energies was observed for, presumably, the same experimental conditions, as illustrated in Fig. 5.18. The top and middle panels depict the mean value of the proton cut-off energy at each measuring day and for each nominal pulse energy, as measured by the TP and the ToF from the CLPU, respectively. Most of the depicted data at the lower laser energies were retrieved from single-shot irradiations, while long multi-shot

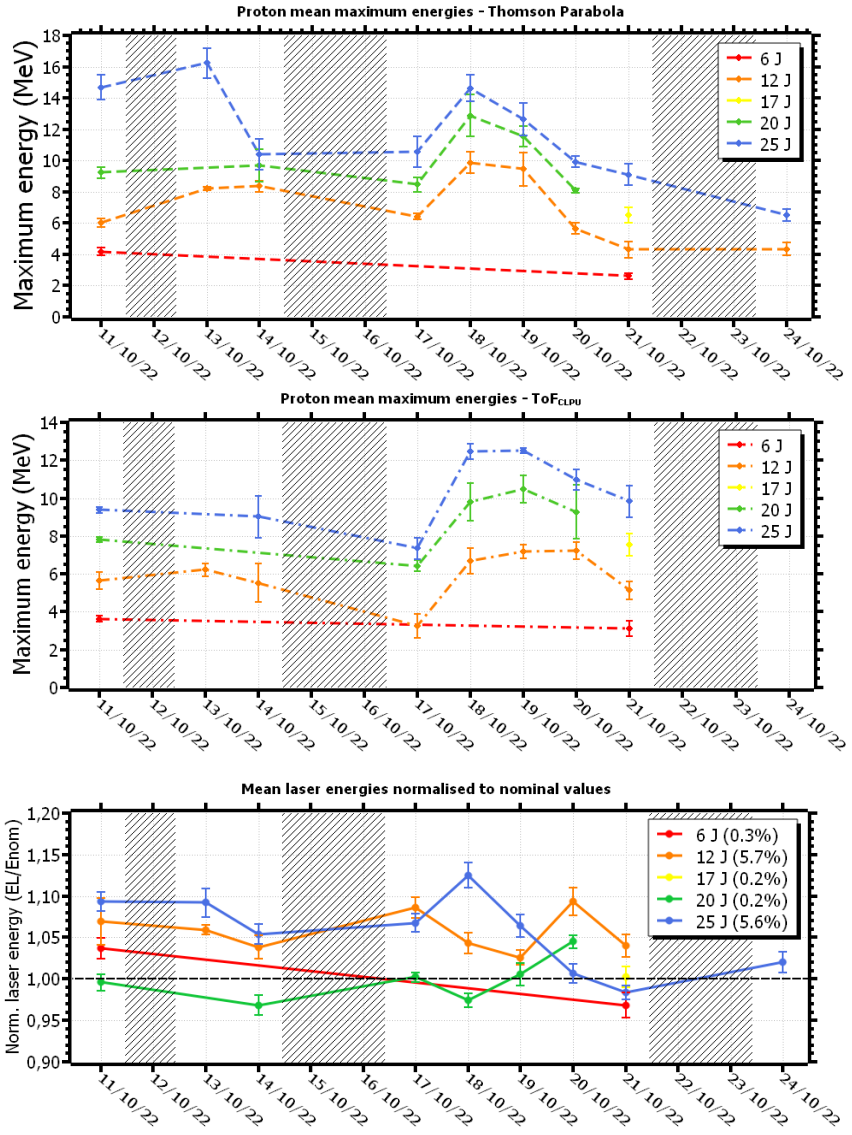

FIGURE 5.18: Evolution of the maximum energies at the TP and at the ToF (CLPU), and of the laser pulse energy. Greyed-out days represent weekends or local holidays.

series were also considered for the cases at higher energy. No measurements at every nominal laser energy (6, 12, 17, 20, and 25 J) were performed on each day. Greyed-out days indicate weekends or local holidays. As can be seen, the proton cut-off energy curves noticeably vary on a day-to-day basis, following a similar profile whichever laser energy. This leads to that, in some cases, the cut-off energy at 20 or even 12 J is of the same order as the case at 25 J on

a different day. Even so, the scaling of the cut-off energies is consistent within the same day. The observed day-to-day variability complicate in principle the comparison between data from different measuring days, as well as the systematic study and the overall characterisation of the ion beam. Some applications that required absolute calibration, as for example radioisotope production, reported in Ch. 6, were similarly biased. With respect to neutron generation, the main objective of the experimental campaign, this led to additional uncertainties regarding the dependence of the neutron flux on the ion beam properties, both during the experiment and for the later analysis.

This issue may be partly attributed to the variability of the maximum energy of the laser pulses on each day, depicted in the lower panel in Fig. 5.18. The curves represent the laser pulse energy on each day, averaged over all the shots at the same energy and normalised to its corresponding nominal energy. The day-to-day evolution of this parameter, for the maximum pulse energy (blue curve), follows a similar profile as the cut-off energy evolution in the upper and middle panels. Data at laser energies lower than this case show no apparent correlation with the proton energies. Although the maximum pulse energy only refers to the nominal case at 25 J, the variation of this magnitude may be related to the variation of other parameters of the laser system, as the pulse duration or its spatial distribution, which could also have a predominant effect on the laser pulses at lower energies. A measurement of the pulse duration for each shot was performed, by using a standard second order auto-correlator, on one of the days of campaign (11/10/21). The average duration within the whole day resulted in 241 fs $\pm$ 16 fs, corresponding to a variation of about 6.5%. Given that no other measurement of this parameter was carried out on a different day, this value alone may only serve to explain the shot-to-shot fluctuations in the proton cut-off energy and temperature of that day.

A representation of the variation of the spot size of the laser focus is depicted in the upper four panels in Fig. 5.19. The two panels on the left display the measured focal spot of the VEGA 3 laser at low power on two different days, while the right panels show their respective effective area above the FWHM threshold, as calculated in Sect. 5.1.1. The difference in size and shape between the two cases can be plainly noticed. The estimated average diameter of the focal spot is 22.6 $\pm$ 2.6 μm for the upper case and 19.1 $\pm$ 1.1 μm for the lower case. For fixed pulse energy and duration, this variation can lead to a fluctuation in the pulse peak intensity about a factor of 1.4, of the same order of the cut-off energy variability. Although these focal images were retrieved at low power mode of the laser system, the same spatial distribution can be expected for the high power mode (at full energy or at a fixed fraction). Any possible

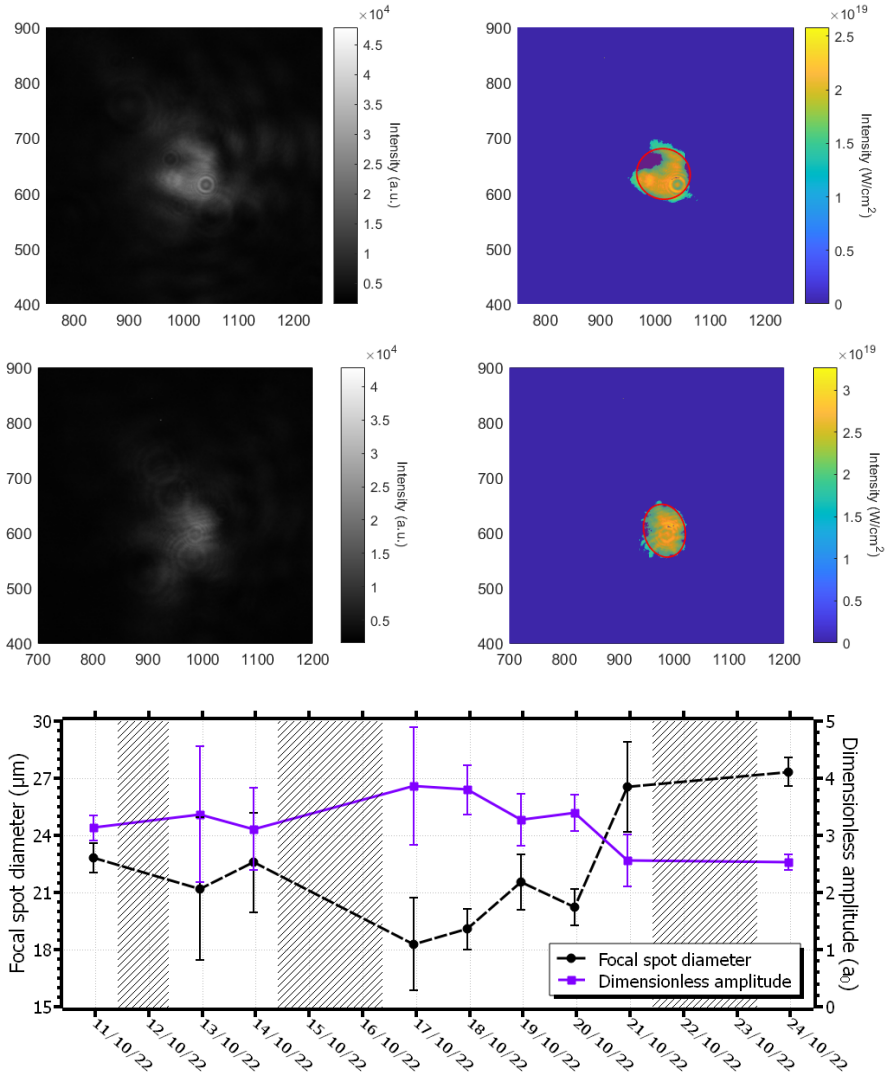

FIGURE 5.19: Laser focus and area above the FWHM in intensity for two different measuring days.

thermal lens effect could not be measured. Regarding the entire experimental campaign, the lower panel in Fig. 5.19 shows the estimated focal spot size (average diameter at the FWHM) and the dimensionless amplitude a_0, calculated via Eq. and 2.7 assuming a fixed pulse duration of 250 fs, on each day. In comparison with the cut-off evolution in the upper panel in Fig. 5.18, the spot diameter (black curve) exhibits a mirrored profile, which contributes to the peak energy of the pulses in the same way as the pulse energy profile. Thus, the dimensionless amplitude, depicted by the purple curve, follows a similar day-to-day trend as the proton cut-off energy.

However, this presumption cannot be considered as the only origin of the day-to-day variability due to the high uncertainty shown by the estimated data.

Temperature scaling

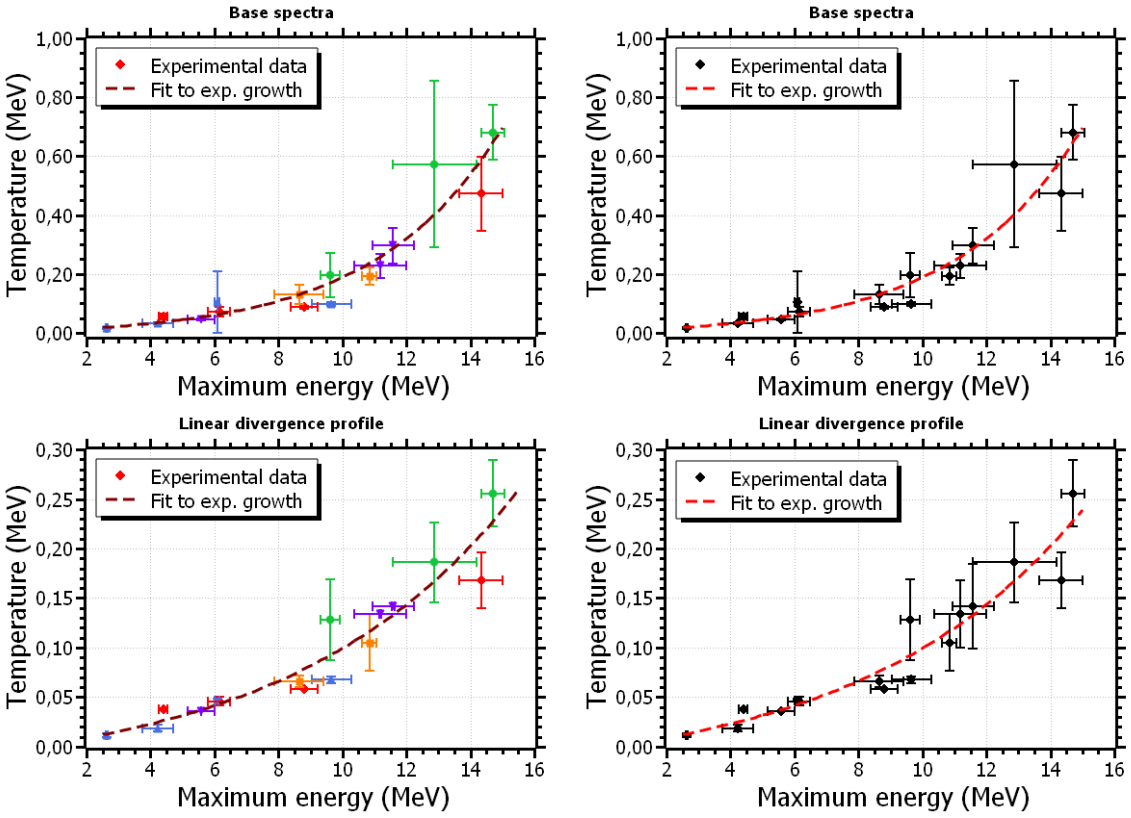

FIGURE 5.20: Scaling of the spectral temperatures and the cut-off energy for several series at different laser energies and on different measuring days.

Fig. 5.20 depicts the correlation between the cut-off energy and the temperature for both the base proton spectra measured at the TP (upper panels) and the corrected spectra assuming a linear divergence profile (lower panels). Each point corresponds to the mean value of a single-shot or multi-shot series at a certain pulse energy each. Data from different days is considered, represented with different colors in the figure, thus demonstrating a strong correlation between both parameters regardless of the laser pulse energy. The displayed data was fitted to various mathematical functions in order to obtain the best approximation: an exponential growth, and

TABLE 5.4: Correlation between the maximum energy and the temperature.

Exp. growth: $T_0 + T_1 \cdot \exp(E_{max}/\tau)$	T_0 (MeV)	T_1 (MeV)	τ (MeV)	R^2	χ^2
Base	-0.012	0.016	3.95	0.908005	0.056405
Linear	-0.032	0.031	6.91	0.914137	0.006140
Parabolic: $T_0 + T_1 \cdot E_{max} + T_2 \cdot E_{max}^2$	T_0 (MeV)	T_1 (-)	T_2 (MeV^{-1})	R^2	χ^2
Base	0.18	-0.061	0.0062	0.906251	0.057480
Linear	0.023	-0.0051	0.0013	0.914031	0.006148
Linear: $T_0 + T_1 \cdot E_{max}$	T_0 (MeV)	T_1 (-)		R^2	χ^2
Base	-0.22	0.048		0.756118	0.149532
Linear	-0.059	0.017		0.859358	0.010058

a parabolic or linear polynomial correlation. Table 5.4 summarises the parameters of each function obtained from the fits, both for the base and the corrected data.

The R^2 and the χ^2 coefficients from a goodness-of-fit analysis for each of the fits are listed in Table 5.4 as well. The highest values of the R^2 coefficient are obtained for the exponential growth dependence on the data —slightly greater than the parabolic dependence, about less than a 1%—. The comparison between the χ^2 coefficients leads to a similar conclusion. Hence, the exponential growth dependence on the data can be considered as the best fit, which is also plotted in Fig. 5.20. While both parameters are expected to escalate with the peak intensity of the laser pulses, such a correlation between them has not been reported in literature. It can be compared with the theoretical estimations given by the isothermal expansion model (see Sect. 2.3.1) and the results obtained in the Particle-In-Cell simulations performed within this work (Sect. 5.3). This comparison will be studied in detail in Sect. 5.4.

5.2.3 Ion source stability

The performance of the multi-shot target assembly during the experimental campaign was rather solid. Typically, around 400 - 500 laser shots (half the target wheel) were performed per day, for a total of ∼3700 shots within the two weeks of experiment. About 60 series of more than 10 shots in multi-shot operation were achieved for laser pulse energies ranging from

12 to 25 J. The highlights of the multi-shot series, only considering those having ion beam diagnostics, are:

- One series of 32 shots at 12 J and 1 Hz.
- One series of 180 shots at 20 J and 0.2 Hz.
- Several series of $\geq$101 shots at 25 J and 0.1 Hz.

In spite of the day-to-day variability of the laser system mentioned in the previous section, the cut-off energies and temperatures within the same measuring day present a high stability. The typical standard deviation is below the 10% in most of the series in multi-shot operation. Panels **(a)**, **(b)**, and **(c)** in Fig. 5.21 depict the proton cut-off energies retrieved from the TP traces for the three above-highlighted multi-shot series at different pulse energies and repetition rates. Panel **(a)** corresponds to the multi-shot series performed at 12 J-energy per pulse and 1 Hz-repetition rate. The shot-to-shot proton cut-off energies measured at the TP (solid purple diamonds), the ToF from I3M (open cyan circles), and the ToF from CLPU (solid magenta squares) are depicted. As this measurement were performed on the same day as the results in the upper panel in Fig. 5.16, it reflects the same behaviour regarding the dependence of the measured cut-off energies with the detection angle. Panels **(b)** and **(c)** represent the cases at 20 J and 0.2 Hz, and at 25 J and 0.1 Hz, respectively.

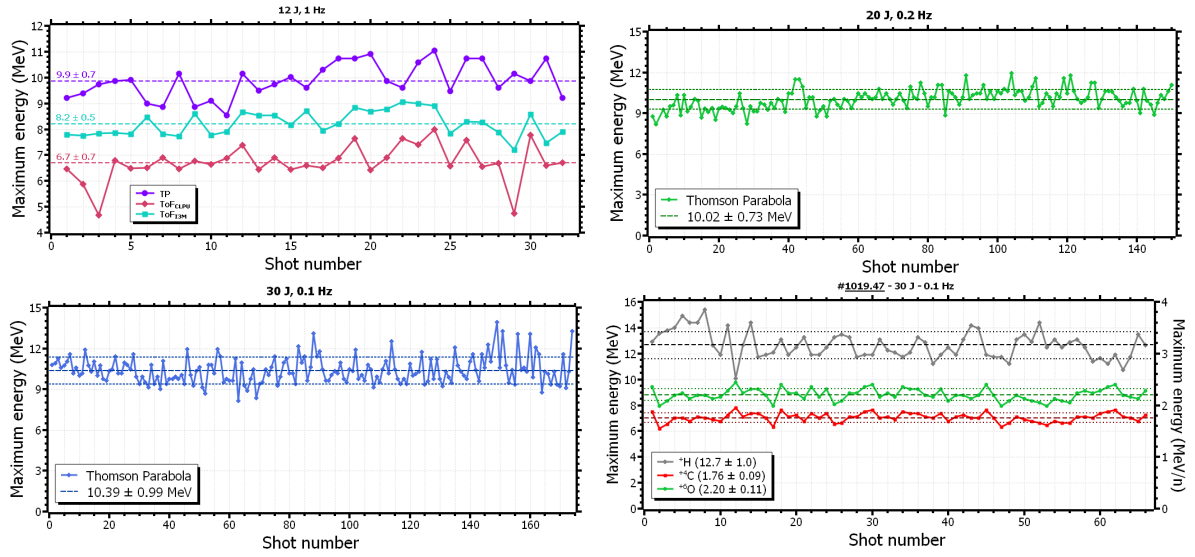

FIGURE 5.21: Proton and ion stability of various series at 12, 20 and 25 J.

Panel **(d)**, on the other hand, depicts the stability in the cut-off energy of another series at 25 J and 0.1 Hz and includes the results obtained for two other ion species ($^{+4}$C and $^{+6}$O). Aside from the signal due to protons ($^{+}$H), these two species exhibit the most intense traces at the images retrieved by the TP system on that day. As both traces are superposed at the high energy range, the same edge was utilised for the calculation of the cut-off energy and the spectrum for both ionic species. Thus, the two curves in panel **(d)** are equal but for a different central energy per nucleon, given by the charge-to-mass ratio of each ion.

It can be noticed that the range of the cut-off energies for the three series in panels **(a-c)** is of the same order, despite the different energy per pulse in each case. As each series was performed on a different day, this was mainly caused by the variability of the laser system discussed in the previous section. Regarding each series, the shot-to-shot oscillation may be partly originated by fluctuations in the energy and the duration of the laser pulses. According to the measured data, a standard deviation of about 1.3% and 6.5%, respectively, is calculated for these fluctuations, which may affect the cut-off energies about a overall factor of 2.5 according to Eq. 2.18.

All the depicted series in Fig. 5.21 exhibit a dispersion in the cut-off energy of less than 10%, regardless of the operation rate of the target assembly and the pulse energy, for long multi-shot series of up to 180 shot points. Thus, it demonstrates the shot-to-shot stability of the proton source, and consequently of the target system and its functioning procedure. Although a micron-accuracy positioning was not required for these series, in contrast to the experimental case at the L2A2, a singular challenge for the target assembly within this campaign resided in the proper synchronisation between the laser pulses, the relay system, and the refreshment of the target surface, while handling the huge EM pulses produced at the interaction.

The spectral temperature of each shot of the same three highlighted multi-shot series is shown in Fig. 5.22. Each panel in the figure depicts the temperature calculated via the fit of the base and corrected —linear— spectra from the TP to a Maxwell-Boltzmann distribution. In comparison to the observed shot-to-shot stability of the maximum energy in Fig. 5.21, the temperature presents higher data dispersion, showing standard deviations between 10 and 40%. This factor is more prominent for the temperatures estimated from the base spectra. As can be seen in the figure, specifically for the series shown in panel **(c)**, some of the calculated values are up to a factor of 2 higher than the estimated standard deviation, indicated in the legend in each figure. Even for similar maximum energies, the shape of the spectral distributions was not homogeneous between shots and some of them exhibit a significant variation in temperature.

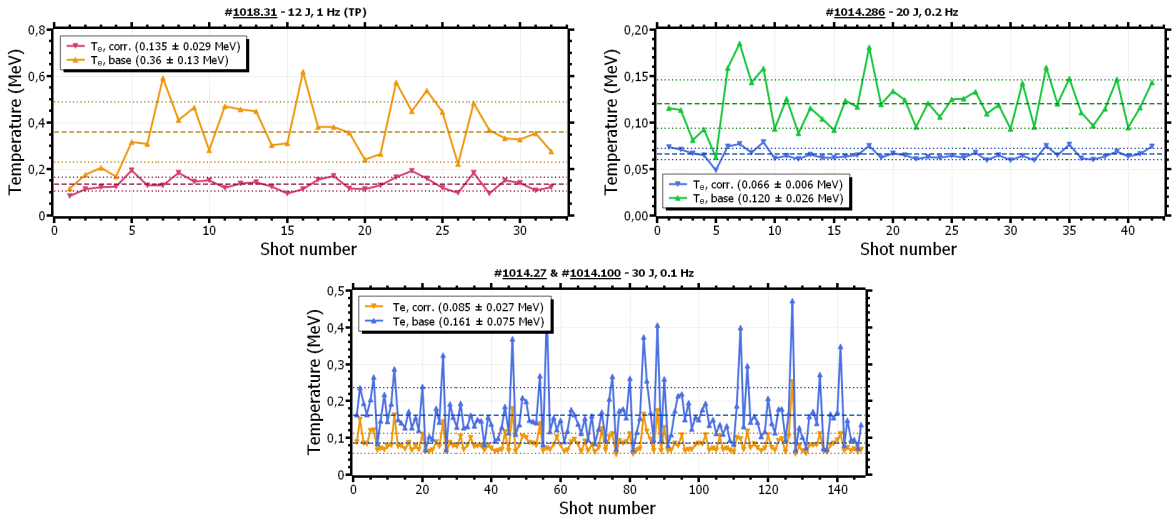

FIGURE 5.22: Temperature stability of various series at 12, 20 and 25 J.

Others, however, present a two-temperatures distribution near the highest energy region, thus complicating the fit to a pure Maxwell-Boltzmann exponential decay. These results, denoted as open symbols in Fig. 5.22, were excluded from the analysis by means of a χ^2 goodness-of-fit evaluation at $\alpha = 0.05$.

5.3 Particle-In-Cell simulations

Particle-In-Cell (PIC) two-dimensional simulations on laser-driven ion acceleration were performed as a supplementary study to the experiments. By means of these simulations, the experimental cases within the L2A2 and the CLPU campaigns were reproduced in order to infer the scaling laws of the relevant parameters, and as a qualitative comparison to the experiemental data presented throughout previous sections. In this way, the irradiation of a thin target foil of a material of low atomic number —specifically aluminium, as used in the experiments— with a ultraintense femtosecond laser pulse at a certain angle of incidence was simulated. The simulations presented in this section were carried out by means of the Smilei code, running at the FinisTerrae II and FinisTerrae III clusters at the Centro de Supercomputación de Galicia (CESGA). The *happi* module from Smilei was used for the analysis of the resulting data and its graphical representation.

5.3.1 Simulation parameters

TABLE 5.5: Parameters for the laser-driven proton acceleration simulations, performed by means of the Smilei code, for the cases at L2A2 and CLPU.

		L2A2	CLPU	
General	Spatial resolution	10×20	25×25	nm
	Simulation box	24×72	65×80	μm
	Temporal resolution	0.03	0.051	fs
	Simulation duration	900	1530	fs
	Number of patches	32×32	64×64	
Target	Foil thickness	2 - 12	7	μm
	Particles-per-cell	100	100	
	Initial ion density	$50n_c$	$50n_c$	
	Degree of ionisation	+13	+4	
	Preplasma extension	0.05	1.32	μm
	Preplasma scale-length	0.5	0.5	λ_L
	Proton layer thickness	100	200	nm
	Particles-per-cell	900	900	
	Initial proton density	$100n_c$	$100n_c$	
	Degree of ionisation	+1 or 0*	0*	
Laser	Wavelength	800	800	nm
	Pulse duration (FWHM)	25	250	fs
	Focal spot size (FHWM)	2.5	20	μm
	Dimensionless amplitude	9.6	1.5 - 3.9	
	Incidence angle	45	10	deg.

*: neutral proton layer, dynamic field-ionisation activated.

The implemented parameters for the simulation of the experimental conditions at the L2A2 and at the CLPU are listed in the two columns of Table 5.5. Regarding the former, the simulation box had a size of 24×72 μm^2, corresponding to 1600×2400 cells at a 10×25 nm spatial resolution, comparable to the typical values reported in literature[47, 49]. The temporal resolution was set to 0.03 fs, satisfying the CFL condition, for a total simulation time of 900 fs. Due to the larger duration (∼250 fs) and spatial length (∼75 μm) of the VEGA 3 laser pulses, the duration of the simulation and the box size in the longitudinal x-direction were escalated about a factor 1.7 and 2.7, respectively, so the entire pulse could enter the simulation box before reaching the target. As the computing resources would have significantly increased, the spatial

and temporal resolutions were accordingly escalated to 25×25 nm and 0.051 fs. This corresponds to a total of 2624×3200 number of cells, that is, 65×80 μm^2, and 1530 fs-duration. The size of the transversal y-dimension of the box in both cases was sufficient so the laser pulse, entering the simulation from the left boundary — the negative x box side—, had enough lateral space from the adjacent box side at the defined incidence angle.

The target foil was defined orthogonal to the x-axis and along the entire y-dimension of the box. Its thickness was fixed to 7 μm for the CLPU simulations, as in the experimental situation, and was varied from 1 to 12 μm for the simulations of the L2A2 conditions, corresponding to the range of available foil thicknesses at the facility. The initial particle density was set to 50 times the critical density n_c, having a typical, reasonable number of 100 particles-per-cell. As dynamic field-ionisation would require an elevated amount of computing resources, the common approach consists of pre-ionising the material up to a certain degree of ionisation. In this way, part of the energy from the laser pulse is absorbed by the ions instead of being entirely transferred to the electrons, which would lead to a certain overestimation of their energies. Therefore, the target consisted of an aluminium foil fully ionised (+13) for the L2A2 simulation, and partly ionised (+4) for the CLPU case. The target was hence defined as a neutral plasma so the electron density n_e was set to $n_e = d \cdot n_i$, being n_i the ion density and d its degree of ionisation.

An expanding preplasma was configured in the frontal face of the target, to account for the ionisation produced by the prepulses or the pedestal of the laser. The particle density profile of this preplasma was an exponential growth following expression

$$n_i = 50 n_c \exp[(\frac{x - x_0}{L_g}) - 1] \tag{5.3}$$

where n_c is the critical density, L_g the plasma scale-length, and x_0 the x-position of the target foil inside the simulation box. The longitudinal extension of the preplasma was estimated from the ion sound speed (Eq. 2.2.5) for an electron temperature calculated via Eq. 2.2.23. The intensity of the prepulses or pedestal above the ionisation threshold ($\sim 10^{16}$ W/cm^2), obtained from the experimental temporal traces of STELA and VEGA 3 (Figs. 3.4 and 3.6), was utilised for the calculation of this electron temperature. The advance of these contributions with respect to the main laser pulse defined the expansion time of the preplasma. Given that this time interval is several orders of magnitude longer than the duration of the laser pulse —and therefore longer

than the laser-plasma interaction—, enough for the thermalisation of the preplasma, it was set to a neutral aluminium plasma at the same ionisation degree as the target. Some simulations were performed having the preplasma composed of neutral ionised hydrogen ($^{+1}$H and electrons) instead, yet no significant difference was observed. For simplicity and better computing performance, the preplasma composition was set to ionised aluminium. For VEGA 3 laser, considering the temporal trace shown in Fig. 3.6, the extension of the preplasma can be estimated as Δx = 1.05 μm = 1.32λ_L. The same analysis for the STELA laser gives an estimation of Δx = 50 nm = 0.066λ_L, due to its ultra-high contrast, which was approximated to a step density profile for some of the simulations[108].

The rear side of the target foil, on the other hand, was coated with a ultra-thin film of hydrogen, representing the contamination layer from which protons are accelerated trough the TNSA mechanism. The thickness of this film was set to a few times the spatial resolution of the simulation. The particle density and the number of particles per cell were increased to 100n_c and 900 particles-per-cell, respectively, for improved resolution. Different approaches were considered for the simulations of the L2A2 and CLPU experiments. For the former, the hydrogen film was ionised up to a neutral plasma of protons and electrons. For the later, the film was composed of neutral hydrogen atoms and dynamic field-ionisation was activated. As detailed in the section below, the effect of these two methods on the resulting proton beam was evaluated by performing comparative simulations. No appreciable difference was found, but for varying the execution time of the simulation.

Regarding the configuration of the laser pulse, a two-dimensional Gaussian pulse travelling towards the positive x-direction at the experimental incidence angle was defined. The pulse was focalised onto the target surface at half the transversal length of the simulation box, i.e., at (x_0, $y_{max}/2$), down to a focal spot of 2.5 or 20 μm-diameter, depending on the simulated case. As indicated in Table 5.5, the characterisation of the laser pulses in the simulations replicated the experimental parameters present within each campaign. Silver-Müller absorbing boundary conditions for the electromagnetic fields were set at each side of the simulation box other than the laser entrance boundary.

5.3.2 Simulation results

By means of the simulations presented in this section, the systematic scaling of the proton maximum energies and temperatures were studied upon the variation of several experimental

parameters of interest, such as the target thickness or the laser pulse energy. As the main objective of these simulations is the qualitative comparison with the experiments performed within this work, as well as its extrapolation for future research, practical magnitudes and parameters were analysed.

The properties of the accelerated particle beams, as well as other extensive magnitudes as the electric and magnetic fields or the particle densities, were examined at each simulation. The diagnosis tools from the Smilei code were utilised for the retrieval of these data. The energy of the protons and the electrons accelerated at the rear side of the target was measured via a screen diagnostic, placed at the right boundary of the simulation box. Each particle crossing the screen was histogrammed according to its energy and type. The duration of the simulation was sufficient to let most of the accelerated protons reach the screen. Also, the electric field and the particle densities over a two-dimensional grid centred at the target were recorded over fixed time steps within the entire extent of the simulation.

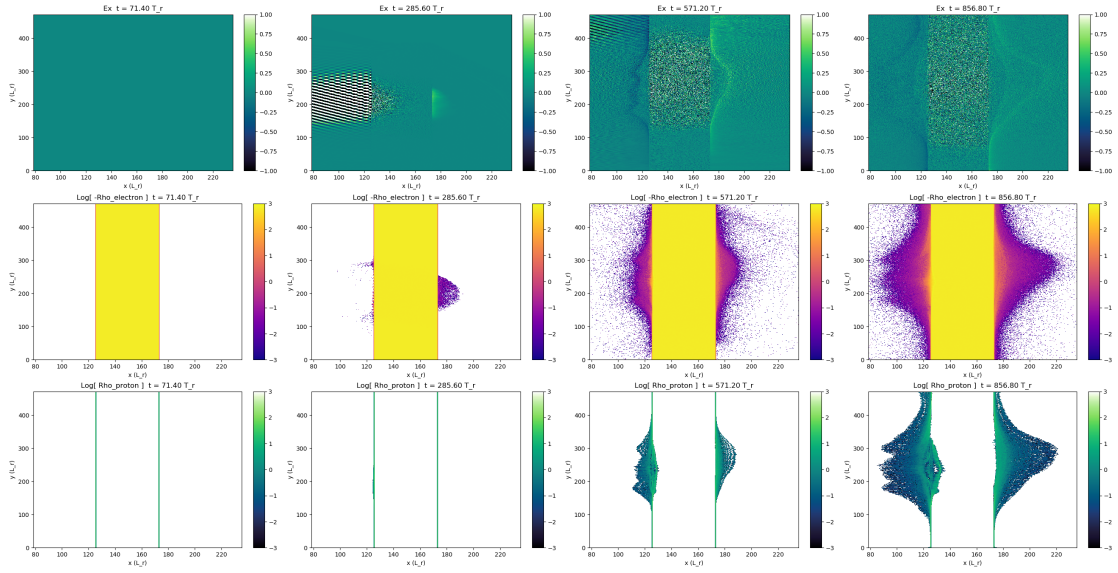

FIGURE 5.23: Evolution of the electric field, the electron density and the proton density.

As an illustrative example, Fig. 5.23 shows the evolution of the electric field in $\hat{x}$ (E_x) **(a)**, the electron density (n_e) **(b)**, and the proton density (n_p) **(c)** for a simulation using arbitrary parameters from the left column in Table 5.5. Each image, at four different times (0, 150, 300, and 600 fs), depicts the defined two-dimensional grid around the target foil at which each

magnitude is evaluated. Colour bars indicate the value of each of them, in linear scale for the electric field, and logarithmic for both particle densities. The later are expressed in arbitrary units, proportional to the ion critical density. As can be seen in the images, the laser pulse enters from the left side of the box and impinges on the target foil, which is initially neutral. The following simulation steps can be described through the TNSA mechanism: the electric field from the laser pulse accelerates the electrons towards the target, and emerge from the rear side as a negative-charged cloud. A charge-separation field, of about 0.4 TV/m, is generated between the electron cloud and the proton film, that then accelerates the later as a sheath that propagates to the right side of the simulation box. A less efficient acceleration of both electrons and protons is observed as well in the frontal face of the target. Thus, it can be seen that the TNSA mechanism can be qualitatively reproduced through these simulations. From this reference example, the systematic study on some parameters of interest was carried out, as will be presented throughout the following discussion.

Target thickness

The scaling of the main spectral parameters of the proton beam with the thickness of the target was evaluated. This was motivated by the flexibility of the target system developed within this work to host target foils of different thickness or composition. Although no experimental study on this dependence nor results were presented in Sects. 5.2 and 5.3, the incoming series of experiments at the L2A2 may utilise aluminium and Mylar foils down to 1 μm-thick. Thus, aluminium foils of thicknesses 1, 2, 6 and 12 μm were simulated considering the experimental parameters at the L2A2. The size of the simulation box along the x-direction was escalated with the target thickness up to 40.96 μm, in order to maintain the distance between the rear side of the target and the diagnosis screen. This distance was sufficient so the ions could be accelerated up to their maximum energies.

The results from the simulation at each target thickness are depicted in panels **(a)** and **(b)** in Fig. 5.24. Panel **(a)** presents the proton energy spectra for all the simulated cases, while panel **(b)** plots the maximum energy (green curve, left axis) and the temperature (red curve, right axis) obtained at each of them. The later was calculated by fitting the corresponding spectrum in panel **(a)** to Eq. 2.26. An increase of both parameters with the target thickness is expected[70] and observed. While it is not contemplated in the simulated case, target thicknesses below a certain critical value are presumably affected by the ASE component of the laser pulses or the prepulses in the experimental situation, depending on the contrast of the laser. This critical

value can be estimated to a few hundreds of nanometres for the STELA laser, and up to 1 or 2 μm for VEGA 3.

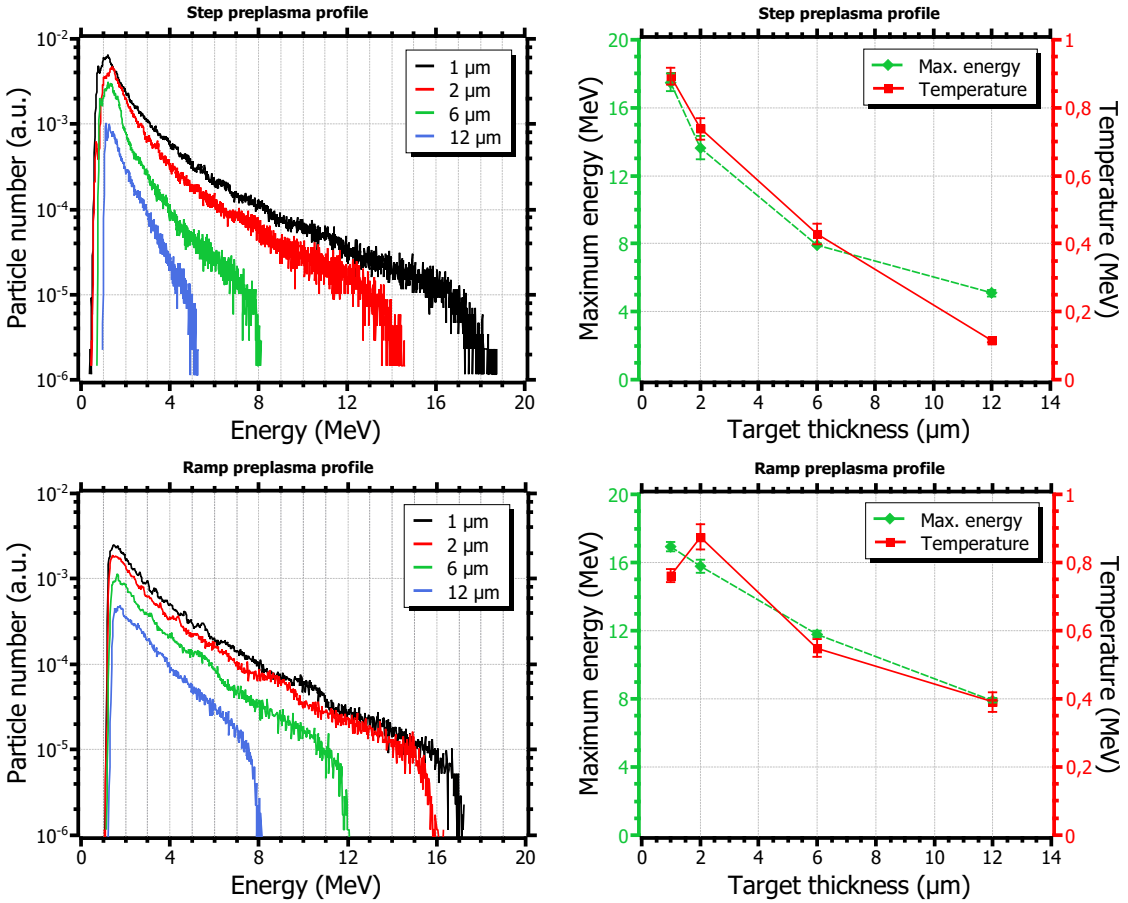

FIGURE 5.24: Electron and proton spectra from PIC simulations for various target thicknesses at L2A2.

These results can be compared with the experimental measurements at the L2A2. The simulations indicate that the maximum energies obtained experimentally, up to 2 MeV for a 2.5 μm-diameter focal spot (Fig. 5.8, panels **(c)** and **(d)**), may be systematically low. Thus, for aluminium foils of 12 μm-thick, a cut-off energy of around 5 MeV would be expected. Regarding the temperature, the simulations exceed the experimental values (Fig. 5.9) about a factor of 1.4. The results from the simulations, however, may be overestimated as well, as the maximum energy of almost 20 MeV obtained for target thickness of 1 μm suggests. The comparison between these two results, as well as with data from recent publications, will be detailed in section

5.4.

Increasing the length of the preplasma to $1.5\lambda_L$, of the same order the estimation for the CLPU simulations, leads to an enhancement of the proton maximum energies about a factor of 1.5. This is depicted in the two bottom panels (**(c)** and **(d)**) in Fig. 5.24, showing the proton spectra and the dependence of the parameters on the target thickness. Concerning the temperature, an increase of a factor of $\sim$1.3 is observed as well. This may lead to the conclusion that a certain preplasma extension is required in order to efficiently accelerate the electrons from the frontal side of the target, following the arguments discussed in Ch. 2. For the relativistic regime, $J \times B$ mechanism is enhanced at the critical density limit of a growing density profile. In the absence of this profile, other less efficient pushing mechanisms in this range of laser intensities, such as vacuum heating acceleration, are the responsible of the electron injection inside the target.

Dynamic field-ionisation

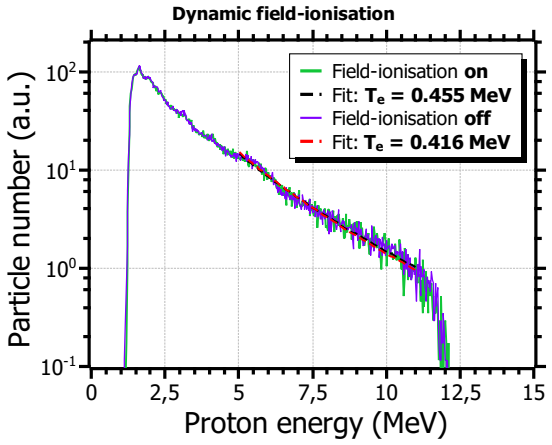

FIGURE 5.25: Proton spectra from PIC simulations having dynamic ionisation of the proton layer activated (green curve) or deactivated (purple curve).

Several simulations were performed to investigate the effect of dynamic field-ionisation of the hydrogen rear-side layer on the properties of the accelerated proton beam. A comparative example between two of these simulations, either considering dynamic field-ionisation or a neutral plasma of protons, is shown in Fig. 5.25. The figure depicts the proton spectra obtained for the simulation parameters of the L2A2 case, at 6 μm-target thickness and a preplasma length of

TABLE 5.6: Comparison of the cut-off energy and the temperature between experiment and simulation. *: data from a different day.

E_L (J)	E_{max}^{sim} (MeV)	E_{max}^{exp} (MeV)	Factor	T_e^{sim} (MeV)	T_e^{exp} (MeV)	Factor
6	5.77	4.25*	1.36	0.226	0.012	22.2*
12	8.92	9.9	0.90	0.313	0.135	2.31
20	11.65	12.9	0.90	0.384	0.186	2.06
25	13.03	14.6	0.89	0.405	0.256	1.58

$1.5\lambda_L$. It can be seen that both spectra are essentially identical in terms of their shape and normalisation. The temperature of each was calculated by means of a fit to a Maxwell-Boltzmann distribution (Eq. 2.2.26), as in previous cases. Both the temperatures and the maximum energies differ by less than a 10%. Therefore, both approaches for the simulation of the contaminant layer at the rear side of the targets can be validated. For the following, the simulations reproducing the experimental situation at the CLPU were performed with dynamic field-ionisation, while for the simulations regarding the parameters at the L2A2 an initially ionised neutral hydrogen layer was considered, as indicated in Table 5.5.

Laser energy

As for the experimental results measured within the CLPU campaign, the scalings of the proton cut-off energy and temperature were studied in terms of the laser pulse energy. The simulations were performed taken into consideration the parameters summarised in the column on the right in Table 5.5. Fig. 5.26 portrays a two-dimensional representation of the electric field **(a)** and the electron and proton densities **(b-c)**, evaluated over the simulation grid, at 1000 fs after the start of the simulation. As in the previous case, the electron cloud is formed at the rear side of the targets and the charge-separation electric field is generated peaking at the ion front, which clearly expands as a density sheath. The oscillation pattern in the electric field (panel **(a)**) from the interference of the incident and reflecting components of the laser pulse can be observed in the frontal side of the target.

In regard to the nominal laser energies used in the experiments performed at the CLPU, laser pulses of 6, 12, 20, and 25 J were simulated. The resulting proton spectra, for each case, are depicted in the left panel in Fig. 5.27. A direct proportionality between the laser energy and the

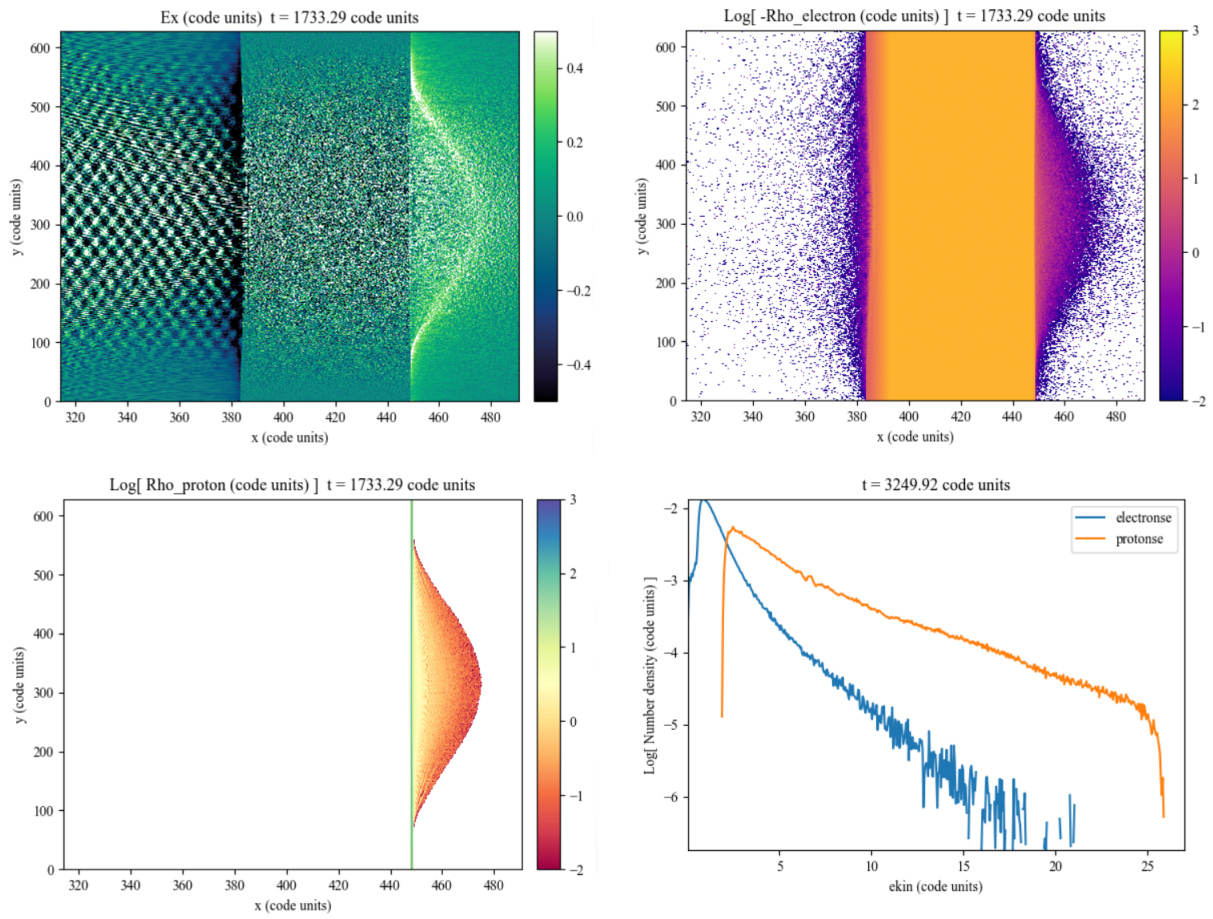

FIGURE 5.26: Proton spectra from PIC simulations for various laser pulse energies (VEGA 3).

three main parameters characterising the spectral distributions (particle number, cut-off energy, and temperature) can be observed. The right panel in the same figure indicates the retrieved values of the cut-off energy (green curve, left axis), and the calculated temperatures (red curve, right axis) assuming a Maxwell-Boltzmann distribution. Such a dependence on the laser energy implies a similar dependence on the peak intensity of the laser pulses, as expressed via the top axis in the figure.

Table 5.6 compares the results from these simulations with the experimental measurements from the CLPU campaign, for each simulated laser energy. The experimental values for the 12, 20, and 25 J cases correspond to the averaged results from the TP of the reference day with the highest proton energies observed (18/10/22). As no shots were performed on this

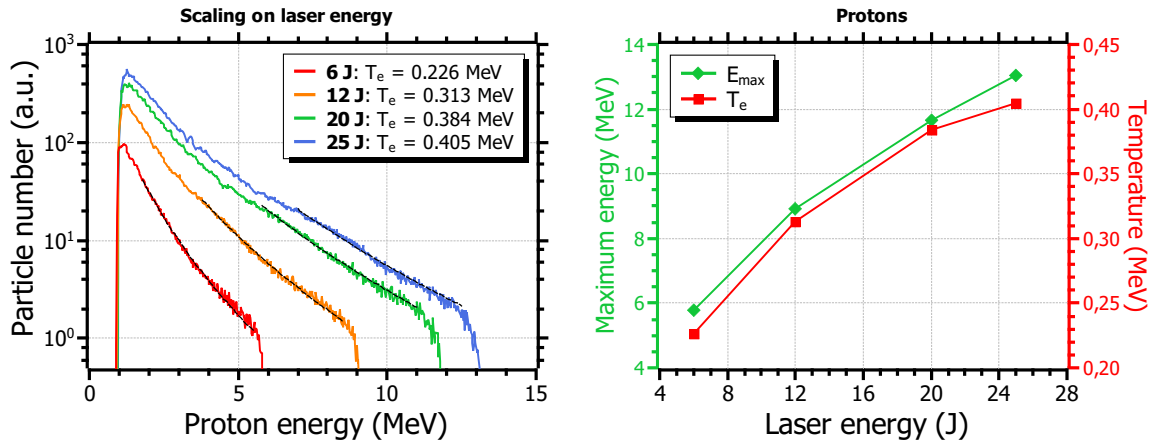

FIGURE 5.27: Proton spectra from PIC simulations for various laser pulse energies (VEGA 3).

day at 6 J, the values listed in Table 5.6 for this energy are from another day of campaign (21/10/22). The experimental temperatures correspond to the corrected spectra considering a linear divergence profile, in order to directly compare experiment and simulation. It is worth noting that the displayed maximum energies differ by a 10%, while the comparison between the temperatures results in around a factor of 2. While the observed scalings, simulated and measured, are reciprocally consistent, considering the results from a different measuring day within the CLPU campaign leads to a different comparison, due to the experimental day-to-day variability of the results. This is illustrated by the case at 6 J-pulse energy in the Table. Sect. 5.4 will delve into the comparison between these results its relation to data from published literature.

Taking into consideration the temporal trace of the laser pulses at CLPU, displayed in Fig. 3.6, the relative intensity of the prepulses or the pedestal for laser pulse energies below 20 J may not be sufficient to ionise the surface of the target before the arrival of the main pulse. Thus, in contrast to the simulated case presented here, the length of the induced preplasma may be shorter or even suppressed for these lower pulse energies. The same plasma length was configured for all the performed simulations, in order to directly compare the results and their scaling. More realistic simulations would account for this, for which it could be convenient to have temporal traces empirically measured at laser energies below the maximum.

Other considerations

The simulation results presented in this section must be considered as merely qualitative. A complete reproducibility of experimental data is not commonly achieved nor sought on this topic, as numerous uncertainties and complex interactions arise at the experimental case that may not contemplated in the simulations. In addition, the performed simulations are two-dimensional. Three-dimensional simulations, which in principle would be more realistic, are highly expensive in terms of computing resources and were not attempted. Such an in-depth analysis is beyond the scope of this thesis.

Some of the parameters that were fixed within these simulations can be explored in further iterations. Of special interest is the plasma scale-length, whose modification can lead to a significant variation of the results. While this parameter is a current subject of study in the literature and it is often used as scaling parameter, the analysis performed in this work has employed a constant value in the typical range of study. Together with this parameter, the influence of the length of the preplasma are typically analysed in publications. A simple evaluation of this parameter serves as a example: taking into consideration the simulations with VEGA 3 laser, an increase in the preplasma length up to 3 λ_L or 5 λ_L leads to an increase of the proton maximum energy of about a 140% or a 190%, respectively, for the case at 6 J-pulse energy.

A more exhaustive analysis on these parameters would be required in order to infer their correlation with the spectral parameters and its relation the experimental situation, i.e., to infer scaling laws. However, the simulations presented in this work have a supplementary role as a contribution with additional background to the experimental results. A complete analysis may have supposed an entire chapter of a doctoral thesis.

5.4 Scaling laws

This section details the comparison between the experimental results obtained at each campaign, the data from the PIC simulations, and some theoretical estimations given by the isothermal model described in Ch. 2, as well as a review of recently published experimental measurements in the literature. As will be seen through the analysis, some of the data are not directly comparable but in a qualitative manner. Nevertheless, some extrapolations could be inferred as a basis for some estimations on radioisotope production, which will be described in Ch. 6. As

introduced in Ch. 2 and mentioned in previous sections, the temperature of the ion spectral distribution constitute a relevant parameter for applications that require the absolute calibration. In the particular case of radioisotope production, of special interest under the scope of this work, this parameter plays an important role, along with the particle flux. Thus, its characterisation and scaling is essential for any precise estimation of the activities that can be produced.

TABLE 5.7: Main experimental parameters of published data reviewed in this work. From left to right: pulse energy, pulse duration, focus spot size, wavelength, peak intensity, dimensionless laser amplitude, protons maximum energy, target material, target thickness and laser contrast. For those references with spectra measured for different experimental conditions it is shown the case with the highest cut-off energy. Values denoted with a hyphen are not specified in the original study.

Ref.	E_L (J)	t_L (fs)	d_f (μm)	λ_L (nm)	I_L (W/cm^2)	a_0	E_{max} (MeV)	Material	D (μm)
[109]	0.13	39	10	800	$4.2{\cdot}10^{18}$	1.40	0.26	Au	2.48
[110]	0.71	55	7.5	800	$2.1{\cdot}10^{19}$	3.09	1.35	Cu	5
L2A2	0.92	35	24	800	$3.6{\cdot}10^{18}$	1.29	1.55	Al	12
[102]	0.005	40	1.8	780	$3.5{\cdot}10^{18}$	1.24	1.78	ethyl.glyc.	0.55
[47]	2.4	25	5.5	800	$1.0{\cdot}10^{20}$	6.80	6.90	Cu	1
[108]	-	-	-	800	$1.3{\cdot}10^{20}$	7.75	7.40	Al	0.1
[111]	2.0	35	4.0	800	$5.0{\cdot}10^{19}$	4.81	7.78	formvar	0.015
[108]	3.0	30	7.0	800	$2.0{\cdot}10^{20}$	9.62	9.00	Al	2
[57]	1.8	30	5.6	800	$1\text{-}9{\cdot}10^{19}$	2-6.4	1-11	Al	0.12
[112]	0.18	60	5.0	790	$1.5{\cdot}10^{17}$	0.26	0.29	Cu	5
[36]	0.43	55	6.6	800	$2.0{\cdot}10^{18}$	0.96	0.50	Cu	5
[113]	0.20	60	-	790	$7.2{\cdot}10^{18}$	1.81	0.99	Al	12
[40]	0.088	60	5.2	800	$6.8{\cdot}10^{18}$	1.77	1.20	Cu	5
[114]	0.7	30	4.0	800	$1.0{\cdot}10^{20}$	7.79	2.75	polymide	12.5
[49]	0.8	30	3.5	820	$2.0{\cdot}10^{20}$	9.76	3.46	polymide	7.5
[70]	0.3	30	3.0	800	$1.0{\cdot}10^{19}$	2.15	3.97	Al	0.1
[115]	1.7	34	14	800	$2.3{\cdot}10^{19}$	3.26	4.00	polymide	7.5
[116]	1.8	40	5.0	1060	$1.6{\cdot}10^{20}$	11.5	4.36	polymide	12.5
CLPU	6-25	250	22	800	$<3{\cdot}10^{19}$	1.5-3.9	<15	Al	7

In order to stablish scaling laws for the three parameters characterising the energy distribution of laser-accelerated protons, a bibliographic study was carried out regarding proton spectra

reported in literature for over a range of comparable laser pulse intensities. Within this study, only data from ultra-short moderate-energy laser systems were considered. In particular, pulse durations around 60 fs and pulse energies up to 3 J. Therefore, TNSA is expected to be the predominant ion acceleration mechanism in all cases. Special care was taken regarding the the diagnosis devices used for the measurements, as all the considered studies use a TP detection system, which in principle is not affected by heavier ion contributions. Other sets of data measured with ToF detectors were also considered, but only regarding the cut-off energy, as in principle the presence of heavier ions in the ToF signals could affect the temperature calculation. Table 5.7 summarises the main experimental conditions for each publication. The first eight rows correspond to the data measured with TP spectrometers, along with one of the experimental results at the L2A2 (Fig. 5.7, left panel). Proton spectra from these data were fitted to Eq. 2.2.26 in order to estimate the characteristic temperature and the distribution amplitude, given that most of them are calibrated in $\mathrm{MeV}^{-1}\cdot\mathrm{srad}^{-1}$. The next ten rows list the sets of data obtained with ToF detectors. Finally, last row includes the parameters at the experimental campaign in the CLPU, for comparison.

Fig. 5.28 depicts the compiled values for the maximum energy **(a)**, the temperature **(b)**, and the particle number **(d)** as a function of the laser dimensionless amplitude a_0 for the set of measurements considered in this study. Panel **(d)**, on the other hand, plots the spectral temperature in terms of the maximum energy. In these figures, data are organised according to the thickness of the targets over three ranges: below 1 μm (black dots), between 1 and 6 μm (red diamonds), and thicker than 6 μm (blue triangles). Data points corresponding to the experimental campaigns performed within this thesis are also included, after being corrected in solid angle to $\propto \mathrm{srad}^{-1}$ units. The green inverted triangles in each panel represent the results from different measurement days within the entire CLPU campaign, which will be commented later on this section.

Panel **(a)** shows a clear correlation between the laser peak intensity and the proton maximum energy. This correlation also depends on the target thickness, as discussed in Ch. 2 and in agreement with the PIC simulation results shown in the previous section. This graph includes both the data measured with TP and with ToF. According to the scaling laws obtained from the isothermal model ($\propto \sqrt{I_L \lambda_L^2}$), a linear correlation between the cut-off energy and the laser dimensionless amplitude is proposed for each thickness range. The resulting fits are in good agreement with the experimental data. In panel **(b)**, the correlation of the temperature with the laser intensity seems to be rather unclear. For target thicknesses thinner than 1 μm and thicker

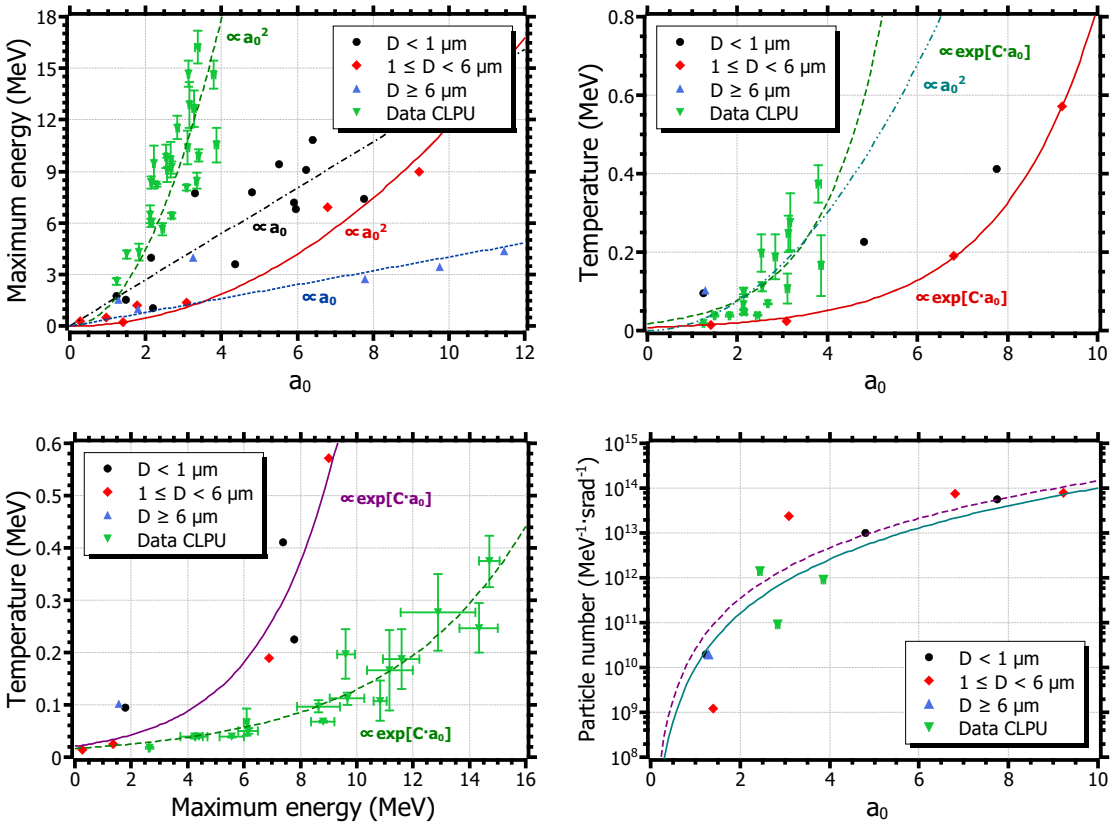

FIGURE 5.28: Proton spectra from PIC simulations for various laser pulse energies (VEGA 3).

than 6 μm, there is not enough data to apply an effective fit. For targets between 1 and 6 μm, data was fit to a growing exponential dependence, instead of a linear correlation as expected from the poderomotive scaling.

Regarding the data from the CLPU experiment, it can be clearly seen in panels **(a-c)** that they belong to a different regime, presumably due to the longer pulse duration and higher pulse energy. However, the correlations between the cut-off energy, the temperature, and the dimensionless amplitude seem to be rather solid, regardless of the discussed day-to-day variability. The proposed quadratic and exponential scalings shown in the figures for both parameters are not supported by the theoretical background discussed in Ch. 2, as in principle the derivation of $J \times B$ and TNSA regimes leads to linear scalings. Further diagnosis and analysis of the the laser-plasma interaction conditions present at the experiment should be performed in order to

understand this circumstance.

The correlation between the cut-off energy and the temperature in panel **(c)** is apparently independent of the target thickness for each pulse duration regime. Therefore, following the fit evaluation carried out for the CLPU results in Sect. **??** —also plotted in the figure—, short pulse duration data were fitted to an exponential growth function. Regarding the spectral amplitude depicted in panel **(d)**, all the considered data seems to follow the same trend regardless of the target thickness or the pulse duration regime. The shown curves correspond to two different power fits $\propto a_0^{\alpha}$ with $\alpha = 3 - 4$, applied to all the data. The data from the CLPU campaign shown in the figure was obtained through a calibration using the radioactive activation measurements from the radioisotope production part of the experiment. This calibration is described in Sect. 6.1.6.

A comparison between short and long laser pulses can be performed in light of the scalings shown in Fig. 5.28. Typical laser systems with long pulse durations are of the order of 500 fs – 1 ps[52, 53], and exhibit pulse energies above 100 J. Through certain special techniques, their pulse duration can be reduced down to a minimum of 300 fs. On the other hand, most of high-repetition Ti:Sa lasers produce pulses of several tens of fs and below 10 J-pulse energy. Thus, the VEGA laser system under the configuration utilised at the CLPU experimental campaign is of special interest, as it stays within an intermediate point. From panel **(a)** in Fig. 5.28 it can be seen that, for a given laser pulse intensity, increasing either or both the pulse duration or the pulse energy leads to a greater conversion efficiency to proton energies. From the formulation of the isothermal model and the results from the PIC simulations, this can be understood as a longer acceleration time for the ions under the influence of the charge-separation electric field. Hence, a higher energy is obtained at the end of the process (see the dependence on t_{acc} in Eq. 2.2.29). As seen in panel **(b)**, a similar outcome results for the temperature, but at a lower proportion, as indicates the comparison in panel **(c)** with the curve for short pulse duration.

5.5 Conclusions

The target assembly system developed in this work and described in Ch. 4 was utilised in two experimental campaigns regarding laser-driven ion acceleration, at the L2A2 and the CLPU facilities. Within these experiments, the target assembly was used as a multi-shot, long operation time ion source. The performance of this system, along with the implemented correction

and positioning procedure, was evaluated in terms of its shot-to-shot stability and its operation at high repetition rates —up to 10 Hz for the L2A2 laser—. Overall, the obtained results regarding laser-driven ion acceleration show a dispersion in the cut-off energy below 15%. This was obtained using two laser systems, STELA and VEGA 3, with very different parameters and conditions. Concerning the spectral temperature, the dispersion is slightly higher, of about 30% in some cases. These results validate the performance of the target system in regard to its stability and reproducibility, which in addition turns to be a flexible system that can be adapted to different facilities.

Within the experimental campaign at the CLPU, laser pulses of up to 25 J and 250 fs were focussed on aluminium foils of 7 μm-thickness. Although a day-to-day variability of the laser conditions was observed, proton beams with a cut-off energy in the order of 12 – 15 MeV were systematically measured. Several multi-shot series of hundreds of shots at different laser energies (12, 20, and 25 J) and repetition rates (1, 0.2, 0.1 Hz, respectively) were achieved using the PW VEGA 3 laser line. By the time of writing, this performance constitute a novel achievement in the context of long, high-repetition rate sustained operation at such laser pulse intensities.

The results from the experimental campaigns, together with data recently reported in literature, were analysed in order to infer scaling laws of the main parameters of the ion spectral distributions with respect to the intensity of the laser pulses. This analysis was motivated by the notorious absence of published studies on the determination and scaling of these parameters, aside from the cut-off energy. For some applications, as radioisotope production explored in the following chapter, the characterisation of these parameters is essential. The analysis was supported by two-dimensional Particle-In-Cell simulations reproducing the experimental situation at the L2A2 and the CLPU. In a qualitative means, the results from the simulations are in good agreement with the experimental data and the expected scalings.

Within the analysis presented in this work, different behaviours were observed between long ($\sim$250 fs for 25 J laser pulses at VEGA 3) and short ($\leq$ 60 fs) pulse durations. The conversion efficiency to proton energies seems to be greater for the former case. A linear correlation of the cut-off energy with respect to the laser intensity was proposed for the results from the CLPU experiment, while the typical scaling given by the ponderomotive potential were applied to short pulse duration data. Regarding the temperature and the spectral amplitude, respective exponential growth and power scalings were obtained as the best fit to the experimental and

reviewed data.

Chapter 6

Radioisotope production from laser-accelerated ion beams

This chapter addresses the viability study of laser-driven ions as a potential mechanism for the production of radioisotopes at the required dose levels in PET imaging. Sect. 6.1 describe the experiment performed on radioisotope production at the CLPU facility. Within this section, Sects. 6.1.1 – 6.1.3 introduce the detection system that was developed for the measurement of the produced radioactive samples activation, as well as its efficiency calibration. The experimental set-up is described in Sect. 6.1.4, and the obtained results discussed in Sect. 6.1.5. The radioisotope activities were used to calibrate the ion spectra presented in Ch. 5 within Sect. 6.1.6. Given the experimental results shown in this chapter, additional scalings and extrapolations are explored in Sect 6.2 for other parameters or operation regimes. Sect. 6.3 presents the final conclusions.

6.1 Experiments at the Centro de Láseres Pulsados

The experiments on radioisotope production consist in the irradiation of a sample target of a specific material with a beam of certain charged particles, coming from a laser-driven source in the case described here. The transmutation of the target occurs via nuclear reactions induced by these particles, and the amount of interactions can be measured at a later time through the radioactive decay of the activated nuclei. Within this chapter, the production of ^{11}C was studied by the irradiation of a boron target with laser-accelerated MeV-order protons. The boron nuclei can be in this way transmuted by means of the nuclear reaction ^{11}C(p,n)^{11}B. The achieved proton energies at the CLPU campaign, as seen in Ch. 5, are far higher than

the cross-section threshold of this reaction, at about 2 MeV. Moreover, a significant part of their energy spectra reaches the main peak of the excitation function. As a β^+ radioisotope, ^{11}C nuclei decay emitting a positron that, upon annihilating with a electron from the medium, produce two backscattered photons at 511 keV. The produced ^{11}C activity was characterised by the measurement of these γ-photons in coincidence. Through the experimental procedure presented here, the viability of laser-driven ion acceleration as an approach to radioisotope production was evaluated. In particular, the radioactive activity levels achievable in the context of the required doses for preclinical medical imaging.

6.1.1 Target and diagnosis system

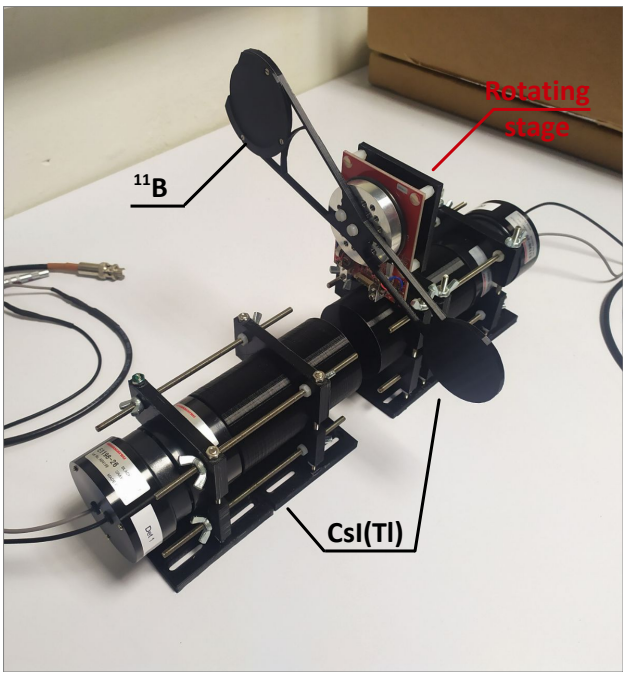

FIGURE 6.1: Detection device for radioisotope production.

The radioactive activity during the radioisotope production experiments performed within the CLPU campaign was measured via the detection device shown in Fig. 6.1, developed at the L2A2. This device, that comprises both the activation target and diagnosis systems, consists of a pair of radiation detectors situated in coincidence configuration, in order to correlate the backscattered photons from the positron annihilation. Each detector is composed of a CsI(Tl) cylindrical scintillator, attached to a Hamamatsu R6231 high-voltage photomultiplier (PMT)

with a Scionix silicon pad. CsI(Tl) inorganic crystals have a intermediate density (4.5 g/cm^3) and a relatively high effective atomic number ($Z_{eff} \approx 54$), that grant a high detection response to photons of energies between 0.05 and 8 MeV. Thus, they result in a suitable choice for the detection of the γ-rays produced in de radioactive decay of commonly-used PET radioisotopes. The scintillators have a diameter of 2" (50.8 mm) and 40 mm-length, and are covered by a plastic shell of 0.5 mm-thickness to reduce external light noise. The PMTs are energised by using a NHQ 225M high-voltage power supply. Both detectors are connected to separate channels of a CAEN N5668B spectroscopic amplifier, in order to shape and discriminate the retrieved signals from the radioactive decay of the samples. The output signals are digitalised by means of a CAEN DT5781 multi-channel analyser (MCA), and sent to a PC for their visualisation and analysis.

A rotating stage (ELL18K by Thorlabs) is mounted on a plastic structure on top of one of the detectors. The stage supports a paddle-like piece that holds a natural boron disc (99.9% purity) of 2"-diameter and 2 mm-thickness. This holder can rotate along 360°, thus placing the boron disc under the path of the ion beam, for nuclear activation during the laser irradiations, or between the two detectors, for the activity characterisation.

6.1.2 Calibration of the detector efficiencies

In order to precisely measure the radioactive activity level achieved, a previous calibration of the detection system is required. As state in Ch. 3, radiation detectors are characterised by their efficiency curves, in terms of the energy of the incoming photons. These efficiency curves were empirically determined and validated through numerical Montecarlo simulations. The former were performed by studying the response of the CsI(Tl) detectors to a collection of calibration radioactive sources with photopeaks within a range of several hundreds of keV, following the standard procedure described in Ch. 3. The measurements were carried out for several source-detector distances between 6.5 and 24.5 mm, in order to obtain the calibration curves for different geometries and increase the reliability of the intrinsic efficiency. Considering the radioactive source as a point source, the geometric factor at each distance was estimated from Eq 3.14, from which the intrinsic efficiency of the detectors was calculated using Eq. 3.13. The total photopeak efficiency was obtained from Eq. 3.12 and the measured count rate R_{ph}.

Regarding the Montecarlo simulations, the EnsarRoot code[117] was utilised. As in other Montecarlo simulation codes commonly employed for nuclear physics, the detector and the

source volumes are defined inside a simulation box, together with their composition. The source is then configured as an emitter of a certain particle with an specific distribution, both in energy and emission angle. In this way, a point source was defined as an isotropic emitter of γ-photons at the photopeak energy of each calibration source. In addition, the same source-detector configurations as in the experimental case were simulated. A certain number of events, i.e., emissions of a single particle from the source distribution, is defined for each simulation. On execution, an iterative procedure begins: for each simulation time step, the interaction of each particle with the medium material is simulated by means of random number generation. The probability, the type (total photoelectric absorption, Compton effect, etc), and the parameters (scattering angle, deposited, energy, etc) of each possible interaction are thus determined. In this case, the total photopeak efficiency can be directly calculated from the quotient of the photopeak counts divided by the total number of events simulated. From this values, the intrinsic factor was estimated considering the point source geometric factor and Eq. 3.12.

Fig. 6.2 depicts some examples of both the experimentally measured calibration spectra and the simulated spectra at each photopeak energy. The intrinsic efficiency curves obtained from the two methods are shown in Fig. 6.3. Although they are not completely compatible as the error bars do not match at some energies, the tendency and order of magnitude are rather similar. This slight inconsistency may partly come from superposition of the Compton border and the photopeak and from the point source assumptions in the experimental case, which define the geometric efficiency calculation. The calibration sources used have a certain lateral extension that leads to a decrease in the detection efficiency, specially for the high energy range. The intrinsic efficiency of each detector at 511 keV results in 0.349 and 0.348. This energy is relevant within the scope of this work, as corresponds to γ-photons produced by the electron-positron annihilation related to β^+ emitters.

Extensive sources

Being the Montecarlo simulations validated by the comparison to the experimental calibration, other cases using extensive sources were simulated. The geometric efficiency, whose analytical calculation becomes more complicated for other distributions of the source than the point case, was evaluated via Eq. 3.12 and the intrinsic efficiency curves obtained from the Montecarlo simulations in the previous section. Fig. 6.4 represents the geometric efficiency curves for four source distributions: a point source (black dots), an homogeneous square source of dimensions 2×2” (red squares), an homogeneous disc source of 2”-diameter (green diamonds), and a

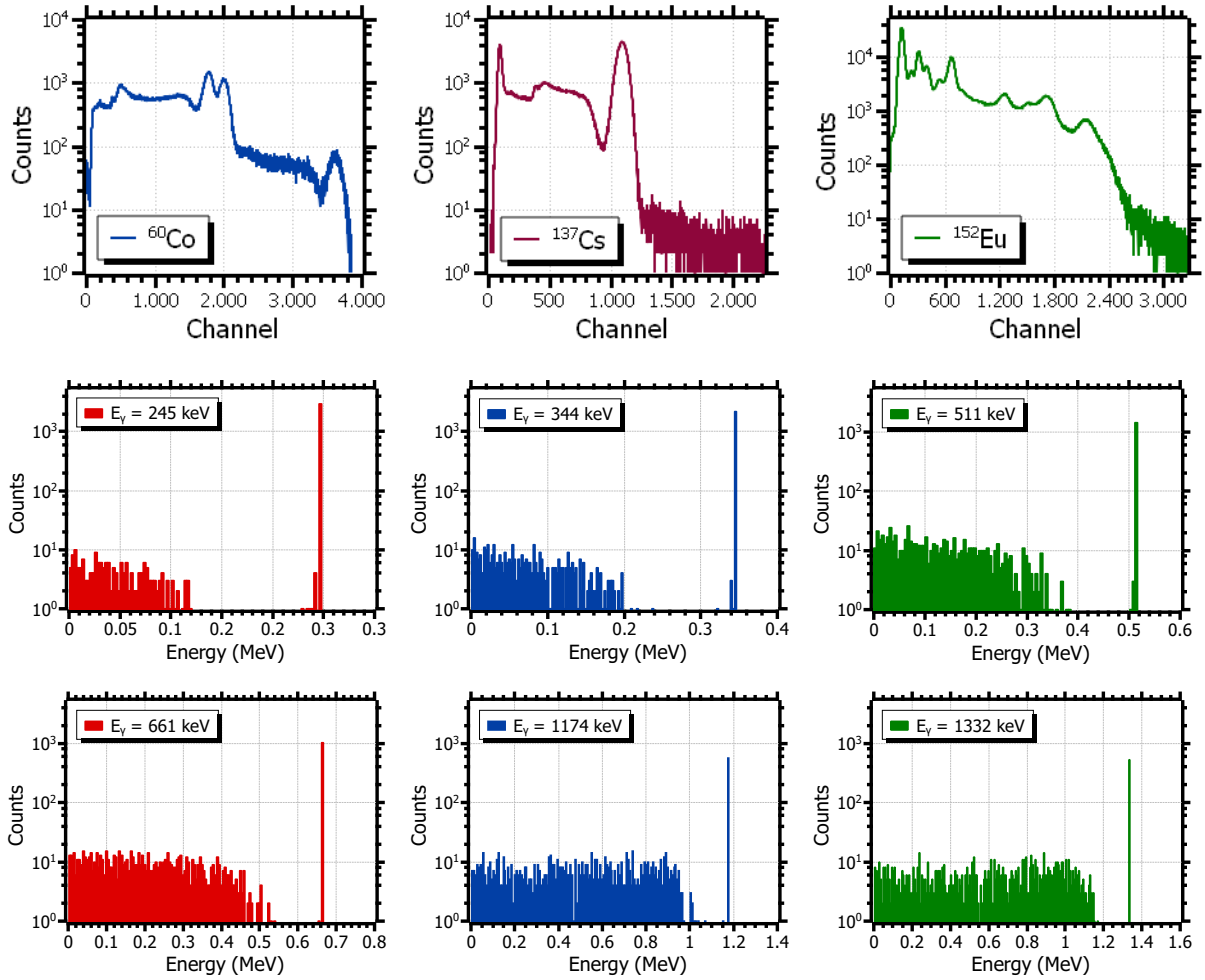

FIGURE 6.2: Examples of ^{60}Co, ^{137}Cs, and ^{152}Eu decay spectra.

circular source with the same diameter (blue triangles) having a Gaussian-like emission distribution (see section below for a detailed explanation). All distributions are isotropic and, except for the point source, two-dimensional and parallel to the front surface of the detectors. The Gaussian-like source was defined using the ASCII generator function of EnsarRoot and providing an ASCII file containing the emission probability distribution calculated in Sect. 6.1.3.

The results shown in Fig. 6.4 exhibit the expected dependency of the geometric efficiency on the source-detector distance. The highest efficiency is obtained for the point source, whichever distance. For extensive emission distributions, the events generated far from the centre have a

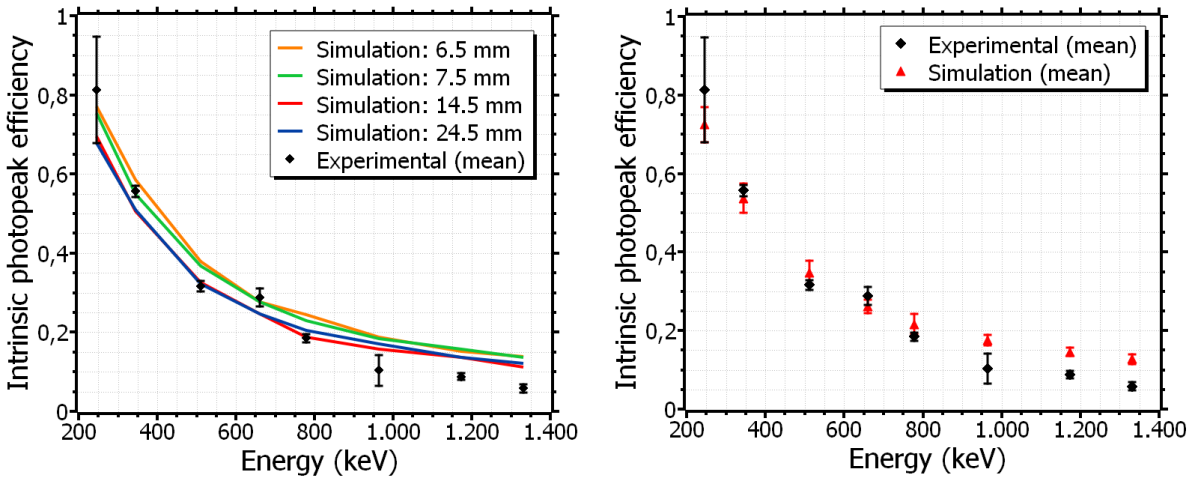

FIGURE 6.3: Comparison of intrinsic efficiencies.

greater probability of escaping without reaching a certain detector, so the efficiency is expected to be lower as in the figure. To this respect, the source with the Gaussian emission distribution, peaking at the centre of its volume, is more similar to the point source than the other cases. Hence, the resulting geometric efficiency is higher than for the homogeneous extensive sources. As the source-detector distance increases the discrepancy in the efficiency between distributions becomes smaller, due to the fact that the source is more comparable to the point case. For short distances the extension and distribution of the source come to be more relevant.

6.1.3 Target activity distribution

The spatial activity distribution of the activation target after the irradiation can be depicted as a non-homogeneous profile. As explained in Sect. 2.3.2, laser-accelerated ion beams exhibit a Gaussian divergence profile whose width follows a linear or a parabolic dependence on the particle energy (Eqs. 2.31 and 2.32). Hence, a Gaussian-like activation profile is expected to be induced in the production target as well.

To verify this assumption, the activity distribution of the irradiated target was estimated by using a MATLAB code. Through this calculation, a proton —or other ion species— beam impinges on a production target located at a fixed distance from the ion source. For each energy bin of the ion beam, a Gaussian angular distribution as the one indicated in Eq. 2.30 with a

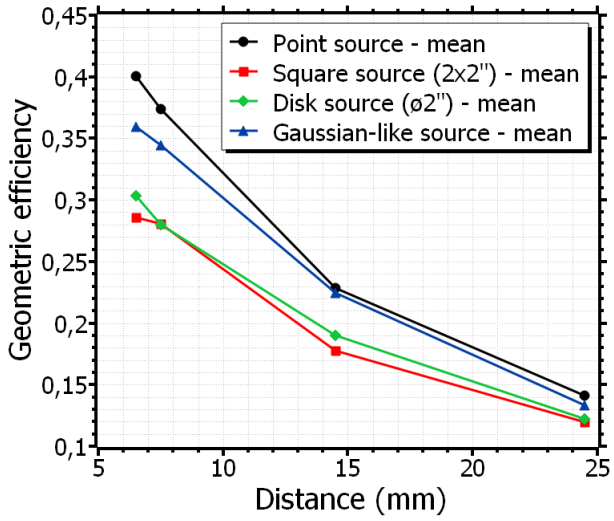

FIGURE 6.4: Simualted intrinsic efficiency for different source sizes.

dispersion given by Eqs. 2.31 or 2.2.32, was defined and normalised to the particle number of that bin. The parameters of both the energy spectra and the beam angular divergence were inserted as inputs to the MATLAB code.

On start-up, an iterative calculation was performed: for the defined iteration depth step, the number of induced nuclear reactions and the ion energy loss were calculated for each angular and energy bin. The reaction cross-section and the stopping power data for this calculation were taken from the EXFOR databaseand the SRIM software, respectively. Particles with energies below the energy threshold of the reaction were removed from the calculation for subsequent iterations. Typically, the thickness of the activation target is larger than the average range of the incoming particles, thus all incidental particles are completely stopped —i.e., removed— inside the target.

For arbitrary input parameters, the final ^{11}C activity distribution of a 2”-diameter, 2 mm-thickness ^{11}B disc at 6 mm of the ion source, produced via reaction ^{11}C(p,n)^{11}B upon the irradiation with a proton beam, is depicted in Fig. 6.5. The resulting activity profile corresponds to the expected two-dimensional Gaussian distribution peaking at the centre of the target disc. The total integrated activity is normalised to unity for its representation. In this example, the solid angle subtended by the disc is smaller than the angular broadness of the proton beam. Hence, the entire area of the boron target becomes activated. No appreciable difference was observed

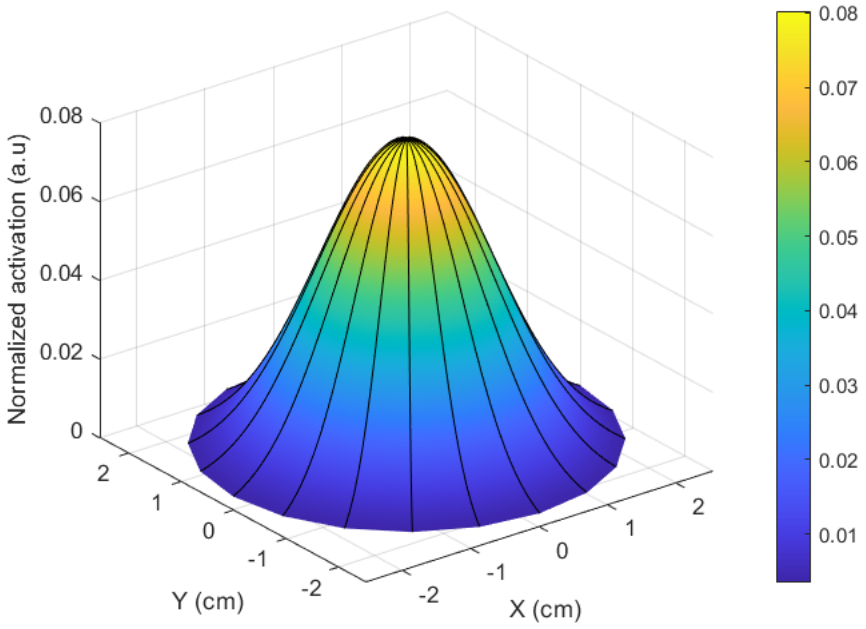

FIGURE 6.5: Estimated activity distribution at the production target after irradiation.

for the either use of a linear or a parabolic dispersion of the Gaussian angular profile of the ion beam.

6.1.4 Experimental set-up

Following the scheme presented in Ch. 5 (Sect. 5.2.1) of the experimental set-up at the CLPU campaign, Fig. 6.6 depicts the experimental arrangement at the interaction chamber including the activation system. The two CsI(Tl) detectors were located facing each other in coincidence configuration at a certain distance of the acceleration target assembly, due to limitations in space close to the TCC. The rotating stage holding the paddle with the boron disc target was then mounted on a optical post on top of a long linear motorised stage.

This arrangement had two predefined positions for the boron disc: one of them right behind the acceleration targets, at 2 cm of the TCC (Fig. 6.7), and the other one between the two CsI(Tl) detectors, at 1.2 cm of each of them. After each irradiation series, the rotating stage resulted being totally frozen by the EM pulses coming from the laser-plasma interaction. The positioning

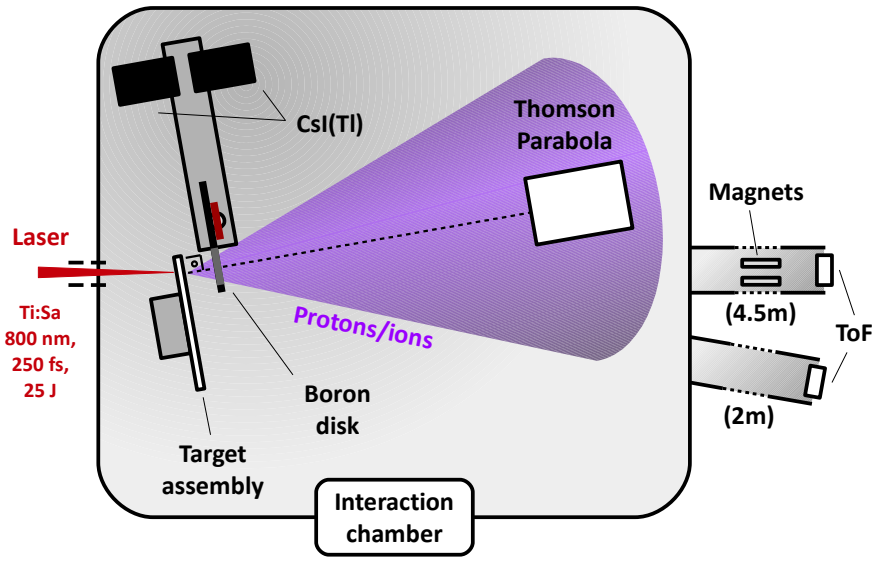

FIGURE 6.6: Chamber scheme.

of the boron target between the CsI(Tl) detectors was performed by the lab technician instead, according to the radioprotection safety protocols, once the chamber was vented about 10 - 20 minutes after the end of the irradiation.

In order to increase the detection efficiency for the activity measurements, an aluminium plate of 2 mm-thickness was placed at the front face of each CsI(Tl) detector as a moderator. A certain amount of the positrons emitted at the ^{11}C decay escaping from the activation target could then reach one of the plates and be annihilated there into the two 511 keV gamma photons. Positrons emitted at the ^{11}C decay have an average energy of 385.7 keV and a maximum energy of 960.4 keV. Inside a material, these positrons are slowed down, according to their stopping power, by experiencing elastic or inelastic scattering or radiation emission processes. The probability of being annihilated dramatically increases when their energy is reduced below 100 keV. The projected range of $\sim$1 MeV electrons or positrons inside aluminium is about 1.9 mm, as tabulated in the NIST database. Thus, the chosen thickness for the moderator plates was sufficient to slow incoming positrons down to the annihilation cross-section peak energy.

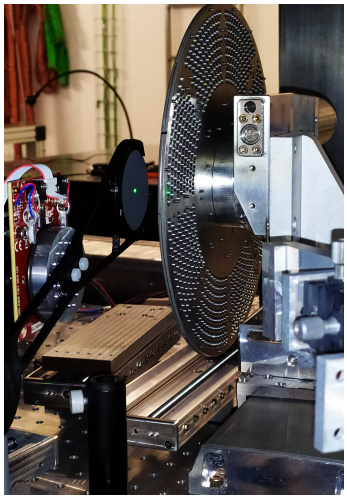

FIGURE 6.7: Set-up for the irradiation of the boron disc.

TABLE 6.1: Experimental parameters and ^{11}C production results for each irradiation series.

Laser energy (J)	**Rep. rate (Hz)**	**Number of shots (#)**	**Prod. per shot (10^6 nuclei)**	**Activity per shot (kBq)**	**Total activity (kBq)**
12	0.2	40	3.2	1.8	68.6
20	0.1	10	5.7	3.2	31.5
25	0.1	20	21.7	12.4	233.8

6.1.5 Production of ^{11}C

The production of ^{11}C through the proton-induced ^{11}C(p,n)^{11}B reaction by the irradiation of the boron target was successfully achieved within this campaign. The activation measurements consisted of three multi-shot series performed at different laser energies, 12, 20, and 25 J. Each series took place on a different day so the presence of ^{11}C was completely dissipated from the boron disc before the next irradiation. Hence, the day-to-day variability of the laser system, and therefore of the ion beam maximum energies, had an influence on the measurements, leading to similar activation results for presumably different experimental conditions. Table 6.1 summarises the experimental parameters of each irradiation series.

After placing the activated boron disc between the two CsI(Tl) detectors at the end of each

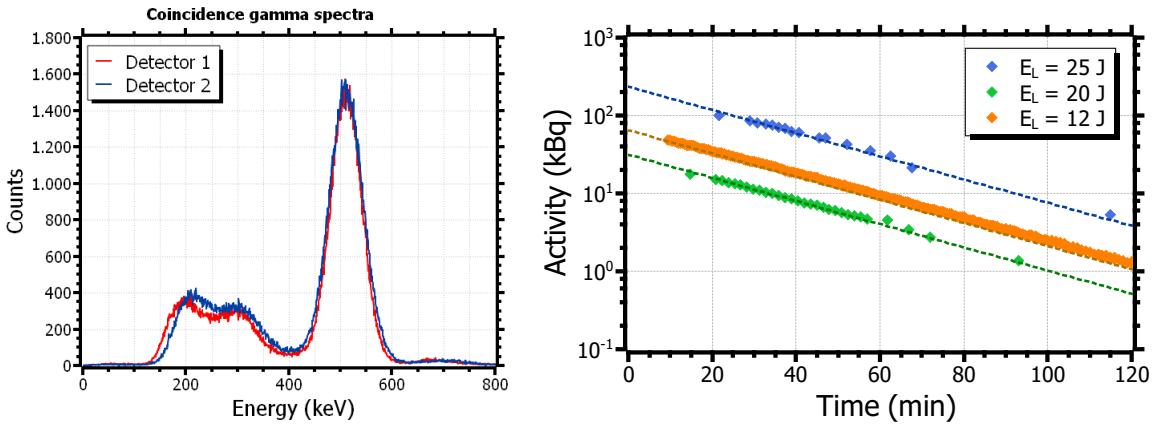

FIGURE 6.8: ^{11}C coincidence spectrum at each detector.

irradiation, the activity of the sample was measured within time intervals ranging from 1 to 5 minutes over two or three ^{11}C half-life periods (20.23 min). The decay energy spectra obtained for the two detectors at one of these measurements is shown in the left panel in Fig. 6.8. The 511 keV line from the annihilation of the β^+-disintegration positrons can be observed in both signals. As the measurements were performed in coincidence configuration, the total number of counts of each measured spectra corresponds to the real number of distinct decay events detected. The instantaneous radioactive activity at a certain time was then obtained via expression

$$A = R^c_{ph}/\varepsilon^c_t = \frac{\Delta N_{ph}}{\Delta t}(\varepsilon^c_g \cdot \varepsilon^{ph\,2}_i)^{-1} \tag{6.1}$$

where ΔN_{ph} is the number of detected events within the measurement time interval Δt, and ε^c_t is the total photopeak efficiency of the detector at 511 keV for coincidence configuration, which is calculated from the geometric ε^c_g and the intrinsic photopeak ε^{ph}_i efficiencies. This equation comes from Eq. 3.12, taking in consideration that the intensity and the branching ratio of the decay mode are $I_\gamma = BR = 1$ and additional considerations regarding the detection efficiency. In the particular experimental detection configuration, the evaluation of the total geometric efficiency ε_g must be carefully calculated as it involve multiple successive processes.

The complete detection picture is represented in Fig. 6.9. The generation and the detection of the 511 keV γ-photons from the annihilation can be separated into two main channels. Through

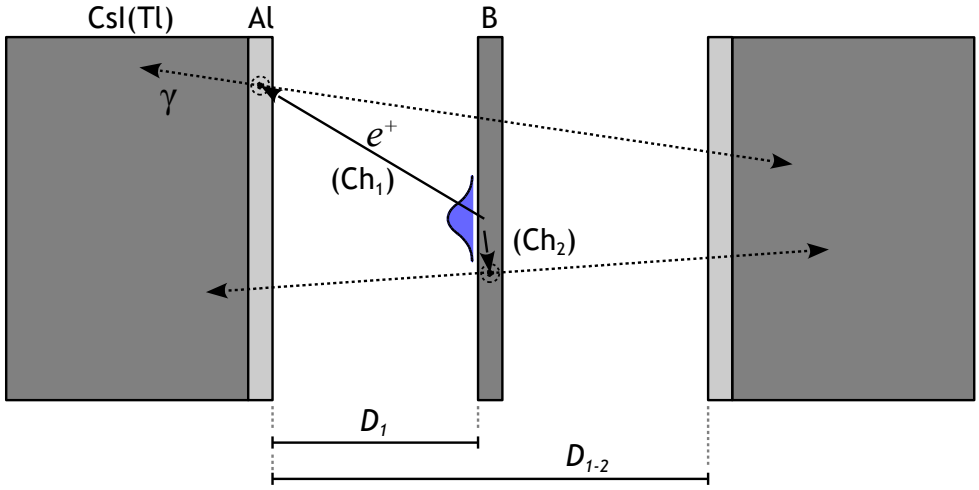

FIGURE 6.9: Scheme of the experimental coincidence configuration.

the first one, a certain fraction of the β^+ positrons from the ^{11}C will escape from the boron target without annihilating. Some of the escaping positrons will reach the aluminium moderator in front of the detector and will be disintegrated there. Then, for the coincidence detection of the two backscattered γ-photons, each of them must be emitted from the aluminium plate in the direction of each detector. The geometric efficiency associated to this detection channel can be estimated as

$$\varepsilon_g^{ch1} = [\varepsilon_{g,1} \cdot \varepsilon_{g,2}]^{ch1} = P_{esc}^{B} \cdot \varepsilon_g^{gauss}(D_1) \cdot P_{annih}^{Al} \cdot \varepsilon_{g,1}^{sq}(0) \cdot \varepsilon_{g,2}^{sq*}(D_{1-2}) \tag{6.2}$$

In this expression, P_{esc}^{B} is the fraction of positrons escaping from the boron target and P_{annih}^{Al} is the probability of annihilating inside the aluminium moderator. The geometric efficiency ε_g^{gauss} corresponds to a radioactive source with a Gaussian distribution, as estimated in Sect. 6.1.3, located at a certain distance, and determines the fraction of escaping positron that reaches the aluminium plate. The product $\varepsilon_{g,1}^{sq} \cdot \varepsilon_{g,2}^{sq*}$ denotes the probability that a pair of γ-photons emitted from a homogeneous squared source is detected in coincidence by two detectors at given distances. The asterisk notation indicates that both probabilities are conditioned, as the emission direction of the two photons is correlated. Following the scheme in Fig. 6.9, D_1 is the distance between the boron target and the aluminium plate, and D_{1-2} is the distance between detectors.

For the second detection channel, the positron is instead annihilated within the boron target, and the and each photon is symmetrically emitted towards detector. In this case, the geometric efficiency can be obtained from

$$\varepsilon_g^{ch2} = [\varepsilon_{g,1} \cdot \varepsilon_{g,2}]^{ch2} = (1 - P_{esc}^B) \cdot \varepsilon_{g,1}^{gauss}(D_1) \cdot \varepsilon_{g,2}^{gauss*}(D_1) \tag{6.3}$$

where the product $\varepsilon_{g,1}^{gauss} \cdot \varepsilon_{g,2}^{gauss*}$ represents the probability that the two photons, emitted from a gaussian-like distribution between the detectors, reaches each of them in coincidence. Thus, the total geometric factor indicated in Eq. 6.1 is the sum of the geometric efficiency of the two described channels, i.e.,

$$\varepsilon_g^c = \varepsilon_g^{ch1} + \varepsilon_g^{ch2} \tag{6.4}$$

Now, for the estimation of the fraction of positrons that escape from the boron target, P_{esc}^B, a simple MATLAB code was developed. Through this code, the production of ^{11}C inside boron via ^{11}B(p,n)^{11}C induced by a Maxwellian incidental proton beam was calculated as a function of the depth within the target. Fig. 6.10 depicts the normalised number of nuclei produced at each spatial step (red curve) and the accumulated production (blue curve) considering the spectral parameters of the experimental series with the highest cut-off energy in Table 6.1 (20 J). The resulting curves show that more than half the final number of transmutations is produced within the first 100 μm of target, and by 200 μm in depth almost the 80% has been produced. Given that the boron target is 2 mm-thick, it can be assumed that all the ^{11}C nuclei are concentrated in the frontal surface of the target. Therefore, from a geometrical perspective, half the disintegration positrons are emitted outwards the boron target, leading to the first detection channel, and the other half is emitted inwards the target. From the tabulated data in the NIST database, the projected range of $\sim$1 MeV positrons in natural boron is between 1.8 and 2.1 mm. Hence, mostly all the positrons emitted towards the target are annihilated, leading to the second detection channel. The fraction of positrons following each channel was then set to $P_{esc}^B = (1 - P_{esc}^B) \approx 0.5$.

Regarding the first channel, the geometric factor $\varepsilon_{g,1}^{gauss}(D_1)$ was obtained from a efficiency curve similar to the one depicted in Fig. 6.4 for a Gaussian distribution (blue triangles) at $D_1 = 10$ mm. This curve was estimated from Montecarlo simulations considering an activity

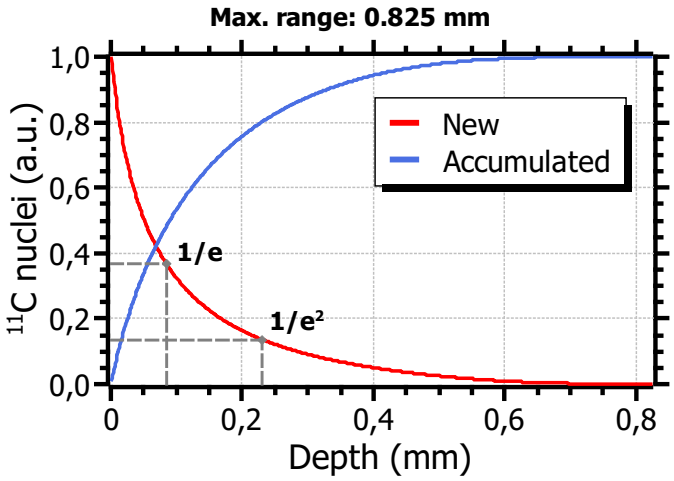

FIGURE 6.10: Number of interactions of a maxwellian proton beam in boron via reaction ^{11}B(p,n)^{11}C as a function of the depth within the target.

distribution calculated from the geometric parameters at the CLPU experiments. The geometric efficiency of a squared homogeneous source in terms of the distance was equally obtained from the red curve in Fig. 6.4 for the rest of the geometric factors in Eq. 6.2. The probability of a detection in the farthest detector (number 2) conditioned to a detection in the nearest detector (number 1) can be expressed as $P(d_2|d_1) = P(d_2 \cap d_1)/P(d_1)$, where $\cap$ denotes the intersection of both events. While $P(d_2 \cap d_1)$ is in principle not known, it can be approximated to $P(d_2)$. This is equivalent to assume that the detection in coincidence is similar to the most restrictive condition: that the photon is emitted within the solid angle of the farthest detector. From this assumption, one can obtain that $\varepsilon_{g,1}^{sq} \cdot \varepsilon_{g,2}^{sq*} = \varepsilon_{g,1}^{sq} \cdot \varepsilon_{g,2}^{sq}/\varepsilon_{g,1}^{sq} = 2 \cdot \varepsilon_{g}^{sq}(D_{1-2})$. The factor two is introduced to account for the backscattered emission of the two photons, that subtends twice the solid angle.

In the second channel case, due to the symmetry of the configuration, it can be directly seen that $P(d_1|d_2) = P(d_1|d_1) = 1$. Hence, $\varepsilon_{g,1}^{gauss} \cdot \varepsilon_{g,2}^{gauss*} = 2 \cdot \varepsilon_{g}^{gauss}$. Considering Eqs. 6.2 – 6.4 and the intrinsic efficiency at 511 keV from Fig. 6.3, the obtained total photopeak efficiency in coincidence configuration was ε_t^c = 0.038.

For each laser energy, the activity curve after the irradiation was obtained by fitting the measured data to Eq. 2.37, as depicted in the right panel in Fig. 6.8. A half-life of 20.23 min was obtained from the fit, thus demonstrating, along with the 511 keV-photopeak energy

of the decay spectra, the production of ^{11}C. The peak activity A_0, achieved immediately after the last shot of each irradiation series —i.e., at $t = 0$—, could be directly obtained from this expression. A simple MATLAB code was developed on the basis of Eq. 2.39, that accounts for the evolution of a radioactive sample considering its production rate and radioactive decay. Thus, from the peak activity, the laser pulse frequency and the number of shots of the series, this code was used to calculate the activity per shot, and therefore the production of ^{11}C nuclei per shot (assuming $\lambda_{^{11}C} = 5.7 \cdot 10^{-4}$ s^{-1}). Both the peak activity and the activity per shot of each series are shown in Table 6.1. The highest activity achieved during the entire experimental campaign was 263 kBq, obtained after 20 shots at 0.1 Hz-repetition rate for an energy per pulse of 25 J, corresponding to an activity per shot of 13.9 kBq. Regarding the other activation series at lower pulse energies, peak activities of between 30 and 80 kBq were measured, for activities per shot in the order of 3 kBq.

6.1.6 Absolute normalisation of the laser-accelerated proton spectra

The ^{11}C production results were used for the absolute calibration of the proton spectra measured within the experimental campaign and presented in Sect. 5.2.3. Through this calibration, the number of particles —presumably protons, as no other species could induce ^{11}C production— of each ion pulse could be estimated. Due to the day-to-day variability of the laser pulse parameters, the results from the calibration described in this section are only applicable to the day at which they were measured and cannot be extrapolated. However, they may serve as a order of magnitude evaluation.

This calibration is based on the principle that the amount of ^{11}C nuclei is directly related to the flux of the incidental ion beam, in turn characterised by the parameter N_0 in the spectral distribution given by Eq. 2.26. A higher number of particles per ion pulse would lead to a higher number of nuclear interactions at the activation target and therefore, both the total and per pulse induced radioactive activities would be increased. The MATLAB code described in Sect. 6.1.3 for the calculation of the activity distribution of an irradiated target was executed for the experimental parameters at each irradiation, using an arbitrary number of particles between 10^8 and 10^{10} MeV^{-1}. The resulting integrated activity was then compared to the experimental measurement, and the proton flux was normalised according to the obtained scaling factor, for each laser energy, via

$$N_0\ (\#\text{parts}) = \frac{A_{exp}}{A_{sim}} \cdot N_0\ (\text{a.u.}) \tag{6.5}$$

In this expression, N_0 denotes the number of protons as in Eq. 2.26, and A_{exp} and A_{sim} are the activities obtained experimentally and from the calculation, respectively.

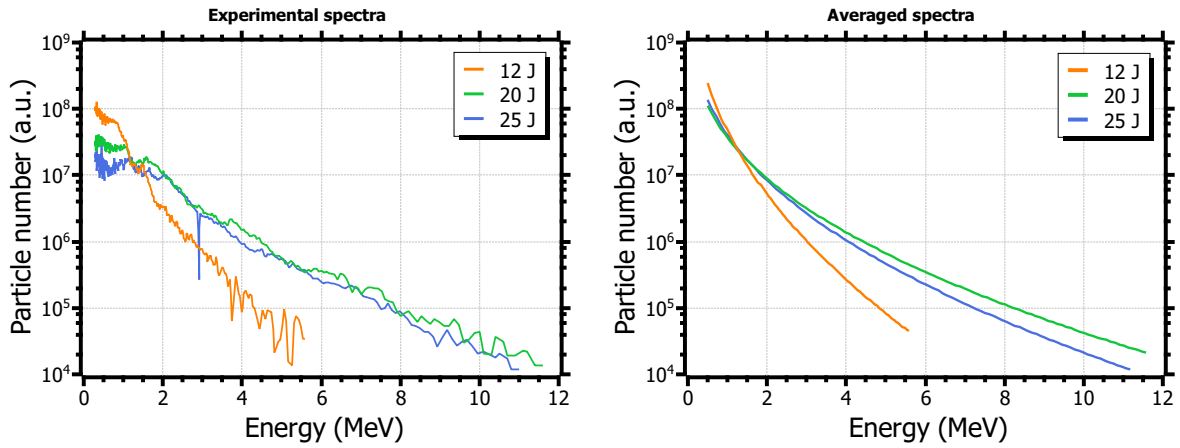

FIGURE 6.11: Spectra utilised for the absolute normalisation of the proton beam flux. Experimental spectra from the TP (left), and averaged from all the available spectra at the nominal laser energy (right) on each day.

The experimental proton spectra were retrieved from the TP traces (Sect. 5.2.2) measured on the day corresponding to each activation series. The analysed data was taken from the available single-shot series of the same laser energy as for the activation, given that no multi-shot series were performed without catcher during each of these days. Following Eqs. 5.1 and 5.1, the solid angle factor covered by the boron disc can be approximated to Ω_{tot} as its size is larger than the beam spread at its location (2 cm from the TCC). All the single-shot spectra at each laser energy were analysed in this way, and then the spectral and angular parameters were averaged to obtain a single value for each case. The left panel in Fig 6.11 depicts an example of one of these TP spectra for each of the laser energies. The corresponding averaged spectra, defined by the N_0, T_e, and E_{max} parameters according to a Maxwell-Boltzmann distribution (Eq. 2.26), are shown in the right panel in the same figure.

The calculation using the aforementioned MATLAB code was executed for the following input parameters: the average cut-off energy, known from the spectra; the average temperature, obtained from the fit; an arbitrary particle number $N_0 = 10^{10}$; and an assumed beam divergence

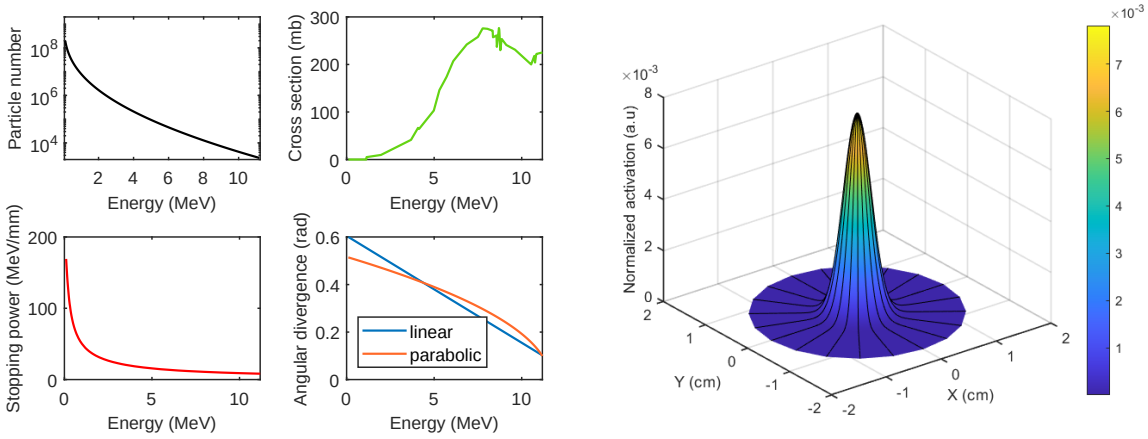

FIGURE 6.12: Input parameters for the activity calculation and activity distribution on the boron target.

TABLE 6.2: Proton spectral calibration (base spectrum) for N_0 (a.u.) = $1{\cdot}10^{10}$.

$\mathbf{E}_L$ (J)	$\mathbf{E}_{max}$ (MeV)	$\mathbf{K}_B\mathbf{T}_e$ (MeV)	$\mathbf{A}_{sim}$/shot (kBq)	$\mathbf{A}_{exp}$/shot (kBq)	$\mathbf{N}_0$ (# parts.)
12	5.6 ± 0.4	0.10 ± 0.02	0.17	1.8	$1.1{\cdot}10^{11}$
20	11.6 ± 0.6	0.30 ± 0.06	4.5	3.2	$7.1{\cdot}10^{9}$
25	11.2 ± 0.8	0.23 ± 0.04	1.74	12.4	$7.1{\cdot}10^{10}$

according to Eq. 2.31 and experimental data. The average range of 18 MeV protons inside solid natural boron is 1.8 mm, which is below the thickness of the boron disc target. Thus, all protons are expected to either be completely stopped or induce the nuclear production reaction inside the activation target. The left panel in Fig. 6.12 depicts these input parameters (**(a)** the energy spectra at different laser energies, **(b)** the production cross-section, **(c)** the stopping power of protons inside boron, and **(d)** the beam angular divergence profile), while the right panel in the same figure shows the activity distribution at the boron disc for the case at 20 J. Table 6.2 summarises the results of this calibration for each laser energy.

The obtained proton fluxes do not show any consistent scaling with the laser pulses energy, as each measurement was performed at a different day. Furthermore, the flux for the case at 12 J is almost an order of magnitude greater than for the cases at 20 and 25 J. As the cut-off energy of the proton beam at 12 J is below the cross-section main peak (∼8 MeV), the

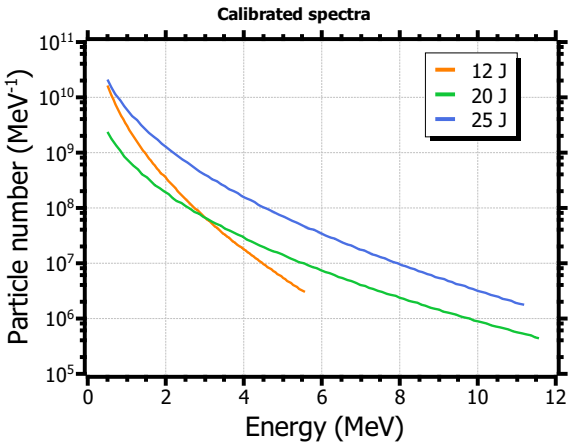

FIGURE 6.13: Resulting calibrated spectra after the normalisation from the experimental activity measurements.

calibration calculation gives an overestimated proton flux in order to compensate this and result in a similar activity per pulse. Fig. 6.13 depicts the obtained spectra at each laser energy after the calibration. The data obtained from this analysis is included in panel **(d)** in Fig. 5.28 in Ch. 5.

6.2 Estimations and extrapolations

The results obtained at the experimental campaign at the CLPU can be extrapolated to longer operation times. The left panel in Fig. 6.14 depicts the activity over time estimated using Eq. 2.39, considering the production per shot from the three multi-shot activation series performed (Table 6.1). Saturation —secular equilibrium— occurs at about one hour after the first shot for laser pulse energies (and corresponding repetition rates) of 12 and 20 J, and about two hours for the case at 25 J. The maximum achievable activity in secular equilibrium is equal to the production rate R as

$$A_{max} = R = P \cdot f_N \tag{6.6}$$

where f_N denotes the laser operation rate and P refers to the amount of ^{11}C nuclei per shot produced. This results in around 0.6 MBq for 12 and 20 J, and about 2 MBq of ^{11}C for 25 J. For

the later, a peak ^{11}C activity of ∼0.95 MBq would be induced after completing an entire sector from the target wheel, i.e., 101 shots (about 15 minutes of operation at 0.1 Hz).

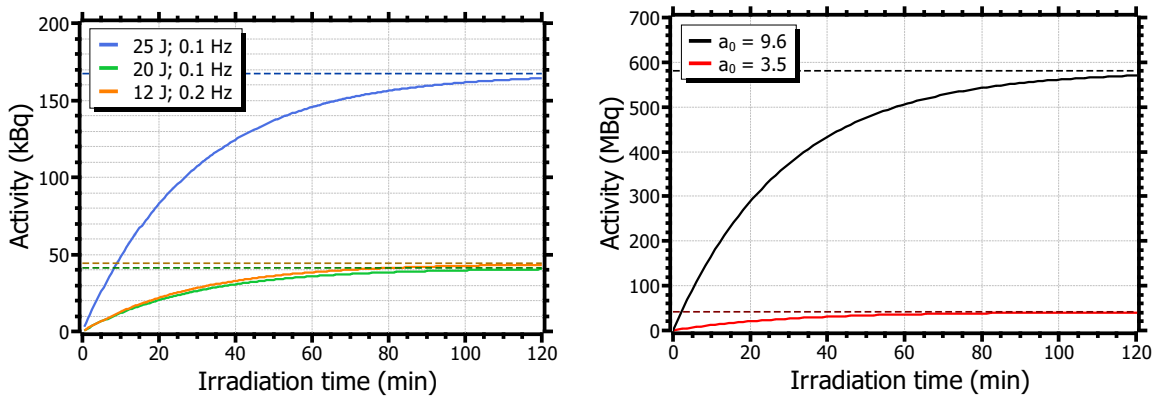

FIGURE 6.14: Estimation of the evolution of the produced ^{11}C activity for the experimental case at the CLPU (left) and at the L2A2 (right).

The production that could be achieved at the L2A2 facility can be estimated from the scaling laws obtained in Sect. 5.28 in Ch. 5. For optimised experimental parameters, the maximum achievable intensity at the STELA system is $a_0 = 9.6$. That correspond, according to the scalings shown in the figure, to a cut-off energy of around 10 MeV and a temperature of 0.7 MeV, assuming a target foil of $1 - 6$ μm-thickness. Regarding the spectral amplitude, the scaling predicts a value of $6{\cdot}10^{13}$ MeV^{-1}srad^{-1}. The left panel in Fig. 6.14 represents the activity curve considering these parameters and a repetition rate of 10 Hz (black curve). As shown, within 15 min of operation an activity level of 234 MBq would be roughly obtained. The secular equilibrium regime would be reached in two hours but for a higher maximum activity, as the production rate is a factor of 100 higher than for the case at the CLPU. The estimated number of ^{11}C nuclei per shot is $5.8{\cdot}10^{7}$, which corresponds to an activity per shot of 33.3 kBq.

Following the final discussion in Ch. 5, the estimations on radioisotope production using long (∼250 fs) and short (<60 fs) pulse durations can be compared. Thus, considering the same scalings from 5.28 as in previous paragraph but for a comparable intensity $a_0 = 3.5$, the spectral parameters are $E_{max} = 1.8$ MeV, $T_e = 0.04$ MeV, and $N_0 = 4{\cdot}10^{12}$ MeV^{-1}srad^{-1}. The resulting activity evolution is depicted in the left panel in Fig. 6.14 (red curve). An activity per shot of 2.3 kBq could be produced, that is, about $4.1{\cdot}10^{6}$ nuclei of ^{11} per shot. These numbers can be compared with the measured activities at the CLPU campaign, shown in Table 6.1. Regarding

the closest case (25 J and a_0 = 3.9), the activity per shot obtained at the CLPU experiment is a factor of six higher than the estimation for the L2A2. It can be concluded that, as the conversion efficiency to proton energies is higher for longer pules, such laser systems are able to produce higher radioactive doses per shot and are in principle more appropriate. However, for high-repetition rate systems, this difference can be overcompensated leading to a higher production rate and thus a higher secular limit within the production. In addition, these dose levels would be achieved in shorter times. For a irradiation of 15 minutes, the estimated activity for the L2A2 is 16 MBq under these conditions, while for the CLPU the estimation gives about 0.95 MBq.

This analysis can be compared with recent publications as well, regarding high repetition-rate table-top lasers. For similar experimental conditions as at the L2A2, Tayyab *et al.*[47] measured ^{11}C activities of 5.2 kBq/shot using the same ^{11}B(p,n)^{11}C reaction, which correspond to ∼45 MBq after 20 min of irradiation at 10 Hz. This is a factor of 6 lower than the optimum estimation at the L2A2. A major source of uncertainty in the calculations presented in this section is the proper determination of the spectral amplitude N_0 through the scalings. As the estimated production escalates linearly with this parameter, an overestimation within its calculation may lead to an activity equally overestimated. On the other hand, similar variations in the temperature may lead to significant fluctuation of the resulting production, as depicted in Fig. 2.4. The same result is observed regarding the estimation of Fritzler *et al.* in [48], of 13.4 MBq of ^{11}C after 30 min of irradiation of thin 6 μm-thickness Al foils with a 10 Hz high-repetition rate laser (∼1 J, 40 fs) via the ^{11}B(p,n)^{11}C reaction. This would roughly correspond to about 7.5 MBq after 15 min. This result is in good agreement with the measurement by Tayyab, given that the acceleration target is much thinner for the later. With respect to this activity level, the estimation for the L2A2 seems to be again overestimated.

6.3 Conclusions

The production of ^{11}C was successfully achieved and demonstrated during the experimental campaign at the CLPU facility. A peak radioactive activity of 234 kBq was reached within the whole campaign, for a series of 20 shots at 0.1 Hz and 25 J-pulse energy. The maximum activity per shot was almost 12.5 kBq, for the same series. Increasing the irradiation time up to the completion of the entire target wheel —808 shots, which at 0.1 Hz would be more than 2 hours— would lead to 2.2 MBq, almost in the range of PET preclinical imaging. Achieving

operation at 1 Hz, even for lower pulse energies, could increase the obtained dose up to this range.

Based on the scalings of the main spectral parameters characterising laser-driven proton beams performed in Ch. 5, some estimations on radioisotope production were performed. Regarding the optimised experimental case at the L2A2, the calculated activity of ^{11}C after 15 minutes of irradiation at 10 Hz is of the order of 230 MBq, far higher than the expected dose level. The comparison between these estimations and data from recent literature indicate that these estimations are overestimated. The principal sources of uncertainty come from the distribution amplitude and temperature given by the scalings. While the cut-off energy is a recurrent subject of analysis in studies on this topic, the temperature is rarely investigated. The results presented in this work show that this parameter can be more relevant than the maximum energy of the accelerated particles. A variation of a 30% in the temperature leads to a variation of the expected activity about a factor of 6.

The effect of the pulse duration on the achievable dose level of ^{11}C was also studied. The estimations show that long pulses ($\sim$250 fs) are preferred in terms of the production per shot, due to the higher conversion efficiency to proton energies. However, short pulses at high-repetition rates constitute a more effective approach to increase the long-term maximum attainable activity.

Chapter 7

Summary and conclusion

7.1 Conclusions

This doctoral thesis has investigated the potential of laser-driven proton sources as an efficient means to radioisotope production, and presented some experimental results on this topic. In particular, the production of ^{11}C from the proton-induced nuclear reaction ^{11}B(p,n)^{11}C was studied and measured. The experimental results have shown promising ^{11}C activity levels, highlighting the viability of the approach of this thesis. Through a combination of experimental design, simulations, and analysis of the obtained results, the evaluation of the feasibility and effectiveness of utilizing laser-driven proton sources has been performed.

The first step was the development of a multi-shot target assembly capable of operating at high repetition rates over long irradiation times. This assembly consist of a multi-target wheel-like holder hosting the acceleration targets, mounted on a set of three high-precision moving stages. Some of the key features of this system are its flexibility to use targets of different materials and thicknesses, and the its high accuracy and shot-to-shot stability. In addition, the target assembly was adapted to various experiments in facilities with laser systems of different parameters and regimes, where it show a great performance. Together with this design, a correction and positioning procedure was developed and implemented through a control software. This procedure, based on the mapping of the target surface prior to the irradiation, allows for the positioning of the targets at the focus of the laser with micron accuracy at repetition rates up to 10 Hz. Its accurate performance at such operation rate suppose a novel achievement regarding recently published data on this topic[98, 99, 105].

The target assembly described above was firstly utilised at the commissioning campaign of the Laser Laboratory for Acceleration and Applications (L2A2), at the Universidade de Santiago de Compostela, for the development of a ion source. Proton beams of cut-off energies up to 2 MeV were successfully measured at multi-shot series of up to 808 shots at high repetition rates. These results show great stability both in maximum energy (below 15%) and spectral temperature ($\sim$30%), thus validating the performance of the target assembly and the positioning procedure.

The target system was then adapted and used at an experimental campaign at the Centro de Láseres Pulsados. As highlights, several multi-shot series of more than 101 shots at 25 J-pulse energy and 0.1 Hz-repetition rate were achieved. Other series using laser pulses of 12 and 20 J at 1 and 0.2 Hz, respectively, were performed. Again, the obtained results exhibited great shot-to-shot stability in terms of the cut-off energy and the temperature. One of the objectives of this campaign was the production of radioisotopes from laser-accelerated ion beams. In particular, the production of ^{11}C was investigated, of special interest in PET imaging techniques. The activation measurements were carried out by irradiating a boron target with laser-accelerated proton beams at three different laser energies: 12, 20, and 25 J. The maximum ^{11}C activity attained within the entire campaign was 234 kBq, from a single series of 20 shots at 25 J and 0.1 Hz. This corresponds to an activity per shot of 12.4 kBq, that is, about $22{\cdot}10^6$ ^{11}C-nuclei per shot.

The experimental situations at the L2A2 and the CLPU were reproduced via Particle-In-Cell simulations using the Smilei code, regarding laser-driven proton acceleration. These simulations were used to support the experimental data in a qualitative means, and to evaluate the dependence of the spectral properties of laser-accelerated proton beams on some experimental parameters. The analysed parameters are the pulse energy and the target thickness, in good agreement with the dependence reported in literature. By comparing the experimental results obtained within this thesis with recently published data, the scaling of the main spectral parameters with the intensity of the laser pulses were inferred. Different scaling laws were found for long pulse durations ($\sim$250 fs) and ultra-short pulses ($\leq$ 60 fs) regarding the cut-off energy and the temperature. This circumstance was attributed to a higher conversion efficiency to proton energies for pulses with longer durations.

The results from these scaling laws were used to estimate and escalate the production of ^{11}C

at the L2A2 and the CLPU. The results from these estimations can be considered as overestimated, as seems to indicate the comparison with recent publications. For the experimental situation at the L2A2, the estimation gives a peak activity of 230 MBq after 15 minutes of irradiation at 10 Hz, which is a factor of 6 higher than the value obtained in [47] for a similar laser system. Concerning the comparison between long and short pulse durations, their effects were evaluated in terms of the attainable activity levels of ^{11}C. Results indicate that the higher efficiency of longer pulses lead to higher activities per pulse. However, a key parameter is the repetition rate of the laser, which allow for reaching higher maximum activities before reaching secular equilibrium.

7.2 Future research

Although this doctoral thesis has addressed several key aspects of radioisotope production from laser-driven proton sources, there are several elements for future research which require further exploration:

Firstly, in order to exploit the flexibility of the multi-shot target assembly, other target thicknesses could be explored. Given the ultra-high contrast ratio of the laser system at the L2A2, targets thinner than 1 μm could in principle be used, leading to the notable increase in the resulting ion energies. Targets of different materials or even micro-structured could be investigated. The use of such targets has been reported in literature as a means to enhance some properties of the laser-plasma interaction or the ion acceleration processes.

Secondly, the optimisation of the laser-driven ion source at the L2A2 would lead to the stable production of proton pulses of up to 10 MeV. These proton beams could be then used to produced radioisotopes used in PET medical imaging. Given the stability and the repeatability of the multi-shot target assembly as an ion source, as well as its precise operation, experiments aiming for specific dose levels could be performed. On the other hand, measurements using a TP spectrometer, currently under development at the L2A2, could provide information about the species composition of the accelerated ion beams.

Furthermore, expanding the range of radioisotopes produced using laser-driven proton sources is an area of interest for future investigations. While this thesis focused on the production of a specific radioisotope, there are numerous other isotopes with diverse applications in fields such as medicine, industry, and fundamental research. Exploring different target materials, target

geometries, and irradiation schemes can allow for generating a wider variety of radioisotopes with varying half-lives, decay modes, and chemical properties. In particular, the use of deuterated acceleration targets to produce deuteron beams has been recently studied. These deuterons can be used as well to produce radioisotopes, as there are many nuclear reactions induced by them. In relation with the work presented here, the reaction channel ^{10}B(d,n)^{11}C can be used to produce ^{11}C from a deuteron beam.

Bibliography

[1] William Kruer. *The physics of laser plasma interactions*. crc Press, 2019.

[2] M. Ettehadi-Abari et al. "Absorption of short laser pulses in underdense plasma by considering ohmic heating and ponderomotive force effects". In: *Plasma Physics and Controlled Fusion* 57.8 (2015), p. 085001. DOI: 10.1088/0741-3335/57/8/085001. URL: https://dx.doi.org/10.1088/0741-3335/57/8/085001.

[3] S. C. Wilks et al. "Absorption of ultra-intense laser pulses". In: *Phys. Rev. Lett.* 69 (9 1992), pp. 1383–1386. DOI: 10.1103/PhysRevLett.69.1383. URL: https://link.aps.org/doi/10.1103/PhysRevLett.69.1383.

[4] Stephen P. Hatchett et al. "Electron, photon, and ion beams from the relativistic interaction of Petawatt laser pulses with solid targets". In: *Physics of Plasmas* 7.5 (May 2000), pp. 2076–2082. ISSN: 1070-664X. DOI: 10.1063/1.874030. eprint: https://pubs.aip.org/aip/pop/article-pdf/7/5/2076/12332262/2076_1_online.pdf. URL: https://doi.org/10.1063/1.874030.

[5] S. J. Pestehe and M. Mohammadnejad. "Semi-analytical model of laser resonance absorption in plasmas with a parabolic density profile". In: *Plasma Physics and Controlled Fusion* 52.6 (2010), p. 065012. DOI: 10.1088/0741-3335/52/6/065012. URL: https://dx.doi.org/10.1088/0741-3335/52/6/065012.

[6] Andrea Macchi. *A superintense laser-plasma interaction theory primer*. Springer Science & Business Media, 2013.

[7] H. Schwoerer. "High-Intensity Laser-Matter Interaction". In: *Lasers and Nuclei: Applications of Ultrahigh Intensity Lasers in Nuclear Science* (2006), pp. 7–23.

[8] N. G. Denisov. "On a singularity of the field of an electromagnetic wave propagated in an inhomogeneous plasma". In: *SOVIET PHYSICS JETP-USSR* 4.4 (1957), pp. 544–553.

[9] Peter Mulser and Dieter Bauer. *High power laser-matter interaction*. Vol. 238. Springer, 2010.

[10] Scott C. Wilks and William L. Kruer. "Absorption of ultrashort, ultra-intense laser light by solids and overdense plasmas". In: *IEEE Journal of Quantum Electronics* 33.11 (1997), pp. 1954–1968.

[11] F. Brunel. "Not-so-resonant, resonant absorption". In: *Physical review letters* 59.1 (1987), p. 52.

[12] Paul Gibbon. *Short pulse laser interactions with matter: an introduction*. World Scientific, 2005.

[13] Z. Y. Ge et al. "Resonant absorption and not-so-resonant absorption in short, intense laser irradiated plasma". In: *Physics of Plasmas* 20.7 (July 2013). 073301. ISSN: 1070-664X. DOI: 10.1063/1.4813254. eprint: https://pubs.aip.org/aip/pop/article-pdf/doi/10.1063/1.4813254/16032523/073301_1_online.pdf. URL: https://doi.org/10.1063/1.4813254.

[14] Paul Gibbon and A. R. Bell. "Collisionless absorption in sharp-edged plasmas". In: *Physical review letters* 68.10 (1992), p. 1535.

[15] WLl Kruer and Kent Estabrook. "JxB heating by very intense laser light". In: *The Physics of fluids* 28.1 (1985), pp. 430–432.

[16] Hong-bo Cai et al. "Short-pulse laser absorption via JxB heating in ultrahigh intensity laser plasma interaction". In: *Physics of plasmas* 13.11 (2006), p. 113105.

[17] L. Robson et al. "Scaling of proton acceleration driven by petawatt-laser-plasma interactions". In: *Nature Physics* 3 (Dec. 2007), p. 58. DOI: 10.1038/nphys476. URL: https://www.nature.com/articles/nphys476.

[18] J. Fuchs et al. "Laser-driven proton scaling laws and new paths towards energy increase". In: *Nature Physics* 2 (Dec. 2006), p. 48. DOI: 10.1038/nphys199. URL: https://www.nature.com/articles/nphys199.

[19] M. H. Key et al. "Hot electron production and heating by hot electrons in fast ignitor research". In: *Physics of plasmas* 5.5 (1998), pp. 1966–1972.

[20] G. Malka and J. L. Miquel. "Experimental confirmation of ponderomotive-force electrons produced by an ultrarelativistic laser pulse on a solid target". In: *Physical review letters* 77.1 (1996), p. 75.

[21] M. Roth and M. Schollmeier. "Ion Acceleration—Target Normal Sheath Acceleration". In: *CERN Yellow Reports* 1.0 (Nov. 2016), p. 231. DOI: 10.5170/CERN-2016-

001.231. URL: https://e-publishing.cern.ch/index.php/CYR/article/view/222.

[22] Z. L. Chen et al. "Z-dependence of hot electron generation in femtosecond laser interaction with solid targets". In: *Journal of Physics B: Atomic, Molecular and Optical Physics* 37.3 (2004), p. 539.

[23] V. M. Gordienko et al. "Experimental characterization of hot electron production under femtosecond laser plasma interaction at moderate intensities". In: *Plasma physics and controlled fusion* 44.12 (2002), p. 2555.

[24] A. R. Bell et al. "Fast-electron transport in high-intensity short-pulse laser-solid experiments". In: *Plasma physics and controlled fusion* 39.5 (1997), p. 653.

[25] M. G. Haines et al. "Hot-electron temperature and laser-light absorption in fast ignition". In: *Physical Review Letters* 102.4 (2009), p. 045008.

[26] C. D. Chen et al. "Bremsstrahlung and K-alpha fluorescence measurements for inferring conversion efficiencies into fast ignition relevant hot electrons". In: *Physics of plasmas* 16.8 (2009), p. 082705.

[27] Y. Ping et al. "Absorption of short laser pulses on solid targets in the ultrarelativistic regime". In: *Physical review letters* 100.8 (2008), p. 085004.

[28] Toshiki Tajima and John M. Dawson. "Laser electron accelerator". In: *Physical review letters* 43.4 (1979), p. 267.

[29] Hiroyuki Daido, Mamiko Nishiuchi, and Alexander S. Pirozhkov. "Review of laser-driven ion sources and their applications". In: *Reports on Progress in Physics* 75.5 (2012), p. 056401. DOI: 10.1088/0034-4885/75/5/056401. URL: https://doi.org/10.1088%2F0034-4885%2F75%2F5%2F056401.

[30] Andrea Macchi, Marco Borghesi, and Matteo Passoni. "Ion acceleration by superintense laser-plasma interaction". In: *Rev. Mod. Phys.* 85 (2 2013), pp. 751–793. DOI: 10.1103/RevModPhys.85.751. URL: https://journals.aps.org/rmp/abstract/10.1103/RevModPhys.85.751.

[31] Victor Malka et al. "Principles and applications of compact laser–plasma accelerators". In: *Nature physics* 4.6 (2008), pp. 447–453.

[32] Ken W. D. Ledingham et al. "Towards laser driven hadron cancer radiotherapy: A review of progress". In: *Applied Sciences* 4.3 (2014), pp. 402–443.

[33] S. C. Wilks et al. "Energetic proton generation in ultra-intense laser–solid interactions". In: *Physics of plasmas* 8.2 (2001), pp. 542–549.

[34] A. J. Mackinnon et al. “Enhancement of proton acceleration by hot-electron recirculation in thin foils irradiated by ultraintense laser pulses”. In: *Physical review letters* 88.21 (2002), p. 215006.

[35] P. Mora. “Plasma Expansion into a Vacuum”. In: *Physical Review Letters* 90.18 (May 2003), p. 185002. DOI: 10.1103/PhysRevLett.90.185002. URL: https://journals.aps.org/prl/abstract/10.1103/PhysRevLett.90.185002.

[36] Y. Oishi et al. “Dependence on laser intensity and pulse duration in proton acceleration by irradiation of ultrashort laser pulses on a Cu foil target”. In: *Physics of Plasmas* 12.7 (2005), p. 073102. DOI: 10.1063/1.1943436. eprint: https://doi.org/10.1063/1.1943436. URL: https://aip.scitation.org/doi/10.1063/1.1943436.

[37] K. Zeil et al. “The scaling of proton energies in ultrashort pulse laser plasma acceleration”. In: *New Journal of Physics* 12.4 (2010), p. 045015. DOI: 10.1088/1367-2630/12/4/045015. URL: https://doi.org/10.1088%2F1367-2630%2F12%2F4%2F045015.

[38] M. Borghesi et al. “Multi-MeV proton source investigations in ultraintense laser-foil interactions”. In: *Physical Review Letters* 92.5 (2004), p. 055003.

[39] Hironori Takahashi et al. “Generation of MeV-Order Deuterons by Focusing Low-Terawatt Tabletop Laser Pulses onto Microporous Polytetrafluoroethylene Film Loaded with Deuterated Polystyrene”. In: *Japanese Journal of Applied Physics* 44.No. 13 (2005), pp. L419–L421. DOI: 10.1143/jjap.44.l419. URL: https://doi.org/10.1143%2Fjjap.44.l419.

[40] Takashi Fujii et al. “MeV-order proton and carbon ion acceleration by irradiation of 60 fs TW laser pulses on thin copper tape”. In: *Applied Physics Letters* 83.8 (2003), pp. 1524–1526. DOI: 10.1063/1.1605248. eprint: https://doi.org/10.1063/1.1605248. URL: https://aip.scitation.org/doi/10.1063/1.1605248.

[41] S. Steinke et al. “Acceleration of high charge ion beams with achromatic divergence by petawatt laser pulses”. In: *Phys. Rev. Accel. Beams* 23 (2 2020), p. 021302. DOI: 10.1103/PhysRevAccelBeams.23.021302. URL: https://journals.aps.org/prab/abstract/10.1103/PhysRevAccelBeams.23.021302.

[42] M. Tanabashi et al. "Review of Particle Physics". In: *Phys. Rev. D* 98 (3 2018), p. 030001. DOI: 10.1103/PhysRevD.98.030001. URL: https://link.aps.org/doi/10.1103/PhysRevD.98.030001.

[43] S. Takács et al. "Validation and upgrading of the recommended cross section data of charged particle reactions used for production of PET radioisotopes". In: *Nuclear Instruments and Methods in Physics Research Section B: Beam Interactions with Materials and Atoms* 211.2 (Nov. 2003), pp. 169–189. URL: http://link.aip.org/link/?RSI/72/4477/1.

[44] IAEA. *Charged Particle Cross-Section Database for Medical Radioisotope Production: Diagnostic Radioisotopes and Monitor Reactions*. TECDOC Series 1211. Vienna: INTERNATIONAL ATOMIC ENERGY AGENCY, 2001. URL: https://www.iaea.org/publications/6050/charged-particle-cross-section-database-for-medical-radioisotope-production-diagnostic-radioisotopes-and-monitor-reactions.

[45] R. A. Snavely et al. "Intense High-Energy Proton Beams from Petawatt-Laser Irradiation of Solids". In: *Phys. Rev. Lett.* 85 (14 2000), pp. 2945–2948. DOI: 10.1103/PhysRevLett.85.2945. URL: https://journals.aps.org/prl/abstract/10.1103/PhysRevLett.85.2945.

[46] P. McKenna et al. "Characterization of proton and heavier ion acceleration in ultrahigh-intensity laser interactions with heated target foils". In: *Physical Review E* 70.3 (2004), p. 036405.

[47] M. Tayyab et al. "Experimental investigation on nuclear reactions using a laser-accelerated proton and deuteron beam". In: *Plasma Physics and Controlled Fusion* 61.11 (2019), p. 115007. DOI: 10.1088/1361-6587/ab4339. URL: https://iopscience.iop.org/article/10.1088/1361-6587/ab4339.

[48] S. Fritzler et al. "Proton beams generated with high-intensity lasers: Applications to medical isotope production". In: *Applied Physics Letters* 83.15 (Aug. 2003), pp. 3039–3041. DOI: 10.1063/1.1616661. eprint: https://doi.org/10.1063/1.1616661. URL: https://doi.org/10.1063/1.1616661.

[49] Alexander S. Pirozhkov et al. "Laser-Driven Proton Acceleration Research and Development". In: *Advances in Solid State Lasers*. Ed. by Mikhail Grishin. Rijeka: IntechOpen, 2010. Chap. 25. DOI: 10.5772/7967. URL: https://www.intechopen.com/books/advances-in-solid-state-lasers-development-and-

applications/laser-driven-proton-acceleration-research-and-development.

[50] Mahmoud L. Firouzbakht, David J. Schlyer, and Alfred P. Wolf. "Yield Measurements for the 11B(p,n)11C and the 10B(d,n)11C Nuclear Reactions". In: *Nuclear Medicine and Biology* 25.2 (Feb. 1998), pp. 161 –164. ISSN: 0969-8051. DOI: https://doi.org/10.1016/S0969-8051(97)00136-4. URL: http://www.sciencedirect.com/science/article/pii/S0969805197001364.

[51] Zhanliang Sun. "Production of nuclear medicine radioisotopes with ultra-intense lasers". In: *AIP Advances* 11.4 (2021), p. 040701.

[52] Sachie Kimura and Aldo Bonasera. "Deuteron-induced reactions generated by intense lasers for PET isotope production". In: *Nuclear Instruments and Methods in Physics Research Section A: Accelerators, Spectrometers, Detectors and Associated Equipment* 637.1 (May 2011), pp. 164 –170. ISSN: 0168-9002. DOI: https://doi.org/10.1016/j.nima.2011.02.043. URL: http://www.sciencedirect.com/science/article/pii/S0168900211003561.

[53] I. Spencer et al. "Laser generation of proton beams for the production of short-lived positron emitting radioisotopes". In: *Nuclear Instruments and Methods in Physics Research Section B: Beam Interactions with Materials and Atoms* 183.3-4 (2001), pp. 449–458.

[54] E. Lefebvre et al. "Electron and photon production from relativistic laser-plasma interactions". In: *Nuclear Fusion* 43.7 (July 2003), pp. 629–633. ISSN: 1741-4326. DOI: 10.1063/1.2178653. URL: https://aip.scitation.org/doi/10.1063/1.2178653.

[55] M. Seimetz et al. "Detailed requirements for a laser-based proton/ion accelerator for radioisotope production". In: *2015 IEEE Nuclear Science Symposium and Medical Imaging Conference (NSS/MIC)*. 2015, pp. 1–5. DOI: 10.1109/NSSMIC.2015.7582187. URL: https://ieeexplore.ieee.org/abstract/document/7582187.

[56] M. Borghesi et al. "Fast Ion Generation by High-Intensity Laser Irradiation of Solid Targets and Applications". In: *Fusion Science and Technology* 49.3 (2006), pp. 412–439. DOI: 10.13182/FST06-A1159. eprint: https://doi.org/10.13182/FST06-A1159. URL: https://www.tandfonline.com/doi/abs/10.13182/FST06-A1159.

[57] S. Fourmaux et al. "Investigation of laser-driven proton acceleration using ultra-short, ultra-intense laser pulses". In: *Physics of Plasmas* 20.1 (2013), p. 013110. DOI: 10.1063/1.4789748. eprint: https://doi.org/10.1063/1.4789748. URL: https://aip.scitation.org/doi/10.1063/1.4789748.

[58] Theodore H. Maiman et al. "Stimulated optical radiation in ruby". In: (1960).

[59] Arthur L. Schawlow and Charles H. Townes. "Infrared and optical masers". In: *Physical Review* 112.6 (1958), p. 1940.

[60] Nikolai Gennadievich Basov, Oleg Nikolaevich Krokhin, and Yurii Mikhailovich Popov. "Generation, amplification, and detection of infrared and optical radiation by quantum-mechanical systems". In: *Uspekhi Fizicheskikh Nauk* 72.2 (1960), pp. 161–209.

[61] Fred J. McClung and Robert W. Hellwarth. "Giant optical pulsations from ruby". In: *Applied Optics* 1.101 (1962), pp. 103–105.

[62] Herman A. Haus. "Mode-locking of lasers". In: *IEEE Journal of Selected Topics in Quantum Electronics* 6.6 (2000), pp. 1173–1185.

[63] P. McKenna et al. "Characterization of multiterawatt laser-solid interactions for proton acceleration". In: *Review of Scientific Instruments* 73.12 (Mar. 2019), pp. 4176–4184. ISSN: 0034-6748. DOI: 10.1063/1.1516855. URL: https://aip.scitation.org/doi/10.1063/1.1516855.

[64] Lieselotte Obst et al. "Efficient laser-driven proton acceleration from cylindrical and planar cryogenic hydrogen jets". In: *Scientific Reports* 7.1 (Aug. 2017), p. 10248. ISSN: 2045-2322. DOI: 10.1038/s41598-017-10589-3. URL: https://www.nature.com/articles/s41598-017-10589-3.

[65] Donna Strickland and Gerard Mourou. "Compression of amplified chirped optical pulses". In: *Optics communications* 55.6 (1985), pp. 447–449.

[66] Aurélie Jullien et al. "10e10 temporal contrast for femtosecond ultraintense lasers by cross-polarized wave generation". In: *Optics letters* 30.8 (2005), pp. 920–922.

[67] Friedrich Carl Alwin Pockels. *Lehrbuch der kristalloptik*. BG Teubner, 1906.

[68] C. Thaury et al. "Plasma mirrors for ultrahigh-intensity optics". In: *Nature Physics* 3 (Apr. 2007), p. 424. DOI: https://doi.org/10.1038/nphys595. URL: https://www.nature.com/articles/nphys595.

[69] M. Kaluza et al. "Influence of the Laser Prepulse on Proton Acceleration in Thin-Foil Experiments". In: *PRL* 93.4 (July 2004), p. 045003. DOI: 10.1103/PhysRevLett.

93.045003. URL: https://journals.aps.org/prl/abstract/10.1103/PhysRevLett.93.045003.

[70] D. Neely et al. "Enhanced proton beams from ultrathin targets driven by high contrast laser pulses". In: *Applied Physics Letters* 89.2 (2006), p. 021502. DOI: 10.1063/1.2220011. eprint: https://doi.org/10.1063/1.2220011. URL: https://aip.scitation.org/doi/10.1063/1.2220011.

[71] J. Benlliure et al. "Validation of the radiation shielding for the Laser Laboratory for Acceleration and Applications". In: *Nuclear Instruments and Methods in Physics Research Section A: Accelerators, Spectrometers, Detectors and Associated Equipment* 916 (2019), pp. 158 –168. ISSN: 0168-9002. DOI: https://doi.org/10.1016/j.nima.2018.10.217. URL: http://www.sciencedirect.com/science/article/pii/S0168900218315407.

[72] L. Martín et al. "Improved stability of a compact vacuum-free laser-plasma X-ray source". In: *High Power Laser Science and Engineering* 8 (2020), e18. DOI: 10.1017/hpl.2020.15. URL: https://www.cambridge.org/core/journals/high-power-laser-science-and-engineering/article/improved-stability-of-a-compact-vacuumfree-laserplasma-xray-source/594C572C3937DFB5738A

[73] L. Volpe et al. "Generation of high energy laser-driven electron and proton sources with the 200 TW system VEGA 2 at the Centro de Laseres Pulsados". In: *High Power Laser Science and Engineering* 7 (2019), e25. DOI: 10.1017/hpl.2019.10. URL: https://www.cambridge.org/core/journals/high-power-laser-science-and-engineering/article/generation-of-high-energy-laserdriven-electron-and-proton-sources-with-the-200-tw-system-vega-2-at-the-centro-de-laseres-pulsados/7045225598333BD35DF9C0A15C758F01.

[74] P. R. Bolton et al. "Instrumentation for diagnostics and control of laser-accelerated proton (ion) beams". In: *Physica Medica* 30.3 (May 2014), pp. 255 –270. ISSN: 1120-1797. DOI: 10.1016/j.ejmp.2013.09.002. URL: http://www.sciencedirect.com/science/article/pii/S1120179713003979.

[75] Fabrizio Bisesto et al. "Review on TNSA diagnostics and recent developments at SPARC-LAB". In: *High Power Laser Science and Engineering* 7 (2019), e56. DOI: 10.1017/hpl.2019.41. URL: https://www.cambridge.org/core/journals/high-power-laser-science-and-engineering/article/review-

on-tnsa-diagnostics-and-recent-developments-at-sparclab/B440C51C869AED1D23AC766AF28C8AAA.

[76] M. Seimetz et al. "PADC nuclear track detector for ion spectroscopy in laser-plasma acceleration". In: *Physica Medica* 76 (2020), pp. 72 –76. ISSN: 1120-1797. DOI: https://doi.org/10.1016/j.ejmp.2020.06.005. URL: http://www.sciencedirect.com/science/article/pii/S1120179720301381.

[77] X. H. Xu et al. "Detection and analysis of laser driven proton beams by calibrated Gafchromic HD-V2 and MD-V3 radiochromic films". In: *Review of Scientific Instruments* 90.3 (2019), p. 033306. DOI: 10.1063/1.5049499. eprint: https://doi.org/10.1063/1.5049499. URL: https://aip.scitation.org/doi/10.1063/1.5049499.

[78] I. W. Choi et al. "Absolute calibration of a time-of-flight spectrometer and imaging plate for the characterization of laser-accelerated protons". In: *Measurement Science and Technology* 20.11 (2009), p. 115112.

[79] R. Prasad et al. "Calibration of Thomson parabola—MCP assembly for multi-MeV ion spectroscopy". In: *Nuclear Instruments and Methods in Physics Research Section A: Accelerators, Spectrometers, Detectors and Associated Equipment* 623.2 (2010). 1rs International Conference on Frontiers in Diagnostics Technologies, pp. 712 –715. ISSN: 0168-9002. DOI: https://doi.org/10.1016/j.nima.2010.02.078. URL: http://www.sciencedirect.com/science/article/pii/S0168900210002767.

[80] G. V. O'Rielly, N. R. Kolb, and R. E. Pywell. "The response of plastic scintillator to protons and deuterons". In: *Nuclear Instruments and Methods in Physics Research Section A: Accelerators, Spectrometers, Detectors and Associated Equipment* 368.3 (1996), pp. 745 –749. ISSN: 0168-9002. DOI: https://doi.org/10.1016/0168-9002(95)00671-0. URL: http://www.sciencedirect.com/science/article/pii/0168900295006710.

[81] J. S. Green et al. "Characterisation of plastic scintillators for detection of laser-accelerated protons". In: (2011).

[82] P. Bellido et al. "Characterization of protons accelerated from a 3 TW table-top laser system". In: *Journal of Instrumentation* 12.05 (2017), T05001–T05001. DOI: 10.1088/1748-0221/12/05/t05001. URL: https://iopscience.iop.org/article/10.1088/1748-0221/12/05/T05001.

[83] J. J. Thomson. "XXVI. Rays of positive electricity". In: *The London, Edinburgh, and Dublin Philosophical Magazine and Journal of Science* 21.122 (1911), pp. 225–249. DOI: 10.1080/14786440208637024. eprint: https://doi.org/10.1080/14786440208637024. URL: https://doi.org/10.1080/14786440208637024.

[84] D. C. Carroll et al. "A modified Thomson parabola spectrometer for high resolution multi-MeV ion measurements–Application to laser-driven ion acceleration". In: *Nuclear Instruments and Methods in Physics Research Section A: Accelerators, Spectrometers, Detectors and Associated Equipment* 620.1 (2010). COULOMB09, pp. 23–27. ISSN: 0168-9002. DOI: https://doi.org/10.1016/j.nima.2010.01.054. URL: https://www.sciencedirect.com/science/article/pii/S0168900210001221.

[85] Carlos Salgado-Lopez et al. "Angular-resolved Thomson parabola spectrometer for laser-driven ion accelerators". In: *Sensors* 22.9 (2022), p. 3239.

[86] John Hammersley. *Monte carlo methods*. Springer Science & Business Media, 2013.

[87] M. Shoucri, B. Afeyan, and M. Charbonneau-Lefort. "Numerical simulation for ion acceleration in an intense laser wave incident on an overdense plasma". In: *Journal of Physics D: Applied Physics* 41.21 (Oct. 2008), p. 215205. ISSN: 1361-6463. DOI: 10.1088/0022-3727/41/21/215205. URL: https://iopscience.iop.org/article/10.1088/0022-3727/41/21/215205/meta.

[88] N. J. Sircombe, S. J. Hughes, and M. G. Ramsay. "Integrated calculations of short-pulse laser interactions with matter". In: *New Journal of Physics* 15.2 (2013), p. 025025. DOI: 10.1088/1367-2630/15/2/025025. URL: https://iopscience.iop.org/article/10.1088/1367-2630/15/2/025025.

[89] Charles K. Birdsall and A. Bruce Langdon. *Plasma physics via computer simulation*. CRC press, 2004.

[90] Roger W. Hockney and James W. Eastwood. *Computer simulation using particles*. crc Press, 2021.

[91] T. D. Arber et al. "Contemporary particle-in-cell approach to laser-plasma modelling". In: *Plasma Physics and Controlled Fusion* 57.11 (2015), p. 113001. DOI: 10.1088/0741-3335/57/11/113001. URL: https://doi.org/10.1088%2F0741-3335%2F57%2F11%2F113001.

[92] J. Derouillat et al. "Smilei : A collaborative, open-source, multi-purpose particle-in-cell code for plasma simulation". In: *Computer Physics Communications* 222 (2018),

pp. 351 –373. ISSN: 0010-4655. DOI: https://doi.org/10.1016/j.cpc.2017.09.024. URL: http://www.sciencedirect.com/science/article/pii/S0010465517303314.

[93] Jay P. Boris et al. "Relativistic plasma simulation-optimization of a hybrid code". In: *Proc. Fourth Conf. Num. Sim. Plasmas*. 1970, pp. 3–67.

[94] Carlos A. De Moura and Carlos S. Kubrusly. "The courant–friedrichs–lewy (cfl) condition". In: *AMC* 10.12 (2013).

[95] Roberto Lera et al. "Development of a few TW Ti: Sa laser system at 100 Hz for proton acceleration". In: *Applied Physics B* 125 (2019), pp. 1–8.

[96] I. Prencipe et al. "Targets for high repetition rate laser facilities: needs, challenges and perspectives". In: *High Power Laser Science and Engineering* 5 (July 2017), e17. DOI: 10.1017/hpl.2017.18. URL: https://www.cambridge.org/core/journals/high-power-laser-science-and-engineering/article/targets-for-high-repetition-rate-laser-facilities-needs-challenges-and-perspectives/93DD99BE668FFB0A25C13C2E5295DC53.

[97] Takuya Nayuki et al. "Thin tape target driver for laser ion accelerator". In: *Review of Scientific Instruments* 74.7 (2003), pp. 3293–3296. DOI: 10.1063/1.1578156. eprint: https://doi.org/10.1063/1.1578156. URL: https://aip.scitation.org/doi/10.1063/1.1578156.

[98] Ying Gao et al. "An automated, 0.5 Hz nano-foil target positioning system for intense laser plasma experiments". In: *High Power Laser Science and Engineering* 5 (2017), e12. DOI: 10.1017/hpl.2017.10. URL: https://www.cambridge.org/core/journals/high-power-laser-science-and-engineering/article/an-automated-05-hz-nanofoil-target-positioning-system-for-intense-laser-plasma-experiments/8A6D8618C7A1FA34C59ABA61

[99] Yonatan Gershuni et al. "A gatling-gun target delivery system for high-intensity laser irradiation experiments". In: *Nuclear Instruments and Methods in Physics Research Section A: Accelerators, Spectrometers, Detectors and Associated Equipment* 934 (2019), pp. 58 –62. ISSN: 0168-9002. DOI: https://doi.org/10.1016/j.nima.2019.04.071. URL: http://www.sciencedirect.com/science/article/pii/S0168900219305455.

[100] Rosaletizia Zaffino et al. "Preparation and characterization of micro-nano engineered targets for high-power laser experiments". In: *Microelectronic Engineering* 194 (2018),

pp. 67 –70. ISSN: 0167-9317. DOI: 10.1016/j.mee.2018.03.011. URL: http://www.sciencedirect.com/science/article/pii/S0167931718301217.

[101] C. Spindloe et al. "High volume fabrication of laser targets using MEMS techniques". In: *Journal of Physics: Conference Series* 713 (2016), p. 012002. DOI: 10.1088/1742-6596/713/1/012002. URL: https://iopscience.iop.org/article/10.1088/1742-6596/713/1/012002.

[102] John T. Morrison et al. "MeV proton acceleration at kHz repetition rate from ultra-intense laser liquid interaction". In: *New Journal of Physics* 20.2 (2018), p. 022001. DOI: 10.1088/1367-2630/aaa8d1. URL: https://iopscience.iop.org/article/10.1088/1367-2630/aaa8d1.

[103] J. Polz et al. "Efficient laser-driven proton acceleration from a cryogenic solid hydrogen target". In: *Nature Scientific Reports* 9.16534 (2019). DOI: 10.1038/s41598-019-52919-7. URL: https://www.nature.com/articles/s41598-019-52919-7.

[104] Sudipta Mondal et al. "Surface plasma attosource beamlines at ELI-ALPS". In: *J. Opt. Soc. Am. B* 35.5 (2018), A93–A102. DOI: 10.1364/JOSAB.35.000A93. URL: http://josab.osa.org/abstract.cfm?URI=josab-35-5-A93.

[105] Timofej Chagovets et al. "Automation of Target Delivery and Diagnostic Systems for High Repetition Rate Laser-Plasma Acceleration". In: *Applied Sciences* 11.4 (2021). ISSN: 2076-3417. DOI: 10.3390/app11041680. URL: https://www.mdpi.com/2076-3417/11/4/1680.

[106] Ilya Alexeev et al. "Determination of laser beam focus position based on secondary speckles pattern analysis". In: *Appl. Opt.* 56.26 (2017), pp. 7413–7418. DOI: 10.1364/AO.56.007413. URL: http://ao.osa.org/abstract.cfm?URI=ao-56-26-7413.

[107] F. Nürnberg et al. "Radiochromic film imaging spectroscopy of laser-accelerated proton beams". In: *Review of scientific instruments* 80.3 (2009), p. 033301.

[108] P. K. Singh et al. "Intensified proton and carbon ion flux from femtosecond laser driven plasma source". In: *Physics of Plasmas* 25.11 (2018), p. 113113. DOI: 10.1063/1.5053964. eprint: https://doi.org/10.1063/1.5053964. URL: https://aip.scitation.org/doi/10.1063/1.5053964.

[109] D. Batani et al. "Proton acceleration measurements using fs laser irradiation of foils in the target normal sheath acceleration regime". In: *Physics of Plasmas* 25.5 (Mar.

2019), p. 054506. ISSN: 1070-664X. DOI: 10.1063/1.5029854. URL: https://aip.scitation.org/doi/10.1063/1.5029854.

[110] Akifumi Yogo et al. "Laser prepulse dependency of proton-energy distributions in ultraintense laser-foil interactions with an online time-of-flight technique". In: *Physics of Plasmas* 14.4 (2007), p. 043104. DOI: 10.1063/1.2721066. eprint: https://doi.org/10.1063/1.2721066. URL: https://aip.scitation.org/doi/10.1063/1.2721066.

[111] A. Lübcke et al. "Prospects of target nanostructuring for laser proton acceleration". In: *Scientific Reports* 7 (Mar. 2017), p. 44030. DOI: 10.1038/srep44030. URL: https://www.nature.com/articles/srep44030.

[112] Hiroaki Kishimura et al. "Enhanced generation of fast protons from a polymer-coated metal foil by a femtosecond intense laser field". In: *Applied Physics Letters* 85.14 (2004), pp. 2736–2738. DOI: 10.1063/1.1803915. eprint: https://doi.org/10.1063/1.1803915. URL: https://aip.scitation.org/doi/10.1063/1.1803915.

[113] I. Spencer et al. "Experimental study of proton emission from 60-fs, 200-mJ high-repetition-rate tabletop-laser pulses interacting with solid targets". In: *Phys. Rev. E* 67 (4 2003), p. 046402. DOI: 10.1103/PhysRevE.67.046402. URL: https://journals.aps.org/pre/abstract/10.1103/PhysRevE.67.046402.

[114] M. Nishiuchi et al. "Focusing and spectral enhancement of a repetition-rated, laser-driven, divergent multi-MeV proton beam using permanent quadrupole magnets". In: *Applied Physics Letters* 94.6 (2009), p. 061107. DOI: 10.1063/1.3078291. eprint: https://doi.org/10.1063/1.3078291. URL: https://aip.scitation.org/doi/10.1063/1.3078291.

[115] M. Nishiuchi et al. "Efficient production of a collimated MeV proton beam from a polyimide target driven by an intense femtosecond laser pulse". In: *Physics of Plasmas* 15.5 (2008), p. 053104. DOI: 10.1063/1.2928161. eprint: https://doi.org/10.1063/1.2928161. URL: https://aip.scitation.org/doi/10.1063/1.2928161.

[116] Akifumi Yogo et al. "Measurement of DNA Double-Strand Break Yield in Human Cancer Cells by High-Current, Short-Duration Bunches of Laser-Accelerated Protons". In: *Japanese Journal of Applied Physics* 50.10 (2011), p. 106401. DOI: 10.1143/jjap.

50.106401. URL: https://iopscience.iop.org/article/10.1143/JJAP.50.106401.

[117] Pablo Cabanelas et al. "EnsarRoot: The framework for simulation and data analysis for ENSAR". In: *Journal of Physics: Conference Series*. Vol. 1024. 1. IOP Publishing. 2018, p. 012038.